Investigating the auroral electrojet system from satellite magnetic data

Thesis presented by

Cecilie Drost Aakjær

DTU Space - National Space Institute
Technical University of Denmark
Kongens Lyngby, Denmark

August 2017

Investigating the auroral electrojet system from satellite magnetic data

PhD Thesis

Cecilie Drost Aakjær
National Space Institute, Technical University of Denmark,
Diplomvej 371, DK-2800 Kongens Lyngby

Supervised by
Nils Olsen, National Space Institute, Technical University of Denmark
Christopher Finlay, National Space Institute, Technical University of Denmark

2. edition
ISBN: 978-87-91694-37-0

Preface

This PhD thesis presents the culmination of a three year study carried out in the geomagnetism department at the National Space Institute, DTU Space, at the Technical University of Denmark. The study is funded partially by the Research council of Norway, and supervised by Professor Nils Olsen and Dr. Christopher C. Finlay. At the beginning of my PhD, I was told that a PhD would transform me from a student to a scientist. At the time, it scared me, because how could anyone learn this much in three years? Looking back now, I realize how much I have developed both in academia and on a personal level, and to that I owe a great thanks to my supervisor, Nils Olsen. Though busy, Nils always found the time for me when needed, and I never left his office without new ideas for improving my model. When Nils was away, the door of Christopher Finlay was always open, to discuss results and texts or to help me past mathematical obstacles, and to that I am very grateful.

To finish a PhD, you need to work hard - to enjoy the process, you need to find inspiration in your field of subject and support in your home and working environment. I, fortunately experienced both. The geomagnetism group has played the role of supporting colleagues well and provided a base where I have enjoyed coming to work. I would also like to give a heartfelt thanks to Birte Hede, for making sure that my life as a PhD student has run as smooth as possible and to always be there if I needed someone to talk to. In the final part of my PhD, I have exploited the goodwill of many. It means a lot to me that so many have taken their time to proofread parts of my thesis and provide supporting peptalks - Thank you, Ashley, Peter, Nils, Chris, Lars, Stavros, Eigil, Nynne, Magnus and Niels for this great help. I furthermore owe a great thanks to Liisa Juusola and Ashley Smith for discussions on ionospheric currents, and to provide comparable plots for inter model comparisons of the auroral electrojet system.

Last, but not least, I would like to thank ESA for providing the prompt access to the *Swarm* Level 1b data, and to the Reasearch Council of Norway, through the PETROMAKS research programme, to provide the funds necessary for the completion of the PhD.

Kongens Lyngby, May 2017

Cecilie Drost Aakjær

Acronyms and symbols

Acronyms

AE	Auroral electrojet
AMPERE	Active magnetosphere and planetary electrodynamics response experiment
ASM	Absolute scalar magnetometer
ATG	Along track gradient
CGM	Corrected Geomagnetic
CHAMP	Challenging minisatellite payload
CME	Coronal mass ejection
DEMA	Danish Emergency Management Agency
Dst	Disturbance storm-time
EAEJ	Eastern auroral electrojet
EUV	Solar extreme ultraviolet radiation
ESA	European Space Agency
FAC	Field aligned current
GPS	Global positioning system
GSM	Geocentric solar magnetospheric
Kp	Planetarische Kennziffern (Planetary K index)
IGRF	International geomagnetic reference field
IM	Intensity model
IMAGE	International monitor for auroral geomagnetic effects
IMF	Interplanetary magnetic field
IRLS	Iterative reweighted least squares
LCM	Line current model
MAD	Mean absolute deviation
MagSat	Magnetic Field Satellite
MHD	Magnetohydrodynamics
MLT	Magnetic local time
NH	Northern Hemisphere

PDF	Probability density function
QD	Quasi dipole
RMS	Root mean square
RC	Ring current
SAC-C	Scientific Application Satellite-C
SECS	Spherical elementary current system
SH	Southern Hemisphere
Sq	Solar quiet
SVD	Singular value decomposition
TSVD	Truncated singular value decomposition
UT	Universal time
VFM	Vector fluxgate magnetometer
V_R	Variance ratio
WEAJ	Western auroral electrojet

Symbols

a	Earth's mean radius, set to 6371.2 km
$\boldsymbol{A}$	Design matrix for the calculations of $\boldsymbol{J}$ in the 1D SECS method
$\mathcal{A}$	Semi minor axis of ellipsis
$\boldsymbol{A_{c,r}}$	Curl-free part of $\boldsymbol{A}$ associated with $\boldsymbol{B}_r$
$\boldsymbol{A_{c,\theta}}$	Curl-free part of $\boldsymbol{A}$ associated with $\boldsymbol{B}_\theta$
$\boldsymbol{A_{c,\phi}}$	Curl-free part of $\boldsymbol{A}$ associated with $\boldsymbol{B}_\phi$
$\boldsymbol{A_{d,r}}$	Divergence-free part of $\boldsymbol{A}$ associated with $\boldsymbol{B}_r$
$\boldsymbol{A_{d,\theta}}$	Divergence-free part of $\boldsymbol{A}$ associated with $\boldsymbol{B}_\theta$
$\boldsymbol{A_{d,\phi}}$	Divergence-free part of $\boldsymbol{A}$ associated with $\boldsymbol{B}_\phi$
$\boldsymbol{B}$	Magnetic field
$\boldsymbol{B}_r$	Radial magnetic field
$\tilde{\boldsymbol{B}}$	Radial magnetic field in frequency domain
$\boldsymbol{B}_H$	Horizontal magnetic field
$\boldsymbol{B}^{\text{mod}}$	Modelled estimate of the residual magnetic field observations (used in 1D SECS method)
$\boldsymbol{B}^{\text{obs}}$	Residual magnetic field observations (used in 1D SECS method)
$\boldsymbol{B}_\theta$	θ component of the magnetic field
$\tilde{\boldsymbol{B}}_\theta$	θ component of the magnetic field in frequency domain
$\boldsymbol{B}_\phi$	ϕ component of the magnetic field
$\boldsymbol{B}_{\|\|}$	Field aligned currents
$\delta\boldsymbol{B}$	Residual magnetic field
$\delta\boldsymbol{B}_r$	Radial magnetic field residual

$\delta \boldsymbol{B}_H$	Horizontal magnetic field residual
$\mathcal{B}$	Semi major axis of ellipsis
c	Speed of light
C	Constant
d	Depth of superconductor
$\boldsymbol{D}$	Controlling the measure in which $\boldsymbol{m}$ is minimized in inverse problems
$\boldsymbol{d}^{\text{obs}}$	Residual magnetic field observations (used in LCM)
$\boldsymbol{d}^{\text{mod}}$	Modelled estimate of the magnetif field observations (used in LCM)
$d\delta$	Width of boxfunction
e	Unit charge
$\boldsymbol{E}$	Electric field
$\hat{\boldsymbol{e}}_r$	Unit vector along the radial component of the magnetic field
$\hat{\boldsymbol{e}}_\theta$	Unit vector along the θ component of the magnetic field
$\hat{\boldsymbol{e}}_\phi$	Unit vector along the ϕ component of the magnetic field
$\hat{\boldsymbol{f}}$	Unit vector along constant QD latitude
$\boldsymbol{F}^{\text{obs}}$	Magnetic field intensity
$\boldsymbol{F}^{\text{mod}}$	Main field and magnetospheric contribution to the magnetic field intensity
$\delta \boldsymbol{F}^{\text{obs}}$	Residual magnetic field (ionospheric contribution)
$\boldsymbol{F}_g$	Gravitational force
$\boldsymbol{G}$	Design matrix
$\boldsymbol{G}\dagger$	General inverse of $\boldsymbol{G}$
h	Singular value number
$\boldsymbol{H}$	Horizontal component of the main field
I^M	Magnetic inclination
$\boldsymbol{I}$	Identity matrix
$\boldsymbol{\mathcal{I}}$	Current strength and model parameters for the 1D SECS method
$\boldsymbol{\mathcal{I}}_d$	Divergence-free part of $\mathcal{I}$
$\boldsymbol{\mathcal{I}}_c$	Curl-free part of $\mathcal{I}$
$\boldsymbol{\mathcal{I}}_2$	Current strength and model parameters for the 1D SECS method estimated from synthetic magnetic observations
$\boldsymbol{\mathcal{I}}_{cf}^{TSVD}$	Curl-free part of $\boldsymbol{\mathcal{I}}$ estimated using TSVD regularization
$\boldsymbol{\mathcal{I}}_{df}^{TSVD}$	Divergence-free part of $\boldsymbol{\mathcal{I}}$ estimated using TSVD regularization
$\boldsymbol{j}$	Line current amplitude
$\boldsymbol{j}'$	non-rotated line current amplitude
$\boldsymbol{J}$	Sheet current densities
$\boldsymbol{J}_{cf}$	Curl-free part of sheet current densities
$\boldsymbol{J}_{df}$	Divergence-free part of sheet current densities
$\boldsymbol{J}_r$	Radial component of the sheet current density
$\boldsymbol{J}_\theta$	θ component of the sheet current density
$\boldsymbol{J}_\phi$	ϕ component of the sheet current density

$\boldsymbol{J}^{\text{peak}}$	Geomagnetic activity index of the peak strength and position of the western and eastern electrojet
$\boldsymbol{J}^{\text{tot}}$	Geomagnetic activity index of the total current at $\pm 50\beta$ from the North and South geomagnetic pole
$\boldsymbol{J}^{\text{mod}}$	Modelled estimate of the sheet current densities
$\boldsymbol{J}^{\text{obs}}$	Synthetic observations of the sheet current densities
k	Number of model parameters
K	Boltzman's constant
$\boldsymbol{m}$	Model parameter vector
$\boldsymbol{m}^{LS}$	Model parameter vector estimated with least squares regularization
$\boldsymbol{m}^{Tik}$	Model parameter vector estimated with Tikhonov regularization
$\boldsymbol{m}^{L_2}$	Model parameter vector estimated with Tikhonov regularization and a Huber weghted misfit measure
$\boldsymbol{m}^{L_2,D_1}$	Model parameter vector estimated with minimization of the first order along track differences on data and a Huber weighted misfit measure
$\boldsymbol{m}^{TSVD}$	Model parameter vector estimated with TSVD regularization
$\boldsymbol{m}^{maxent}$	Model parameter vector estimated with Maximum entropy regularization
$\boldsymbol{m}^{L_1}$	Model parameter vector estimated with minimization of an L_1 norm of the second order along track differences of model parameters along with a Huber-weighted misfit measure
$\boldsymbol{m}^{L_1,D_I}$	Model parameter vector estimated with minimization of an L_1 norm of the first order along track differences of model parameters along with a Huber-weighted misfit measure
M	Size of model parameter vector
$\boldsymbol{M}$	Design matrix for 1D SECS method
$\boldsymbol{M}_{c,r}$	Curl-free part of $\boldsymbol{M}$ associated with $\boldsymbol{B}_r$
$\boldsymbol{M}_{c,\theta}$	Curl-free part of $\boldsymbol{M}$ associated with $\boldsymbol{B}_\theta$
$\boldsymbol{M}_{c,\phi}$	Curl-free part of $\boldsymbol{M}$ associated with $\boldsymbol{B}_\phi$
$\boldsymbol{M}_{d,r}$	Divergence-free part of $\boldsymbol{M}$ associated with $\boldsymbol{B}_r$
$\boldsymbol{M}_{d,\theta}$	Divergence-free part of $\boldsymbol{M}$ associated with $\boldsymbol{B}_\theta$
$\boldsymbol{M}_{d,\phi}$	Divergence-free part of $\boldsymbol{M}$ associated with $\boldsymbol{B}_\phi$
n	Number of observations
n_e	Electron density
n_i	Ion density
N	Size of observation vector
$N(A)$	Null space of $\boldsymbol{m}$
N_e	Number density of electrons
p	Pressure
P_l	Associated Legendre function
$\tilde{P}_l$	Non-normalized associated Legendre function
Q	Q-response

$\tilde{Q}$	Q-response in frequency domain
$\boldsymbol{Q}^A$	Diagonal matrix in maximum entropy solution to inverse problems. Defined on page 58
$\boldsymbol{Q}^B$	Matrix in maximum entropy solution to inverse problems. Defined on page 58
$\boldsymbol{r}$	Radius
$\hat{\boldsymbol{r}}$	Radial unit vector
r_c	Radius of superconducting layer
$\boldsymbol{r}_k$	Radius of the model parameters
$\boldsymbol{r}_n$	Radius of the satellite orbit (observations)
r_I	Radius of the ionosphere, 110 km above the Earth's mean radius
$R(A)$	Solution space of $\boldsymbol{m}$ in $\boldsymbol{d}$
R^M	Model space
s	Sensitivity of Huber weights
t	Time
T	Temperature
$\mathcal{T}$	Period
$\boldsymbol{U}$	An $N \times N$ orthonormal matrix consisting of basis vectors spanning the data space, R^N used in SVD
$\boldsymbol{v}$	Bulk velocity
v_i	Drift velocity of ions
v_e	Drift velocity of electrons
$\hat{\boldsymbol{v}}$	Unit vector along satellite track
$\boldsymbol{V}$	Magnetic potential
$\boldsymbol{V}^{\text{ground}}$	Magnetic potential at ground
$\boldsymbol{V}^{\text{sat}}$	Magnetic potential at satellite altitude
V_R	Variance ratio
$\boldsymbol{W}^d$	Controlling the minimization norm of the model parameters
$\boldsymbol{W}^m$	Controlling the weight of individual observation points - Huber weights
$\boldsymbol{X}$	An $M \times M$ orthonormal matrix spanning the model space R^M
$\boldsymbol{Z}$	Vertical component of the main field.
α^2	Regularization parameter (damping parameter) for regularized inverse problems
$\boldsymbol{\beta}$	Arc length angle of the satellite track
γ	Rotation angle of ellipsis
Γ	Transformation factor between ζ and χ
δ	Angle between rotated and non-rotated currents
$\delta \boldsymbol{F}$	Magnetic field intensity caused by the auroral electrojet currents
$\delta \boldsymbol{F}^{mod}$	Modelled estimate of δF
$\delta\theta^{\text{mod}}$	Model spacing
$\delta\theta^{\text{obs}}$	Observation spacing
Δ	Distance between line currents
Δd	Residuals between the observations and the model estimates

ϵ_0	Permittivity of free space
ϵ	Regularization parameter from Ekblom measure, ensuring non-singular solution at $j_k = 0$
ε	Truncation parameter used in TSVD solutions
ε_A	Truncation parameter for design matrix $\boldsymbol{A}$
ε_M	Truncation parameter for design matrix $\boldsymbol{M}$
ε_d	Truncation parameter for the divergence-free part of the calculations in $\boldsymbol{M}$
ε_c	Truncation parameter for the curl-free part of the calculations in $\boldsymbol{M}$
ζ	Internal ionospheric expansion coefficient
η	Horizontal distance between line current and observation point
θ	Co-latitude
θ_c	Latitude of the centre of a synthetic electrojet
ι	Internal induced expansion coefficient
κ	Singular value number
μ_0	Permeability of free space
ξ	Radial distance between line current and observation point
ρ	Mass density
σ_c	Conductivity
$\sigma^2_{\Delta\delta d}$	Variance of the residuals between the observations and the model estimates
$\sigma^2_{d^{obs}}$	Variance of the magnetic observations
Σ_P	Pedersen conductance
Σ_H	Hall conductance
Υ	Eccentricity of ellipsis
ϕ	Longitude
ϕ^d	Objective function for misfit between predicted data and observations
$\phi^{d,tar}$	Target misfit between predicted data and observations
ϕ^m	Objective function for structure of model parameters
$\boldsymbol{\Phi}$	Objective function for the inverse problems
χ	External ionospheric expansion coefficient
ω	Angular frequency
ω_s	Regularization parameter of maximum entropy solution

Coordinate systems

(r', θ', ϕ')	Local spherical coordinate system to the given SECS, with $\theta' = 0$ at the pole.
(r, θ, ϕ)	Coordinate system in which the 1D SECS or LCM grid is defined.
(r_k, θ_k, ϕ_k)	Positions of the model parameters (1D SECS poles or line currents).
(r_n, θ_n, ϕ_n)	Positions of the magnetic field observations.
GSM	Fixed with respect to the Earth-Sun line with x pointing towards the sun, and z a projection of the Earth's magnetic dipole onto the plane perpendicular to x (positive towards north).
QD	Magnetic apex coordinate system, described on page 33.

Abstract

Description of the magnetic signature from ionospheric currents is the main limiting factor in geomagnetic reference modelling. The objective of this PhD thesis is to develop a robust orbit-by-orbit measure of the auroral electrojet currents from satellite magnetic observations. Two methods, the *line current model* (LCM) and 1D *spherical elementary current system* (SECS) model are compared through validation of both synthetic case examples and CHAMP and *Swarm* observations. The robustness and ability to handle orbit sensitive factors are tested for both methods by investigating dependence on regularization methods and parameters. Results from these tests, makes the line current model the preferred candidate for a possible automatic near-real-time estimation of the sheet current densities based on four key findings: (1) A remarkably high performance ratio of 99.87% (2) the possibility of a common regularization parameter (3) 0.97 squared coherence between the side-by-side flying *Swarm* Alpha and Charlie, indicating a method invariant to small changes and (4) the inability to obtain a robust implementation of the 1D SECS method. The preferred regularization method for the LCM is found as an L_1 model norm minimization of the second order along track derivatives of the model parameters along with a robust treatment of input data to account for a possible non-Gaussian error distribution. From application of the LCM to 10 years of CHAMP and 2 years of *Swarm* Alpha and Bravo observations, a dataset comprised of sheet current density profiles and orbit specific geomagnetic activity indices for more than 140,000 northern and southern geomagnetic pole crossings is created. The geomagnetic indices represent the peak intensity of the auroral electrojets and an estimate of the total polar current and are applicable in both statistical investigations and as a data selection criteria. From this dataset space-time and statistical investigations of the auroral electrojet system are performed, highlighting inter-hemispherical similarities and asymmetries, such as a consistently smaller southern auroral oval. The LCM thus provides a strong tool for investigations of the auroral electrojet currents.

Resumé

Ionosfæriske strømme og bestemmelsen deraf er den primære begrænsende faktor inden for modellering af geomagnetiske referencemodeller. Formålet med denne ph.d. er at udvikle en robust metode til at estimere de ionosfæriske, polare elektrojetstrømme på individuelt orbit basis fra magnetiske satellitobservationer. 1D SECS metoden sammenlignes med en liniestrømsmodel (LCM) gennem validering af både syntetiske og satellitobservationer fra CHAMP og *Swarm*. Robustheden og evnerne til at håndtere orbitspecifikke faktorer testes for begge metoder ved at undersøge afhængigheden af regularseringsmetoder og parametre. Disse tests fremhæver linistrømsmodellen som den foretrukne kandidat til en mulig automatisk bestemmelse af de polare ionosfæriske strømme på baggrund af fire primære årsager: (1) metoden virker i 99.87% af de testede tilfælde (2) muligheden for en fælles regulariseringsparameter på tværs af geomagnetisk aktivitetsniveau (3) strømdensiteter baseret på *Swarm* Charlie observationer beskriver 97% af variansen i estimater på baggrund af Alpha, hvilket indikerer at metoden er ufølsom overfor små variationer i inputdata (4) det var ikke muligt at opnå en robust implementering af 1D SECS metoden. En minimering af L_1 normen af anden ordens differencerne af modelparametrene samt en robust (Huber) vægtning af input data findes som den foretrukne regulariseringsmetode. To orbitspecifikke geomagnetiske indeks samt profiler af ionosfæriske strømtætheder findes på basis af kørsel af 10 års CHAMP og 2 års *Swarm* Alpha og Bravo observationer for mere end 140.000 overflyvninger af den magnetiske syd og nordpol. De geomagnetiske indeks repræsenterer maks og minimum intensitet af strømprofilen, $\boldsymbol{J}^{\text{peak}}$, samt et estimat af den totale polar strøm $\boldsymbol{J}^{tot}$ og kan anvendes både i statistiske undersøgelser og som kriterie for dataudvælgelse. Statistiske undersøgelser af den tidslige udvikling af de polare strømtætheder samt forskelle mellem den nordlige og sydlige halvkugle undersøges på baggrund af $\boldsymbol{J}^{peak}$ og $\boldsymbol{J}^{tot}$. Undersøgelser viser blandt andet en signifikant mindre oval på den sydlige halvkugle.

Contents

Preface i

Acronyms and symbols iii

Abstract xi

Resumé xiii

1 Why investigate the auroral electrojet system? 1

2 Solar wind interaction with Earth's magnetic field 7
2.1 Basic space plasma physics . . . 7
2.2 Earth's magnetic environment . . . 9
2.3 Dungey cycle, reconnection and energy transport into the ionosphere . . . 13
2.4 Magnetic storms and substorms - The Akasofu model . . . 21
2.5 Societal space weather effects . . . 25
2.6 Monitoring the disturbance level using magnetic indices . . . 26

3 Preparing Swarm and CHAMP magnetic field observations for ionospheric current models 29
3.1 Satellite magnetic observations . . . 29
3.2 Pre-processing of the magnetic field observations . . . 32

4 Mathematical description of two models describing the auroral electrojet system 35
4.1 Line current model . . . 35
4.2 Spherical elementary current system . . . 41

5 Discrete linear inverse problems and how to solve them 49
5.1 What is an inverse problem? . . . 49
5.2 Solutions and regularization . . . 52

6 Validation of the 1D SECS method through application of satellite magnetic observations 61
6.1 Estimation of the ionospheric current densities . . . 61
6.2 A synthetic test case . . . 62

6.3 A test applying CHAMP and *Swarm* magnetic data . . . 65
6.4 Discussion of the 1D SECS method . . . 75
6.5 Summary on applying the 1D SECS approach to CHAMP and *Swarm* magnetic data . . . 78

7 Application of the ionospheric line current method to satellite magnetic observations 79
7.1 Test with synthetic data . . . 79
7.2 Applying LCM to *Swarm* Alpha orbit no 3334 . . . 80
7.3 Estimating the regularization parameter and sensitivity to small scale variations 88
7.4 Applying rotation of the line currents along constant QD latitude . . . 91
7.5 Inter model comparison and discussion on their differences . . . 94

8 Statistical analyses of the auroral electrojet system estimated from satellite observations 101
8.1 Space-time development of auroral electrojets in a three week period around Equinox . . . 101
8.2 Geomagnetic and solar wind activity . . . 109
8.3 Hemispherical differences . . . 125
8.4 Further applications . . . 130

9 Summary and conclusions 133

Bibliography 137

Appendix 151

A Determining polar ionospheric electrojet currents from Swarm satellite constellation magnetic data 151

B Synthetic test case of the 1D SECS method 167

C Positions of peak sheet current density 185

D Results from intensity model 193

Chapter 1

Why investigate the auroral electrojet system?

Earth's magnetic field, although invisible to the human eye, affects our lives in many ways - it shields us from the ionized particles from the solar wind, lead to the ever breathtaking Aurora Borealis and Aurora Australis, and has since the discovery of the compass in the 11^{th} century provided a means for navigation on travels across large distances. Exploitation of the magnetic field is not limited to humans, several species of birds and turtles are found to navigate according to the magnetic field [Wiltschko and Wiltschko, 2005], when migrating between feeding grounds [Frankel, 1984; Thorup, 2007; Lockwood, 2013].

The invention of the magnetic compass is usually credited to Chinese scientists more than 2000 years ago, though not theorised until 1600 when William Gilbert proposed the idea that Earth behaves like a giant magnet [Gilbert, 1958]. The connection between the auroral displays and the magnetic field was discovered by Olof Hjorter in 1741 through observations of large disturbances in the magnetic field simultaneously to large auroral displays. The home of these geomagnetic storms, described by Alexander von Humboldt, the ionosphere - to which this PhD project has been devoted - was, however, not discovered until the development of the first magnetometer and magnetic observatory by Carl Friedrich Gauss [Gauss, 1839; Glassmeier and Tsurutani, 2014]. Gauss furthermore established the method for separating external and internal components of the magnetic field, along with a method for estimating the strength of the magnetic field at a different height (*e.g.* the ionosphere) by considering the magnetic field as a potential field. Magnetic observatories grew gradually from 1839, reaching 170 by 1960 [Amm and Viljanen, 1999; Lockwood, 2013].

For the previous few hundred years, information gained from magnetic field ground observations has led to many discoveries within the near-Earth environment, which allowed descriptions of both internal (core and crustal) and external (magnetospheric and ionospheric) contributions. With the dawn of the space age, new possibilities was launched in geomagnetism - with satellites, such as MagSat [Langel et al., 1982] and CHAMP [Reigber et al., 2002] providing high quality data from regions where data had previously been scarce or absent. From these high quality data, geomagnetic reference models [*e.g.* Olsen et al., 2014; Finlay et al., 2016b; Lesur et al., 2010] provide a valid description of the internal core, crust and large scale magnetospheric ring current contributions, describing the main parts of the Earth's magnetic field.

Also quiet time (non-polar) ionospheric Sq-current contributions are well described by present geomagnetic models [*e.g.* Sabaka et al., 2004, 2015]. However, large spatial and temporal variability in the ionospheric, polar region, electrical currents makes their description difficult, and their prediction nearly impossible. This makes the ionospheric currents the main limiting factor in the accuracy of geomagnetic field models [Friis-Christensen et al., 2006; Olsen and Stolle, 2012].

Ionospheric currents, their magnetic signature and secondary inducing effects are some of the strongest manifestations of space weather, and thus plays an important part in it's understanding. With increasing technology and dependence on satellite availability in terms of *e.g.* GPS signal in navigation, space weather is of growing concern. Induction in the established power grid can furthermore during highly disturbed conditions overload, causing major power cuts, as was experienced in the nine hour blackout, affecting six million people in Québec, Canada in 1989 [Pirjola et al., 2005]. Improved modelling and better understanding of both the cause and variation of the space-time structure of the polar magnetic field disturbance is therefore of crucial importance in both advances in fundamental space research and societal issues. It has therefore been the focus of many geomagnetic investigations.

The polar magnetic field disturbances consist primarily of two constituents: 1) horizontal ionospheric E-region electrical currents at an altitude of approximately 110 km, forming the auroral electrojet system and 2) currents flowing along field-lines in the region above the ionosphere, feeding the auroral electrojet system by connection to the magnetosphere. These *Field-aligned currents* (FACs) cause large magnetic field disturbances in the East-West magnetic field component at satellite altitude. FACs cannot be uniquely determined from ground. Several techniques [*e.g.* Ritter and Lühr, 2006; Juusola et al., 2006; Lühr et al., 2015] have, however, successfully been developed for their determination by application of satellite observations.

Ground based studies have lead to major discoveries such as the link between the solar activity and the strength of the auroral electrojet system [Nishida and Maezawa, 1971], theoretically predicted by Dungey [1961] and the development of a polar substorm [Akasofu, 1964]. Several indices, such as the Kp [Bartels, 1957] and AE [Sugiura and Davis, 1966] has been developed for monitoring the geomagnetic state of the ionosphere. Application of these indices are, however, restricted by magnetometer station positions. With the use of primarily Northern Hemisphere measurements, indices reflect mainly ionospheric activity in that hemisphere. Early studies of the ionospheric currents was often based on a 90° clockwise rotation of the magnetic perturbation vector, representing the equivalent current system during substorm activity [*e.g.* Kisabeth and Rostoker, 1974] or from assumption of the ionospheric conductance [Fukushima, 1976]. Ground based studies have furthermore been utilized in statistical studies of the entire polar region [*e.g.* Friis-Christensen and Wilhjelm, 1975; Kamide et al., 1981; Friis-Christensen et al., 1985a; Richmond et al., 1998; Moretto et al., 2004; Gjerloev and Hoffman, 2014] along with more local, individual case studies of the auroral electrojet system using *e.g.* a chain [Amm, 1997] or grid [Weygand et al., 2012] of observations.

Ground based magnetic field studies are only capable of providing information about the equivalent currents (strictly horizontal currents, causing the observed ground magnetic field residuals). The launch of magnetic satellites enabled observations, providing additional information about

FACs. Few event-based studies of conjugate ground observations in Greenland and Antarctica [*e.g.* Kim et al., 2015] have estimated interhemispherical differences at specific conjugate observations. Satellites, however, provide access to observations on both the Southern and Northern Hemisphere of the current system, allowing interhemispherical comparisons, and entire sheet current density profiles along the satellite track. These advantages has been utilized in several studies of the ionospheric currents using satellite measurements of *e.g* the Magsat, Ørsted, and CHAMP satellites [Olsen, 1996; Ritter et al., 2003; Juusola et al., 2006]. Application of satellite data thus provide the information needed for investigations of a sheet current density profile for a single satellite crossing [Amm and Viljanen, 1999; Olsen and Stolle, 2012].

Olsen [1996] presented a model study of the auroral electrojet system based on single polar crossings of MagSat consisting of a series of line currents perpendicular to the satellite track. The method was later applied to CHAMP scalar magnetic satellite data by Ritter et al. [2003] and Ritter et al. [2004], and to multi-satellite mission data by Moretto et al. [2002] and Olsen et al. [2002]. An alternative approach for monitoring auroral activity was presented by Juusola et al. [2006]. Here they present a 1D version of the 2D *Spherical Elementary Current System* (SECS) method [Amm, 1997] for application of CHAMP magnetic residual vector data. The application of vector data allows investigations of the 3D polar current system, the auroral electrojet system and associated FACs. It may, however, also introduce complications in computation and an additional error source from larger contamination by *e.g.* the FACs in the radial magnetic vector component. A third, more simple approach, to monitor the auroral activity is the application of CHAMP magnetic scalar data to an *intensity model* (IM), presented by Vennerstrom and Moretto [2013]. They present a method, describing the auroral electrojet system from two infinite line currents, representing the eastward and the westward electrojet. From satellite magnetic field perturbations, intensity and position of the two line currents are estimated by the maximum gradients. Their method thus roughly correspond to estimating the amplitude and position of the auroral electrojets from the current profiles determined from the line current model of Olsen [1996].

Application of satellite data in statistical studies of the auroral electrojet system is presented in a range of studies of the Northern Hemisphere [*e.g.* Friis-Christensen et al., 2017]. Exploitation of the coverage of satellite observations through investigations of the auroral electrojet system in both hemispheres such as Juusola et al. [2009] and Vennerstrom and Moretto [2013] are, however, scarce. More studies are conducted in statistical patterns of the FACs alone [e.g. Juusola et al., 2014; Coxon et al., 2016]. Combining the data from several magnetic missions provide a valuable basis for statistical investigations, such as the dependence on solar wind parameters along with interhemispherical differences with season. The resent study by Laundal et al. [2016a], presents such a statistical investigation of the 3D polar current system based on decomposition of the ionospheric currents into a toroidal and poloidal field. With the launch of the three satellite constellation, *Swarm* [*e.g.* Friis-Christensen et al., 2008], in November 2013, a new period dawned for geomagnetic satellite surveys. Improvement in data quality with the high precision global measurements of the magnetic field has enabled the discovery and investigation of low intensity ionospheric currents on a global scale down to a few nT [Stolle et al., 2016]. The unique constellation of the satellites provides, before unobtainable, insights in the ever changing magnetic environment of the Earth. From novel discoveries from jet streams in the Earth's core [Livermore et al., 2016] to the discovery of supersonic plasma

jets in the outer atmosphere [ESA, 2017b] and interhemispherical asymmetry in the seasonal variation [ESA, 2017d]. The important and very interesting results have through increased media focus [*e.g.* BBC, 2016] on the magnetic field, put the field of geomagnetism in the public eye.

The focus of this thesis

With the work presented in this PhD thesis, we seek the possible near-real-time monitoring of the spatial and temporal structure of the auroral electrojet activity from satellite magnetic observations.

- We aim at developing a reliable method, able to return an entire current profile for the Northern and Southern auroral region. From the theory of inverse problems, estimates of the ionospheric current auroral electrojet system are found from two pre-specified physical models: The 1D SECS method presented in Juusola et al. [2006] and the *line current model* (LCM) of Olsen [1996], both applied to CHAMP and *Swarm* satellite magnetic data. Through a series of investigations in regularization method and parameters, the two methods are tested for reliability and facilitation of near-real-time implementation. Application of the methods to *Swarm* magnetic data, enables new insights concerning the ionospheric currents, along with exploration of previously unobtainable results thanks to the unique constellation of the satellites.

- From application of the method to satellite, residual, magnetic data, we aim at providing a data set of the sheet current density profiles, $\boldsymbol{J}$, for (nearly) all CHAMP and *Swarm* satellite crossings. A dataset such as this can provide the basis for many space-time and statistical investigations of the auroral electrojet system.

- Estimation of peak strength and position of the westward and eastward electrojet, $\boldsymbol{J}^{\text{peak}}$, along with the along-track integration of the current profile, $\boldsymbol{J}^{\text{tot}}$, furthermore, provides satellite-specific indices. These indices will, in contrast to others provide a direct measure of the disturbance level of a specific satellite orbit, important for data-selection in *e.g.* internal field modelling.

Thesis outline

The study is divided into three main parts, with chapters one to five describing background information, chapter six to eight, the validation, discussion and application of the line current model and 1D SECS method, and chapter nine summarizing the key findings. Chapter two gives a short introduction to basic space plasma physics, along with descriptions of the theoretical background of the ionospheric sheet current densities and their effects. The applied data and preprocessing of CHAMP and *Swarm* satellite data is described in Chapter three, and in Chapter four, a mathematical description of the line current model and 1D SECS method is provided. Chapter five describes the tool, linear inverse problem theory, applied to solve the equations given in chapter four, along with a description of all later applied regularization methods. Chapter six provides an in-depth study of the effects of regularization methods and changes to a set of adjustable parameters on the resultant 3D sheet current density profiles for the 1D SECS method. The line current method is in a similar way performance tested in Chapter seven, which also provides an inter-model comparison of the estimated sheet current

densities. The following chapter eight, presents a few examples, highlighting the large range of uses, provided by a data set consisting of all ten years of CHAMP and two years of *Swarm* data for the line current model. Finally, summary and conclusions are provided in Chapter nine. The most important results are presented in Chapters 7 and 8.

Chapter 2

Solar wind interaction with Earth's magnetic field

The Earth's magnetic field, currents and solar wind interaction form a very complicated system. The following theory chapter will not claim to provide a full explanation of plasma physics and the dynamics concerning the solar wind dynamics and the interactions with the Earth's magnetosphere. It will, however, briefly explain some basic principles utilised later in this thesis, preparing the reader with the most important principles of the theory of ionospheric currents. The ionospheric magnetic field sources presented here mainly focus on those important to the polar regions.

2.1 Basic space plasma physics

All matter in and above the ionosphere acts as a plasma. Plasma physics is a newer field of subject within geophysics, and is not claimed to be fully understood. This section will try to highlight the most important features of such magnetic plasma, with focus on terms necessary for understanding the principles and discussion in this thesis. Derivations of the equations given here can be found in Baumjohann and Treumann [2012]. Most of the movement can be described by assuming the plasma behaving like an electrically conducting fluid, moving with a bulk velocity, $\boldsymbol{v}$. This is described by the *magnetohydrodynamics* (MHD) approximation, working on the quasi-stationary electrodynamics boundary, where the time derivative of the electric field is very small. For most cases, this will be a valid approximation; exceptions such as reconnection will be discussed later.

The magneto part of magnetohydrodynamics tells us how currents, magnetic ($\boldsymbol{B}$) and electric ($\boldsymbol{E}$) fields change moving in a magnetic (and electric) field. The governing set of equations is for magneto part of plasma physics, as with any electrodynamics, the Maxwell equations [Griffiths, 1981]

$$\nabla \cdot \boldsymbol{E} = \frac{1}{\epsilon_0}\rho \qquad \text{(Gauss's law for electric fields)}, \tag{2.1}$$

$$\nabla \cdot \boldsymbol{B} = 0 \qquad \text{(Gauss's law for magnetic fields)}, \tag{2.2}$$

$$\nabla \times \boldsymbol{E} = -\frac{\partial \boldsymbol{B}}{\partial t} \qquad \text{(Faraday's law)}, \tag{2.3}$$

$$\nabla \times \boldsymbol{B} = \mu_0 \boldsymbol{J} \qquad \text{(Ampère's law)}. \tag{2.4}$$

ρ is here the charge density, ϵ_0 the permittivity of free space, μ_0 the permeability of free space, $\boldsymbol{J}$ the current density, t the time and c the speed of light. The displacement current, $\mu_0\epsilon_0\frac{\partial \boldsymbol{E}}{\partial t}$ in Ampères law is ignored with the quasi-stationary assumption ($v << c$). The plasma properties are governed by the hydrodynamics part and can be described from

$$\boldsymbol{E} + \boldsymbol{v} \times \boldsymbol{B} = \frac{1}{\mu_0 \sigma_c}\boldsymbol{J} + \frac{1}{n_e}(\boldsymbol{J} \times \boldsymbol{B} - \nabla \boldsymbol{p}_E) + \frac{m_e}{ne^2}\left(\frac{\partial \boldsymbol{J}}{\partial t} + \nabla(j\boldsymbol{v} - \boldsymbol{v}j)\right)$$
$$\text{(Generalized Ohm's law)}, \tag{2.5}$$

$$\rho\frac{d\boldsymbol{v}}{dt} = -\nabla p + \boldsymbol{F_g} + \boldsymbol{J} \times \boldsymbol{B} \qquad \text{(Equation of motion)}, \tag{2.6}$$

$$\frac{\partial \rho}{\partial t} + \nabla \cdot (\rho \boldsymbol{v}) = 0 \qquad \text{(Equation of continuity)}, \tag{2.7}$$

$$P = (n_e - n_i)KT \qquad \text{(Equation of state)}. \tag{2.8}$$

Here, p is pressure, $\boldsymbol{F_g}$ is the gravitational force, σ_c is conductivity, n_e and n_i are electron and ion densities, K boltzmanns constant and T, temperature [Baumjohann and Treumann, 2012].

The generalized Ohm's law (Equation 2.5) can be broken into four terms: (1) $\frac{1}{\mu_0\sigma_c}\boldsymbol{J}$ describes how collisions lead to currents; (2) $\frac{1}{n_e}(\boldsymbol{J} \times \boldsymbol{B})$ is the Hall term, which can be approximated to zero for a gradient and collision free medium; (3) $\frac{1}{n_e}(\nabla p_E)$ describes the pressure gradient, which often is so small it can be ignored. (4) $\frac{m_e}{ne^2}\left(\frac{\partial \boldsymbol{J}}{\partial t} + \nabla(j\boldsymbol{v} - \boldsymbol{v}j)\right)$, describes the motion of electrons compared to ions. All of these terms can, under the MHD assumptions, be assumed zero, resulting in the simplified Ohm's law

$$\boldsymbol{E} = -\boldsymbol{v} \times \boldsymbol{B} \Longrightarrow \boldsymbol{v} \propto \boldsymbol{E} \times \boldsymbol{B}. \tag{2.9}$$

This means that the plasma will move proportional to the $\boldsymbol{E} \times \boldsymbol{B}$ under the MHD assumptions. This is called the $\boldsymbol{E} \times \boldsymbol{B}$ drift. The simplified Ohm's law tells us that we don't need to look into the movement of the electrons and ions separately. We can, as long as the MHD assumptions hold, treat the plasma as a fluid defined from the bulk flow velocity, $\boldsymbol{v}$.

From Ohm's law one can find the induction equation, describing how the magnetic field changes in a plasma

$$\frac{\partial \boldsymbol{B}}{\partial t} = \frac{1}{\mu_0\sigma_c}\nabla^2\boldsymbol{B} + \nabla \times (\boldsymbol{v} \times \boldsymbol{B}), \tag{2.10}$$

consisting of the diffusion term, $\frac{1}{\mu_0\sigma_c}\nabla^2\boldsymbol{B}$, and the convection term, $\nabla \times (\boldsymbol{v} \times \boldsymbol{B})$. There are thus, under the given assumptions, basically two ways to change the magnetic field within a

plasma. The ratio between the convection term and the diffusion term is given by the Reynolds number

$$R_m = \frac{\text{convection}}{\text{diffusion}} = \frac{\nabla \times (\boldsymbol{v} \times \boldsymbol{B})}{\frac{1}{\mu_0 \sigma_c} \nabla^2 \boldsymbol{B}}. \tag{2.11}$$

When the convection term is much larger than the diffusion term ($R_m >> 1$), the magnetic field is said to be frozen into the plasma, moving with the plasma (frozen-in flux theorem). This is the case, *e.g.* along magnetic field lines, where the conductivity is very high, resulting in particles moving almost freely along magnetic field lines. The frozen-in flux theorem can be applied almost anywhere in the magnetosphere, except *e.g.* in reconnection and shock fronts [Laundal, 2010; Baumjohann and Treumann, 2012].

The equation of motion (Equation 2.6) describes the force balance including three important forces: the pressure gradient, ∇p, the gravitational force, $\boldsymbol{F_g}$, and the Lorentz force, $\boldsymbol{J} \times \boldsymbol{B}$. The Lorentz force can, with the application of Ampère's law (Equation 2.4) be split into two forces

$$\boldsymbol{J} \times \boldsymbol{B} = \frac{1}{\mu_0} (\boldsymbol{B} \cdot \nabla) \boldsymbol{B} - \nabla \frac{B^2}{2\mu_0}. \tag{2.12}$$

(1) The magnetic tension force, $\frac{1}{\mu_0}(\boldsymbol{B} \cdot \nabla)\boldsymbol{B}$, acting to straighten bent magnetic field lines. The magnetic tension is a function of the curvature of the magnetic field line, with a stronger force for small curves. (2) The magnetic pressure force, $\nabla \frac{B^2}{2\mu_0}$, counteracts gradients in the magnetic field [Kivelson and Russell, 1995; Baumjohann and Treumann, 2012; Coxon, 2015].

2.2 Earth's magnetic environment

The dominant magnetic field in the near-Earth environment is that of the Earth (the geomagnetic field). Contained within the magnetosphere, the geomagnetic field varies in strengths with position between approximately 65,000 nT near the poles and 35,000 nT near the Equator at the Earth's surface. In our solar system, however, the dominant magnetic field is the Sun's. In combination with magnetic perturbations from other planets, this is known as the *Interplanetary Magnetic Field* (IMF). The IMF is carried with plasma, primarily consisting of electrons and protons continuously emitted by the Sun (solar wind). The magnetosphere acts as an obstacle for the solar wind, protecting the Earth from the ionized solar wind plasma. The boundary between the magnetosphere and the solar wind, the magnetopause, which changes with solar wind properties (*e.g.* plasma density, velocity and direction of the IMF), marks the origin of solar wind-magnetosphere interaction. This interaction is highly dynamic and forms the core of ionosphere dynamics (elaborated in Section 2.3) [Forbes, 1987; Maule, 2005; Olsen and Stolle, 2012].

The geomagnetic field resembles to a first approximation a dipole field with a dipole tilt of 11° with respect to the rotational axis and is predominantly driven by a self-sustaining dynamo in the liquid outer core. The total magnetic field, measured at ground or space, is, however, the sum of the dipole-like core field, the crustal field from magnetized rocks, magnetic field

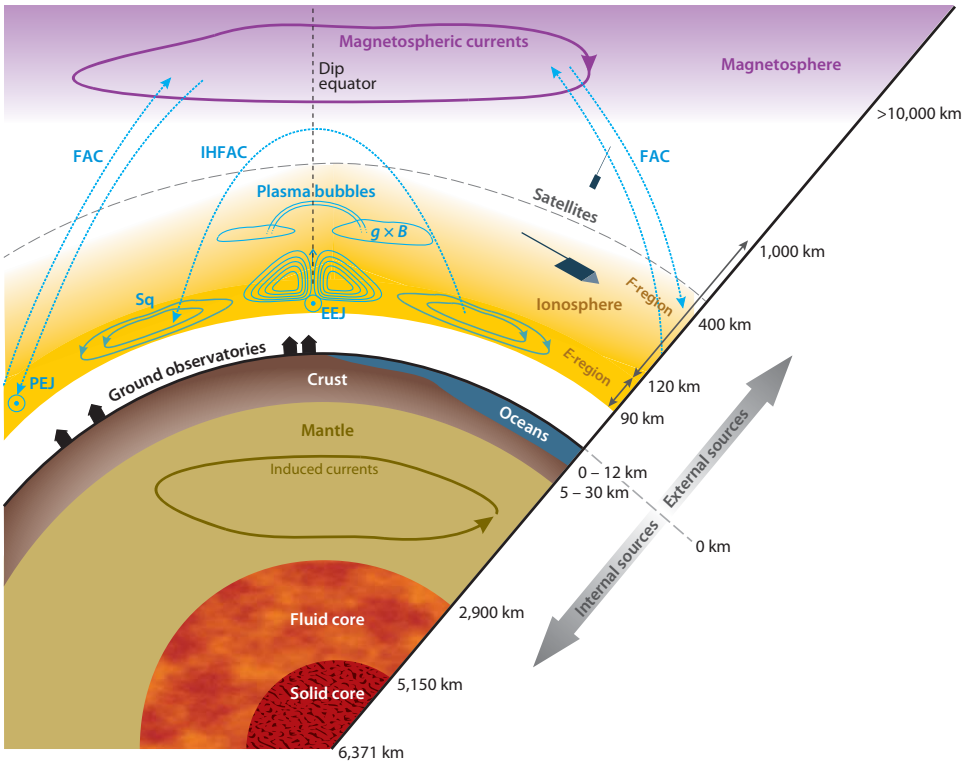

Figure 2.1: Sources to the Earth's magnetic field as a function of depth. The figure is reprinted from Olsen [2016].

from electric currents in the ionosphere, magnetosphere and oceans and from secondary Earth-induced currents. Figure 2.1 shows a sketch of the various sources in reference to their origin. Starting at the centre of the Earth, these are, (1) core field, (2) secondary Earth-induced currents in the mantle, crust and oceans (3) crustal field, (4) ionospheric currents and (5) magnetospheric currents. Each source can be described by a specific spatial and temporal characteristics. More details on the various sources are given in the following subsections [Olsen and Stolle, 2012; Olsen, 2016].

Core field

By far the largest contribution to the Earth's magnetic field ($> 93\%$) comes from the self-sustaining geodynamo in the Earth's liquid outer core (2900 to 5150 km depth), also called the main field. The liquid core has a temperature well above the Curie temperature. It is therefore not possible for the core material to be directly magnetized. The core field is produced by a geodynamo. A dynamo is a device transforming mechanical energy (such as motion - kinetic energy) into electrical energy (currents). The geodynamo is driven by convection in the outer core, consisting of a liquid iron alloy with $\sim 8\%$ nickel and $6 - 10\%$ lighter elements (possibly oxygen and sulphur). The motion of the highly conducting alloy produces electrical currents, which in turn induces a magnetic field. The core field typically changes only a little ($\sim 1\%$) on a time-scale of about half a year (secular variation) [*e.g.* Jackson et al., 2000; Finlay et al., 2016b] but experience larger changes on longer time scales (pole reversals) [*e.g.* DeMets et al., 1994] with highly variable frequency of occurrence from a few hundred thousand years

to millions of years. The signature of the core field closely resembles a dipole [Forbes, 1987; Merrill and McFadden, 1999; Maule, 2005].

Crustal field

Unlike the core field, the cooler crust of magnetized rocks (5-30 km depth), allow both remanent and induced magnetism. The crustal field is much weaker than the core field and contributes with approximately 3% of the total field strength. Remanent magnetism is primarily created (neglecting induction by the core field in the continental crust) when magnetic minerals surface with magma along spreading ridges. These rocks will be a snapshot of the ambient magnetic field at the time the rocks cooled below the Curie temperature, contributing to the total magnetic field with the direction determined from this point. Together, these rocks provide important information about past magnetic fields and has been a key contributor in support of palaeomagnetic theories relating to plate tectonics, continental drift and polar reversals and wandering [Forbes, 1987]. Changes to the crustal field will occur alongside formation of new rocks in the spreading zones. They will therefore primarily be on a spatial scale, with temporal changes happening on geological time scales. The core and crustal field describe together the internal part of the Earth's magnetic field [Maule, 2005; Olsen and Stolle, 2012].

Magnetospheric currents

The external magnetospheric and ionospheric fields change, unlike the main field, on a much shorter time scale. These are primarily driven by the interaction between the solar wind and the Earth's magnetosphere. The main magnetospheric current systems are given in Figure 2.2: The dayside magnetopause currents (green), also called the Chapman-Ferraro currents, the cross-tail currents (blue) on the nightside and the ring and partial ring current (purple) in the equatorial plane. The Chapman-Ferraro currents are located at the magnetospheric boundary with the solar wind, and is caused by a charge separation of ions and electrons caused by the meet between the solar wind and the northward magnetic field of the Earth. At the boundary, electrons will be deflected westward and ions eastward, thus creating a net eastward current. The current is created all along the magnetospuase with directions given in Figure 2.2.

The cross-tail current is formed in the region where the stretched tails oppositely directed fields meet. As a positively charged particle moves in the magnetic field, it will rotate clockwise in the northern part of the tail, and counter clockwise in the southern part of the tail. This creates a net westward motion of positively charged particles, and an eastward motion for negatively charged particles, forming a net westward cross-tail current.

The last contribution, the ring current, is as the others, formed by charge separation. When charged particles are injected towards the Earth in connection with night time reconnection in the tail (described in Section 2.3), gradients in the magnetic field forces ions and electrons to drift around the Earth in opposite directions. This causes a net current flowing westward around the Earth. The strength of the ring current is dependent on the amount of charged particles drifting, and thus dependent on the solar wind and IMF parameters. The strength of this is therefore highly dynamic, and can during magnetic storms (see Section 2.4) cause large contributions to the magnetic field observations. During substorm activity a partial ring

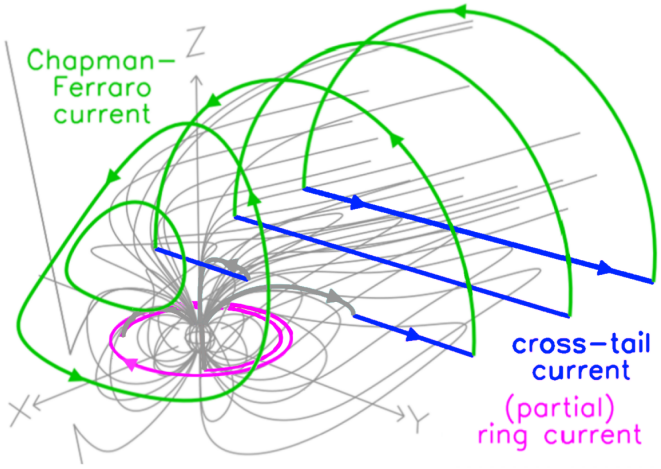

Figure 2.2: Magnetospheric currents. Magnetopause (Chapman-Ferraro) currents are shown in green, cross-tail currents in blue, magnetic field lines in grey and the ring current in purple. The figure is a combination of two figures by Milan et al. [2017].

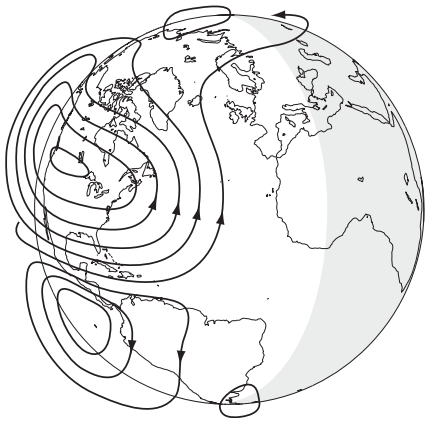

Figure 2.3: Solar quiet current system. The figure is reprinted from Viljanen [2012].

current forms in the midnight sector, which is believed to close in the ionospheric substorm electrojet described in Section 2.4 [Kivelson and Russell, 1995; Prölss, 2010; Coxon, 2015]

Ionospheric currents

The key ionospheric contributor to the magnetic field in the polar regions is the convection and substorm electrojets, driven by daytime and night time reconnection with the solar wind (Dungey cycle). A detailed description of this is presented in Section 2.3.

The ionospheric currents consists, besides the convection and substorm electrojet of the solar quiet current system (the magnetic perturbation being referred to as the Sq variation), presented in Figure 2.3. This twin-vortex current system is driven by difference in neutral wind collisions with ions and electrons in the ionosphere. Collisions with ions will, due to the larger size, be much more frequent than collisions with the electrons. This will cause a net motion of ions compared to electrons along the direction of the neutral wind, with a resultant net

current along this. The neutral wind is driven by solar radiation heating of the atmosphere, creating a circular tidal motion, and is therefore restricted to the illuminated part of the Earth (daytime), with almost vanishing contributions during night time [Baumjohann and Treumann, 2012; Coxon, 2015].

The magnetospheric and ionospheric contributions are often referred to as the external sources, due to their external origin when measured from ground. Understanding the processes of the external sources to the magnetic field is important when modelling internal sources, since a wrong interpretation could lead to contamination of the data used for internal modelling [Finlay et al., 2016a].

2.3 Dungey cycle, reconnection and energy transport into the ionosphere

Interaction between the solar wind and the Earth's magnetosphere results in a convective system. This convective system was first hypothesized by Dungey [1961] and is believed to be the main transport of solar wind particles into the magnetosphere [Borowski, 2016]. The hypothesis is based on reconnection, connecting the IMF to the Earth's magnetic field. A process, which only recently has been measured directly by the NASA's Magnetospheric Multiscale Mission (MMS) [Burch et al., 2016].

The MHD approximation makes no distinction between the different components of the plasma and requires therefore that any changes in the field must be on smaller time scales than the ion cyclotron frequency. The same applies for the length scales. The MHD approximation is therefore restricted to long time and large spatial scales. At these very low frequencies the quasi-stationary electrodynamics assumption can be applied, where only current flow is considered. Reconnection, on the other hand works on both small time and spatial scales, and the MHD assumption is said to be broken. Reconnection happens where two oppositely directed field lines meet, reconnects to each other changing the magnetic topology. When the magnetic field lines move in towards each other, sharp gradients in the magnetic field are formed, causing the magnetic field to vanish in the middle. This gradient will, due to the small length scale, act differently on ions and electrons, moving them in different directions. The frozen-in flux assumption thus no longer applies, allowing field lines to diffuse through the current sheet. This diffusion can under certain circumstances lead to two magnetic field lines interconnecting in a so-called X-line. The newly formed highly curved magnetic field lines will from a strong magnetic tension be ejected from the reconnection region [Baumjohann and Treumann, 2012; Coxon, 2015].

Figure 2.4 gives a schematic representation of the Dungey cycle, following a single field line trough 9 positions, marked by the numbers on the figure in both the magnetosphere (top) and the ionospheric footprint (bottom). The ever changing IMF (1'), merges through magnetic reconnection with the magnetic field of the Earth (1) on the dayside, opening the before closed field line. The magnetic field line is then moved with the solar wind down-tail across the polar cap. The magnetospheric and ionospheric part of the field line will be dragged along, however not perfectly [Burch et al., 2004], from magnetic tension of the field line. Continuous dayside reconnection will force the field line towards the centre of the tail (5). This causes a stretching

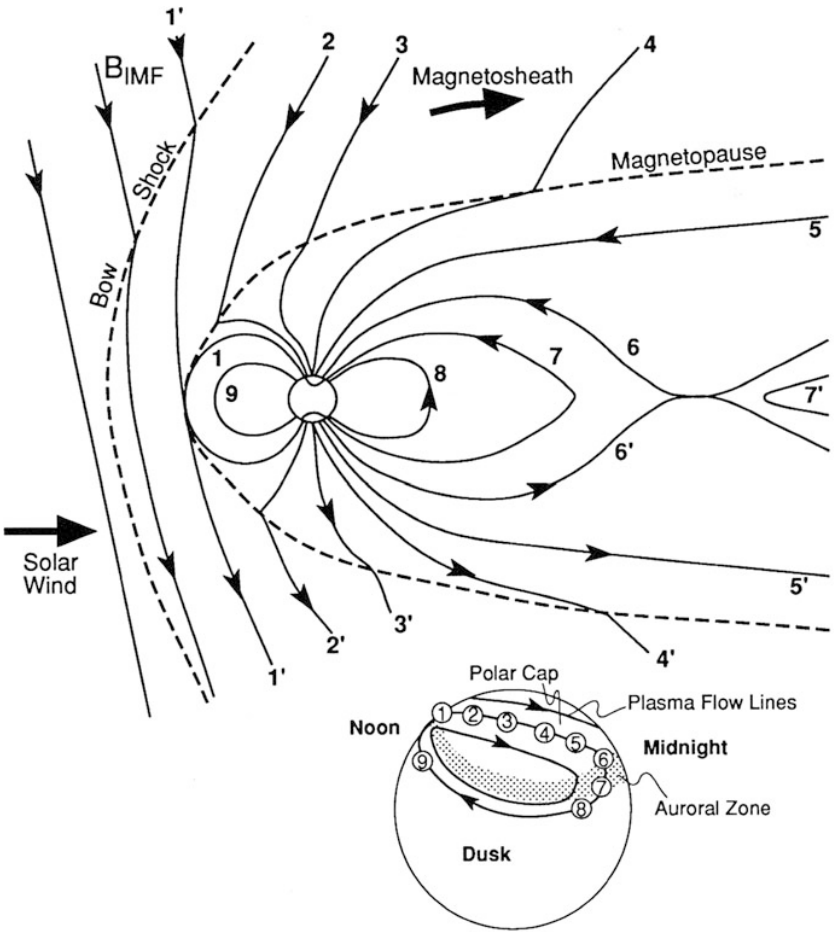

Figure 2.4: Dungey cycle with ionospheric footprint, following a single field line through 9 positions. The figure is reprinted from Hughes [1995]; Ashour-Abdalla [2015].

of the tail, and an additional night side reconnection, due to the opposite directed field lines in the middle of the tail (6), leaving a closed, but stretched field line (7). The stretched magnetic field line will be subject to a magnetic stress, leading to a relaxing and shortening of the magnetic field line (8), causing an earthward motion. This earthward motion has been shown to be in the form of a jet, called a bursty bulk flow [Angelopoulos et al., 1992, 1994]. The convection circulation is closed by a return flow to the dayside, maintaining the dayside magnetic field (9) [Baumjohann and Treumann, 2012; Ashour-Abdalla, 2015; Laundal, 2010].

Ionospheric footprint

The presented convective system has an ionospheric footprint as shown in the bottom part of Figure 2.4. The numbers coincide with the numbering of the field lines given in the top figure. The movement of the magnetic field lines across the ionosphere results from the frozen-in-flux approximation in a movement of charged particles, present all along the magnetic field line. Low conductivities above the ionosphere, however, fails to provide a suitable environment for a perpendicular current flow to the field lines. Since plasma is a quasi-neutral gas with the

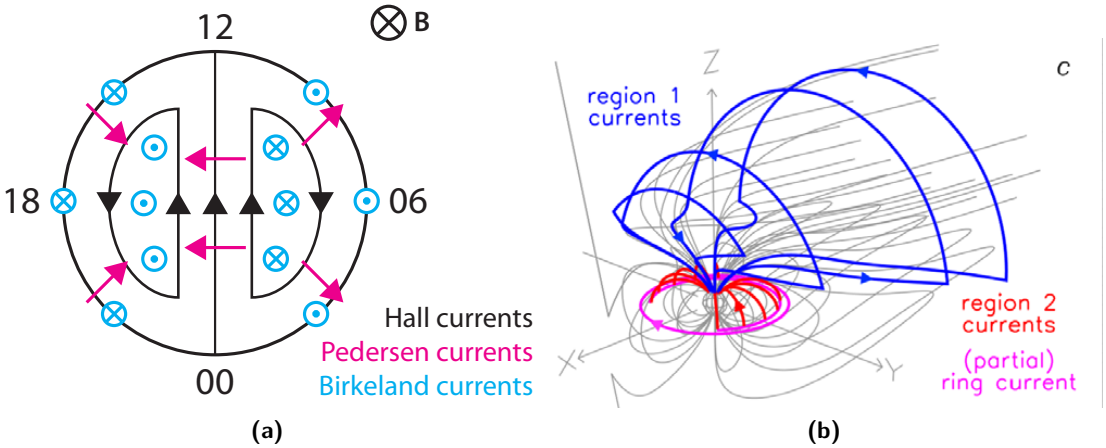

Figure 2.5: (a) Ionospheric equivalent current system and the associated FACs (blue). Pedersen currents are given in pink, and hall currents in black. A reference main magnetic field is given in the corner. The figure is reprinted from Coxon [2015]. (b) perspective view of the Region 1 (blue) and 2 (red) FACs along with the (partial) ringe current (pink). The figure is reprinted from Milan et al. [2017]

same amount of ions and electrons, a current, with current density given as

$$\boldsymbol{j} = eN_e(v_i - v_e), \tag{2.13}$$

emerges only when charge separation occurs. e is here the unit charge, N_e, the number density of electrons and v_i and v_e the drift velocity of the electrons and ions accordingly. Above the ionospheric E-region, the particle density is so small that the plasma can be assumed collisionless. The particles will in this region therefore undergo $E \times B$ drift (along convection pattern given by the Dungey cycle) with a charge independent velocity, and no associated perpendicular currents [McPherron, 1991; Baumjohann and Treumann, 2012].

In the ionospheric E-region, collision becomes more frequent, interrupting the $E \times B$ drift of the ions and electrons. The collision frequency of the charged particles is determined by their individual radius, making collisions more frequent for ions (larger). The deceleration of the ions in the $E \times B$ direction is thus larger, resulting in a net charge separation, and thereby current (Equation 2.13). The current will be along the flow lines of the Dungey cycle ($E \times B$ drift), presented in Figure 2.4, in the opposite direction of the convection flow. This describes a Hall current cell, closing self-consistently, assuming uniform conductance. These are presented by the black lines in Figure 2.5(a) as a function of *magnetic local time* MLT. A reference main magnetic field is given in the corner [Prölss, 2010; Coxon, 2015].

Collisions also provide the means for a different type of currents in the ionosphere, namely the Pedersen currents. This current is, as the Hall currents, a result of charge separation. When particles accelerates after being brought to stop from a collision, ions and electrons are accelerated in different direction as a result of the charge dependent Lorentz force. The principle is described schematically in Figure 2.6. The resultant current is parallel to the electric field and perpendicular to the magnetic field, which yields a current perpendicular to the Hall current, equatorward in the morning sector (0-12 MLT) and poleward in the evening sector (12-24 MLT). Across the polar cap, a current flows from the dawn to dusk. A simplified structure

of the Pedersen currents is shown in pink in Figure 2.5(a) [Baumjohann and Treumann, 2012; Coxon, 2015].

Pedersen currents do not close within the ionosphere, as is the case with the Hall currents. The current budget is solved by the presence of FACs, also called Birkeland currents after Kristian Birkeland who hypothesised the presence [Birkeland, 1908]. FACs are generated at gradients in Pedersen and Hall conductances (for non-uniform conductance) and along non-zero electric field. This is in the boundaries of the auroral oval, as described by the blue circles in Figure 2.5(a). The currents are divided in the Region 1 (poleward) and Region 2 (equatorward) currents described in Figure 2.5(b). The Region 1 currents (blue) are on the boundary to the open field lines and map therefore to the magnetopause deep in the magnetotail. The Region 2 currents (red) are in a region of the ionosphere populated by closed field lines, and map to the partial ring current in the near-Earth equatorial plane [Prölss, 2010; Baumjohann and Treumann, 2012].

Opposite directed magnetic signatures from the Pedersen currents and FACs will according to the Fukushima theorem [Fukushima, 1976] cancel each other out below the ionosphere, assuming uniform conductance and vertical FACs. The theorem is illustrated in Figure 2.7, showing the magnetic contribution from the Pedersen currents in pink and the FACs in blue as seen above the polar cap (a) and a perspective look around a Region 1 current (b). Pedersen currents are denoted J_P and Region 1 and 2 currents as J_1 and J_2 accordingly in the figure. Below the ionosphere, contributions from the FACs and Pedersen currents will add to zero and it is thereby not possible to measure these from the ground. At satellite height this is not the case. The deviation of the real FAC flow from a radial flow (to a non-uniform conducting ionosphere and non-vertical FACs), creates toroidal currents in the magnetosphere, resulting in a poloidal magnetic field, leaking below the ionosphere. This effect is, however, shown to be weak and can therefore be ignored [*e.g.* Richmond, 1974; Untiedt and Baumjohann, 1993].

Since the conductivity is larger in the auroral oval due to particle precipitation along the magnetic field lines, a full self-consistent current closure is not present for the Hall currents. The currents are partly fed by the FACs in the noon sector with a return flow along FACs in the midnight sector. This creates two noon to midnight currents, namely the *westward*

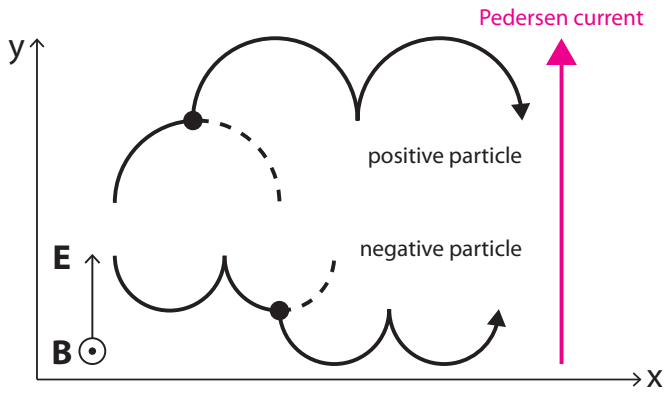

Figure 2.6: Schematics of Pedersen currents caused charge separation from collisions in the ionosphere. The figure is reprinted from Coxon [2015].

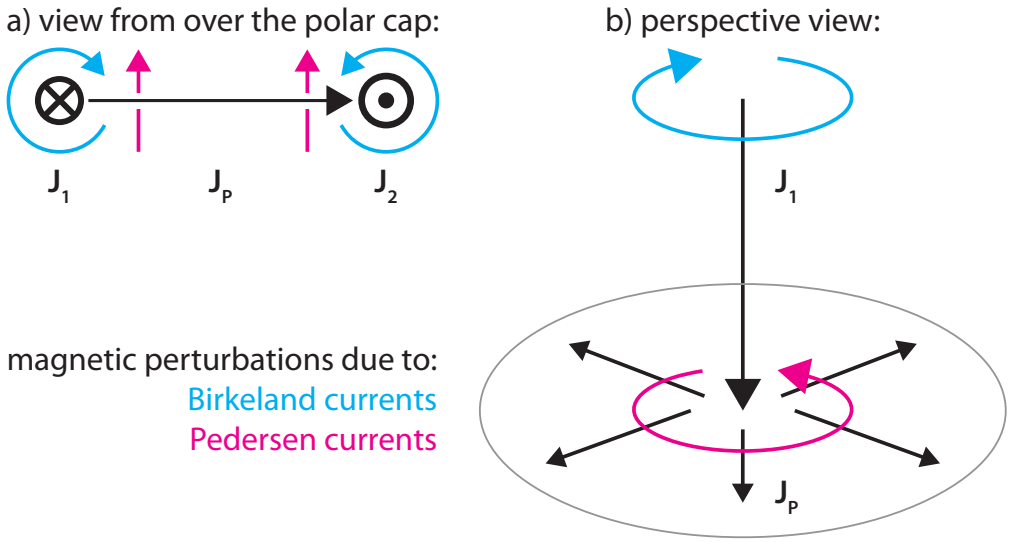

Figure 2.7: Principle of the Fukushima theorem described from magnetic perturbations caused by a single FAC and the associated Pedersen currents. Pedersen current perturbations are given in pink and FACs in blue. The actual currents are given in Black, with $\boldsymbol{J_p}$ denoting the pedersen currents and $\boldsymbol{J_1}$ a region 1 FAC. The figure is reprinted from Coxon [2015].

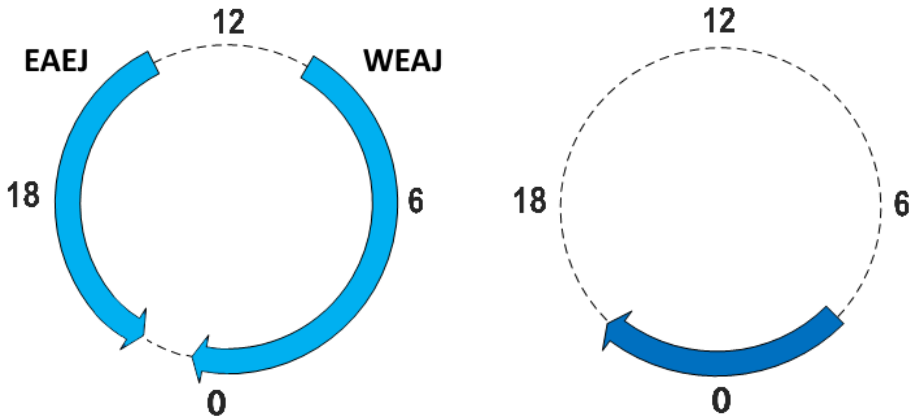

(a) Auroral electrojet system **(b)** Substorm electrojet

Figure 2.8: Schematics of the auroral electrojet currents (left) and substorm electrojet (right) Inspired by Baumjohann and Treumann [2012].

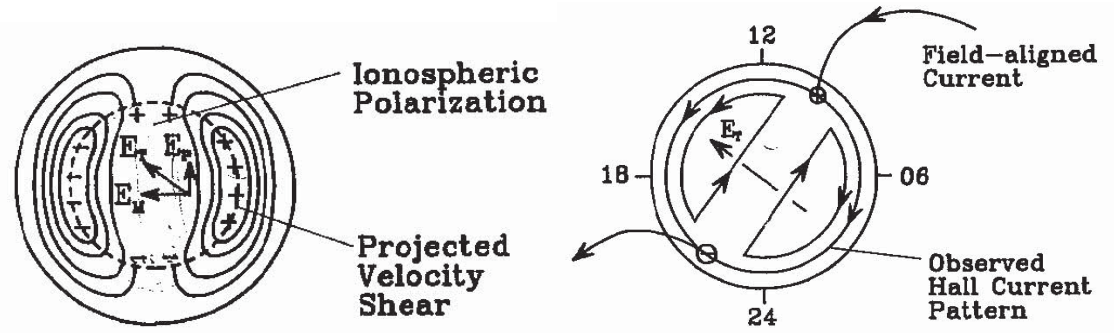

Figure 2.9: Principle of polarization effects resulting in a rotation of the two-cell convection pattern. The figure is reprinted from McPherron [1991].

auroral electrojet (WEAJ) in the morning sector (0-12 MLT) and *eastward auroral electrojet* (EAEJ) in the evening sector (12-24 MLT). The westward and eastward auroral electrojets are also called the convection electrojets from the plasma convection (Dungey cycle) origin. Figure 2.8(a) illustrates the convection electrojets positions as a function of MLT. Together with the substorm electrojet (Figure 2.8(b)), they form the ionospheric equivalent current system, which in this thesis will be referred to as the auroral electrojet system. The substorm electrojet is, as the name reveals, an electrojet tied to substorm activity which is elaborated in Section 2.4 [Baumjohann and Treumann, 2012].
Ionospheric conductivity gradients results in a charge accumulation, producing an electric field, modifying the total electric field in the ionosphere. This polarization effect results in a rotation of the two-cell convection pattern described in Figure 2.9, away from noon-midnight symmetry. (a) shows the ionospheric polarization, and (b) the resultant Hall convection cells. The rotation results in peak intensities of the eastward electrojet around 18 MLT and around 03 MLT for the westward electrojet [McPherron, 1991].

Auroral electrojet system - dependence on IMF

Since the Hall currents and thereby the auroral electrojet system are governed by the large scale Dungey cycle, small changes in the convection pattern will modify the ionospheric footprint. The magnitude and shape of the ionospheric footprint is thus highly dependent on the direction of the IMF [Friis-Christensen and Wilhjelm, 1975; Cowley and Lockwood, 1992; Lockwood, 2013]. The north-south component in *Geocentric Solar Magnetospheric*[1] (GSM) coordinates, B_z, is the key parameter for reconnection to occur, and affects thereby the intensity of the convection currents. The strongest currents are found for a southward (negative) B_z [*e.g.* Cowley et al., 1991; Weimer, 2001].

The east-west component of the IMF has a slightly different effect on the convection pattern. During reconnection with $B_y > 0$, newly opened field lines in the Northern and Southern Hemispheres will be affected by oppositely directed east-west stresses, resulting in an asymmetrical transport into the tail, reconnection between asymmetrical field lines and in turn an asymmet-

[1] The GSM coordinate system is fixed with respect to the Earth-Sun line with x pointing towards the sun. z is a projection of the Earth's magnetic dipole onto the plane perpendicular to x.

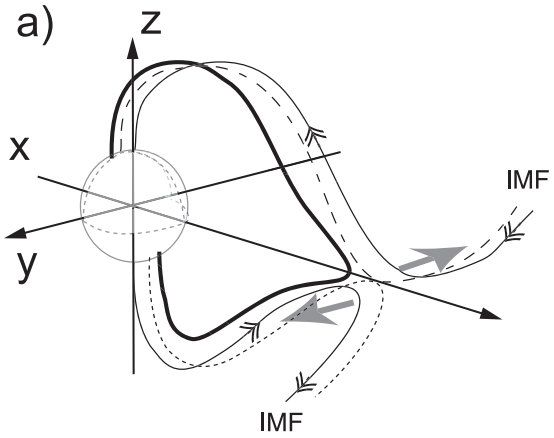

Figure 2.10: Principle of asymmetric reconnection in the tail caused by an asymmetrical transport of field lines to the tail. The figure is reprinted from Østgaard and Laundal [2013].

rical convection pattern in the ionosphere. The principle of asymmetrical reconnection in the tail is shown in Figure 2.10 [Cowley et al., 1991; Østgaard and Laundal, 2013; Friis-Christensen et al., 2017].

The overall convection pattern as a function of clock angle (B_z and B_y dependence) is given in Figure 2.11 in form of the electrical potential. Large electrical potential refers here to a strong current, and vice versa. Several other studies, such as Weimer [2001] (FAC pattern) and Grocott and Milan [2014] show similar dependencies both from model studies and observations. The convection pattern for the Northern and Southern Hemisphere is found almost identical, with mirror values of B_y. B_y has, due to the asymmetrical reconnection opposite effects on the Northern and Southern Hemisphere. For a purely southward IMF (Sector 4 in the figure) the convection pattern is very similar to the two-cell schematic presentation of the Hall currents in Figure 2.5(a). The presence of a positive B_y component (negative on the Southern Hemisphere) skews the convection pattern (Sector 3) consistently with the principle of asymmetrical reconnection in the magneto tail. When $B_y < 0$ ($B_y > 0$ on the Southern Hemisphere), the same skewness is not found, failing to fulfil the otherwise expected mirror symmetry. The lack of mirror symmetry is supported by a numerical MHD simulation by Tanaka [2001]. A Northward IMF (Sector 7, 0 and 1) results in a weak convection pattern from the lack of dayside reconnection [Haaland et al., 2007].

Further information on the IMF dependence of the ionospheric convection system can be found in [*e.g.* Friis-Christensen and Wilhjelm, 1975; Friis-Christensen et al., 1985b; Cowley and Lockwood, 1992; Weimer et al., 2010; Haaland et al., 2007].

Ionospheric conductivity - diurnal and seasonal dependence

The ionospheric conductivity is, as previously stated, important for the formation of the auroral electrojet system, with the Sun as the primary source. This subsection therefore provides a short introduction to the origin and causes to modifications. Ionospheric ionization, and thereby the conductivity, is controlled through two principle sources: auroral particle precipi-

tation and *solar extreme ultraviolet* (EUV) radiation. The Dungey cycle provides not only the convection of charged particles, but also the transport of those particles into the ionosphere in the form of particle precipitation. A side effect of this is the radiation from excited states (caused by collisions) of precipitating solar wind particles, causing the visual evidence of the Dungey cycle in form of the aurora. On the Sun-facing side of Earth, solar ultraviolet radiation is absorbed in the ionosphere, producing heat along with ionization [Meng, 1979; Elphinstone et al., 1996; Guo et al., 2014].

The geometry of the auroral precipitation is controlled by interaction with IMF and will align with the ionospheric convection pattern. The solar extreme ultraviolet radiation will on the other hand depend on solar zenith angle, with reference to a geographical coordinate system. With a different magnetic pole displacement in the Southern and Northern Hemisphere, this will cause a non-conjugate dayside conductivity in the auroral oval, and with that interhemispherical differences in the auroral electrojet system. The larger pole displacement in the Southern Hemisphere will furthermore cause stronger EUV conductivities due to more hours of solar illumination. The actual shape of the current cell is furthermore shown [Laundal et al., 2016b,a] to be affected by sunlight, with a closer resemblance to the convection pattern during sunlit conditions (summer) [Friis-Christensen and Wilhjelm, 1975; Meng, 1979; Guo et al., 2014].

The two principle conductivity sources have been shown to result in a local time dependence, with the dayside (noon-sector) dominated by solar EUV emissions and the night side by particle precipitation. This local time dependence is associated with diurnal variations in both auroral oval size [Meng, 1979] and strength of the auroral electrojet system [Guo et al., 2014]. Investigations of the diurnal variation of the auroral oval have revealed a 24-hour oscillation with an

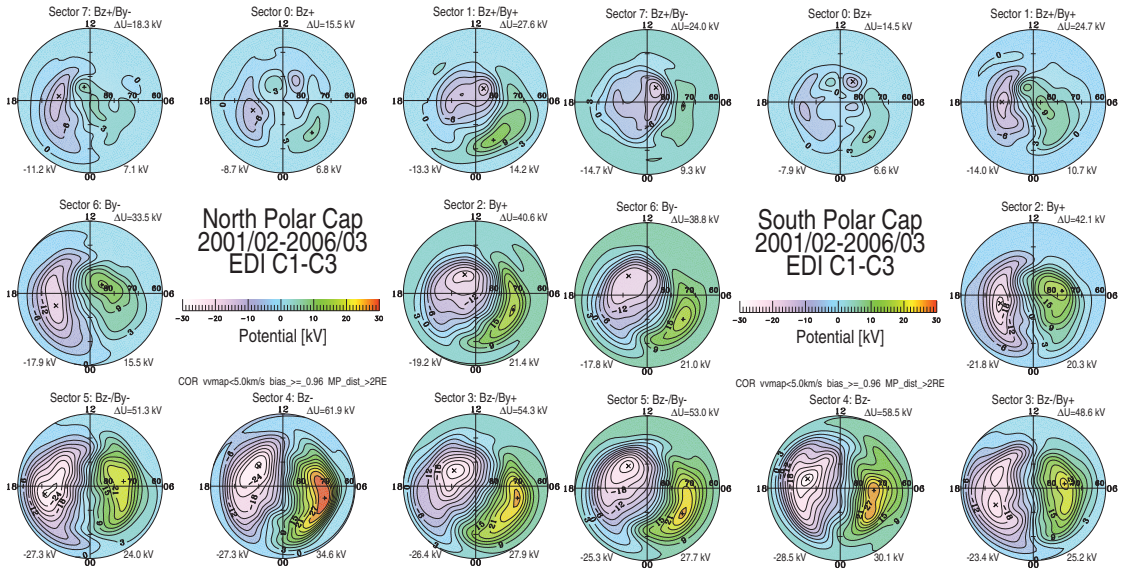

(a) North **(b)** South

Figure 2.11: Electric potential binned according to IMF clock angle. From Haaland et al. [2007].

amplitude of approximately four degrees, associated with the daily precession of the geomagnetic pole and the following variation in EUV conductivity. Geomagnetic pole displacement causes a diurnal variation in solar EUV conductivity, with maximum conductivity at magnetic noon[2] ($\sim$ 18.00 UT) on the Northern Hemisphere. The maximum in EUV conductivity is found with an associated smaller auroral oval [Meng, 1979; Laundal et al., 2016a].

Variations in solar illumination cause furthermore a seasonal dependence on the current system, with stronger conductivities during local summer. Other effects, such as the equinoctial effect [Bartels, 1932; McIntosh, 1959] and the semiannual variation caused by the Russell-McPherron effect [Russell and McPherron, 1973], cause a decrease in the westward electrojet during winter and stronger currents around equinox. The Russel-McPherron effect is caused by an annual variation in dipole axis tilt, causing variations in the IMF-geomagnetic field configuration, with an optimum for dayside reconnection around equinox. A southward IMF is statistically more likely during equinox, since the dipole is tilted along the Earth's orbital track during this season. Stronger currents are therefore expected during equinox [Weimer et al., 2010; Guo et al., 2014; Coxon et al., 2016].

The westward and eastward electrojet has on the Northern Hemisphere been shown [*e.g.* Singh et al., 2013; Guo et al., 2014] to exert different annual variations, with maximum and minimum in eastward electrojet during summer and winter accordingly and a semiannual variation in the westward electrojet with maxima around equinox. The semiannual variation in the westward electrojet is believed to be due to the Russel-McPherron effect [Guo et al., 2014].

2.4 Magnetic storms and substorms - The Akasofu model

The formation and definition of a substorm is not fully established. Many theories are presently on the table, such as *e.g.* the near-Earth neutral line model [McPherron et al., 1973; Baker et al., 1996] and the current sheet disruption model [Lopez et al., 1994; Lopez, 2000]. This section will focus only on the effects of a substorm on the auroral electrojet system. For the sake of explaining the different substorm phases, we have adopted the theory by [McPherron et al., 1973]. The general structure of the ionospheric convection and auroral oval during a substorm was first proposed from ground observations by Akasofu [1964] and later confirmed from satellite observations [*e.g.* Anger et al., 1973; Akasofu et al., 1973; Rostoker et al., 1980]. The original substorm model [Akasofu, 1964] consisting of an expansion and recovery phase was later modified by the addition of the preluding growth phase by McPherron [1970] [McPherron, 1991; Elphinstone et al., 1996].

A substorm is a release of energy stored in the magnetosphere through enhanced tail reconnection, and is often associated with bright and dynamic aurora [Milan et al., 2007]. This release of energy will not only enhance the convection electrojets (WAEJ and EAEJ), but also form a so-called substorm current wedge and the associated substorm electrojet across the midnight sector. The substorm electrojet, schematized in Figure 2.8 is a westward flowing current, adding to the strength of and expanding the WAEJ into the evening sector. A new study by Friis-Christensen et al. [2017] shows, unlike previous assumptions, how the substorm

[2]Magnetic noon is the time of smallest solar zenith angle at the geomagnetic pole.

electrojet is present not only during substorms (disturbed conditions) but also for geomagnetic quiet conditions. The geometry of the current wedge is shown, together with the Dungey cycle in Figure 2.12. (b) and (d) show the noon-midnight cross section of the magneosphere, while (a) and (c) presents a perspective view. The top figures show the system during the growth phase of a substorm, and the bottom during the expansion phase. The substorm current wedge is only present during the expansion phase, and is marked as the purple line in (c). The blue arrows indicate the solar wind flow, yellow the magnetopause currents, blue lines the closed field lines, and red the open field lines. X_{TL} in (d) marks the magnetic tail reconnection site and the black arrow the earthward jetting of the newly closed magnetic field lines. [Lockwood, 2013; Laundal, 2010; Milan et al., 2017]

Phases of a magnetic substorm

A substorm is believed to have three distinct phases, a growth phase, an expansion phase and a recovery phase. The last two are presented in the classical substorm diagram by Akasofu [1964] in Figure 2.13. Figure 2.13(a) gives the quiet time conditions preceding the substorm. The growth phase is recognized by an erosion of the dayside magnetosphere by dayside reconnection, transporting magnetic flux to the magnetotail in form of energy stored in the lobes of the tail. The increased number of open field lines due to prevailing dayside reconnection results in an equatorward expansion of the polar cap and auroral oval. The auroral oval thus expands and shrinks according to input of solar wind energy [McPherron et al., 1973; Baker et al., 1996; Campbell, 2003].

In the expansion phase, given in Figure 2.13(b) to (d) and the bottom row of Figure 2.12, the dayside reconnection is joined by a night time reconnection, resulting in a sudden release of energy. This energy is transported into the ionosphere by the earthward motion caused by the night time reconnection. The time of the nightside reconnection is called the onset or breakup of the substorm, and is marked by a brightening and poleward motion of the equatormost arc, consistent with a contracting polar cap. The expansion phase is where the most dynamic and bright aurora is observed under the auroral oval. The auroral breakup is first seen around midnight, but expands rapidly north and westward with what is called a westward travelling surge. The substorm electrojet is concentrated in the active breakup region and expands westward, into the evening sector, along with the westward travelling surge. The last phase of a substorm is the recovery phase, where the northernmost arc reaches it's highest latitude (smallest polar cap) and the state of the ionosphere returns to pre-substorm conditions. This is illustrated in Figure 2.13(e) and (f) [Akasofu, 1964; Elphinstone et al., 1996; Baumjohann and Treumann, 2012; Milan et al., 2017].

A magnetic substorm is recognized primarily by the distinct magnetic perturbation to the horizontal magnetic field at ground level. A magnetic observatory positioned directly below a westward flowing current (westward or substorm electrojet) on the northern hemisphere, will observe a distinct negative baseline deviation in the horizontal magnetic field component.

Short on magnetic storms

The sunward plasma convection from the outer magnetotail towards the inner magnetotail associated with the substorm expansion phase contributes not only to an enhancement of the

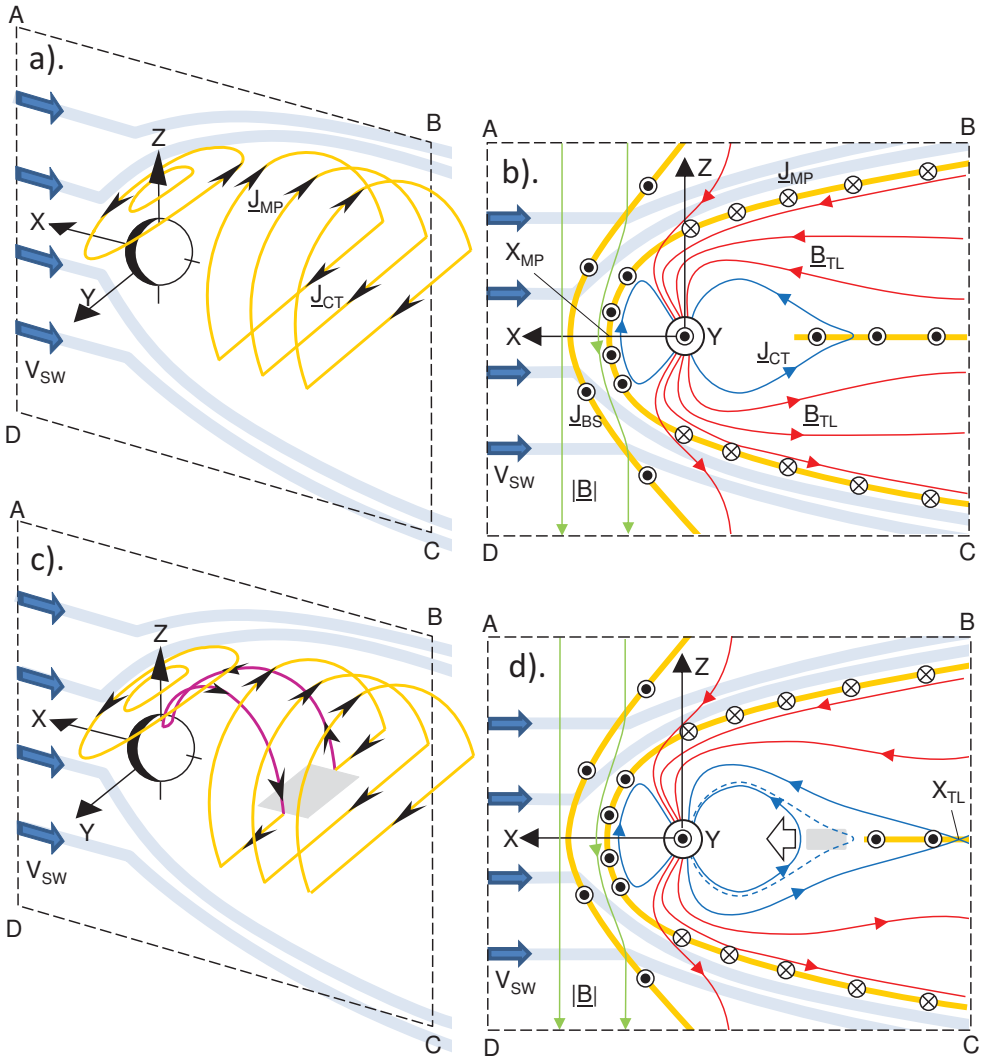

Figure 2.12: Schematics of the Earth's magnetospheric current systems during the growth phase (top panel) and the expansion phase (bottom panel) in a perspective view (a,c) and as a noon-midnight cross section. Blue arrows indicate the solar wind flow and yellow the magnetopause currents. blue lines marks close field lines, red, open field lines and green, the field lines of IMF. The substorm current wedge and corresponding substorm electrojet is marked in purple. The figure is reprinted from Lockwood [2013]

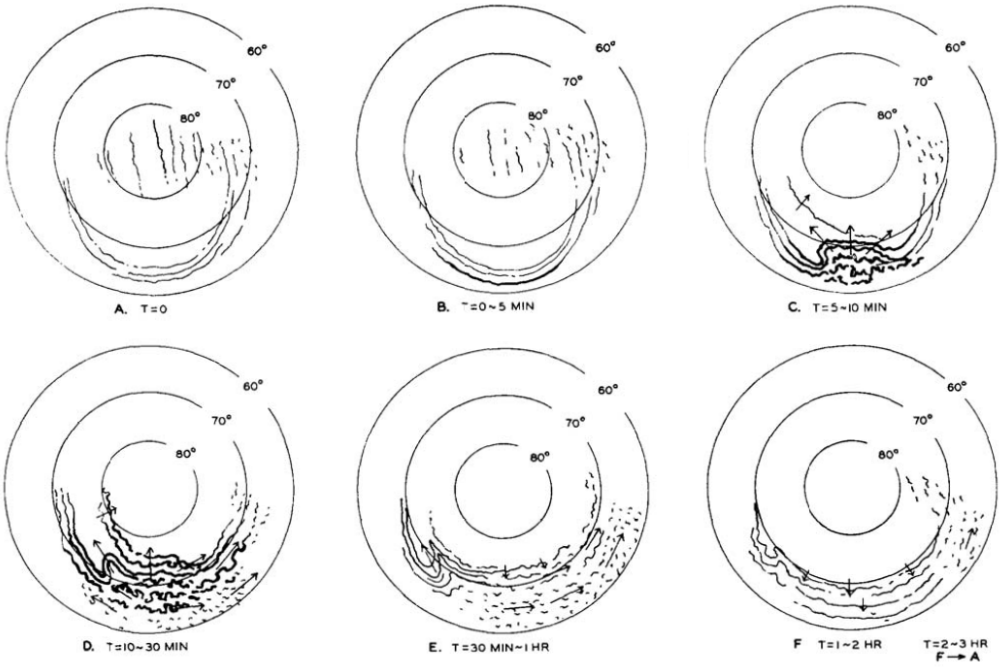

Figure 2.13: Visualization of aurora during (a) Quiet arc, (b - d) substorm expansion phase and (e - f) growth phase, as first presented in Akasofu [1964].

convection electrojets, but also to an enhancement of the ring current. A typical substorm time scale is approximately $1/2$ to 1 hour. A geomagnetic storm on the other hand is recognized from a significant enhancement of the ring current over a longer period of time (more than one hour), consistent with a prolonged strong southward IMF. The exact relationship between the magnetic storms and substorms is a matter of definition and is today still unclear. Magnetospheric and ionospheric dynamics is comprised of a variety of dynamic changes sometimes resembling the state of an isolated magnetic substorm. These events are called sawtooth events [Belian et al., 2013]. Some [*e.g.* McPherron, 1991; Pulkkinen et al., 2007] believe them to be a series of intense substorms, while others [Fung et al., 2016] find them to represent their own specific class of magnetospheric activity [McPherron, 1991; Milan et al., 2017].

Secondary induced currents in the Earth's upper mantle and lithosphere

During active conditions (geomagnetically disturbed) temporal variations in the auroral electrojet system result in a time varying component of the magnetic field. This magnetic signature induces a secondary current in the conducting upper mantle and lithosphere opposite to the ionospheric currents, which in turn causes a magnetic field signature. The contribution from these geomagnetically induced currents can during geomagnetically disturbed periods be very important - especially when performing ground observations. The contribution to the local electrojet index IL[3] was during quiet conditions estimated by Tanskanen et al. [2001] to approximately $10-20\%$. At highly disturbed times, IL can be up to 40% of the signal at ground level. The induced currents depend greatly on the conductivity structure of the Earth, on the temporal and spatial structure of the auroral electrojet system and on the location of the mea-

[3]Locally derived electrojet index from the Scandinavian IMAGE magnetometer chain [Kauristie et al., 1997]

surements relative to the source current. Especially the spatial structure of the conductivity of the Earth can be challenging [Mareschal, 1986; Juusola, 2009].

2.5 Societal space weather effects

Space weather has an increasing effect on life in the modern world, with more and more technology dependent on GPS. An example is the effect on navigation, a well know phenomena in the aviation industry. Airlines prefer to take the shortest route between two cities, marked by the great circle distance. Flying between parts of North America and Europe, however, puts the flight path through regions with magnetic observations highly disturbed by the auroral electrojet system. These disturbances cause irregularities in the navigational systems and especially, approach and landing services, which will force the plane to make an emergency landing at nearest airport. The health of passengers and staff is furthermore affected by an increased particle radiation during geomagnetically disturbed conditions. Understanding space weather effects in the ionosphere is of increasing interest with increasing use of polar routes [Pirjola et al., 2005; EASA, 2012]. Space weather is furthermore found responsible for increased drag on low-altitude spacecrafts [Pirjola et al., 2005; Liu and Lühr, 2005] and instabilities in the reliability and performance level of ground-based and spaceborn technological systems. Ground-based systems mainly experience problems caused by geomagnetically induced currents. The geomagnetically induced currents are electrical currents induced in the conducting upper layers of the Earth by the time variable ionospheric currents, causing large problems for directional drilling in polar regions. Relying on GPS signal when drilling below the Earth surface is not possible, since the GPS signal is absorbed in the surrounding material. Companies therefore often turn to the magnetic field for orientation. Since the magnetic field changes with both position (local crustal field changes) and time, navigation becomes difficult. During disturbed times, geomagnetically induced currents can cause large deviations (estimated up to 40% of the signal [Tanskanen et al., 2001]) from the quiet time reference models, used as reference to the magnetic field measured in the drill hole. The companies are therefore, to avoid loss of direction, forced to stop drilling during periods of high geomagnetic activity [Pirjola et al., 2005; Poedjono et al., 2013].

Induction in the established power system during highly disturbed times, may overload the system, causing major powercuts, threatening the modern life. A threat, which recently caused the Danish emergency management agency to acknowledge space weather as one the the top 13 largest threats against Denmark. Electromagnetic disturbances caused in the fall of 2015 the closure of a Swedish airport due to blackout in the radar systems, during a magnetic storm [Pulkkinen et al., 2005]. In 1989 geomagnetically induced currents caused a nine hour blackout for six million people in Québec, Canada, and in 1859, the Carrington event[4] caused powerful currents in the telegraphic network, causing telegraphers to experience electric shocks and papers to burst into flames. Consequences can only be speculated, should an event as powerful as the Carrington event happen today, with all the modern electrical technology. The auroral electrojet system is one of the strongest manifestations of space weather, and plays therefore an important role in it's understanding. [Viljanen and Pirjola, 1994; Viljanen et al., 1999; Pirjola et al., 2000; DEMA, 2017].

[4] The Carrington event is the largest known geomagnetic storm [Shea et al., 2006].

2.6 Monitoring the disturbance level using magnetic indices

External sources can as previously mentioned not be assumed stationary in either time or space. With the solar wind as the driving mechanism of the currents, changes in the solar wind will affect the external contribution to the magnetic field. In order to correct for these external sources when dealing with *e.g.* internal field modelling, it is important to have a measure of the disturbance of the ionosphere and magnetosphere. Geomagnetic indices such as Dst, RC, AE and Kp have over the years provided such a measure of the degree of disturbance.

Kp index

One widely spread activity measure of ionospheric currents is the 3 hour range index, Kp [Bartels, 1957]. Kp, or planetary K value, is derived from the average of 13 observatory K values [Bartels et al., 1939] to provide an index for the global disturbance. The K values are estimated as the range value (difference between absolute maximum and minimum) of geomagnetic activity for each component, H (horizontal), Z (vertical) and D (declination) (subtracted quiet day variation) of the magnetic field at a given observatory. The range is then converted into the quasi-logarithmic K index based on a latitude dependent conversion table individual for each observatory [Rostoker, 1972; Campbell, 2003]. The Kp index is provided and managed by GFZ [2017].

AE index

The Kp index provides a capable measure of the general state of planetary geomagnetic activity. It does, however, not distinguish between magnetospheric ring current activity and auroral electrojet activity. A more direct measure of the auroral zone activity is provided by the AE index [Sugiura and Davis, 1966]. To obtain this, measurements from 12 observatories in the sub-auroral zone, evenly spaced along the auroral oval are used. The index is derived based on perturbations to the horizontal field. Treating the auroral electrojets as two separate currents, one flowing towards the east, and one flowing towards the west, the horizontal component of the magnetic field will provide a good measure of the strength of this. The sign of the deviation from a quiet field will give the direction of the current, with a positive deviation for an eastward current and a negative deviation for a westward current. A schematic example of the change in the horizontal component strength below a westward flowing current is given in Figure 2.14. At any given time, the most positive and negative deviation of all the observatories provides the upper and lower limit of deviation. These are called the AL and AU index, providing an individual measure of the strength of the western and eastern electrojet. Given the geometry of the electrojet system (see Figure 2.8), the most positive deviation is found in the evening sector and the most negative in the morning sector according to MLT. The combined AE index ($AU - AL$) will therefore be a measure of the intensity for the most active local times, around midnight [Rostoker, 1972; Campbell, 2003]. The AE index is provided by WDCG [2015].

Dst and RC index

As the AE index was introduced to give an indication of auroral electrojet strength, so was the Dst index [Sugiura, 1964] introduced to provide a measure of the ring current strength. The basic idea behind the Dst index is similar to the idea behind the AE index. Dst indicates the

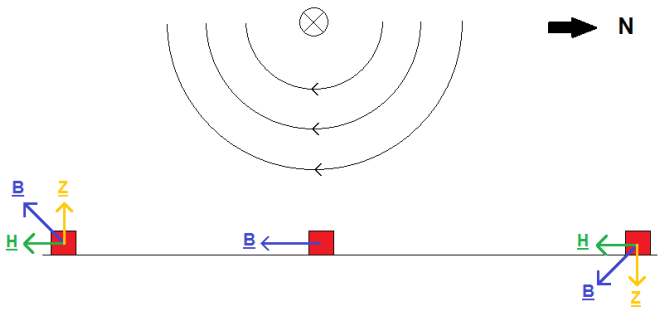

Figure 2.14: Mangetic field perturbations at three observatories below a westward current on the Northern Hemisphere. Magnetic perturbations is given in blue, with the horizontal component in green and the vertical component in yellow.

global part of the geomagnetic disturbance after subtracting typical quiet day variation from low-latitude observatory data. The aim is to estimate the magnetic disturbance due to the ring current, which will contribute only with a magnetic field deviation along the geomagnetic axis. Therefore only the deviation in the horizontal component of the magnetic field is needed for the index. The subtraction of the quiet day Sq current system signature is not perfect, since it is estimated from quiet time only, and enhancements during magnetic storms has not been accounted for [Rostoker, 1972; Campbell, 2003], resulting in a bias for geomagnetic active periods. The Dst index is provided by WDCG [2015].

The RC index provides a similar index to the Dst index, namely a measure of the ring current strength. As an attempt to avoid contamination by the Sq current system, only night time data is applied. Furthermore, a better baseline stability is applied along with more observatories. The RC index is derived from an hour-by-hour spherical harmonic analysis of night time data from 21 worldwide stations located at mid or low latitudes [Olsen et al., 2014].

Chapter 3

Preparing Swarm and CHAMP magnetic field observations for ionospheric current models

The two methods described in this thesis, 1D SECS and LCM are both based on magnetic satellite observations. The following chapter provides a short introduction to magnetic satellite missions, along with a description of the preprocessing necessary for implementation of the named methods. Finally, the chapter will provide a short introduction to the coordinate system in which our results are presented.

3.1 Satellite magnetic observations

Satellite technology has greatly advanced the science of geomagnetism. The first dedicated satellite mission to study the Earth's magnetic field was the eight month NASA satellite mission, Magsat [Langel et al., 1982], launched in 1979. 20 years later, the Danish Ørsted satellite [Neubert et al., 2001; Olsen, 2007] was launched carrying two magnetometers. The satellite was planned as a 14 months mission, but lasted more than a decade. The satellite has provided important information about the changes in the magnetic field down to a spatial scale, not before obtainable [Hulot et al., 2002] along with increased understanding of the ionospheric and magnetospheric current systems [Christiansen et al., 2002]. The evolution of the magnetic field was followed up by the launch of the Argentinian SAC-C [Colomb et al., 2004] and German CHAMP [Reigber et al., 2002] satellites, providing important information *e.g.* of the development of Earth's crustal magnetic field [Friis-Christensen et al., 2006; ESA, 2017c].

The 10 year CHAMP satellite mission has furthermore provided many important science results for the auroral electrojet system, including Ritter et al. [2003] and Juusola et al. [2007]. On board the CHAMP satellite was (1) a dual-frequency GPS receiver for precise tracking of the satellite, (2) an accelerometer measuring the non-gravitational orbit perturbations, such as air drag and solar and Earth radiation pressure, (3) a startracker for precise inertial orientation, (4) a retro-reflector for additional tracking from ground, (5) a digital ion drift meter to measure the electrical field vector along orbit and finally (6) the magnetometer instrument package, consisting of an Overhauser scalar magnetometer and two fluxgate vector magnetometers [Reigber et al., 2002].

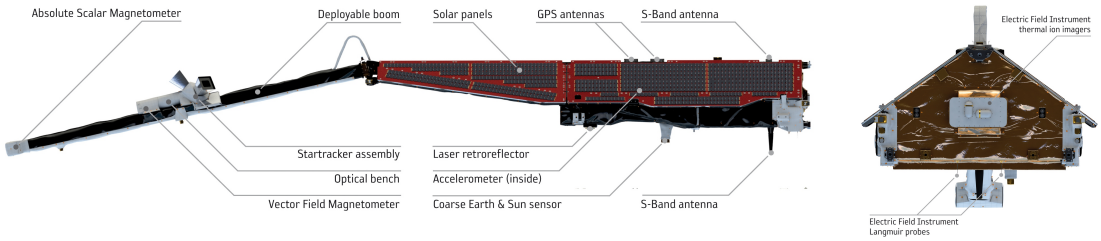

Figure 3.1: Instrument description of the *Swarm* satellite, reprinted from ESA [2017a].

Although missions, such as CHAMP, has provided high quality magnetic observations, irregularities in especially the external fields, has proven difficult to model for single satellite missions. The launch of the three satellite constellation *Swarm* mission on the 22nd of November 2013, opened up a new way to investigate both internal and external sources to the Earth's magnetic field. The specificly designed constellation provides comparable measurements across local times and heights, enabling important investigations of *e.g.* the longitudinal dependence of the auroral electrojet system. Previous missions, furthermore, revealed that measurements from a full solar cycle is important for distinguishing between solar cycle and short-term secular variation effects. The main objective of the *Swarm* mission is to provide the best ever survey of the Earth's magnetic field, to gain new insights in understanding the Earth's interior and near Earth magnetic environment by addressing the challenges of separating contributions from various field sources. The primary research objectives are categorized in four main groups: (1) Core dynamics, including geodynamo process and core-mantle interaction, (2) crustal magnetisation, (3) three dimensional electrical conductivity of the mantle and (4) magnetospheric and auroral electrojet systems [Friis-Christensen et al., 2006; Olsen et al., 2013].

The three identical *Swarm* satellites, Alpha, Bravo and Charlie, carries a range of magnetic instruments onboard (see Figure 3.1). The core instrument on the satellites are the high-precision *Vector Fluxgate Magnetometers* (VFM), providing measurements of the magnitude and direction of the magnetic field. The orientation of the magnetic vector is provided by the Startracker. The *Absolute Scalar Magnetometer* (ASM) provides scalar measurements of the magnetic field mainly for calibration of the vector field magnetometer. The accelerometer provides information about the air drag and wind around the satellites by measuring the non-gravitational acceleration in its respective orbit, used for derivation of air density models and solar wind effects on upper-atmosphere dynamics. At the front of the each satellite an electric field instrument provides high resolution measurements of plasma density, drift and velocity to characterise the electric field in the near-Earth environment. The Langmuir probes provides measurements of electron density, electric potential and the electron temperature of the satellite environment. Precise orbit determination is found from the GPS receivers and the GPS validating laser retroreflector [ESA, 2017c].

The satellites were launched on one launch vehicle, and flew up until February 2014 in close orbit formation. Since then, satellite Alpha and Charlie have flown side-by-side with an east-west separation of 1.4° at an altitude of approximately 450 km (as of January 2017) in a near-polar

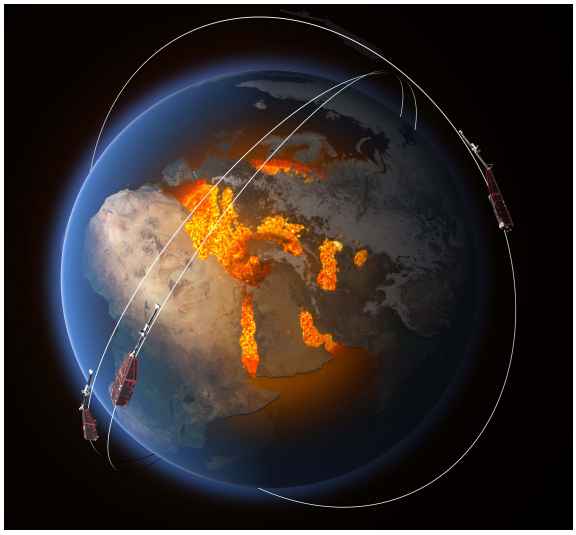

Figure 3.2: Swarm orbit constellation [ESA, 2017a].

orbit with an inclination of $87.4°$. Bravo flies in a slightly higher orbit of approximately 520 km altitude with an inclination of $88°$. The difference in orbital inclination results in different local time drift rates between satellite Alpha/Charlie and Bravo, with a six hour separation reached in 2018. An illustration of the *Swarm* constellation is given in Figure 3.2.

The mission was designed as a four year mission. The lifetime is, however, expected to be much longer, dependent on orbital manoeuvres. The orbital manoeuvres are determined by the science community to gain the best possible scientific results from the mission. If no manoeuvres are done, re-entry is expected for the lower pair between 2022 and 2028, see Figure 3.3. The decision will be a trade-off between mission length (long term variations), and enough low-orbit measurements, important for internal field modelling, and ionospheric current determination.

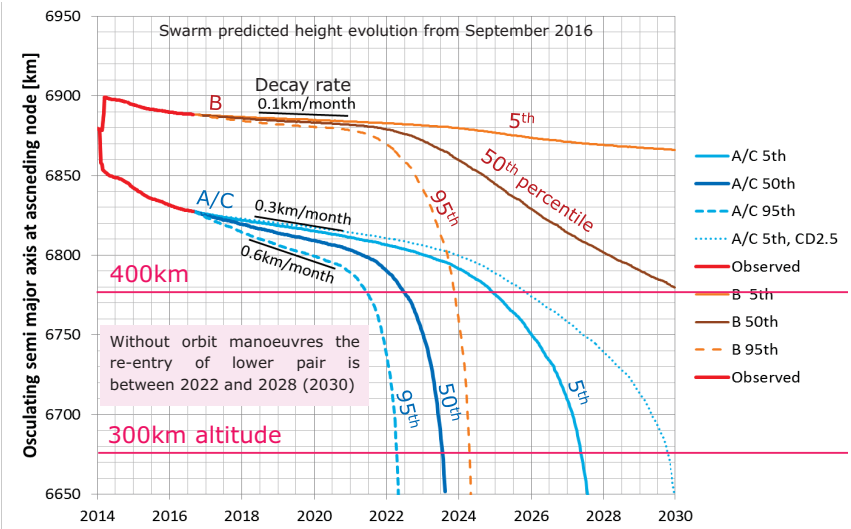

Figure 3.3: Orbit evolution of the three *Swarm* satellites [ESA, 2016].

Further information about the *Swarm* products, can be found *e.g.* on the ESA webpage [ESA, 2017c] and in the paper by Olsen et al. [2013].

3.2 Pre-processing of the magnetic field observations

Two different methods are presented in this thesis, the LCM and 1D SECS method. The two methods are optimized for working with both CHAMP and *Swarm* magnetic field observations, thereby expanding the use of both methods. The *Swarm* and CHAMP satellites provide calibrated and formatted time series of observations from each of the three satellites as *Level-1b* (L1b) data (level-3 data for CHAMP), given in physical SI units in geo-localized reference frames. The products used in this thesis are MAG LR L1B 1 Hz scalar and vector measurements of the magnetic field intensity, F^{obs}, provided by the ASM and VFM instrument [Olsen et al., 2013].

The magnetic field observations provided by CHAMP and *Swarm* contains the full magnetic field, including all magnetic sources (see Section 2.2). To estimate the ionospheric contribution we need to remove contributions from the core, crust and magnetosphere. For the scalar field, the ionospheric contribution, δF^{obs} is found as

$$\delta F^{obs} = F^{\text{obs}} - F^{\text{mod}}, \tag{3.1}$$

where F^{mod} is the contribution from core, crust and magnetosphere provided by the CHAOS-5 model [Finlay et al., 2015]. The same approach is followed for each component of the vector field. Studying the residual magnetic field of strengths down to a few nT, removal and determination of, especially the core field with strengths up to $\sim 70,000$ nT, is crucial. A discussion of the separation of the ionospheric signal from other sources using geomagnetic models, such as CHAOS-5, is discussed in Stolle et al. [2016]. They find a deviation of the ionospheric signal of up to 10 to 15% based on lithospheric and quiet-time magnetospheric signal. The magnetospheric correction is found by the *RC* index (Section 2.6). Figure 3.4 shows the magnetic field for a typical orbit as a function of *Quasi Dipole* (QD) latitude (see later subsection for details) after the removal of the core field (a and b), core plus crustal field (c and d) and finally the removal of core, crust and magnetospheric contribution (e and f). Focusing on the bottom row, we see a typical contribution from the ionosphere. At night (left), only polar regions (auroral electrojet system) contributes to the ionospheric magnetic field. The signature is, especially for the southern pole (negative QD latitudes) consistent with the signature of a single westward electrojet around $65°$. During the day (right), low latitude regions shows sign of the solar illumination dependent Sq current system. The high latitude electrojet signal is, however, still visible.

Vector vs. scalar field measurements

The LCM and 1D SECS methods differ mainly in the way the ionospheric currents are estimated. Differences in input data, however, also affects the methods ability to accurately determine the ionospheric currents. The LCM uses scalar data as input, and is therefore only able to determine the equivalent current system (auroral electrojet system). The 1D SECS method, however, uses the full potential of satellite data, by using the full vector field provided by

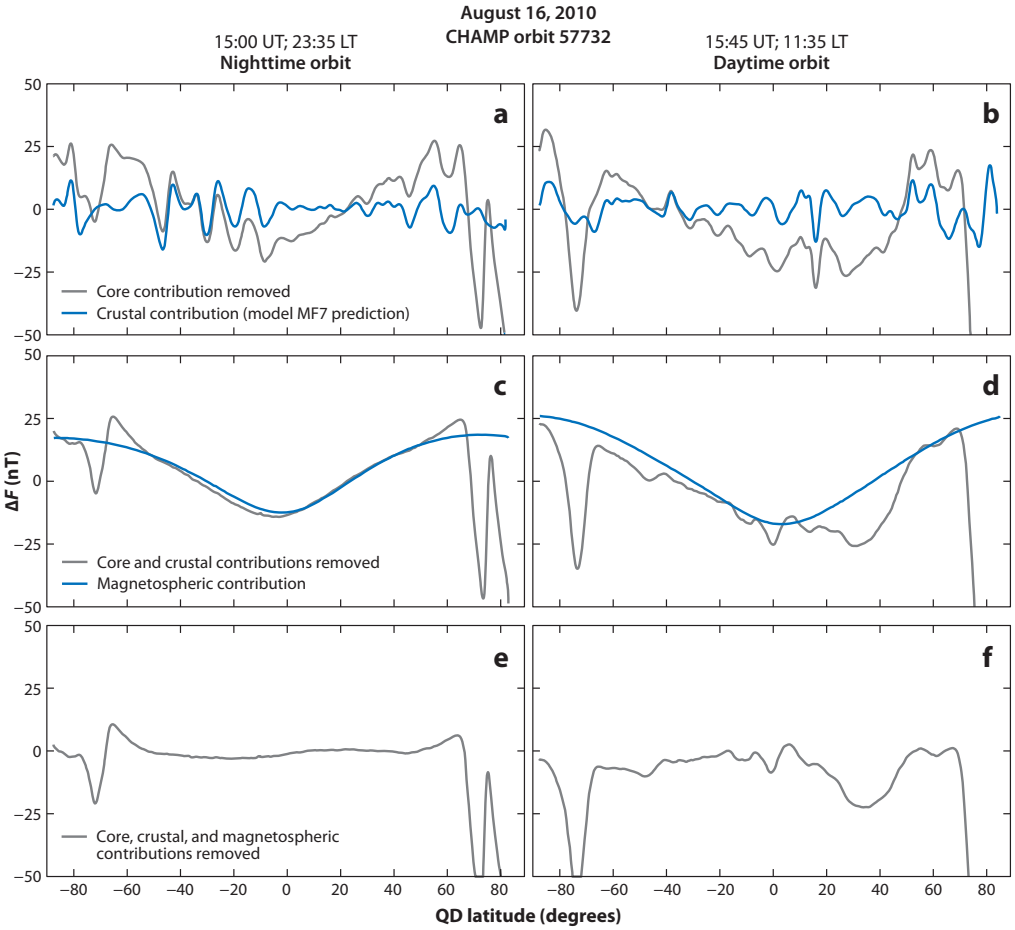

Figure 3.4: Magnetic field intensity observations as a function of QD latitude from a typical satellite night time (left) and daytime (right) orbit, deducted the main field (top row), main field and crustal field (middle row) and the full modelled estimate of core, crust and magnetosphere, $\boldsymbol{F}^{\text{mod}}$. The figure is reprinted from Olsen and Stolle [2012].

CHAMP and *Swarm*. It enables determination of both the auroral electrojet system and the FACs. The use of vector data introduces, however, also complications in terms of computation and an additional error source due to stronger contamination of the radial magnetic vector component from FACs compared to only using measurements of the field intensity (scalar observations).

Choosing the correct coordinate system for presenting the ionospheric sheet current densities

Many different coordinate systems are used as reference for studying the high-latitude geospace. Laundal and Gjerloev [2014] argue how a correct choice in coordinate system is important, especially when considering longitudinal or UT variations. They furthermore argue that when analysing ionospheric currents, the appropriate current system is a *corrected geomagnetic* (CGM) coordinate system, such as the apex *quasi-dipole* (QD) coordinate system [Richmond, 1995]. To give the best possible presentation of our estimates of the auroral electrojet system, all results in this thesis are given in the QD coordinate system.

Conversion to the QD system from a geographical coordinate system involves a scaling of the vector to compensate for variations in magnetic field strength seen in a geographical grid and a rotation to a non-orthogonal set of base vectors. Geographical coordinates are converted from field line tracing along an International Geomagnetic Reference Field (IGRF) [Thébault et al., 2015] model line to the geodetic height (maximum height above the field line above the Earth, taking the Earth's elliptical shape into account). The QD longitude is then found as the centred dipole longitude of this point. The corresponding QD latitude is determined by mapping back to a spherical Earth along a dipole field line [Laundal and Gjerloev, 2014; Laundal and Richmond, 2017].

Chapter 4

Mathematical description of two models describing the auroral electrojet system

4.1 Line current model

The line current model (LCM), first presented by Olsen [1996], takes advantage of the fact that electric currents are predominantly confined to the direction along the geomagnetic main field, $\boldsymbol{B}_0$, due to the nearly vanishing transverse electrical conductivity in the region above 300 km altitude. These FACs will not, assuming a uniform ambient field ($\boldsymbol{B}_0$), contribute to the parallel magnetic field, and thereby the intensity of the magnetic field, $F = B_{||}$. Even for a more realistic distribution of currents, the FAC contribution to F is negligible. In the ionospheric E-region, the transverse conductivity are in contrast comparably large, allowing horizontal currents. These currents will cause magnetic signatures, measurable in the magnetic field intensity. We are therefore able to apply magnetic field intensity anomalies ($\delta F = F^{\text{obs}} - F^{\text{mod}}$), such as the ones described in Section 3.2 on page 32, to investigate the horizontal, ionospheric, E-region currents.

From the magnetic field residuals, we estimate, using basic trigonometry, the intensity of the magnetic field as

$$\delta F = \delta B_{||} = \delta B_r \sin I^M + \delta B_H \cos I^M, \tag{4.1}$$

where δB_r and δB_H are the horizontal and radial component of the residual magnetic field. The magnetic inclination I^M, is found from the main field model, CHAOS-5, as

$$\tan I^M = \frac{Z}{H} = \frac{-B_r}{\sqrt{B_\theta^2 + B_\phi^2}} \Leftrightarrow I^M = \arctan\left(\frac{-B_r}{\sqrt{B_\theta^2 + B_\phi^2}}\right). \tag{4.2}$$

Z and H are here the vertical and horizontal part of the main field model in a local cartesian coordinate system. B_r, B_θ and B_ϕ are the radial, θ and ϕ component of the main field in a spherical, geocentric coordinate system described by CHAOS-5.

Geometry of the line current model

The method is based on a series of line currents placed in the ionospheric E-layer with an along track horizontal separation of $\Delta = 113$ km, corresponding to 1°. Figure 4.1 describes

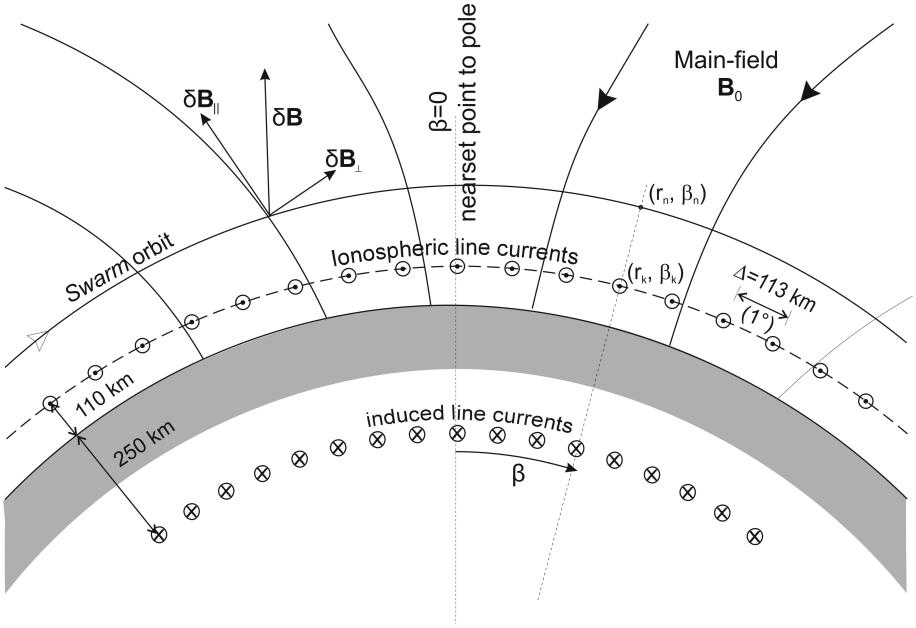

Figure 4.1: Geometry of the line current model. Reprinted from Aakjær et al. [2016].

the geometry of the model, where subscript n refers to points along the satellite track, and k the locations of the line currents. The altitude of the line currents are assumed constant at 110 km. The magnetic field contribution from the line currents is a Laplacian potential field in the region above the ionosphere. The spatial structure of the ionospheric currents and the strength of the magnetic field are thus dependent on the distance to the measurements. A typical rule of thumb states that, for a potential field like the magnetic field, only structures of wavelength larger than the distance to the measurements can be resolved. With satellites such as CHAMP and *Swarm* flying at altitudes about 340 km above the ionosphere it is hardly possible to distinguish between a series of discrete line currents separated by 1° and a continuous current distribution. The discrete line current method with a 1° spacing is therefore preferred over a continuous current distribution to ease computations. The magnetic input data can from a similar argument be down sampled from 1 s to 10 s data. The secondary Earth induced currents in the electrically conducting lithosphere and upper mantle is considered by assuming a superconductor at depth, d. This acts as a mirror for the primary currents in the ionosphere and places the currents at depth $2d = 250$ km, corresponding to induction effects with a 1h period.

The satellite orbit is along almost constant longitude. In most cases it is therefore possible to use latitude as an along-track measure. Since magnetic satellites such as *Swarm* and CHAMP fly in an inclined orbit, longitudinal independence is not a valid assumption for the region closest to the pole. This result in a non-equidistant spacing of line currents along latitude. We therefore use, as presented in Olsen [1996], an along-track parameter, β, describing the distance from the closest approach ($\beta = 0$) to the geomagnetic North (or South) pole. This is defined as the arc length angle of the track and can be estimated from the cosine rule in spherical geometry,

$$\cos\beta = \cos\theta \cdot \cos\theta_0 + \sin\theta \cdot \sin\theta_0 \cdot \cos(\phi - \phi_0), \tag{4.3}$$

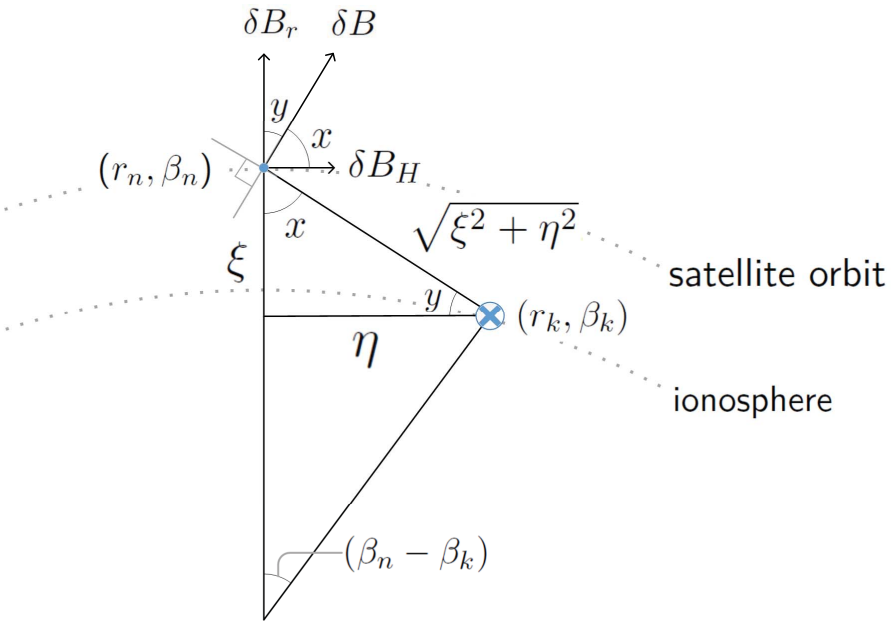

Figure 4.2: Geometry of the contributions of one line current to the magnetic field.

where (θ, ϕ) is the coordinate in which β is estimated, and (θ_0, ϕ_0) is the reference location of the closest approach to the pole. (θ_0, ϕ_0), and thereby the β parameter, is orbit specific and needs to be estimated for each orbit. To distinguish between ascending and descending part of the orbit, all β values for the ascending part of the orbit, prior to (θ_0, ϕ_0) are set to $-\beta$.

Contribution from a single line current

The magnetic field contribution, δF_n, from a single infinite line current, perpendicular to the satellite track, carrying a steady current of strength j'_k, can be evaluated from Ampére's law (Equation 2.4). Figure 4.2 gives the geometry of the situation, with the line current placed at (r_k, β_k) and observation at (r_n, β_n). The direction of the magnetic field contribution is determined from the right hand rule. Symmetry arguments claims a constant magnitude of δF_n around an amperian loop centred at the wire of radius $\sqrt{\xi^2 + \eta^2}$. Ampére's law can be converted from differential form to integral form by application of Stoke's theorem $\left(\int_S (\nabla \times \boldsymbol{v}) \cdot d\boldsymbol{a} = \oint_P \boldsymbol{v} \cdot d\boldsymbol{l}\right)$

$$\mu_0 j'_k = \oint \boldsymbol{\delta B} \cdot d\boldsymbol{l} = \delta B \oint dl = \delta B \; 2\pi\sqrt{\xi^2 + \eta^2}. \tag{4.4}$$

The mathematical description of η and ξ are found through geometric observations as

$$\begin{aligned} \eta &= r_k \sin(\beta_n - \beta_k), \\ \xi &= r_n - r_k \cos(\beta_n - \beta_k). \end{aligned} \tag{4.5}$$

Here, r_k is the radius of the ionosphere set to $a + 110$km, with a (6371.2 km) as the radius of the Earth, and r_n the radius of the satellite orbit. Solving for δB, we get

$$\delta B = \frac{\mu_0 j'_k}{2\pi} \frac{1}{\sqrt{\xi^2 + \eta^2}}. \tag{4.6}$$

The parallel contribution is estimated by projecting δB onto horizontal and radial components. From basic trigonometry we get

$$\delta B_r = \delta B \cdot \cos y = \delta B \cdot \frac{\eta}{\xi^2 + \eta^2} = \frac{\mu_0 j'_k}{2\pi} \frac{\eta}{\xi^2 + \eta^2}, \tag{4.7}$$

$$\delta B_H = \delta B \cdot \cos x = \delta B \cdot \frac{\xi}{\xi^2 + \eta^2} = \frac{\mu_0 j'_k}{2\pi} \frac{\xi}{\xi^2 + \eta^2}. \tag{4.8}$$

Combining the results of Equation 4.1, 4.7 and 4.8,

$$\delta F_n = \frac{\mu_0 j'_k}{2\pi} \frac{\eta}{\xi^2 + \eta^2} \sin I_n^M + \frac{\mu_0 j'_k}{2\pi} \frac{\xi}{\xi^2 + \eta^2} \cos I_n^M = \frac{\mu_0}{2\pi} \frac{\xi \cos I_n^M + \eta \sin I_n^M}{\xi^2 + \eta^2} \cdot j'_k, \tag{4.9}$$

yields the magnetic contribution of the n'th line current perpendicular to the magnetic field intensity residual evaluated at (r_n, β_n).

Rotation of the line currents along constant magnetic latitude

Previously presented results, based on the above method [*e.g.* Olsen et al., 2002; Moretto et al., 2002; Ritter et al., 2004] assumed the line current perpendicular to the satellite track. For orbits, where this is not a good approximation, an assumption like this will lead to a systematic underestimation of the sheet current densities. A more accurate assumption would be to assume the currents along constant QD latitude ($\boldsymbol{j}$) [Laundal and Gjerloev, 2014]. The non-rotated currents ($\boldsymbol{j'}$) are a projection of the real current, and will therefore be dependent on the angle between $\boldsymbol{j}$ and $\boldsymbol{j'}$, δ, see Figure 4.3(a). The non-rotated current, $\boldsymbol{j'}$, is described in terms of $\boldsymbol{j}$ and δ as

$$\boldsymbol{j'} = \boldsymbol{j} \cos \delta. \tag{4.10}$$

From basic trigonometry, given in Figure 4.3(b), δ can be estimated from the along track unit vector, $\hat{\boldsymbol{v}}$, the unit vector along $\boldsymbol{j'}$, $\hat{\boldsymbol{r}} \times \hat{\boldsymbol{v}}$, and the unit vector along constant QD latitude and $\boldsymbol{j}$, $\hat{\boldsymbol{f}}_{\mathbf{1}}$ [Laundal and Richmond, 2017]

$$(\hat{\boldsymbol{r}} \times \hat{\boldsymbol{v}}) \cdot \hat{\boldsymbol{f}}_{\mathbf{1}} = |\hat{\boldsymbol{r}} \times \hat{\boldsymbol{v}}| \, |\hat{\boldsymbol{f}}_{\mathbf{1}}| \cos \delta \Longleftrightarrow \cos \delta = (\hat{\boldsymbol{r}} \times \hat{\boldsymbol{v}}) \cdot \hat{\boldsymbol{f}}_{\mathbf{1}}. \tag{4.11}$$

Comparing Equation 4.10 and 4.11 we find that the rotated currents can be estimated by multiplying the results of the non-rotated current strength with a scaling factor of $1/\left[(\hat{\boldsymbol{r}} \times \hat{\boldsymbol{v}}) \cdot \hat{\boldsymbol{f}}_{\mathbf{1}}\right]$. $\cos \delta$ will always be less than or equal to one, amplifying the estimates of the rotated currents compared to the non-rotated estimates. Substituting Equation 4.10 and 4.11 into Equation 4.9 we find the magnetic signature from the rotated currents as

$$\delta F_n = \frac{\mu_0}{2\pi} \frac{\xi \cos I_n^M + \eta \sin I_n^M}{\xi^2 + \eta^2} \left((\hat{\boldsymbol{r}} \times \hat{\boldsymbol{v}}) \cdot \hat{\boldsymbol{f}}_{\mathbf{1}} \right) j_k. \tag{4.12}$$

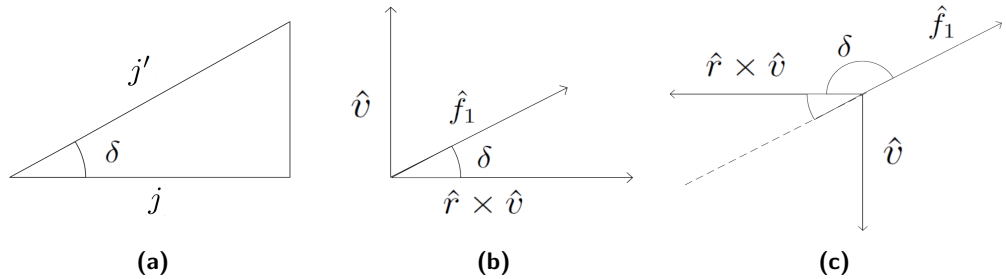

(a) **(b)** **(c)**

Figure 4.3: geometry of the rotated and non-rotated line currents.

Rotation of the line currents furthermore, introduces a direction of the line current, according to the flight direction of the satellite, compared to the direction of the current. This is presented in the difference in δ between Figure 4.3(b) and (c). By application of the same scaling factor for both ascending and descending orbits, a positive current is found towards east, for a positive current towards the sun in the non-rotated coordinate frame.

The scaling factor for the sheet current densities $\left(1/\left[(\hat{\boldsymbol{r}} \times \hat{\boldsymbol{v}}) \cdot \hat{\boldsymbol{f}}_{\mathbf{1}}\right]\right)$ will due to the geometry of $(\hat{\boldsymbol{r}} \times \hat{\boldsymbol{v}})$ and $\hat{\boldsymbol{f}}_{\mathbf{1}}$, go to infinity when $\hat{\boldsymbol{f}}_{\mathbf{1}}$ is parallel to the satellite track. The method is therefore not able to give an accurate determination of the currents in the region closest to the pole. To asses the problem, and to highlight the unstable regions, we have implemented a truncation value for the angle at 60° degrees. This means that all values where $\cos\delta = (\hat{\boldsymbol{r}} \times \hat{\boldsymbol{v}}) \cdot \hat{\boldsymbol{f}}_{\mathbf{1}} < 0.5$ is set to 0.5.

Inclusion of induced currents and ground observations

The secondary Earth induced currents are, as noted in the description of method geometry, realized through the positions of a superconducting layer at half the depth to the secondary induced currents [Weimer, 2013]. They are implemented in the model, simply by including an additional term of opposite sign and radius of $a - 2d$. This results in a magnetic signature, including the induced current term as

$$\delta F_n = \frac{\mu_0}{2\pi}\left[\frac{\xi \cos I_n^M + \eta \sin I_n^M}{\xi^2 + \eta^2} - \frac{\xi_j \cos I_n^M + \eta_j \sin I_n^M}{\xi_j^2 + \eta_j^2}\right]\left((\hat{\boldsymbol{r}} \times \hat{\boldsymbol{v}}) \cdot \hat{\boldsymbol{f}}_{\mathbf{1}}\right) \cdot j_k, \quad (4.13)$$

with η_j and ξ_j given as

$$\begin{aligned} \eta_j &= (a - 2d)\sin(\beta_n - \beta_k), \\ \xi_j &= r_n - (a - 2d)\cos(\beta_n - \beta_k). \end{aligned} \quad (4.14)$$

The line current method can also be applied to ground observations by changing the sign in front of the cosine terms in the calculations of δF_n, yielding the magnetic signature from a single current, when applied to ground observations, as

$$\delta F_n = \frac{\mu_0}{2\pi}\left[\frac{-\xi \cos I_n^M + \eta \sin I_n^M}{\xi^2 + \eta^2} - \frac{\xi_j \cos I_n^M + \eta_j \sin I_n^M}{\xi_j^2 + \eta_j^2}\right]\left((\hat{\boldsymbol{r}} \times \hat{\boldsymbol{v}}) \cdot \hat{\boldsymbol{f}}_{\mathbf{1}}\right) \cdot j_k. \quad (4.15)$$

Estimating the total contribution from a series of line currents

The total magnetic field disturbance from a series of line currents, presented in Figure 4.1 is found by superposition of single current contributions. This can be evaluated in matrix form as

$$\boldsymbol{d}^{obs} = \boldsymbol{G}\boldsymbol{m}, \tag{4.16}$$

where $\boldsymbol{d}^{obs}$ is the data vector containing the N magnetic field residual observations, δF_n, where $n = 1, ..., N$. $\boldsymbol{m}$ is the line current amplitudes of the individual currents, j_k, of length M, where $k = 1, ..., M$. $\boldsymbol{G}$ is an $N \times M$ matrix describing the relationship between the magnetic field observations and current amplitudes with elements described by

$$g_{n,k} = \frac{\mu_0}{2\pi}\left[\frac{\xi_{n,k}\cos I_n^M + \eta_{n,k}\sin I_n^M}{\xi_{n,k}^2 + \eta_{n,k}^2} - \frac{(\xi_{n,k})_j \cos I_n^M + (\eta_{n,k})_j \sin I_n^M}{(\xi_{n,k})_j^2 + (\eta_{n,k})_j^2}\right]\left((\hat{\boldsymbol{r}} \times \hat{\boldsymbol{v}}) \cdot \hat{\boldsymbol{f}}_{\mathbf{1}}\right). \tag{4.17}$$

Having obtained the individual line currents, j_k, the sheet current density, $J(\beta_k)$, can be estimated as

$$J(\beta_k) = \frac{j_k}{\Delta} = \frac{j_k}{113 \text{ km} \cdot |\cos\delta|}, \tag{4.18}$$

due to the equidistant line current spacing, Δ. For a 1° separation and perpendicular currents at an altitude of 110 km, Δ is equal to 113 km. Rotation of the line currents changes the distance, the distance is therefore adjusted by a factor of $|\cos\delta|$.

4.2 Spherical elementary current system

The spherical elementary current system (SECS) method, presented by Amm [1997], is based on the principle that any horizontal ionospheric current system, together with its FACs can be uniquely constructed as a superposition of two basis vector functions, one curl-free and one divergence-free. The principle is based on Helmholtz's theorem, stating that any vector field can be decomposed into an irrotational (curl-free) and solenoidal (divergence-free) component.

Constructing the basis vector functions

The curl-free component is associated with the radially flowing FACs. These are presented in a local spherical coordinate system (r', θ', ϕ') with $\theta' = 0$ at the SECS pole and corresponding unit vectors $(\hat{e}'_r, \hat{e}'_\theta, \hat{e}'_\phi)$ in Figure 4.4. Feeding the system is a FAC with strength $\mathcal{I}_{cf}$ at $\theta' = 0$. This current is then distributed homogeneously with constant divergence across the sphere along θ', with the following restrictions for the horizontal ionospheric elementary current system, connected with that FAC

$$\left[\nabla \times \mathbf{J}_{cf}(\mathbf{r}')\right]_r = 0, \tag{4.19}$$

$$\nabla_h \cdot \mathbf{J}_{cf}(\mathbf{r}') = C \qquad \text{for} \quad \theta' \neq 0. \tag{4.20}$$

Subscript h denotes the horizontal part of the divergence. Current continuity and a uniform outflow everywhere but at $\theta' = 0$ yields $C = \frac{-\mathcal{I}}{4\pi r_I}$, where r_I is the radius of the ionosphere, yielding

$$\nabla_h \cdot \mathbf{J}_{cf}(\mathbf{r}') = \frac{-\mathcal{I}_{cf}}{4\pi r_I} \qquad \text{for} \quad \theta' \neq 0. \tag{4.21}$$

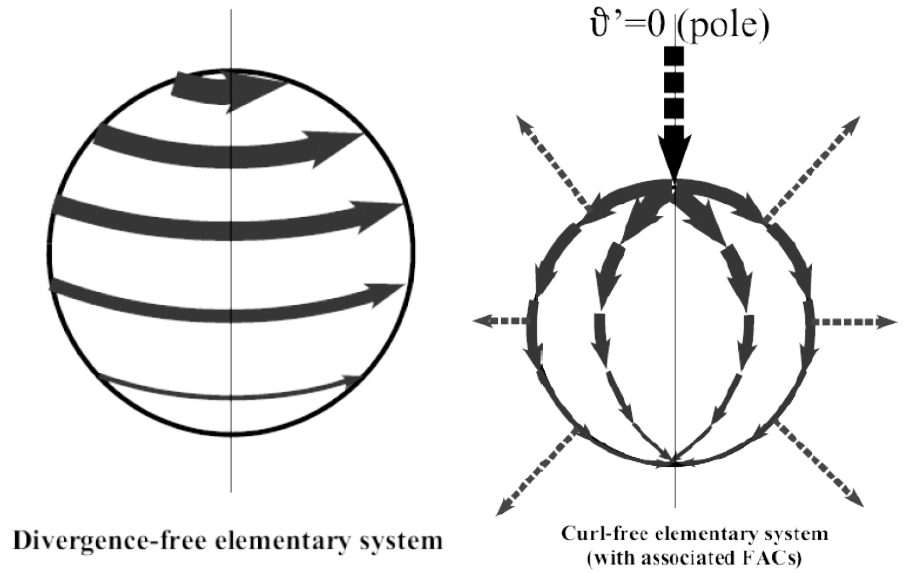

Figure 4.4: Schematic representation of the divergence-free and curl-free basis vector functions. Source: [Vanhamäki et al., 2003].

Integration over θ', using the boundary condition that no horizontal current can be left on the opposite side of the pole ($J(\theta' = 180°) = 0$), yields

$$\boldsymbol{J}_{cf,2D}(\theta', \phi') = \frac{\mathcal{I}_{cf}}{4\pi r_I} cot\left(\frac{\theta'}{2}\right) \hat{e}_{\phi'}. \tag{4.22}$$

This current system corresponds to the current system, known as Pedersen currents, presented by Fukushima [1976]. Provided by Juusola [2009] the following three assumptions hold: (1) constant ratio of Pedersen to Hall conductivities, (2) $(\nabla\Sigma_H(\theta_n, \phi_n) \times \mathbf{E}_\perp(\theta_n, \phi_n))_r = 0$, where Σ_H is the Hall conductance, and $E_\perp$ is the perpendicular electrical field and 3) uniform conductances.

The associated FACs are found, assuming a purely radial flow, from the divergence of Equation 4.22

$$\mathbf{j}_{\parallel,2D}(r', \theta', \phi') = \begin{cases} \frac{\mathcal{I}_{cf}}{4\pi r_I}\left(1 - \frac{2}{\sin\theta'}\delta(\theta')\right)\hat{e}_r, & r' \geq r_I. \\ 0, & r' < r_I. \end{cases} \tag{4.23}$$

The divergence-free part is found from similar constraints: Constant curl, $\nabla \times \mathbf{J}_{cf}(\mathbf{r}') = C$, and zero divergence, $\nabla_h \cdot \mathbf{J}_{cf}(\mathbf{r}') = 0$:

$$\mathbf{J}_{df,2D}(\theta', \phi') = \frac{\mathcal{I}_{df}}{4\pi r_I} cot\left(\frac{\theta'}{2}\right) \hat{e}_{\theta'}. \tag{4.24}$$

The curl-free and the divergence-free elementary current systems (Equation 4.22 and 4.24), span a complete set of basis vector functions, due to their linear independence and the fact that they can uniquely represent any continuously differentiable vector field on a sphere [Amm, 1997, 2001].

Two dimensional SECS

The method can be applied to estimate the auroral electrojet system, by distributing curl-free and divergence-free SECS evenly across the ionosphere. Estimates of the ionospheric current density distribution can be found by matching their magnetic signature with observations of the magnetic field. This is presented in several studies as the 2D SECS method [Amm and Viljanen, 1999; Vanhamäki et al., 2003].

One dimensional SECS

The 2D SECS method was adapted by Vanhamäki et al. [2003] to a one dimensional version, suitable for use with satellite magnetic measurements. This enabled determination of the auroral electrojets and associated FACs. One dimensional refers in this case to no dependence on longitude, corresponding to almost meridional orbits of the magnetic satellites, such as CHAMP and *Swarm*. The 1D SECS method uses two different coordinate systems, a primed, and a non-primed one.

$(r', \theta', \phi') =$ refers to a local spherical coordinate system corresponding to the given SECS, with $\theta' = 0$ at the pole. An appropriate spherical coordinate system oriented such that the pole is at $\theta' = 0$, exists for each SECS.

(r, θ, ϕ)= coordinate system in which the 1D SECS grid is defined. This can, as example, be a geographic, geomagnetic or a case specific coordinate system.

(r_n, θ_n, ϕ_n) = Location of the magnetic observations defined in the unprimed coordinate system.

(r_k, θ_k, ϕ_k) = Location of the 1D SECS poles, defined in the unprimed coordinate system.

The one dimensional version of Equations 4.22, 4.23 and 4.24 is found by integration over longitude, ϕ_k [Vanhamäki et al., 2003],

$$J_\phi(\theta_n, \theta_k) = \frac{\mathcal{I}_{df}}{2r_I} \begin{cases} -\tan(\theta_n/2), & \theta_n < \theta_k. \\ \cot(\theta_n/2), & \theta_n > \theta_k. \end{cases} \tag{4.25}$$

$$J_r(r_n, \theta_n, \theta_k) = \begin{cases} \frac{\mathcal{I}_{cf}}{r_n^2} \left(\frac{1}{2} - \frac{1}{\sin(\theta_k)} \delta(\theta_n - \theta_k) \right), & r_n < r_i. \\ 0, & r_n > r_i. \end{cases} \tag{4.26}$$

$$J_\theta(\theta_n, \theta_k) = \frac{\mathcal{I}_{cf}}{2r_I} \begin{cases} -\tan(\theta_n/2), & \theta_n < \theta_k. \\ \cot(\theta_n/2), & \theta_n > \theta_k. \end{cases} \tag{4.27}$$

The connection to the magnetic field is found using Biot-savart's law and expanding in spherical harmonics

$$B_r = \frac{\mu_0 \mathcal{I}_{df}}{2r_n} \begin{cases} \sum_{l=1}^{\infty} \left(\frac{r_n}{r_i} \right)^l P_l(\cos\theta_k) P_l(\cos\theta_n), & r_n < r_i. \\ \sum_{l=1}^{\infty} \left(\frac{r_i}{r_n} \right)^{l+1} P_l(\cos\theta_k) P_l(\cos\theta_n), & r_n > r_i. \end{cases} \tag{4.28}$$

$$B_\theta = \frac{\mu_0 \mathcal{I}_{df}}{2r_n} \begin{cases} \sum_{l=1}^{\infty} \left(\frac{r_n}{r_i} \right)^l \left(\frac{1}{l} \right) P_l(\cos\theta_k) \tilde{P}_l^1(\cos\theta_n), & r_n < r_i \\ \sum_{l=1}^{\infty} \left(\frac{r_i}{r_n} \right)^{l+1} \left(\frac{1}{l+1} \right) P_l(\cos\theta_k) \tilde{P}_l^1(\cos\theta_n), & r_n > r_i. \end{cases} \tag{4.29}$$

$$B_\phi = \frac{\mu_0 \mathcal{I}_{cf}}{2r_n} \begin{cases} -\cot(\theta_n/2), & r_n > r_i, \theta_n > \theta_k. \\ \tan(\theta_n/2), & r_n > r_i, \theta_n < \theta_k. \\ 0, & r_n < r_i. \end{cases} \tag{4.30}$$

Where P_l is the associated legendre functions. $\tilde{P}_l^1$ is the non-normalized associated legendre function (of order 1). This is different from the P_l^1 Schmidt semi-normalized function typically used in geomagnetism. The non-normalized $\tilde{P}_l^1$ can be written in terms of the Schmidt normalized legendre function as the first derivative,

$$\tilde{P}_l^1 = \frac{dP_l}{d\theta}. \tag{4.31}$$

The above calculations are elaborated in Vanhamäki et al. [2003] and Juusola et al. [2006].

Induced currents

The expansion of the model to include secondary Earth-induced currents for the divergence-free 1D SECS was presented by Pulkkinen et al. [2003] by including a secondary equivalent current layer inside the Earth's crust. The same approach will be presented here, in a slightly different way.

To introduce a secondary equivalent current layer, we represent the magnetic field vector $\boldsymbol{B} = -\nabla V$ using a spherical harmonic expansion of its scalar potential V. This allows for a separation of the magnetic field into internal and external contributions. At satellite height, both the contributions from the ionospheric equivalent currents and the secondary Earth-induced equivalent currents are measured as internal, giving a potential on the form

$$V^{\text{sat}} = a \sum_{l=1}^{\infty} \left[(\iota_l(t) + \zeta_l) \left(\frac{a}{r_n} \right)^{l+1} \right] P_l(\cos\theta_n). \tag{4.32}$$

ι_l is the internal induced expansion coefficient and ζ_l the internal ionospheric expansion coefficients [Sabaka et al., 2000]. The ionospheric currents are, however, at ground level ($r_n < r_I$) measured as external, while the secondary Earth-induced currents remain internal,

$$V^{\text{ground}} = a \sum_{l=1}^{\infty} \left[\chi_l(t) \left(\frac{r_n}{a} \right)^{l} + \iota_l(t) \left(\frac{a}{r_n} \right)^{l+1} \right] P_l(\cos\theta_n). \tag{4.33}$$

Here χ_l is the external ionospheric expansion coefficient. The radial component of the magnetic field must be continuous, and together with the assumption of zero thickness of the ionosphere, we get

$$B_r(r_n = r_I^+) = B_r(r_n = r_I^-). \tag{4.34}$$

Using $\boldsymbol{B} = -\nabla V$, we find

$$\left. \frac{\partial V^{\text{sat}}}{\partial r_n} \right|_{r_n = r_I^+} = \left. \frac{\partial V^{\text{ground}}}{\partial r_n} \right|_{r_n = r_I^-},$$

$$-\sum_{l=1}^{\infty} \left[(\iota_l + \zeta_l) \left(\frac{a}{r_I} \right)^{l+2} (l+1) \right] P_n(\cos\theta_n)$$
$$= \sum_{l=1}^{\infty} \left[\chi_l \left(\frac{r_I}{a} \right)^{l-1} l - \iota_l \left(\frac{a}{r_I} \right)^{l+2} (l+1) \right] P_l(\cos\theta_n),$$

$$-\sum_{l=1}^{\infty} \zeta_l \left(\frac{a}{r_I} \right)^{l+2} (l+1) = \sum_{l=1}^{\infty} \chi_l \left(\frac{r_I}{a} \right)^{l-1} l. \tag{4.35}$$

A sum of linear independent variables equal to a sum of linear independent variables, will require the variables themselves equal for all l, resulting in

$$-\zeta \left(\frac{a}{r_I} \right)^{l+2} (l+1) = \chi \left(\frac{r_I}{a} \right)^{l-1} l, \tag{4.36}$$

$$\zeta = -\chi \left(\frac{r_I}{a}\right)^{2l+1} \frac{l}{l+1} = -\chi\Gamma. \tag{4.37}$$

Γ is a transformation factor between ζ and χ to perform substitutions at all r

$$\Gamma = \left(\frac{r_I}{a}\right)^{2l+1} \frac{l}{l+1}. \tag{4.38}$$

Calculations of the induced expansion coefficient, ι

The external (inducing) expansion coefficients χ_l are at ground level $(r = a)$ connected to the internal (induced), ι_l, due to the electrical conductivity of the Earth's interior. Each external coefficient will only induce one internal coefficient, assuming a conductivity that depends only on radius (1D Earth). This relationship, given by the Q-response, can in frequency domain be written as

$$\tilde{Q}_l(\omega) = \frac{\tilde{\iota}_l(\omega)}{\tilde{\chi}_l(\omega)} \Leftrightarrow \tilde{\iota}_l(\omega) = \tilde{\chi}_l(\omega)\tilde{Q}_l(\omega), \tag{4.39}$$

where ω is angular frequency and $\tilde{}$ indicates frequency domain. The magnetic field components can be found using $\tilde{B} = -\nabla\tilde{V}$. Using the potential given in Equation 4.33 for $r < r_i$, reveals the following radial magnetic field component

$$\tilde{B}_r(r_n < r_I) = -\sum_{l=1}^{\infty} \left[\tilde{\chi}_l \left(\frac{r_n}{a}\right)^{l-1} l - \tilde{\iota}_l \left(\frac{a}{r_n}\right)^{l+2} (l+1)\right] P_l(\cos\theta_n). \tag{4.40}$$

Inserting the Q-response along with $r = a$, this reduces to

$$\tilde{B}_r(r_n < r_I) = -\sum_{l=1}^{\infty} \tilde{\chi}_l(\omega) \left[l - \tilde{Q}_l(\omega)(l+1)\right] P_l(\cos\theta_n). \tag{4.41}$$

The θ-component is found in the same way as

$$\tilde{B}_\theta(r_n < r_I) = -\sum_{l=1}^{\infty} \tilde{\chi}_l(\omega) \left[1 + \tilde{Q}_l(\omega)\right] \frac{\partial P_l(\cos\theta_n)}{\partial\theta_n}. \tag{4.42}$$

Following a similar approach for the region above the ionosphere, using $r_n = r_I$ and $\zeta = -\chi \left(\frac{r_I}{a}\right)^{2l+1} \frac{l}{l+1}$ yields magnetic field components of

$$\tilde{B}_r(r_n > r_I) = -\sum_{l=1}^{\infty} \tilde{\chi}_l(\omega) \left[\left(\frac{r_I}{a}\right)^{2l+1} l - \tilde{Q}_l(\omega)(l+1)\right] \left(\frac{a}{r_n}\right)^{l+2} P_l(\cos\theta_n), \tag{4.43}$$

$$\tilde{B}_\theta(r_n > r_I) = -\sum_{l=1}^{\infty} \tilde{\chi}_l(\omega) \left[-\left(\frac{r_I}{a}\right)^{2l+1} \frac{l}{l+1} + \tilde{Q}_l(\omega)\right] \left(\frac{a}{r_n}\right)^{l+2} \frac{\partial P_l(\cos\theta_n)}{\partial\theta_n}. \tag{4.44}$$

Considering a 1D conductivity model consisting of an insulating upper mantle of thickness d and a superconductor below depth d, the Q-response will be independent of frequency. This implies zero phase-lag between the external and the induced contributions, allowing the analysis

to be performed in the time-domain separately for each time instant, and Q, with a radius of the superconductor of $r_c = a - d$, of the form

$$Q_l = \frac{l}{l+1}\left(\frac{r_c}{a}\right)^{2l+1}. \tag{4.45}$$

Inserting this, and $\chi_l = -\frac{\mu_0 \mathcal{I}}{2r_I}\left(\frac{a}{r_I}\right)^{l-1}\frac{1}{l}P_l(\cos\theta_k)$, we get

$$B_r = \begin{cases} \frac{\mu_0 \mathcal{I}}{2r_I}\sum_{l=1}^{\infty}\left(\frac{a}{r_I}\right)^{l-1} P_l(\cos\theta_k)\left(1-\left(\frac{c}{a}\right)^{2l+1}\right)P_l(\cos\theta_n), & r_n < r_I. \\ \frac{\mu_0 I_0}{2r_I}\sum_{n=1}^{\infty}\left(\frac{r_i}{r}\right)^{n+2} P_n(\cos\theta_0)\left(1-\left(\frac{c}{r_i}\right)^{2n+1}\right)P_n(\cos\theta), & r > r_i. \end{cases} \tag{4.46}$$

$$B_\theta = \begin{cases} \frac{\mu_0 \mathcal{I}}{2r_I}\sum_{l=1}^{\infty}\left(\frac{a}{r_I}\right)^{l-1} \frac{1}{l}P_l(\cos\theta_k)\left(1+\frac{l}{l+1}\left(\frac{c}{a}\right)^{2l+1}\right)\frac{dP_l(\cos\theta_n)}{d\theta_n}, & r_n < r_I. \\ -\frac{\mu_0 \mathcal{I}}{2r_I}\sum_{l=1}^{\infty}\left(\frac{r_I}{r_n}\right)^{l+2} \frac{1}{l+1}P_l(\cos\theta_k)\left(1-\left(\frac{c}{r_I}\right)^{2l+1}\right)\frac{dP_l(\cos\theta_n)}{d\theta_n}, & r_n > r_I. \end{cases} \tag{4.47}$$

Comparing these equations with Equation 4.28 to 4.29, reveals that B_θ is amplified by induction for $r < r_i$, while induction leads to a weakening of the signal for all other components by the following factors

$$B_r : \begin{cases} 1-\left(\frac{c}{a}\right)^{2n+1}, & r < r_i. \\ 1-\left(\frac{c}{r_i}\right)^{2n+1}, & r > r_i. \end{cases} \tag{4.48}$$

$$B_\theta : \begin{cases} 1+\frac{n}{n+1}\left(\frac{c}{a}\right)^{2n+1}, & r < r_i. \\ 1-\left(\frac{c}{r_i}\right)^{2n+1}, & r > r_i. \end{cases} \tag{4.49}$$

The induced currents will not have any effect on the ϕ component of the magnetic field, since this is determined by the curl-free part of the 1D SECS.

Total current contribution

From the relation between 1D SECS amplitudes, $\mathcal{I}$ (Equations 4.25 to 4.27), and their magnetic signature (Equations 4.46, 4.47 and 4.30), we can model the spatial variation of the ionospheric currents by placing 1D SECS with a one degree separation at the altitude of the ionosphere along the satellite track. The geometry of this is described in Figure 4.5. The total magnetic field caused by the auroral electrojet system is then found as the sum of contributions from all the individual SECS, described in matrix form as

$$\boldsymbol{B} = \boldsymbol{M}\boldsymbol{\mathcal{I}}, \tag{4.50}$$

where $\boldsymbol{B}$ are the N magnetic field observations $\delta B_n = (\delta B_r, \delta B_\theta, \delta B_\phi)_n$ of the residual magnetic field from the ionospheric currents (see Chapter 3), with $n = 1...N$. $\boldsymbol{\mathcal{I}}$ are the M 1D SECS amplitudes, $\mathcal{I}_k = (\mathcal{I}_{df}, \mathcal{I}_{cf})_k$, with $k = 1...M$, and $\boldsymbol{M}$ is a matrix of size $3N \times 2M$ describing the effects of a current system at θ_k to a magnetometer at θ_n. $\boldsymbol{M}$ depends only on the geometry and can be found from Equation 4.46, 4.47 and 4.30.

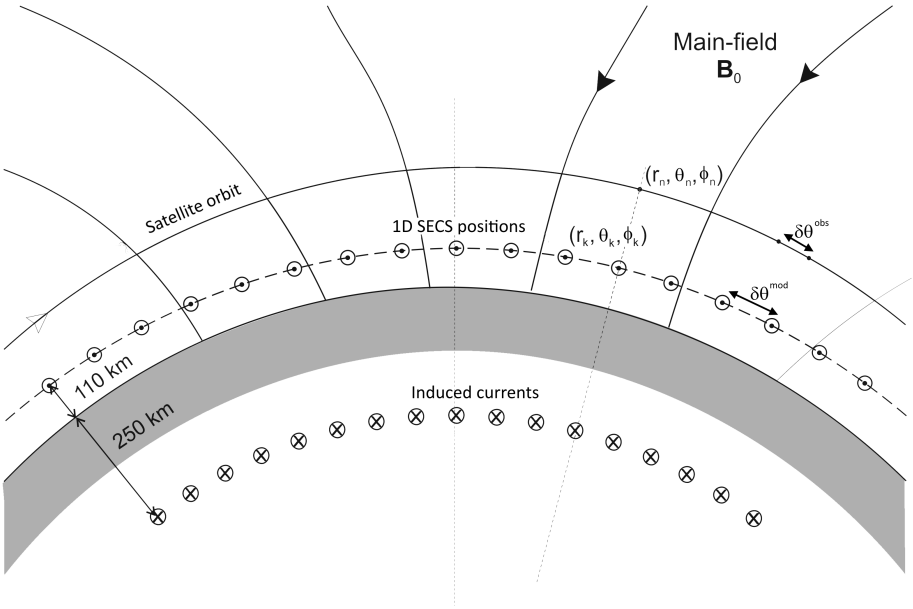

Figure 4.5: Geometry of the 1D SECS method.

Since the aim of the method is to find the individual sheet current densities $(\boldsymbol{J}_r, \boldsymbol{J}_\theta, \boldsymbol{J}_\phi)$, we split Equation 4.50 into separate elements

$$\begin{bmatrix} \boldsymbol{B}_r \\ \boldsymbol{B}_\theta \\ \boldsymbol{B}_\phi \end{bmatrix} = \begin{bmatrix} \boldsymbol{M}_{d,r} & \boldsymbol{M}_{c,r} \\ \boldsymbol{M}_{d,\theta} & \boldsymbol{M}_{c,\theta} \\ \boldsymbol{M}_{d,\phi} & \boldsymbol{M}_{c,\phi} \end{bmatrix} \cdot \begin{bmatrix} \boldsymbol{\mathcal{I}}_{df} \\ \boldsymbol{\mathcal{I}}_{cf} \end{bmatrix} = \begin{bmatrix} \boldsymbol{M}_{d,r} \\ \boldsymbol{M}_{d,\theta} \\ \boldsymbol{M}_{c,\phi} \end{bmatrix} \cdot \begin{bmatrix} \boldsymbol{\mathcal{I}}_{df} \\ \boldsymbol{\mathcal{I}}_{cf} \end{bmatrix}, \tag{4.51}$$

where $\boldsymbol{M}_d$ $(\boldsymbol{M}_{d,r}, \boldsymbol{M}_{d,\theta}, \boldsymbol{M}_{d,\phi})$ and $\boldsymbol{M}_c$ $(\boldsymbol{M}_{c,r}, \boldsymbol{M}_{c,\theta}, \boldsymbol{M}_{c,\phi})$ are the divergence-free and curl-free part of $\boldsymbol{M}$. $\boldsymbol{M}_{c,r}$, $\boldsymbol{M}_{c,\theta}$ and $\boldsymbol{M}_{d,\phi}$ are zero, since the r and θ components are determined solely by the divergence-free SECS, and the ϕ component solely by the curl-free SECS. This reduces $\boldsymbol{M}$ to $(\boldsymbol{M}_{d,r}, \boldsymbol{M}_{d,\theta}, \boldsymbol{M}_{c,\phi})$ of size $3N \times M$. $\boldsymbol{M}_{d,r}$, $\boldsymbol{M}_{d,\theta}$ and $\boldsymbol{M}_{c,\phi}$ have the elements

$$(M_{d,r})_{n,k} = \begin{cases} \frac{\mu_0}{2r_I} \sum_{l=1}^{\infty} \left(\frac{a}{r_I}\right)^{l-1} P_l(\cos\theta_k) \left(1 - \left(\frac{c}{a}\right)^{2l+1}\right) P_l(\cos\theta_n), & r_n < r_I. \\ \frac{\mu_0}{2r_I} \sum_{l=1}^{\infty} \left(\frac{r_I}{r_n}\right)^{l+2} P_l(\cos\theta_k) \left(1 - \left(\frac{c}{r_I}\right)^{2l+1}\right) P_l(\cos\theta_n), & r_n > r_I. \end{cases} \tag{4.52}$$

$$(M_{d,\theta})_{n,k} = \begin{cases} \frac{\mu_0}{2r_I} \sum_{l=1}^{\infty} \left(\frac{a}{r_I}\right)^{l-1} \frac{1}{l} P_l(\cos\theta_k) \left(1 + \frac{l}{l+1} \left(\frac{c}{a}\right)^{2l+1}\right) \frac{dP_l(\cos\theta_n)}{d\theta_n}, & r_n < r_I. \\ -\frac{\mu_0}{2r_I} \sum_{l=1}^{\infty} \left(\frac{r_I}{r_n}\right)^{l+2} \frac{1}{l+1} P_l(\cos\theta_k) \left(1 - \left(\frac{c}{r_I}\right)^{2l+1}\right) \frac{dP_l(\cos\theta_n)}{d\theta_n}, & r_n > r_I. \end{cases} \tag{4.53}$$

$$(M_{c,\phi})_{n,k} = \frac{\mu_0}{2r_n} \begin{cases} -\cot(\theta_n/2), & r_n > r_I, \theta_n > \theta_k \\ \tan(\theta_n/2), & r_n > r_I, \theta_n < \theta_k \\ 0, r_n < r_I \end{cases} \tag{4.54}$$

From the magnetic field observations, $\boldsymbol{B}^{\text{obs}}$, we are able to find the 1D SECS amplitudes, which are then used to determine the sheet current density distribution, $\boldsymbol{J}^{\text{mod}}$, from the relation given in Equation 4.25 to 4.27. Similarly, $\boldsymbol{J}$ can be written on matrix form using Equations 4.25 to 4.27.

$$\begin{bmatrix} \boldsymbol{J}_r \\ \boldsymbol{J}_\theta \\ \boldsymbol{J}_\phi \end{bmatrix} = \begin{bmatrix} \boldsymbol{A}_{d,r} & \boldsymbol{A}_{c,r} \\ \boldsymbol{A}_{d,\theta} & \boldsymbol{A}_{c,\theta} \\ \boldsymbol{A}_{d,\phi} & \boldsymbol{A}_{c,\phi} \end{bmatrix} \cdot \begin{bmatrix} \boldsymbol{\mathcal{I}}_{df} \\ \boldsymbol{\mathcal{I}}_{cf} \end{bmatrix} = \begin{bmatrix} \boldsymbol{A}_{c,r} \\ \boldsymbol{A}_{c,\theta} \\ \boldsymbol{A}_{d,\phi} \end{bmatrix} \cdot \begin{bmatrix} \boldsymbol{\mathcal{I}}_{df} \\ \boldsymbol{\mathcal{I}}_{cf} \end{bmatrix} \tag{4.55}$$

Here $\boldsymbol{A} = (\boldsymbol{A}_{d,r}, \boldsymbol{A}_{d,\theta}, \boldsymbol{A}_{c,\phi})$ is a matrix of equal size to $\boldsymbol{M}$, with the elements

$$(A_{d,\phi})_{n,k} = \frac{1}{2r_I} \begin{cases} -\tan(\theta_n/2), & \theta_n < \theta_k. \\ \cot(\theta_n/2), & \theta_n > \theta_k. \end{cases} \tag{4.56}$$

$$(A_{c,r})_{n,k} = \begin{cases} \frac{1}{r_n^2}\left(\frac{1}{2} - \frac{1}{\sin(\theta_k)}\delta(\theta_n - \theta_k)\right), & r_n < r_I. \\ 0, & r_n > r_I. \end{cases} \tag{4.57}$$

$$(A_{c,\theta})_{n.k} = \frac{1}{2r_I} \begin{cases} -\tan(\theta_n/2), & \theta_n < \theta_k. \\ \cot(\theta_n/2), & \theta_n > \theta_k. \end{cases} \tag{4.58}$$

Solutions to Equation 4.51 and 4.55 enables us to estimate the ionospheric sheet current densities from satellite magnetic field residual observations.

Chapter 5

Discrete linear inverse problems and how to solve them

The theory of inverse problems relates a physical model to observations. This allows estimations of physical parameters impossible to observe directly. Inverse problems thus provides the means for Earth observation studies in areas, such as the interior of the Earth, or regions in the atmosphere, uninhabited by satellites. Inverse theory can furthermore be used to reconstruct a sharper image from a blurred one, by computing the source, or cause, that gives rise to observed data from a mathematical model describing the relation between source and observations. [Hansen, 2010; Mosegaard and Hansen, 2016].

The following chapter will give a short introduction to the method, along with a series of regularization approaches tested in the thesis.

5.1 What is an inverse problem?

Inverse theory does not in itself provide the means for extracting the wanted information. It requires a pre-specified physical model to provide the relation between model parameters and observations. The pre-specified physical model is described in the formulation of the forward problem. To fully understand the inverse problem, one thus have to understand the forward problem, where a desired effect, $\boldsymbol{d}$, is estimated from a known cause, $\boldsymbol{m}$, using the pre-specified physical model, described in the design matrix, $\boldsymbol{G}$,

$$\boldsymbol{d} = \boldsymbol{G}\boldsymbol{m}. \tag{5.1}$$

An example of a forward model could be the estimation of the magnetic field contribution from a known point source charge. The inverse problem would be to estimate the cause (point source charge) from measurements of it's effect - the magnetic signature

$$\boldsymbol{m} = \boldsymbol{G}^{-1}\boldsymbol{d}. \tag{5.2}$$

This can be seen as the linear algebra solution to a series of equations ($\boldsymbol{d} = \boldsymbol{G}\boldsymbol{m}$) and unknowns ($\boldsymbol{m}$). In inverse problems, $\boldsymbol{m}$, is often referred to as the model parameter vector. For an equal amount of unknowns and equations, a unique solution can be found. For the case of a non-square matrix, $\boldsymbol{G}$, unknowns $\neq$ number of equations, this calculation is not trivial.

The solution requires a non-trivial inversion of the non-square matrix, $\boldsymbol{G}$, which is not uniquely determined, leaving some cases without solutions, and others with more than one. The inverse problem thus consists of estimating one set of model parameters, $\boldsymbol{m}$, from a collection which reproduce observations to an appropriate level of misfit and fits within any prior knowledge of the model parameters (cause). Estimation of the auroral electrojet system (cause, $\boldsymbol{m}$) from satellite observations of their magnetic signature (effect, $\boldsymbol{d}^{\text{obs}}$) using the LCM and 1D SECS method to describe their relation (formulated in Equation 4.16 on page 40 and 4.51 on page 47) are exactly examples of discrete inverse problems. Theory of inverse problems can thus provide the means for their solution [Farquharson and Oldenburg, 1998; Hansen, 2010].

Let N be the size of the data vector/observations, and M the number of model parameters. $\boldsymbol{G}$ will then be a matrix of size $N \times M$. The equations given by the inverse problem are uniquely determined only for an exact determined problem ($M = N$) with independent measurements. Most physical systems, however, do not provide enough information to uniquely constrain the equations stated in the inverse problem, resulting in an de facto underdetermined problem. An underdetermined problem is defined for the case of more model parameters than observations ($N < M$). These inverse problems will have more than one solution, dependent on the degree of underdetermined. Apriori information is thus needed to estimate the most plausible solution to the problem. For the underdetermined problems, the design matrix, $\boldsymbol{G}$, is said to be rank deficient or singular, and is thereby non-invertible or ill-conditioned. The condition number reveals the ill-conditioness of the design matrix by measuring the model changes with small variations in the input. Specifically, the condition number is the ratio of the largest to the smallest singular value of $\boldsymbol{G}$. Division with very small numbers can lead to numerical inconsistencies, which in turn can lead to inconsistencies in the determination of the model parameters. An overdetermined case ($N > M$) describes, oppositely, a problem with too much information to solve $\boldsymbol{d} = \boldsymbol{G}\boldsymbol{m}$ with zero error in the case of observation error. The problem can be solved by applying a priori conditions to the solutions, such as assigning different weights for the individual observations.

Differences between problem types can be visualized through a 2D example: Determine the intersection point between a number of lines. If equations for two lines are known, the problem will be exact determined, with only one solution, given by their intersection. An exact estimate will only be present in the case of zero observation error. If only one equation is given (underdetermined problem), the solution is found along the given line, resulting in more than one solution. To find the most probable solution, further information about the intersection must be applied. With three lines (overdetermined problem) not intersecting at the same point, due to observation error, no exact solution can be found that fits all information. The exact solution must in this case lie within the area bounded by the intersecting lines [Aster et al., 2005; Menke, 2012].

The dimensions of the inverse problem, illustrated in Figure 5.1, provide information of the given over-/underdetermined problem at hand:

- R(A) gives the solution space (red) of $\boldsymbol{m}$ in $\boldsymbol{d}$. This is the subspace of $\boldsymbol{m}$ which can be reached by the given design matrix, $\boldsymbol{G}$. If the solution lies outside this subspace of, $\boldsymbol{m}$, $\boldsymbol{G}\boldsymbol{m} = \boldsymbol{d}$ will not have a solution. An example is in the presence of too much observation noise. The dimension of the solution space is called the rank, r.

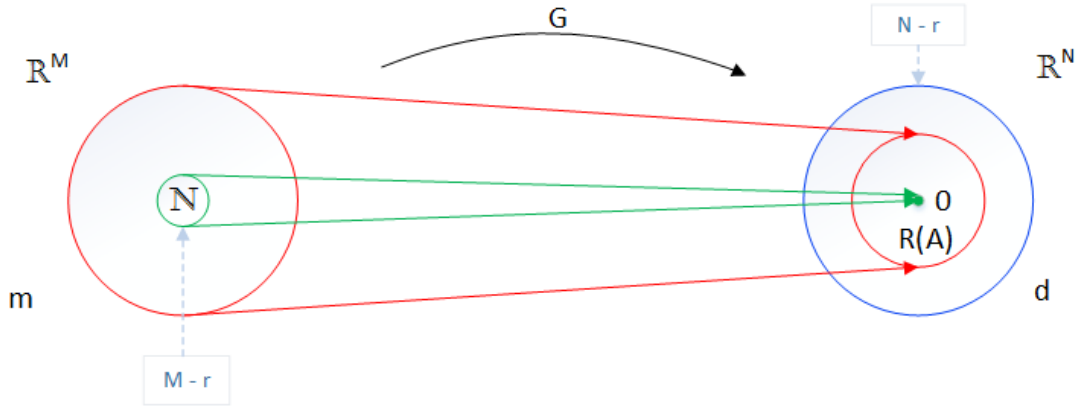

Figure 5.1: Schematics of how different dimensions are related to eachother.

- N(A) gives the null space (green), the subspace of $\boldsymbol{m}$ which gives $\boldsymbol{Gm} = 0$. Ideally this subspace is empty, and it is often very small. The dimension of the null space, $M - r$, provides information about how much information is missing, and can thus be used to describe the underdetermined problem mathematically.
- The blue area marks the non-solvable subspace of dimension $N - r$.

The dimensions can be determined by performing a *singular value decomposition* (SVD) analysis on $\boldsymbol{G}$. SVD is a concept in linear algebra utilizing that any $M \times N$ matrix, $\boldsymbol{G}$, can be written as a product of three matrices,

$$\boldsymbol{G} = \boldsymbol{U}\boldsymbol{\Lambda}\boldsymbol{X}^T. \tag{5.3}$$

$\boldsymbol{U}$ is an $N \times N$ orthonormal matrix consisting of basis vectors spanning the data space, R^N. $\boldsymbol{X}$ is an $M \times M$ orthonormal matrix spanning the model space $\boldsymbol{R}^M$, and $\boldsymbol{\Lambda}$ is a non-negative diagonal $N \times M$ matrix containing M singular values, w_i, in the diagonal. A singular $\boldsymbol{G}$ will contain singular values equal to zero. Figure 5.2 shows how the dimensions of the inverse problem are related to the SVD analysis.

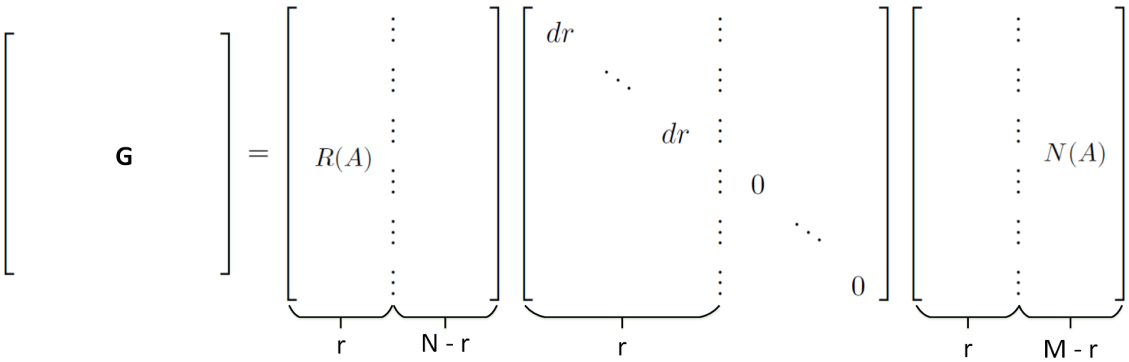

$N(A)$: Any linear combination of vectors in the null space will give the solution zero.
$R(A)$: data is in this part

Figure 5.2: Dimensions of the inverse problem in an SVD analysis.

5.2 Solutions and regularization

An example of a de facto underdetermined problem, despite more observations than model parameters) is the application of satellite data to inverse problems. Satellites provides high density data, usually resulting in an overdetermined inverse problem. A high degree of auto-correlation in the dataset, however, often results in a highly ill-conditioned design matrix, $\boldsymbol{M}$. In this case, the inverse problem can be solved by adopting a regularization approach. The regularization approach will provide a set of restrictions for the solution to help find the most probable set of the model parameters. Many regularization methods has been developed, each designed for application of different apriori information to the problem. The correct regularization approach is found by setting a set of requirements for the solution, controlled by the case-specific objective function, $\boldsymbol{\Phi}$ [Aster et al., 2005; Menke, 2012].

The remaining part of this chapter presents a series of regularization approaches tested during this project, with an objective function especially designed for the inverse problem: determination of sheet current densities from satellite magnetic observations. Our goal is to minimize the misfit between the predicted data, $\boldsymbol{d}^{\text{mod}}$ and observations, $\boldsymbol{d}^{\text{obs}}$, $\boldsymbol{\phi}^d$, along with the amount of structure in the model, $\boldsymbol{\phi}^m$. A similar case study is presented in [Farquharson and Oldenburg, 1998], where they furthermore have included a minimization of the difference between the model and a given reference model. Following their results, we find the objective function

$$\boldsymbol{\Phi} = \alpha^2 \boldsymbol{\phi}^m(\boldsymbol{Dm}) + \boldsymbol{\phi}^d(\boldsymbol{d}^{\text{mod}} - \boldsymbol{d}^{\text{obs}}) - \boldsymbol{\phi}^{d,\text{tar}}. \tag{5.4}$$

α^2, in this thesis also referred to as the damping parameter, is a regularization parameter controlling the balance between the two terms in the objective function. Thus, controlling the balance between the amount of structure in the model parameters and minimizing the predicted data misfit to observations. A high value will decrease the amount of structure in the model parameters, but increase the predicted data misfit to observations. $\boldsymbol{D}$ is a matrix controlling the measure in which $\boldsymbol{m}$ is minimized. An example could be minimization of the first derivative of the model parameters. d^{mod} is the modelled estimate of the observations, using the obtained model parameters, and $\phi^{d,\text{tar}}$ the target model misfit. In this thesis, the target misfit has been ignored, aiming at the smallest possible misfit [Farquharson and Oldenburg, 1998; Aster et al., 2005].

The inverse problem is solved by finding the model, $\boldsymbol{m}$, that minimizes the objective function by differentiating $\boldsymbol{\Phi}$ with respect to the model parameters and equating to zero. The solution to the partial differential of the objective function is estimated by Farquharson and Oldenburg [1998] as

$$\begin{aligned}
&\frac{\partial \boldsymbol{\Phi}}{\partial \boldsymbol{m}} = \frac{\partial \phi^d}{\partial \boldsymbol{m}} + \frac{\partial \phi^m}{\partial \boldsymbol{m}} = 0, \\
&\boldsymbol{G}^T \boldsymbol{W}^d(\boldsymbol{Gm} - \boldsymbol{d}^{\text{obs}}) + \alpha^2 \boldsymbol{D}^T \boldsymbol{W}^d \boldsymbol{Dm} = 0, \\
&\boldsymbol{m} = (\boldsymbol{G}^T \boldsymbol{W}^d \boldsymbol{G} + \alpha^2 \boldsymbol{D}^T \boldsymbol{W}^m \boldsymbol{D})^{-1}(\boldsymbol{G}^T \boldsymbol{W}^d \boldsymbol{d}^{obs}),
\end{aligned} \tag{5.5}$$

where $\boldsymbol{W}^d$ and $\boldsymbol{W}^m$ are weighting matrices, controlling the weights on individual data and model parameters. Equation 5.5 gives the general solution to the p-norm inverse, with the objective function given in Equation 5.4. Estimates of $\boldsymbol{W}^d$ and $\boldsymbol{W}^m$ depends on the model

parameters, $\boldsymbol{m}$, which makes Equation 5.5 a non-linear system of equations, solved by an iterative procedure.

The following sections will provide descriptions of different solution methods, using Equation 5.5 as reference. The regularization approaches can, in most cases be implemented alone. They will, however, be presented in a progressive manner, starting with the simplest inversion, adding more and more regularization.

Simplest solution - the least squares estimate

The simplest and most common way to solve a linear inverse problem, is the unregularized simple least squares solution. This solution is found by setting $\alpha = 0$ and $\boldsymbol{W}^d = \boldsymbol{I}$, corresponding to an objective function minimizing the L_2 norm of the overall misfit $(\boldsymbol{d}^{\text{mod}} - \boldsymbol{d}^{\text{obs}})$, ignoring the model parameter constrain. $\boldsymbol{I}$ is here, the identity matrix. The L_2 norm, defined as

$$||e||_2 = \left[\sum_i |e_i|^2\right]^{1/2}, \tag{5.6}$$

implies that the data and model parameters obeys Gaussian statistics. Successively higher norms gives higher weight to outliers, and opposite for lower norms. Solutions involving other norm minimizations are discussed in later subsections. The least squares solution to the model parameters are given as

$$\boldsymbol{m}^{LS} = (\boldsymbol{G}^T\boldsymbol{G})^{-1}\boldsymbol{G}^T\boldsymbol{d}^{\text{obs}}. \tag{5.7}$$

This solution requires a well-conditioned problem with small data errors and is therefore often not a suitable solution, when dealing with satellite data Aster et al. [2005]; Hansen [2010].

Amplitude damping - zeroth order Tikhonov regularization

Tikhonov regularization [Tikhonov, 1963] is a technique replacing an ill-posed problem with a near well posed problem by minimizing the model misfit and model parameter structure. It provides a way to control data errors from being amplified in the solution, by introducing the damping factor, α^2, keeping $\boldsymbol{W}^d = \boldsymbol{W}^m = \boldsymbol{D} = \boldsymbol{I}$

$$\boldsymbol{m}^{LS} = (\boldsymbol{G}^T\boldsymbol{G} + \alpha^2 I)^{-1}\boldsymbol{G}^T\boldsymbol{d}^{\text{obs}}. \tag{5.8}$$

The term $\alpha^2 I$ ensures no zero singular values, and a solution is thus always possible. The additional term is equal to removing or ignoring the null space of the solutions. The structure of the model parameters goes to zero as $\alpha^2 \to \infty$, and the solution towards an unregularized simple least squares for $\alpha^2 \to 0$ Aster et al. [2005].

The adjustable regularization parameter, α^2, introduces a case specific parameter adjustment. This adjustment is not trivial and will always be a trade-off between goodness of data fit and model complexity, consistent with the two terms in the objective function given in Equation 5.4. A choice in α^2 too small leads to overfitting (fit to noise), while a choice too large leads to a model with suppressed physical signal. The issue lies in finding the best balance between these

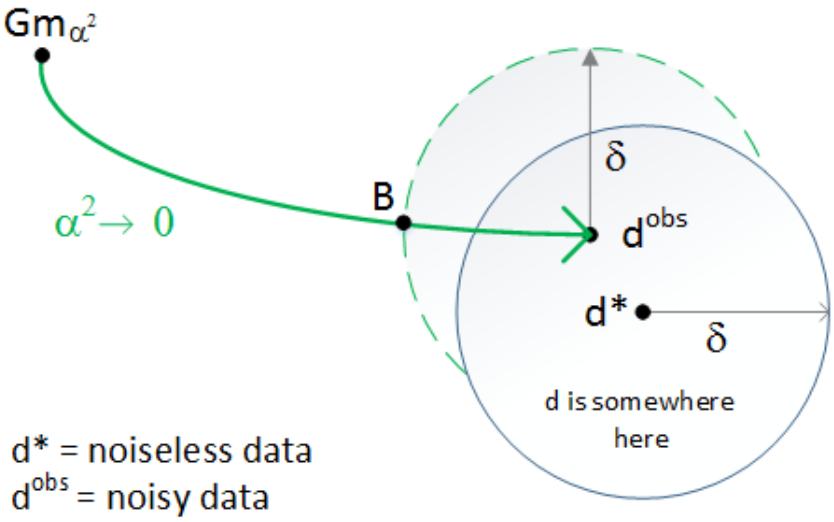

Figure 5.3: Schematics of the Morozov discrepancy principle for choice of α^2 in Tikhonov regularization.

terms. One way to estimate α^2 is by using the Morozov discrepancy principle, in which a true value is assumed, along with a set noise level, δ, larger than 0. The solution is in this way allowed within a range from the true value, estimating a solution which satisfies $\boldsymbol{Gm} - \boldsymbol{d} \approx \delta$. The noiseless solution will lie within the range $\boldsymbol{d} \pm \delta$.

The principle described in Figure 5.3 shows, how the solution goes towards the noisy solution, b, and not the noiseless, true solution, $b*$. The idea is to lower α^2 until the point, B, representing the solution on the boundary to the chosen noise level. This ensures that the data fit lies within the margin of errors. For a solution, with a valid estimate of the error, the Morozov discrepancy principle can be a good way to determine α^2. If this is not the case, as in most geomagnetic surveys, α^2 can be estimated by an L-curve [Hansen, 1992]. The L-curve provides a measure of α^2 without any a priori information, and is found by plotting the L_2 norm of the model complexity, $||\boldsymbol{m}||$, as a function of the L_2 norm of the model misfit, $||\boldsymbol{d}^{\text{mod}} - \boldsymbol{d}^{\text{obs}}||$ for various values of α^2. The idea is to minimize the complexity of the model parameters with no, or only little, increase in model misfit.

Figure 5.4 shows a theoretical L-curve with three highlighted values, α_1^2, α_x^2 and α_a^2. α_1^2 and α_a^2 marks the boundaries of the chosen α^2 range. The theoretical optimal choice, α_x^2, is in or near the corner of the L-curve, where both the complexity of the model parameters and the model misfit is close to minimum [Hansen, 1992; Hansen and O'Leary, 1993; Hansen, 1999].

The inversion is, as previously mentioned, always possible, though still sensible to noise, and solutions should be accepted with care.

Dealing with outliers and non-Gaussian noise - IRLS

Zeroth order Tikhonov regularization, as presented above, requires a Gaussian error distribution. An *Iterative reweighted least squares* (IRLS) [Constable, 1988] approach with Huber weights

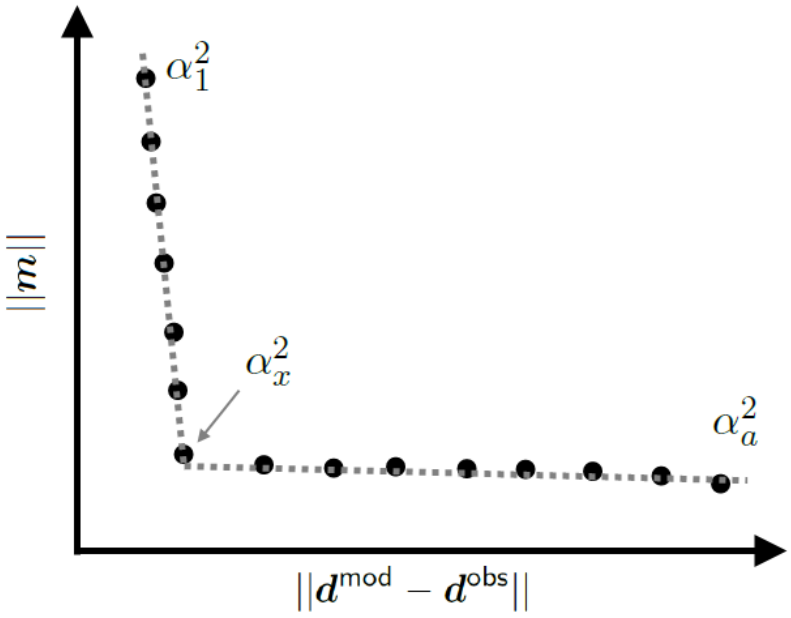

Figure 5.4: Theoretical L-curve, showing the L_2 norm of the model complexity, $||\boldsymbol{m}||$, as a function of the L_2 norm of the model misfit, $||\boldsymbol{d}^{\text{mod}} - \boldsymbol{d}^{\text{obs}}||$ for various values of α^2.

[Huber, 1964] is a technique applicable to handle a possible non-Gaussian error distribution for least squares problems. The idea is to give less weight to outliers, mimicking a Gaussian error distribution. The Huber weights are introduced via the diagonal weight matrix, $\boldsymbol{W}^d$, controlling the weight of individual observation points with the diagonal elements given by

$$w_{i,n} = \frac{1}{\sigma_n^2} \min\left(\frac{s\sigma_n}{|e_{i,n}|}, 1\right). \tag{5.9}$$

Here s is a constant setting the sensitivity of the routine, assigning less weight to all values outside $s\sigma$. The value is typically set to 1.5 [Sabaka et al., 2013], but can be adjusted according to case. n gives the number of measurements, $e_{i,n}$ the current residual and σ the standard deviation of the model residuals of $\Delta d_i = d_i^{\text{obs}} - d_i^{\text{mod}}$.

The model parameter dependence of $\boldsymbol{W}^d$ turns the problem into a non-linear inverse problem. The non-linearity is solved by introduction of the iterative process of IRLS, with weights adjusted for each iteration, i. The solution for the $(i+1)^{\text{th}}$ iteration of the inverse problem is found, based on Equation 5.5, keeping $\boldsymbol{W}^m = \boldsymbol{D} = \boldsymbol{I}$

$$\boldsymbol{m}_{i+1}^{L_2} = (\boldsymbol{G}^T \boldsymbol{W}_i^d \boldsymbol{G} + \alpha^2 \boldsymbol{I})^{-1} \boldsymbol{G}^T \boldsymbol{W}_i^d \boldsymbol{d}^{\text{obs}}. \tag{5.10}$$

To start the iterative process, an initial estimate of the model misfit and $\boldsymbol{W}^d$ is needed. A common choice is a zeroth order Tikhonov estimation of the model misfit and the identity matrix for $\boldsymbol{W}^d$. The iterative process is stopped when converged, which can be estimated either from a plot of the L_2 norm of $\boldsymbol{m}$, or when changes in weights are substantially small, *e.g.* below 1% [Farquharson and Oldenburg, 1998; Aster et al., 2005; Sabaka et al., 2013].

Taking the distribution of the model parameters into account - L_1

The L_2 minimization of the model parameter misfit assumes, similarly to the model misfit, a Gaussin distribution. Not all model parameter distributions are however expected Gaussian. One way to deal with a possible non-Gaussian distribution of model parameters, is by introducing a weight function, $\boldsymbol{W}^m$, in the regularization scheme, associated with the minimization of model complexity, ϕ^m. The weights are introduced, as $\boldsymbol{W}^d$ (using $\boldsymbol{D} = \boldsymbol{I}$ in Equation 5.5), through an IRLS routine with the $(i+1)^{\text{th}}$ element given as

$$\boldsymbol{m}_{i+1}^{L_1,DI} = (\boldsymbol{G}^T\boldsymbol{W}_i^d\boldsymbol{G} + \alpha^2\boldsymbol{W}_i^m)^{-1}\boldsymbol{G}^T\boldsymbol{W}_i^d\boldsymbol{d}^{\text{obs}}. \tag{5.11}$$

The choice in $\boldsymbol{W}^m$ will be highly case sensitive, and requires an interpretation of an initial estimate of the model parameter distribution. An example is given by assumption of a Laplacian distribution of model parameters, corresponding to a minimization of the L_1 norm. The elements of the diagonal matrix, $\boldsymbol{W}^m$,

$$W_{kk}^m = \left(j_k^2 + \epsilon^2\right)^{-\frac{1}{2}}, \tag{5.12}$$

are given by the Ekblom measure [Ekblom, 1987] for the number of model parameter, k. The implementation of the Ekblom L_1 norm requires an extra regularization parameter, ϵ, which ensures a non-singular solution at $j_k = 0$. ϵ is, though technically a regularization parameter, far less case sensitive, compared to *e.g.* α^2 [Farquharson and Oldenburg, 1998; Aster et al., 2005].

Higher order Tikhonov

The full solution, corresponding to Equation 5.5, is found through the implementation of the matrix, $\boldsymbol{D}$, controlling the measure in which the model parameters are minimized:

$$\boldsymbol{m}_{i+1}^{L_1} = (\boldsymbol{G}^T\boldsymbol{W}_i^d\boldsymbol{G} + \alpha^2\boldsymbol{D}_2^T\boldsymbol{W}_i^m\boldsymbol{D}_2)^{-1}\boldsymbol{G}^T\boldsymbol{W}_i^d\boldsymbol{d}^{\text{obs}}. \tag{5.13}$$

In many situations it can be fruitful not to minimize the norm of the model parameters, but the first or second order derivatives thereof. This will again be case sensitive, and require prior knowledge of the structure of the model parameters. Minimizing the direct norm of the model parameters ($\boldsymbol{D} = \boldsymbol{I}$) will filter out solutions with large overall variations in model parameters, damping all variations. Minimizing the first derivatives of the model parameters ($\boldsymbol{D} = \boldsymbol{D}_1$) will minimize the difference between model parameters, favouring relatively flat solutions

$$\boldsymbol{D}_1 = \begin{bmatrix} 1 & -1 & 0 & 0 & 0 & 0 & 0 & 0 & \cdots & 0 & 0 & 0 & 0 \\ 0 & 1 & -1 & 0 & 0 & 0 & 0 & 0 & \cdots & 0 & 0 & 0 & 0 \\ 0 & 0 & 1 & -1 & 0 & 0 & 0 & 0 & \cdots & 0 & 0 & 0 & 0 \\ 0 & 0 & 0 & 1 & -1 & 0 & 0 & 0 & \cdots & 0 & 0 & 0 & 0 \\ 0 & 0 & 0 & 0 & 1 & -1 & 0 & 0 & \cdots & 0 & 0 & 0 & 0 \\ 0 & 0 & 0 & 0 & 0 & 1 & -1 & 0 & \cdots & 0 & 0 & 0 & 0 \\ & & & & \vdots & & & & & & & & \\ 0 & 0 & 0 & 0 & 0 & 0 & 0 & 0 & \cdots & 0 & 0 & 1 & -1 \\ 0 & 0 & 0 & 0 & 0 & 0 & 0 & 0 & \cdots & 0 & 0 & 0 & 0 \end{bmatrix}.$$

Minimizing the first order differences is especially suitable for stepwise structure of model parameters. An expected model structure, containing slopes, will, however, benefit from a minimization of the norm of the second order derivatives of the model parameters, found by setting $\boldsymbol{D} = \boldsymbol{D}_2$, where

$$\boldsymbol{D}_2 = \begin{bmatrix} 1 & -2 & 1 & 0 & 0 & 0 & 0 & 0 & \cdots & 0 & 0 & 0 & 0 \\ 0 & 1 & -2 & 1 & 0 & 0 & 0 & 0 & \cdots & 0 & 0 & 0 & 0 \\ 0 & 0 & 1 & -2 & 1 & 0 & 0 & 0 & \cdots & 0 & 0 & 0 & 0 \\ 0 & 0 & 0 & 1 & -2 & 1 & 0 & 0 & \cdots & 0 & 0 & 0 & 0 \\ 0 & 0 & 0 & 0 & 1 & -2 & 1 & 0 & \cdots & 0 & 0 & 0 & 0 \\ 0 & 0 & 0 & 0 & 0 & 1 & -2 & 1 & \cdots & 0 & 0 & 0 & 0 \\ & & & & \vdots & & & & & & & & \\ 0 & 0 & 0 & 0 & 0 & 0 & 0 & 0 & \cdots & 0 & 1 & -2 & 1 \\ 0 & 0 & 0 & 0 & 0 & 0 & 0 & 0 & \cdots & 0 & 0 & 0 & 0 \\ 0 & 0 & 0 & 0 & 0 & 0 & 0 & 0 & \cdots & 0 & 0 & 0 & 0 \end{bmatrix}.$$

The second order derivative of a slope will not contribute to the norm. Solutions containing slopes will thus not be downweighted. [Farquharson and Oldenburg, 1998; Aster et al., 2005].

Singular Value Decomposition

Singular value decomposition (SVD), described in Section 5.1 provide an alternative way to estimate the inverse of $\boldsymbol{G}$, particularly of interest in ill-conditioned and/or rank deficient systems. From the decomposition of $\boldsymbol{G}$ into $\boldsymbol{U}$, $\boldsymbol{\Lambda}$ and $\boldsymbol{X}$, we can estimate the general inverse of $\boldsymbol{G}$, called the Moore-Penrose pseudoinverse [Aster et al., 2005] as

$$\boldsymbol{G}^{\dagger} = \boldsymbol{X}\boldsymbol{\Lambda}^{-1}\boldsymbol{U}^{T}, \tag{5.14}$$

The use of generalized inverse is however better practice due to numerical accuracy issues in normal least squares solutions. The solution to the inverse problem, becomes in this case

$$\boldsymbol{m}^{SVD} = \boldsymbol{X}\boldsymbol{\Lambda}^{-1}\boldsymbol{U}^{T}\boldsymbol{d}^{\text{obs}}, \tag{5.15}$$

SVD solutions may include terms involving very small non-zero singular values, making the solution very sensitive to small amounts of data noise. The presence of noise will generally have a non-zero projection onto each eigenvector in $\boldsymbol{U}$, and in turn result in very large values in the corresponding model space basis vector, $\boldsymbol{X}$. This presence will be of largest importance in the very small non-zero singular values. The instability of the inversion can, as the least squares solution, be determined by the condition number.

In the case of a singular $\boldsymbol{G}$, $\boldsymbol{\Lambda}$ will contain zero values. The singularity can be solved by setting all $1/w_i$ in the generalized inverse equation to zero. The method can also be applied to include small singular values, setting $1/w_i = 0$ for all $w_i < \varepsilon \cdot max(w_i)$. ε is then the truncation parameter, controlling how much of the variance is believed assigned to data errors. Implementation of the regularization is called a *truncated singular value decomposition* (TSVD) method, and is an additional example of regularization where stable solutions are preferred over data fit. This will not fit the data as well, though ensuring that the data is not overfitted. As the

regularization parameter, α^2, in the Tikhonov solution can be estimated by an L-curve, ε, can be determined from the singular value spectrum, presenting the singular values with increasing κ. κ is here the singular value number. The optimum choice in truncation parameter will be where inclusion of additional eigenvectors adds only little variance to the model estimate. From the SVD composition we expect all singular values to be decreasing with κ [Emery and Thomson, 2004; Aster et al., 2005].

Maximizing the entropy

The maximum entropy solution provides a different way to control the model parameters. Instead of minimizing the model amplitudes, regularization is applied to the model information complexity, given by the model entropy. The solution is found, following [Jackson et al., 2007] as

$$\boldsymbol{m}_{i+1}^{maxent} = (2 \cdot \boldsymbol{G}^T \boldsymbol{W}_i^d \boldsymbol{G} + \alpha^2 \boldsymbol{Q}_i^A)^{-1} \cdot \left(2 \cdot \boldsymbol{G}^T \boldsymbol{W}_i^d \boldsymbol{d}^{\text{obs}} + \alpha^2 (\boldsymbol{Q}_i^A \boldsymbol{m}_i) - 4\omega_s \alpha^2 \boldsymbol{Q}_i^B\right). \tag{5.16}$$

Here, $\boldsymbol{Q}^A$ is a diagonal matrix with elements

$$\boldsymbol{Q}_{kk}^A = \frac{4\omega_s}{\sqrt{\boldsymbol{m}_i^2 + 4\omega_s^2}}, \tag{5.17}$$

and $\boldsymbol{Q}^B$ given as

$$\boldsymbol{Q}_i^B = \log\left(\frac{\sqrt{\boldsymbol{m}_i^2 + 4\omega_s^2}_i + \boldsymbol{m}_i}{2\omega_s}\right), \tag{5.18}$$

with

$$\boldsymbol{\psi}_i = \sqrt{\boldsymbol{m}_i^2 + 4\omega_s^2}. \tag{5.19}$$

The maximum entropy solution favours solutions similar to the solution with minimization of the L_1 norm of the model parameters. It does, however, introduce a second regularization parameter, ω_s. As the solution requires adjustment of both α^2 and ω_s, these have to be optimized together. The solution is furthermore sensitive to the choice in ω_s, which can be difficult to optimize satisfactory. The solution goes towards a zeroth order Tikhonov solution with a Huber weighted data misfit measure for $\omega_s \to \infty$ [Jackson et al., 2007; Kother et al., 2015].

Goodness of fit

The goodness of the model fit needs to be evaluated in terms of the objective function, which in our case was to minimize the data misfit ($\boldsymbol{d}^{\text{mod}} - \boldsymbol{d}^{\text{obs}}$) along with the structure of the model parameters, $\boldsymbol{m}$. The latter is evaluated through an L-curve and through visual inspection of the model parameters. The data misfit, can be evaluated in many ways, such as the *root*

means square (RMS) misfit. In this thesis, we have chosen to evaluate the data misfit by the variance ratio,

$$V_R = \frac{\sigma^2_{\Delta d}}{\sigma^2_{d^{\text{obs}}}}, \tag{5.20}$$

where σ^2 is the variance of the residuals between the observations and the model, $\Delta d = \boldsymbol{d}^{\text{obs}} - \boldsymbol{d}^{\text{mod}}$, and the observations, $\boldsymbol{d}^{\text{obs}}$. The variance in $\boldsymbol{d}^{\text{obs}}$ explained by $\boldsymbol{d}^{\text{mod}}$ is then given by $1 - V_R$.

Chapter 6

Validation of the 1D SECS method through application of satellite magnetic observations

This chapter will examine sheet current densities estimated from the 1D SECS method described in Section 4.2 and investigate how this method adapts to different input data and regularization methods and parameters. This is visualized through first a synthetic data example and later by an application to satellite magnetic field observations. Finally, the results are compared with the results presented by Juusola et al. [2006].

6.1 Estimation of the ionospheric current densities

Equation 4.51 and 4.55 on page 48 can be formulated as a linear inverse problem. From the magnetic field observations, we estimate the model parameters, $\mathcal{I}$. These are then used to estimate the sheet current density, $\boldsymbol{J}^{\text{mod}}$, and to provide estimates for the magnetic field observations, $\boldsymbol{B}^{\text{mod}}$. The full method is described in Figure 6.1.

Solution to the inverse problem

The high frequency data provided by magnetic satellites, will usually result in an overdetermined inverse problem. The individual measurements are, however, as previously mentioned, not independent. This results in a high degree of autocorrelation in the dataset, combined with an ill-posed problem due to the downward continuation from satellite altitude. Without

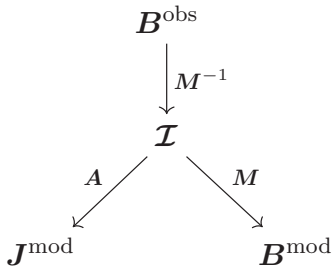

Figure 6.1: Flowchart of sheet current estimates from magnetic field observations by use of the 1D SECS method.

regularization, overfitting is very likely. To avoid this, we find a solution to Equation 4.51 by adopting a regularization approach [Aster et al., 2005; Menke, 2012], using two different strategies. (1) Truncated singular value decomposition, described in Section 5.2 with the solution

$$\boldsymbol{\mathcal{I}}^{\text{TSVD}} = \boldsymbol{X}^{-1}\boldsymbol{\Lambda}\boldsymbol{U}^{T}\boldsymbol{B}, \tag{6.1}$$

and (2) zeroth order Tikhonov regularization and a Huber weighted data misfit measure, implemented through an IRLS technique, as described in Section 5.2 with the solution for the $(i+1)^{\text{th}}$ iteration of the IRLS routine being

$$\boldsymbol{\mathcal{I}}^{L_2}_{i+1} = (\boldsymbol{M}^{T}\boldsymbol{W}^{d}_{i}\boldsymbol{M} + \alpha^2\boldsymbol{I})^{-1}\boldsymbol{M}^{T}\boldsymbol{W}^{d}_{i}\boldsymbol{B}. \tag{6.2}$$

The numerical conditioning of a matrix is assessed by the condition number, which depends in part on the size of the matrix. To minimize the ill-conditiodness, and to allow different regularization parameters (ε and α^2) for the divergence-free and curl-free model parameters, we split the inverse problem stated in Equation 4.51 in two, a divergence-free part and a curl-free part. This eliminates a large part of the zero values in the matrix, $\boldsymbol{M}$, helping the condition number (*i.e.* the ratio of its largest and smallest eigenvalues) and hence the instability of the inversion.

$$\begin{bmatrix} \boldsymbol{B}_r \\ \boldsymbol{B}_\theta \end{bmatrix} = \begin{bmatrix} \boldsymbol{M}_{d,r} \\ \boldsymbol{M}_{d,\theta} \end{bmatrix} \cdot \begin{bmatrix} \boldsymbol{\mathcal{I}}_{df}, \end{bmatrix} \tag{6.3}$$

$$\boldsymbol{B}_\phi = \boldsymbol{M}_{c,\phi} \cdot \boldsymbol{\mathcal{I}}_{cf}. \tag{6.4}$$

Together, $\boldsymbol{M}_{d,r}$ and $\boldsymbol{M}_{d,\theta}$ give $\boldsymbol{M}_d$, and $\boldsymbol{M}_{c,r}$, $\boldsymbol{M}_c$.

6.2 A synthetic test case

To test the method, we applied the 1D SECS approach to a purely one dimensional electrojet, with a starting point of a known ionospheric current density distribution, $\boldsymbol{J}^{\text{obs}}$, $(J_r,\ J_\theta,\ J_\phi)$ along a virtual satellite path. The electrojet was modelled, following Juusola et al. [2006] by a Gaussian current density distribution

$$\boldsymbol{J}_\phi = -Ae^{-\frac{(\theta-\theta_c)^2}{2(\delta\theta)^2}}. \tag{6.5}$$

Here θ_c notes the latitude of the centre of the the electrojet. The remaining components of the sheet current densities are found assuming a radial geomagnetic field ($\boldsymbol{B} = -B\hat{\boldsymbol{e}}_{\boldsymbol{r}}$) and a convection electric field along θ ($\boldsymbol{E} = E\hat{\boldsymbol{e}}_{\boldsymbol{\theta}}$). This yields

$$J_r = -\nabla \cdot \boldsymbol{J}_\theta, \tag{6.6}$$

$$J_\theta = \Sigma_P E, \tag{6.7}$$

$$J_\phi = -\Sigma_H E, \tag{6.8}$$

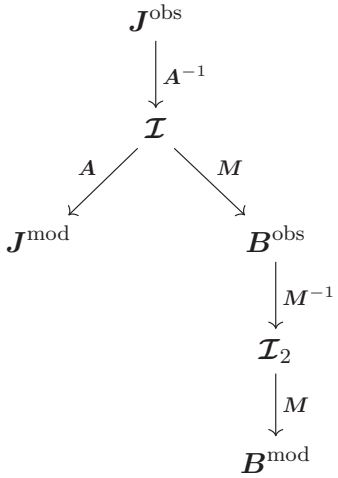

Figure 6.2: Flowchart of 1D SECS synthetic case example.

where Σ_P and Σ_H are the Pedersen and Hall conductances respectively. Using the Pedersen to Hall ratio $\Sigma_H/\Sigma_P = 2$, shown by Untiedt and Baumjohann [1993] we find the current density components, J_r and J_θ as a function of J_ϕ

$$J_r = \frac{1}{r_I}\left(\cot\theta - \frac{\theta - \theta_c}{(\delta\theta)^2}\frac{J_\phi}{2}\right), \tag{6.9}$$

$$J_\theta = -\frac{J_\phi}{2}. \tag{6.10}$$

From the synthetic $\boldsymbol{J}^{\text{obs}}$, we estimate the model parameters $\boldsymbol{\mathcal{I}}$, using TSVD to solve the inversion of $\boldsymbol{A}$

$$\boldsymbol{\mathcal{I}} = \boldsymbol{A}^{-1}\boldsymbol{J}^{\text{obs}} = \boldsymbol{X_A}^{-1}\boldsymbol{\Lambda_A}\boldsymbol{U_A}^T\boldsymbol{J}^{\text{obs}}. \tag{6.11}$$

The synthetic magnetic field observations, $\boldsymbol{B}^{\text{obs}}$, and modelled sheet current density distribution, $\boldsymbol{J}^{\text{mod}}$, are then found using the forward model, presented in Equation 4.50 and 4.55, accordingly. From the synthetic magnetic field observations, we recalculate the model parameters, $\boldsymbol{\mathcal{I}_2}$, again using a TSVD analysis to find the inverse of $\boldsymbol{M}$ (Equation 6.1). Comparison between $\boldsymbol{\mathcal{I}}$ and $\boldsymbol{\mathcal{I}}_2$ provides a means for estimating how well the inversion works.

Finally, the forward model given in Equation 4.50 is used again to estimate the modelled magnetic field observations, using $\boldsymbol{\mathcal{I}_2}$. The different model parameters, design matrices and data vectors used, are illustrated in Figure 6.2. A thorough test of a set of adjustable parameters $\delta\theta^{\text{mod}}$, $\delta\theta^{\text{obs}}$, $d\delta$, ε_A and ε_M along with model and observation range for the synthetic test case is given in Appendix B. Figure 6.3 shows the magnetic field observations in blue and corresponding model fit in red in the left column and the sheet current densities in the right column using $\varepsilon_A = 10^{-3}, \varepsilon_M = 5 \cdot 10^{-12}$, model spacings of $\delta\theta^{\text{mod}} = 0.5^\circ$ and observation spacing of $\delta\theta^{\text{obs}} = 1^\circ$ to represent the best model fit for the synthetic case example. The test shows that it is possible to recover most of the magnetic field perturbations $(\boldsymbol{B}_r, \boldsymbol{B}_\theta, \boldsymbol{B}_\phi)$, and sheet current densities $(\boldsymbol{J}_\theta, \boldsymbol{J}_\phi)$ very accurately using the 1D SECS inverse theory approach from a set of virtual observations of the sheet current densities. We were, however, under

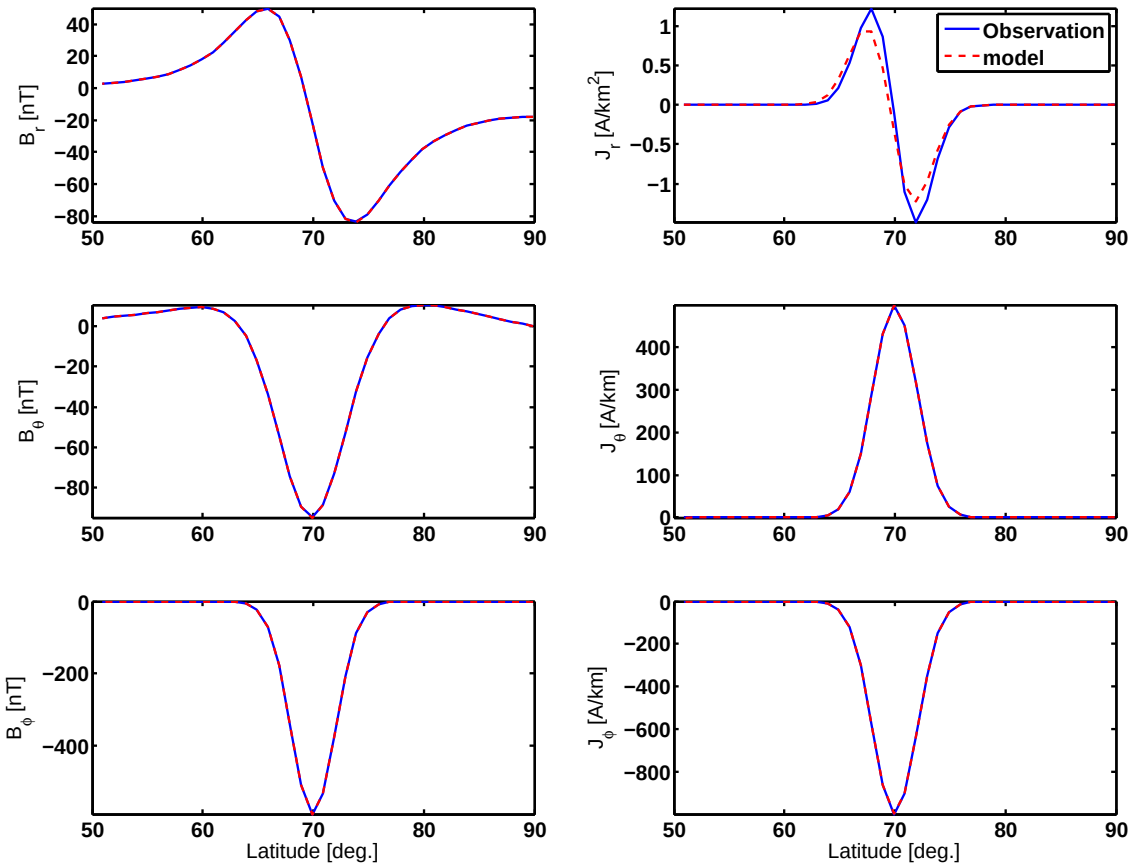

Figure 6.3: Magnetic field, B^{obs} and B^{mod} (first column), and sheet current density, $\boldsymbol{J}^{\text{obs}}$ and $\boldsymbol{J}^{\text{mod}}$ (second column), components. Virtual observations are given in blue, and in red, the corresponding model fit, as a function of latitude. The results are are found using truncation values $\varepsilon_A = 10^{-3}, \varepsilon_M = 5 \cdot 10^{-12}$, model spacings of $\delta\theta^{\text{mod}} = 0.5^\circ$ and observation spacing of $\delta\theta^{\text{obs}} = 1^\circ$ (*i.e.* underdetermined problem).

the conditions tested in Appendix B not able to reproduce the radial component of the sheet current densities with the same level of accuracy. A series of tests leaves us with a set of four categories of adjustable parameters, all inter-dependent and changing according to choice of model setups:

- Truncation parameters, ε_A and ε_M: The results are highly dependent on the choices in SVD truncation parameter. Important parts of the variations are removed if overregularized, and noisy model parameters are returned for a too low regularization parameter.
- The ratio $\delta\theta^{\text{mod}}/\delta\theta^{\text{obs}}$ affects both the shape (disturbance) of the model fit, and the amplitude and horizontal offset of J_r for the virtual observations (see Figure B.19 and B.18). The actual values of the model and observation spacing mainly seem to affect the amplitude height.
- The width of the box-function, $d\delta$, alters the amplitude of the radial component of the sheet current densities (Figure B.17). This seems, however, less sensitive to changes, compared to the other adjustable parameters.

- The range of data and model parameters greatly alters the need for regularization (Figure B.20), and is therefore highly connected to the choice in ε_A and ε_M.

All of this leaves us with a model that is rather sensitive to changes, causing difficulties in estimating the magnetic field perturbations and sheet current densities in a consistent way. Especially difficult in the search for a common set of adjustable parameters satisfying different types of data input, and thereby automatic implementation.

6.3 A test applying CHAMP and *Swarm* magnetic data

The aim of the method is to estimate the ionospheric sheet current densities and their associated FACs from satellite magnetic data. We therefore now apply the method presented in the synthetic case above to 1 second data from a series of individual orbits from the CHAMP and *Swarm* satellites. If the aim was to only estimate the auroral electrojet system, 5 or 10 second data would provide high enough resolution due to the distance from the satellites to the ionosphere. The FACs are, however, also present at satellite orbit height, in situ currents, and the contributions to the magnetic field will therefore change at a much higher frequency, compared to the observed ionospheric contributions. Any unresolved frequencies could introduce errors in the solutions to the FACs, and the higher frequency data is therefore used.

This section will give a description of the results, complications and measures necessary for implementation on real data for a selected number of orbits. The orbits are chosen to represent both disturbed (high Kp) and quiet (low Kp) times. The use of real data will, increase the need for regularization compared to the synthetic case example. We have therefore included an additional inversion method, a Tikhonov regularization, described in Equation 5.8 on page 53. The data selection is limited to higher latitudes (above $40°$), since the 1D SECS method is optimized for the polar regions, and is not optimal for determining contributions from the ring current [Juusola et al., 2006]. The preprocessing of data, presented in Section 3.2, describes how the effect of the large scale magnetospheric contributions are minimized by subtracting the RC index. We find, however, that the best results are found, when only the region of the auroral oval, [58 75] is included as input. This will be elaborated later. All results are presented for the Northern Hemisphere only.

6th of November 2001

The method is first tested on the CHAMP satellite orbit 7383 over the IMAGE magnetometer network chain on the 6th of November, 2001 between 05:04 to 05:08 UT with a corresponding MLT of 8:05 to 7:27. Measurements are taken during a strong substorm with a Kp index of 9^-. This specific orbit has been chosen to enable comparison with Juusola et al. [2006].

Figure 6.4 shows the magnetic field (first column) and sheet current densities (second column) as a function of latitude. The observations are given in blue, and the modelled estimates in dashed red. The solution is found from a TSVD analysis (Equation 6.1) with different truncation values for the divergence-free ($\varepsilon_d = 10^{-2}$) and curl-free ($\varepsilon_c = 10^{-1}$) part of Equation 6.3 and 6.4 and a box-function width of $d\delta = 2.1°$. The truncation values are set to match the values stated in Juusola et al. [2006], and $d\delta$ from the tests performed on the synthetic case.

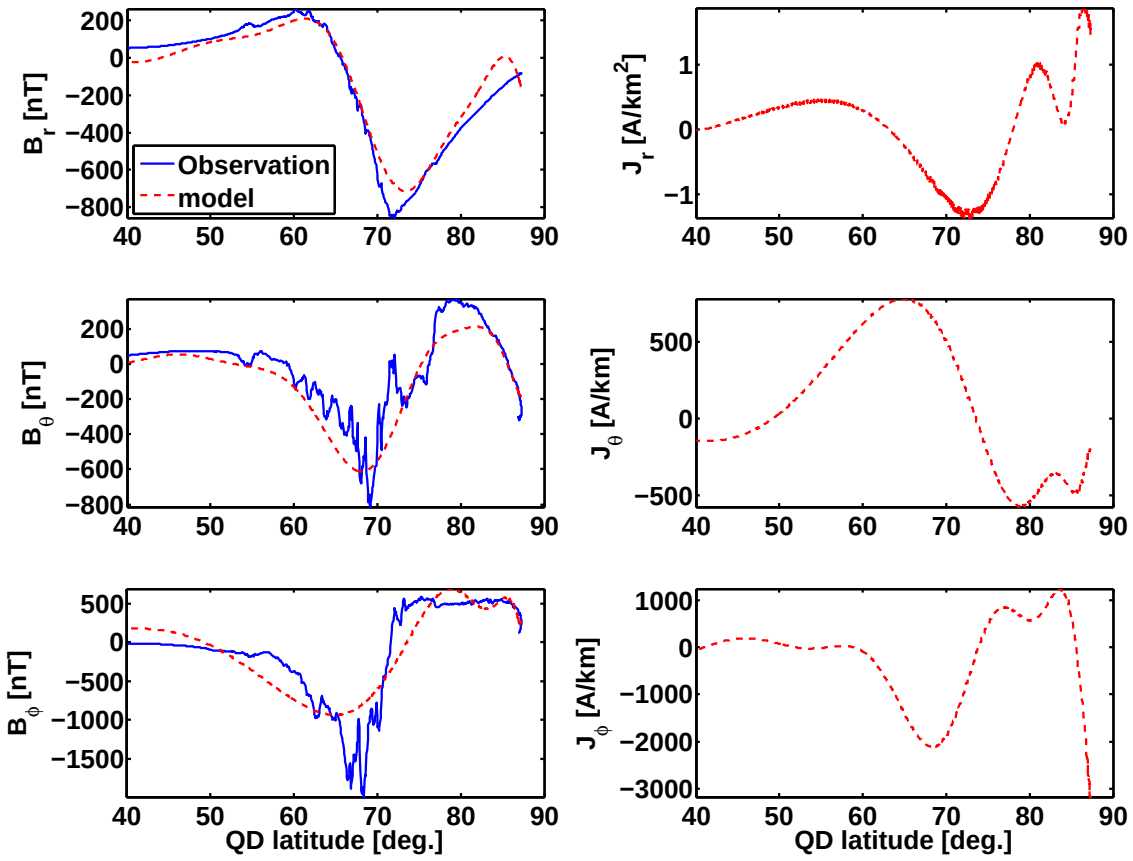

Figure 6.4: Left column: Magnetic field observations (blue) and model fit (red) as a function of magnetic latitude (QD). Right column: Sheet current densities corresponding to the model fit, as a function of QD latitude. All is found for the 6th of November 2001 between 05:04 and 05:08 with an MLT range of 08:05 to 07:27 and $Kp = 9^-$. The model fit is performed with $\varepsilon_c = 10^{-1}$, $\varepsilon_d = 10^{-2}$, $d\delta = 2.1°$, $\delta\theta^{\text{mod}} = 1°$, $\delta\theta^{\text{obs}}$=1s, with an observation and model range of $[40°\ 90°]$.

A model spacing of $0.2°$, observation spacing of 1 second, and a model and observations range of $[40°\ 90°]$ returns an overdetermined inverse problem with 801 observation points and 450 model parameters. The fit returns reasonably low variance ratios of 0.042 for the radial component of the magnetic field, 0.24 for the θ component and 0.23 for the ϕ component. Dealing with real data, these are expected to be higher than the variance ratios given in Table B.1, since in the synthetic case we dealt with noiseless and very smooth data.

Variance ratios for $\boldsymbol{B}_r$ return results an order of magnitude better than the fit for the other components of the magnetic field. The radial component of the magnetic field perturbations will primarily show the large scale ionospheric variations from the Pedersen and Hall currents, since the highly varying FAC contribution is seen primarily in the two horizontal components of the magnetic field. Larger variations in the two horizontal components are therefore expected. To avoid overfitting the data, we need to damp the solution to a degree not permitting the true physical variations, resulting in the smoother model compared to the data shown in Figure 6.4.

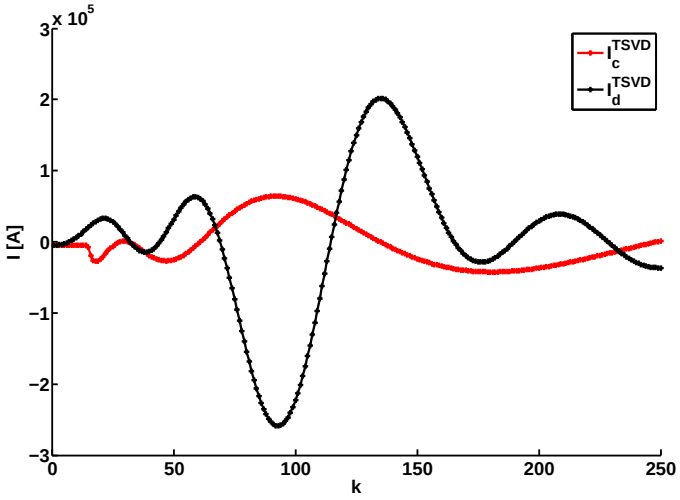

Figure 6.5: Corresponding model parameters for the fit shown in Figure 6.4 for the curl-free (red) and the divergence-free (black) part of the calculations, as a function of model parameter index, k. The model parameters are estimated for orbit number 7383 on the 6$^{\text{th}}$ of November 2001 between 05:04 and 05:08 with an MLT range of 08:05 to 07:27 and Kp= 9^-. The model fit is found with $\varepsilon_c = 10^{-1}$, $\varepsilon_d = 10^{-2}$, $d\delta = 2.1°$, $\delta\theta^{\text{mod}} = 1°$, $\delta\theta^{\text{obs}}$=1s, with an observation and model range of $[40°\ 90°]$.

Both the model fit to the magnetic field perturbations and the sheet current densities are found to be in good agreement with the results presented in Figure 4 in Juusola et al. [2006]. Small differences, especially in the sheet current densities are found, which could be due to differences in the pre-processing of data, or in the implementation of the delta-function, which is not described in the article. Further comparisons are discussed in Section 6.4.

Figure 6.5 shows the corresponding model parameters, $\mathcal{I}_{cf}^{TSVD}$ (red) and $\mathcal{I}_{df}^{TSVD}$ (black) as a function of model parameter index, k. Compared to the model parameters presented in the synthetic case, these have higher complexity, but we still see a high degree of autocorrelation with no sign of overfitting of the data.

Testing additional orbits

The promising results from the 6$^{\text{th}}$ of November 2001 lead us to test the method on additional randomly chosen CHAMP and *Swarm* Alpha orbits. From this, we selected a range involving both disturbed, moderately disturbed and quiet days. The tested days are described in Table 6.1, with corresponding MLT range, orbit numbers and Kp index. The last three columns contain the variance ratios of the model fit to the magnetic field observations. The corresponding individual results are given in Figure 6.6, where the magnetic field observations (blue) are compared with the model estimates (red) in the first column. The second column, of each subfigure, are the corresponding sheet current densities. Figure 6.6(c) is a replica of Figure 6.4, to allow for easier comparison between the different days. The solutions are found using the same adjustable parameters, as for the 6$^{\text{th}}$ of November 2001 ($\varepsilon_d = 10^{-2}$, $\varepsilon_c = 10^{-1}$, $d\delta = 2.1°$, $\delta\theta^{\text{obs}} = 1°$s, $\delta\theta^{\text{mod}} = 0.2°$ and $[40°\ 90°]$). From the figure, it is clear that some

Date	Satellite	Orbit	*Kp*	time range	MLT	B_r	B_θ	B_ϕ
09.08.2000	CHAMP	391	2^+	22:18 to 22:31 UT	00:24	2.35	0.51	0.41
05.11.2001	CHAMP	7368	0^+	05:44 to 05:58 UT	07:40	0.61	0.64	0.41
06.11.2001	CHAMP	7383	9^-	05:00 to 05:19 UT	07:43	0.042	0.24	0.23
20.04.2002	CHAMP	9948	5^o	14:00 to 14:12 UT	15:54	0.38	0.21	0.18
03.03.2014	*Swarm* A	1536	2^-	05:19 to 05:33 UT	16:24	0.14	0.14	0.031
04.03.2014	*Swarm* A	1551	1^o	04:51 to 05:04 UT	16:15	3.51	0.59	0.13

Table 6.1: Information about the tested orbits, presented in Figure 6.6. Values are found with equal adjustable parameters as presented in Figure 6.4 to enable comparisons ($\varepsilon_c = 10^{-1}$, $\varepsilon_d = 10^{-2}$, $d\delta = 2.1°$, $\delta\theta^{\text{mod}} = 1°$, $\delta\theta^{\text{obs}}$=1s, observation and model range of $[40°\ 90°]$). MLT is found for $60°$N QD latitude.

days (*e.g.* 06.11.2001, 20.04.2002 and 03.03.2014) yield better model fits compared to others (*e.g.* 09.08.2000). All of the orbits yields physically realistic sheet current densities, it is, however, difficult to validate their authenticity, when the model fit is not better. Especially the fits of $\boldsymbol{B}_r$ on the 4$^{\text{th}}$ of March 2014 and the 9$^{\text{th}}$ of August 2000 are poor, with variance ratios as high as 3.51 and 2.35, respectively. The poor model fit could be due to large variations in $\boldsymbol{B}_r$ not described by the model. The lowest variance ratios are found for the 6$^{\text{th}}$ of November 2001 and the 3$^{\text{rd}}$ of March 2014.

Measures investigated in an attempt to improve data fit

Due to the sometimes unsatisfactory model fits presented above, we carried out a series of tests, in an attempt to improve the results.

1. Forcing the observed magnetic field perturbations between latitude $40°$N and $50°$N to 0 with cosine tapering at the ends. Ionospheric current signals should be zero in this region, and we therefore assumed the perturbations in this region to be noise. Contributions in this region could be unresolved large scale magnetospheric contributions, not described in the model [*e.g.* Finlay et al., 2016a]. By forcing the signal to zero at low latitudes, we remove any contamination of the data that these currents contribute with, with a possible improvement of the fit in the whole range of data.

2. Removing clearly deviating data. When applying the inverse problem to a highly fluctuating/noisy data set, these can propagate through the inversion and create large errors in the model fit. By removing large outliers, we can give an indication of whether it is the large fluctuations in the input data, or something else, causing the poor model fit.

3. Limit model parameters to the range $[40°\ 89.99°]$. We saw in the synthetic case, how the range of both the observations and model parameters could alter the results. The observations are, due to the inclined orbit of the satellite, not crossing the pole, while the model parameters are set to $[40°\ 90°]$. By removing the model parameter at the pole, we hope to avoid any singularity problems at this specific latitude.

4. Data smoothing. As with test number 2, we try to reduce errors in the model fit, by reducing possible errors in the input data. The data is smoothed with a 10 point running

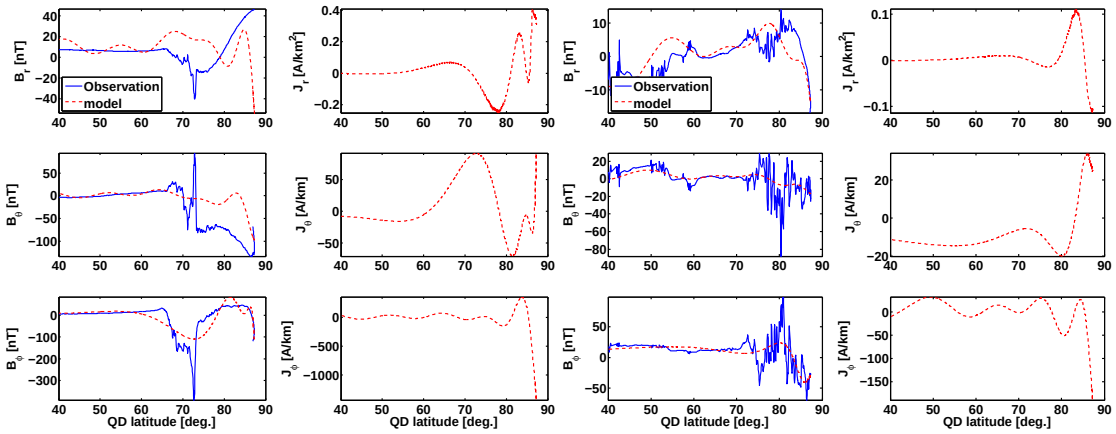

(a) 09.08.2000 **(b)** 05.11.2001

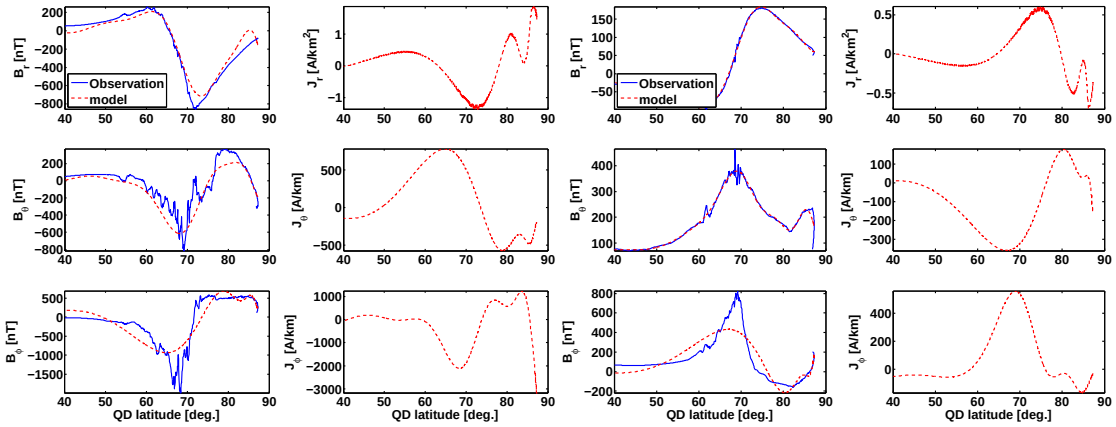

(c) 06.11.2001 **(d)** 20.04.2002

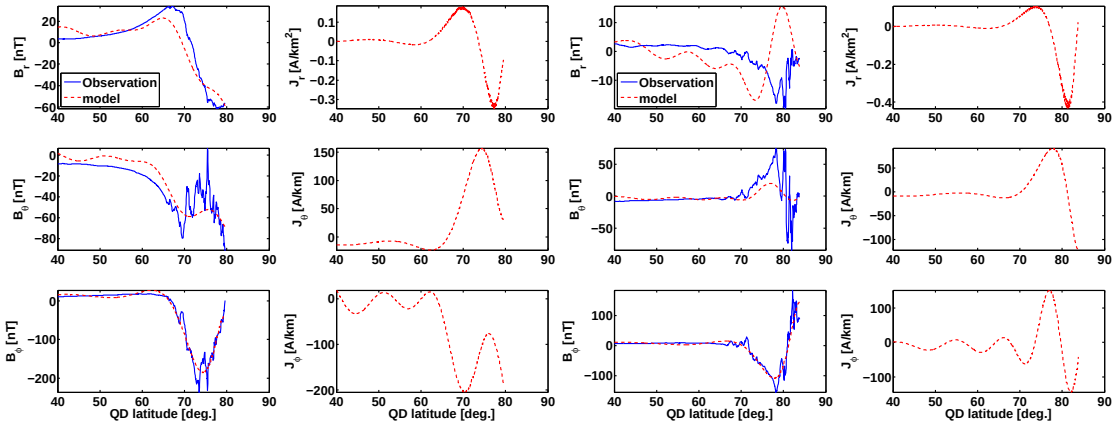

(e) 03.03.2014 **(f)** 04.03.2014

Figure 6.6: As Figure 6.4 for six different days. Information about Kp, MLT, time range and orbit number for the tested days are found in Table 6.1. The results are found with the same set of adjustable parameters as in Figure 6.4.

Test	0	1	2	3	4	5	6	7	8
$\boldsymbol{B_r}$	2.35	2.41	0.28	2.30	2.39	1.69	1.15	1.62	0.022
$\boldsymbol{B_\theta}$	0.52	0.52	0.65	0.53	0.57	0.87	0.38	0.43	0.069
$\boldsymbol{B_\phi}$	0.42	0.42	0.087	0.44	0.42	0.28	1.08	0.19	0.42

Table 6.2: Variance ratios for test 1-8, presented in Figure 6.7 and 6.8. Test 0 indicates when no changes are performed, corresponding to the results presented in Figure 6.6.

mean box-function. Smoothing will, however, due to the in situ FACs remove information about the radial component of the sheet current densities. A smoothing too strong might filter out the information about FACs.

5. Limit the range of data and model parameters to $[50^\circ\ 80^\circ]$. The idea is that a limitation on the data range might limit the influence of possible 2D effects in the polar cap.

6. Changing pole position. In the model, we assume that the measurements are taken along constant latitude. This is strictly not true for points close to the pole. This problem can be amended by moving the pole of the coordinate system in which the 1D SECS grid is defined (r, θ, ϕ), as suggested by Juusola et al. [2006]. Changing the position to 0°N and 20°E, ensures that the assumption of zero ϕ dependence stands, even for positions close to the geographic pole.

7. Orbit across the pole plus cosine tapering at the ends along with changing the pole position to avoid singularity issues at $\theta = 0$. To test if the poor data fit is due to a boundary issue at the pole, we extend the orbit to include data with $\theta < 50^\circ$.

8. Separating all components in three inverse problems. The radial and θ component of the magnetic field returns the worst fits. The reason for this could be that they are described by the same inverse problem. If the two sets of input data ($\boldsymbol{B_r}$ and $\boldsymbol{B_\theta}$) contain contradicting information, it is difficult to find a common set of model parameters. By splitting up the model into separate inverse problems, with separate model parameters, we can estimate whether the problem lies in the inversion method and regularization approach, or if it is simply not possible to find a solution satisfactory for both parameters.

The results of the different tests are given in Figure 6.7 and 6.8. We have chosen to use the orbit from the 9$^{\text{th}}$ of August 2000 for all tests to highlight any improvements for the individual changes, since this day returned one of the poorest data fits in the initial test (Figure 6.6). The figures are presented, as Figure 6.6, with data and model fit in the first column, and sheet current densities in the second. Both are presented as a function of QD latitude. Corresponding variance ratios are given in Table 6.2. All other values, except the changes described in the enumeration above, are kept as in the initial estimation, presented in Figure 6.6.

It is clear from both the figures and the table that some (tests 1, 3 and 4) returns model fit with no or only small improvements. The model fit and model parameters are in these cases very similar with variance ratios ranging between 2.30 and 2.54 for $\boldsymbol{B_r}$, 0.52 and 0.56 for B_θ and 0.42 and 0.44 for $\boldsymbol{B_\phi}$. This tells us that boundary issues at lower latitudes (between 40°N and 50°N), along with model parameters at the pole is not the issue causing the poor model

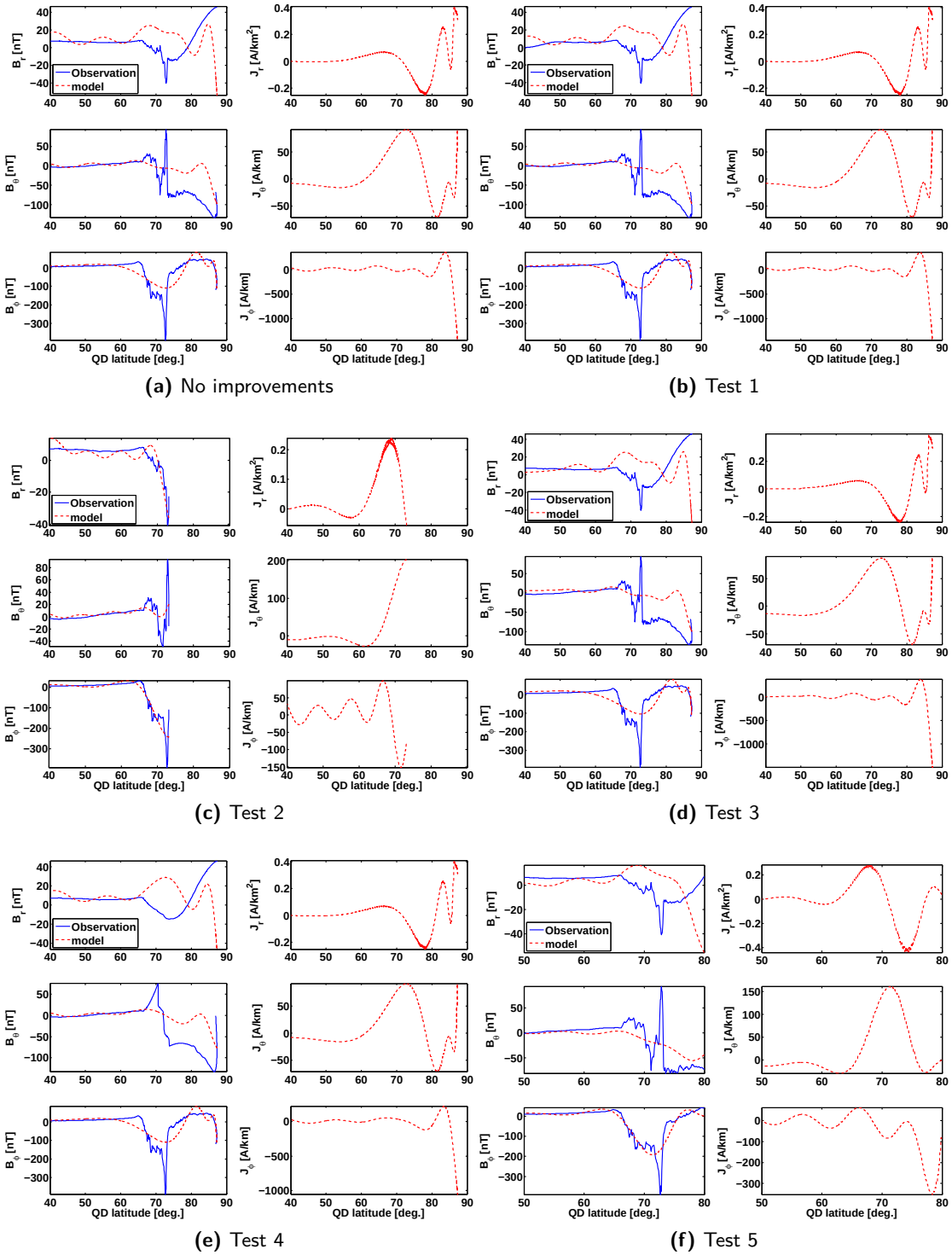

(a) No improvements **(b)** Test 1

(c) Test 2 **(d)** Test 3

(e) Test 4 **(f)** Test 5

Figure 6.7: Magnetic field observations and sheet current densities, similar to Figure 6.4. Each subfigure presents results from the different tests, described in the enumeration on page 68 for the 9th of August 2000, orbit number 391, $Kp = 2^+$, time range of 22:18 to 22.31 UT and an MLT of 00:24 at $60°$N. The results are found, except for the changes described in the enumeration, with the same set of adjustable parameters as in Figure 6.4 ($\varepsilon_c = 10^{-1}$, $\varepsilon_d = 10^{-2}$, $d\delta = 2.1°$, $\delta\theta^{\text{mod}} = 1°$, $\delta\theta^{\text{obs}}$=1s, observation and model range of $[40°\ 90°]$.)

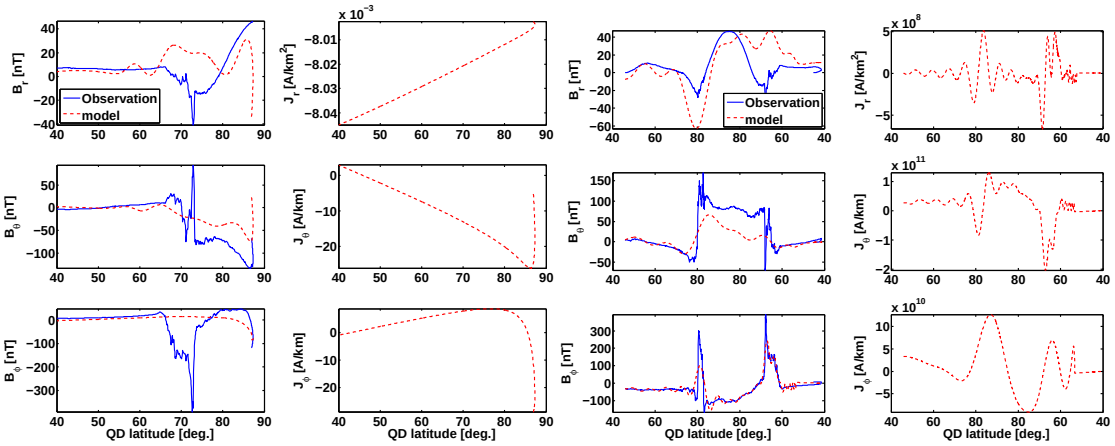

(a) Test 6 **(b)** Test 7

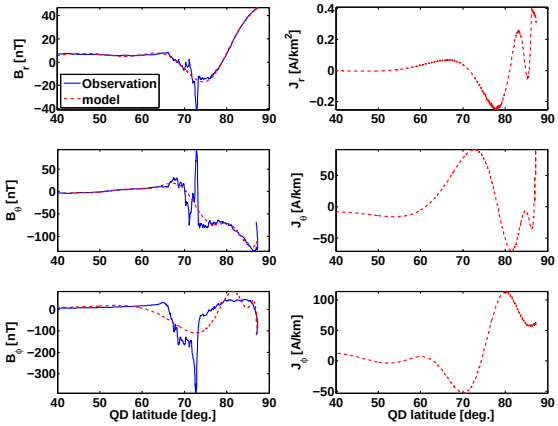

(c) Test 8

Figure 6.8: Continuation of Figure 6.7.

fit. Since a smoothing (test 4) does not alter the results or the data fit, we conclude that the model misfit is not due to outliers in data either. Unexpectedly we do not see a change in $\boldsymbol{J}_r$. It seems that the scale size of this and the other components are determined from the regularization alone, and not affected by smoothing the data. However, an increase in the data smoothing would probably result in a change in resolution of the FACs.

In test 2 (removing large outliers), we find a much improved model fit for $\boldsymbol{B}_r$ and $\boldsymbol{B}_\phi$, with the variance ratio changing from 2.35 to 0.28 and 0.42 to 0.087 accordingly. The variance ratio for $\boldsymbol{B}_\theta$ is, slightly increased from 0.52 to 0.65. The main difference, however, lies in the sheet current densities, where $\boldsymbol{J}_r$ is found almost as a mirror image of all the other estimates of this sheet current density component. This, of course, raises concern as to the stability of the inversion in general, and to the resultant sheet current densities. Since the fit is found for only quiet-time magnetic field disturbances ($\boldsymbol{B}_\theta > -100$ nT), this solution removes large parts of the dataset, with all values at $\theta > 73°$N removed. We therefore conclude that this method puts unwanted restrictions on the tested days, and is therefore not suitable for the intended automatic implementation.

Test	TSVD	IRLS	[58 75] IRLS	[58 75] TSVD
$\boldsymbol{B_r}$	2.35	2.69	1.26	1.08
$\boldsymbol{B_\theta}$	0.52	0.32	0.68	0.67
$\boldsymbol{B_\phi}$	0.42	0.28	0.26	0.18

Table 6.3: Variance ratios for 9th of August 2000, orbit number 391, $Kp = 2^+$, time range of 22:18 to 22:31 UT and an MLT of 00:24 at $60°$N using a TSVD and Tikhonov regularization (IRLS) for two model and observation ranges $[40°90°]$ and $[58°75°]$. The variances are found for the corresponding values to those used to get results presented in Figure 6.6 and 6.9: $\alpha_c^2 = 10^{-22}$ and $\alpha_d^2 = 10^{-24}$ (IRLS), $\varepsilon_c = 10^{-1}$ and $\varepsilon_d = 10^{-2}$ (TSVD) and both use $d\delta = 2.1°$, $\delta\theta^{\text{mod}} = 1°$ and $\delta\theta^{\text{obs}}$=1s.

Results of test 5, 6 and 7 show a slight improvement of model fit in $\boldsymbol{B_r}$ with the variance ratios reduced by a factor of two, compared to the initial tests. In test 5 and 6, one of the θ and ϕ components are improved, while the other results in a worse fit. Test 7 shows an improvement in all three components.

By separating the components completely, and thereby calculating individual model parameters (test 8), it is possible to find a significant improvement in the model fit. The variance ratios are decreased from 2.54 and 0.52 to 0.022 and 0.069 for the radial and θ component. If $\boldsymbol{B_r}$ and $\boldsymbol{B_\theta}$ contain contradicting information, it is impossible to find a model fit suitable for both components. The large improvement in the model fit indicates that this is the case for the tested orbit. It does, however, not solve the issue with modelling, since the calculations described by Equation 4.46 and 4.47 require equal model parameters for these two components. We do therefore not accept this solution.

The choice in $d\delta$ could be affected by the difference in the real data and synthetic data. This has, however not been tested, since it mainly influences the shape and fit of $\boldsymbol{J_r}$. Since this has not been the primary focus of testing real data, this was not investigated further. In conclusion, we did not manage to obtain a robust implementation of the model, suitable for automation. The different changes to the input data and range alter the results, though no solution to the poor model fit is found.

Regularization methods

Since none of the above tests returned satisfactory solutions, we turned our focus towards the regularization method. No improvement was found in the synthetic case. Dealing with real data, however, is different, where coping with noise and fluctuations in data (including outliers) is of increased importance. Instead of the TSVD solution, previously presented, we find an solution to the inverse problem using a zeroth order Tikhonov regularization and a Huber weighted data misfit measure, implemented through an IRLS technique (Equation 6.2). The Huber weighted data misfit measure is implemented specifically to deal with any non-Gaussian noise (outliers) in the data set. We have used regularization parameters, $\alpha_d^2 = 10^{-24}$ and $\alpha_c^2 = 10^{-22}$, estimated from visual inspection of model parameters, to find the results given in Figure 6.9(a) and Table 6.3.

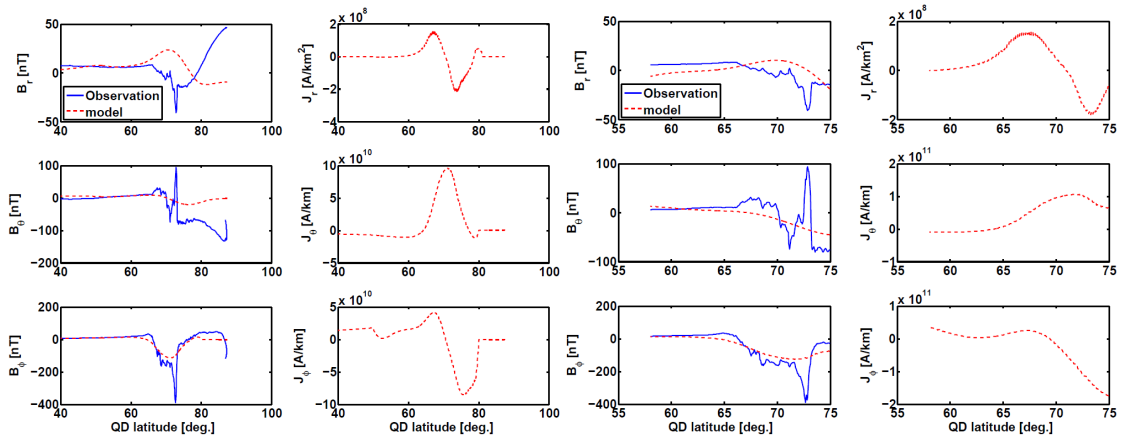

(a) IRLS **(b)** $[58\ 75]$ IRLS

Figure 6.9: As Figure 6.7 for two data and model parameter ranges applying IRLS and Tikhonov regularization for the 9th of August 2000. The results are found with adjustable parameters: $\alpha_c^2 = 10^{-22}$, $\alpha_d^2 = 10^{-24}$, $d\delta = 2.1°$, $\delta\theta^{\text{mod}} = 1°$ and $\delta\theta^{\text{obs}}$=1s.

The figure and corresponding variance ratios show no significant improvement using IRLS solution over the TSVD solution. Juusola et al. [2009] presented their data using a very tight data and model range $[58°75°]$. Their reason for this strict range is that the 1D assumption is mostly applicable to electrojet dominated cases. This cannot be expected to be true for the entire global current system. For a small section, however, this can be an acceptable assumption, when a local independence of the ϕ coordinate is present. This could be the reason, why increased range returns larger variance ratios. This does, however, not explain why the range affects the synthetic example (Appendix B), since this is per definition one dimensional. The results of decreasing the range to $[58°\ 75°]$ is shown in Figure 6.9(b) and the third row of Table 6.3. We see an improvement in the variance ratios very similar to the ones of test 2 given in Figure 6.8(c). This indicates that, as in the synthetic case, the range is important for the quality of the model fit. The largest improvements are found in the fit to the radial component of the magnetic field. Since this component mostly is affected by the horizontal currents, it is expected to be more sensitive towards lack of one dimensionality. The breakdown of the 1D assumption is discussed further in Section 6.4. A positive result of this approach is that the overall shape of the estimated sheet current densities does not change. Peaks are found with similar strength and positions for both inversion methods presented in Figure 6.9. To ensure that the improvement was due to the change in range, we also carried out the test using a TSVD analysis, finding similar variance ratios to the Tikhonov solution (last column of Table 6.3). This indicates that the problem is unlikely to be due to the inversion method, but probably in the correct choice of adjustable parameters ($\delta\theta^{\text{mod}}$, $\delta\theta^{\text{obs}}$, $d\delta$, ε_c, ε_d, α_c and α_d) as well as observation and model range.

Induced currents

In a final attempt to improve the model fit, we tested the effect of the induced currents. This is an addition to the calculations presented by Juusola et al. [2006], and therefore is a plausible explanation of the discrepancies. After carrying out a series of tests, it does, however, not seem to alter the results much, whether we include induced currents in the calculations or not.

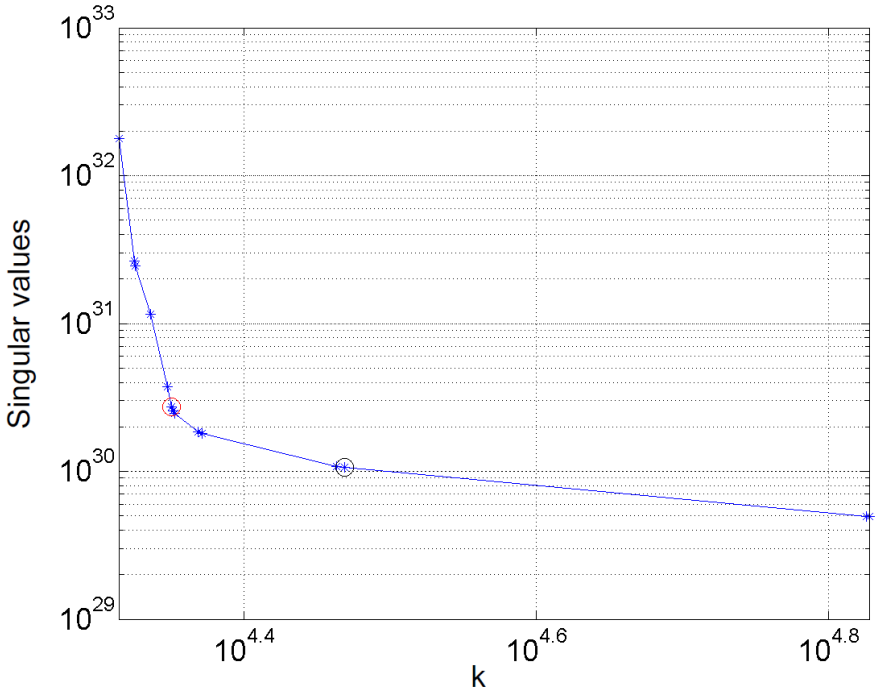

Figure 6.10: Singular value spectrum from the 6th of November 2001, orbit number 7383, between 05:04 and 05:08 with an MLT range of 08:05 to 07:27 and $Kp = 9^-$. The values are found with $\varepsilon_c = 10^{-1}$, $d\delta = 2.1°$, $\delta\theta^{\text{mod}} = 1°$, $\delta\theta^{\text{obs}}$=1s, observation and model range of $[40°\ 90°]$. The red circle represents the results using $\varepsilon_d = 10^{-2}$ and the black, using $\varepsilon_d = 10^{-1}$.

6.4 Discussion of the 1D SECS method

In this section we will present a short discussion of the above presented results. We will start with a discussion on the truncation value ε. Since our initial aim with the model validation, described in the previous sections, was to compare with Juusola et al. [2006] and Juusola et al. [2009], we have until now not tested if the chosen truncation values are also applicable in our case. We therefore conducted a test of the truncation value for the real data case. The results are presented in Figure 6.10, showing the singular value spectrum as described in the theory section 5.2 on page 57. The figure shows the complexity of the model parameters as a function of norm of the model parameters. For easier interpretation, we highlighted two truncation values, red ($\varepsilon_d = 10^{-2}$) and black ($\varepsilon_d = 10^{-1}$). The singular value spectrum is found for ε_d, while keeping ε_c constant. The value chosen in Juusola et al. [2006], $\varepsilon_d = 10^{-2}$, approximately fits with the corner value of the singular value spectrum, indicating this as the optimal truncation value. Lowering this, results (not shown) in a clearly unstable solution. We therefore estimate that the poor model fit is not likely due to a wrongly implemented SVD truncation value.

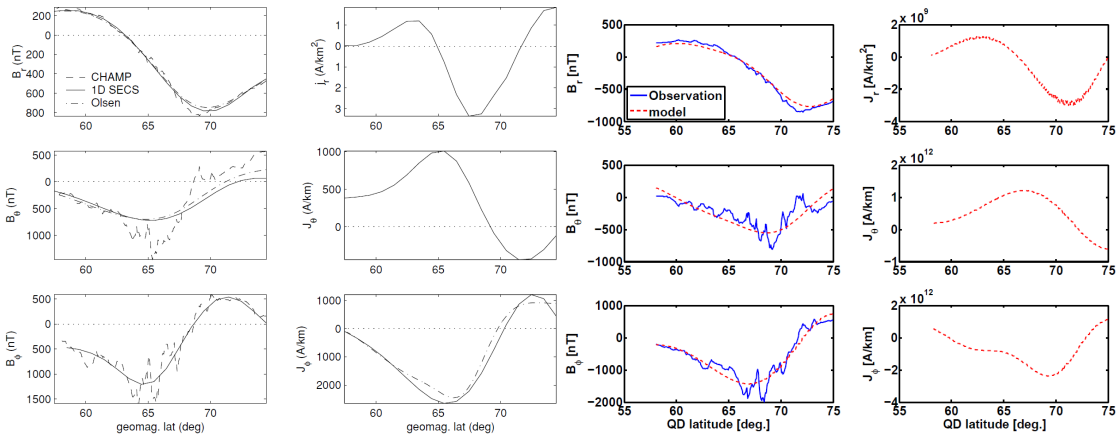

Figure 6.11: (a) Results (Figure 9) from Juusola et al. [2006] and (b), our results for the 6th of November 2001, orbit number 7383, between 05:04 and 05:08 with an MLT range of 08:05 to 07:27 and $Kp = 9^-$. The values are found with $\varepsilon_c = 10^{-1}$, $\varepsilon_d = 10^{-2}$, $d\delta = 2.1°$, $\delta\theta^{\text{mod}} = 1°$, $\delta\theta^{\text{obs}}$=1 s, observation and model range of $[58°\ 75°]$.

Comparisons with Juusola et al. [2006]

The 6th of November 2001 returns the most satisfactory model fit and sensible sheet current densities of the tested days. This day was chosen to enable comparison to the results found by Juusola et al. [2006]. We now provide this comparison in detail to validate the choices in the adjustable parameters. The comparison is accompanied by a discussion concerning why some days provide better fits than others.

Figure 6.11(a) is a replica of Figure 9 from Juusola et al. [2006], while (b) presents our results. We have adjusted the range of our estimate to match that in (a). Similar model fit and sheet current densities are found, indicating that the issues we have faced with the poor data fit do not come from our implementation of the model, but is more likely are a problem inherent in the model itself. The overall shape of the sheet current densities are similar. We do, however, not find the peaks in the same place. All peaks are shifted poleward with approximately $4°$. Since the shift is found in both data and estimated sheet current densities, it is probably caused by differences in coordinate systems.

A study by Vanhamäki et al. [2003] revealed how some shapes of the sheet current densities are better modelled than others. This is shown in Figure 6.12 (Figure 3 in the original paper). They find that rapidly changing currents, such as in subfigures B and C, are more difficult to model compared to the smoother shapes in A and D. This could explain why the best fit is found for the 6th of November 2001 and the 20th of April 2002, which have the smoothest observations, especially for the radial component.

The poor fit for the other days could, however, also be due to the difference in their one dimensionality. Since this is a crucial assumption in the model, a breakdown of one dimensionality would lead to a poor model fit. The one dimensionality can according to Juusola et al. [2006] be tested by estimating the model fit of the θ component of the magnetic field residuals using

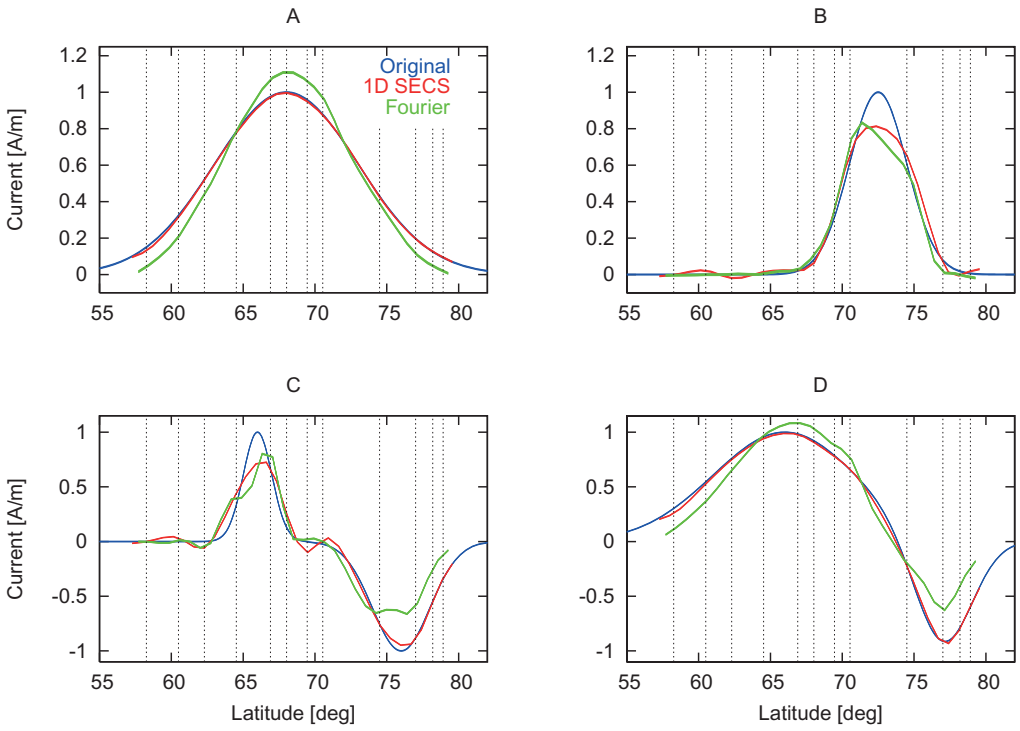

Figure 6.12: Study of the effect of current shapes on the model fit with the 1D SECS approach by Vanhamäki et al. [2003], showing the current as a function of latitude for four different shapes of input.

scaling factors based solely on $\boldsymbol{B}_r$ against observations. In the paper they have considered orbits with errors up to 0.60 as one dimensional, with the error calculated as

$$\text{Error} = \frac{\overline{|\boldsymbol{B}_\theta{}^{\text{obs}} - \boldsymbol{B}_\theta{}^{\text{mod}}|}}{\overline{|\boldsymbol{B}_\theta{}^{\text{obs}}|}}. \tag{6.12}$$

$\overline{|\boldsymbol{B}|}$ is here the mean of the absolute values of $\boldsymbol{B}$. We have found the error estimates, restricting the data and model range to $[58^\circ\ 75^\circ]$ to ensure a better comparison. According to Juusola [2016], approximately 39% of the tested orbits are found below this error level. Our own calculations show, however, that this threshold would exclude all days except the 20$^{\text{th}}$ of April 2004, which has an error estimate of 0.54. Even the 6$^{\text{th}}$ of November 2001 does not make the cut, with an error estimate of 0.82. Juusola et al. [2006] finds this value to 0.50. The only other tested day getting close to acceptance is the *Swarm* orbit on the third of March 2014 where we find an error estimate of 0.63.

The difference of error estimates for the 6$^{\text{th}}$ of November 2001 indicates, despite the visually similar results, differences in method implementation. We would especially expect differences due to the pre-processing of the data. As an example, we have used the RC index instead of Dst index as magnetospheric contribution. This would, however, only provide a very small difference, and the influence of this should lie within the methods ability to deal with small changes. Unfortunately we have shown that small changes in input data do affect the results both in the synthetic case, and when applying the method to real data. The difference in the input data could affect the 1D assumption and thereby lead to a worse model fit. We argue,

however, that with the aim of automatic implementation, a strong sensitivity to small changes such as this is critical.

The influence of the pre-processing can be tested by comparing results with and without removal of the magnetospheric correction. The difference between using DST and RC, should be less than neglecting the magnetospheric correction. This has not been tested in the 1D SECS case, but a study of the magnetospheric correction is described in the discussion of the LCM method (see Section 7.3).

Personal correspondence with Juusola [2016] revealed further differences between the two implementations of the method. These differences are probably where we can find the origin of the discrepancies between Figure 6.11(a) and (b). Adjustment to the magnetic field calculations are needed, when implementing the box function in stead of the delta function. Furthermore, we should not place model parameters at the same positions as the observations, since this might lead to an instability in the model. However, even if we were able to obtain similar model and error estimates, we would find that only approximately 40% of the orbits have errors below 0.6, which is not sufficient for the implementation of the method in an automatic routine.

6.5 Summary on applying the 1D SECS approach to CHAMP and *Swarm* magnetic data

We have tested the 1D SECS method for estimation of the sheet current densities from synthetic and satellite magnetic field observations. Several issues have been raised, including the high sensitivity of the model fit to a set of adjustable parameters, $\delta\theta^{\text{mod}}$, $\delta\theta^{\text{obs}}$, $d\delta$, ε_c, ε_d, α_c and α_d along with model and observation range. A range of tests were conducted applying the method to real satellite data with the aim of improving the method. Some improvements where found, though none of the tests enabled the method to work for all the tested days. The poor fit for most of the tested days is attributed a breakdown of the 1D assumption. This was confirmed by Juusola [2016], who finds a breakdown of the 1D assumption in approximately 60% of their tested days. Even though further improvements were suggested through personal correspondence with Juusola [2016], we decided not to pursue this approach further.

In conclusion; we did not manage to obtain a reliable implementation of the 1D SECS method using CHAMP or *Swarm* satellite magnetic field anomalies to estimate the ionospheric sheet current densities. The breakdown of the 1D assumption for approximately 60% of the orbits makes the method less applicable to automatic implementation on satellite data.

Chapter 7

Application of the ionospheric line current method to satellite magnetic observations

The objective of this chapter is to discuss initial results of the line current model (LCM) and to investigate the effect of model regularization on the estimated sheet current densities. The method is first tested on a synthetic current profile, followed by an investigation of different regularization parameters and methods, along with discussion of robustness providing an estimate of the most accurate description of model parameters.

A mathematical description of the relation between magnetic field residuals and current amplitudes is given in Chapter 4 on page 35, and stated as a linear inverse problem in Equation 4.16 on page 40.

7.1 Test with synthetic data

As an initial test, we applied the method to the magnetic field produced by a synthetic current density distribution. The current density profile is roughly given by a Gaussian distribution on each side of the pole, representing the westward (morning sector) and eastward (evening sector) electrojet. The distribution is given with a positive current towards the sun. The M strengths of the line currents, j_k, (model parameters) are determined by solving the inverse problem described by Equation 4.16 and 4.17 on page 40. The much larger larger distance between satellite and ionosphere ($r_n >> \Delta$) results in an ill-conditioned problem, although formally overdetermined ($N > M$). This results in large variations of the amplitudes of neighbouring line currents for the unconstrained least squares solution. We therefore adopt a regularization approach to avoid this type of instabilities. The type of regularization method can, as described in Chapter 5 have a large influence on the resultant model parameters. The influence is, however, limited when applied to noiseless synthetic data. Figure 7.1 presents the results of the synthetic data applying a zeroth order Tikhonov regularization with the solution, given in Equation 5.8,

$$\boldsymbol{m^{Tik}} = (\boldsymbol{G}^T\boldsymbol{G} + \alpha^2\boldsymbol{I})^{-1}\boldsymbol{G}^T\boldsymbol{d^{obs}}.$$

The figure shows the magnetic field synthetic observations, δF, in green along with the corresponding model estimate in blue as a function of QD latitude (top panel). The middle panel

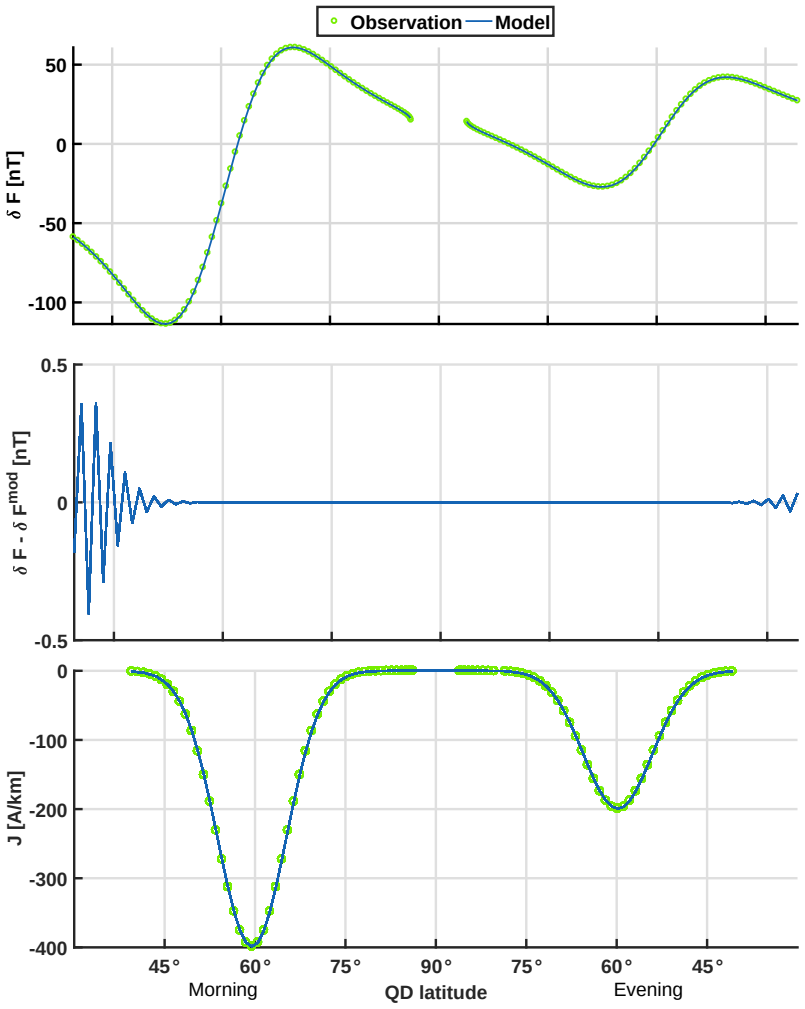

Figure 7.1: Synthetic data example. Top panel: magnetic field synthetic observations (green) and corresponding model estimate (blue) as a function of QD latitude. Middle panel: model residuals. Bottom panel: synthetic sheet current densities (green) and model estimate (blue) as a function of QD latitude.

gives the model residuals, $\delta F - \delta F^{\text{mod}}$, and the bottom panel the synthetic sheet current densities (green) and the model estimate (blue) as a function of QD latitude. The model estimates are found with $\alpha^2 = 7 \cdot 10^{-16}\ \frac{\text{nT}^2}{\text{A}}$. The very low model residuals for both the sheet current densities (< 0.5 A/km $\sim 0.13\%$ of the signal strength) and the magnetic field residuals ($< 10^{-4}$ nT) illustrates how the sheet current densities and magnetic field residuals can be estimated to a very high degree of accuracy.

7.2 Applying LCM to *Swarm* Alpha orbit no 3334

Applying the method to satellite observations is however different, as already shown for the 1D SECS case. Dealing with even slightly noisy data requires more strict regularization and increases the need for choosing the correct regularization method. Initial least squares results revealed a need for a more detailed investigation of regularization methods. We have therefore

conducted a test on a set of different regularization methods. The goodness of regularization is evaluated through a comparison of model parameters and model fit to expectations of data misfit and distribution of model parameters.

It is impossible to find a probability density function, perfectly suitable with the model parameter and misfit distribution. We do, however, aim at a distribution, not excluding any important physics, and thereby important structure of the model parameters. We therefore evaluate the distribution against a set of pre-defined requirements:

1. Absent or weak sheet current densities outside the polar regions (QD latitudes $< \pm 50°$). We assume that all contributions, except the auroral electrojet system and polar cap currents have been removed in the preproccesising (see Section 3.2 on page 32), and do therefore not expect any currents outside this region.

2. High autocorrelation - not wildly fluctuating sheet current densities. Theory [*e.g.* Baumjohann and Treumann, 2012; Weimer, 2001] states the auroral electrojet system, basically as two currents, a westward and an eastward electrojet (see Section 2.3 on page 13). We therefore expect a smooth current system, with one major peak in the morning sector and one in the afternoon sector.

Figure 7.2 shows the model parameters (sheet current densities) as a function of QD latitude for *Swarm* Alpha orbit no. 3334 on the 28th of June 2014 13:42 to 14:08 UT corresponding to a magnetic local time of 19:26 at $60°$ QD latitude, estimated by application of a series of different regularization methods. Orbit 3334 presents a moderately disturbed period with $Kp = 4^-$. Each plot gives the sheet current density, with a positive current from midnight to noon (sunward). Estimates from the presented regularization method and previous panels are given in red and grey accordingly. Short names for each regularization method are printed in the parenthesis. Figure 7.2(a) gives the unregularized least squares solution (LS), (b) zeroth order Tikhonov solution (Tikhonov), (c) zeroth-order Tikhonov solution with a Huber weighted data misfit measure (Tikhonov + Huber) and (d) higher-order Tikhonov regularization with a Huber weighted data misfit measure considering finite along-track differences of the model parameters (1st order Tikhonov + Huber). (e) gives the truncated SVD solution (TSVD), (f) Maximum entropy solution (Maxent + Huber), and (g) L_1 model norm minimization of the second order along-track differences of model parameters and a Huber-weighted data misfit measure on data (L_1 norm of 2nd order Tikhonov + Huber). The comparably large changes in the least squares solution (a), has resulted in an exclusion of this solution from (c) and onwards. Variance ratios (Equation 5.20 on page 59) for all model fits with observations of the magnetic field residuals is given in Table 7.1, and a detailed description on all regularization methods are provided in Section 5.2 on page 52.

Figure 7.2	(a)	(b)	(c)	(d)	(e)	(f)	(g)	
Variance ratio	0.40	7.05	13.8	13.8	6.05	12.7	6.46	$\times 10^{-6}$

Table 7.1: Information about the tested orbits, presented in Figure 7.2.

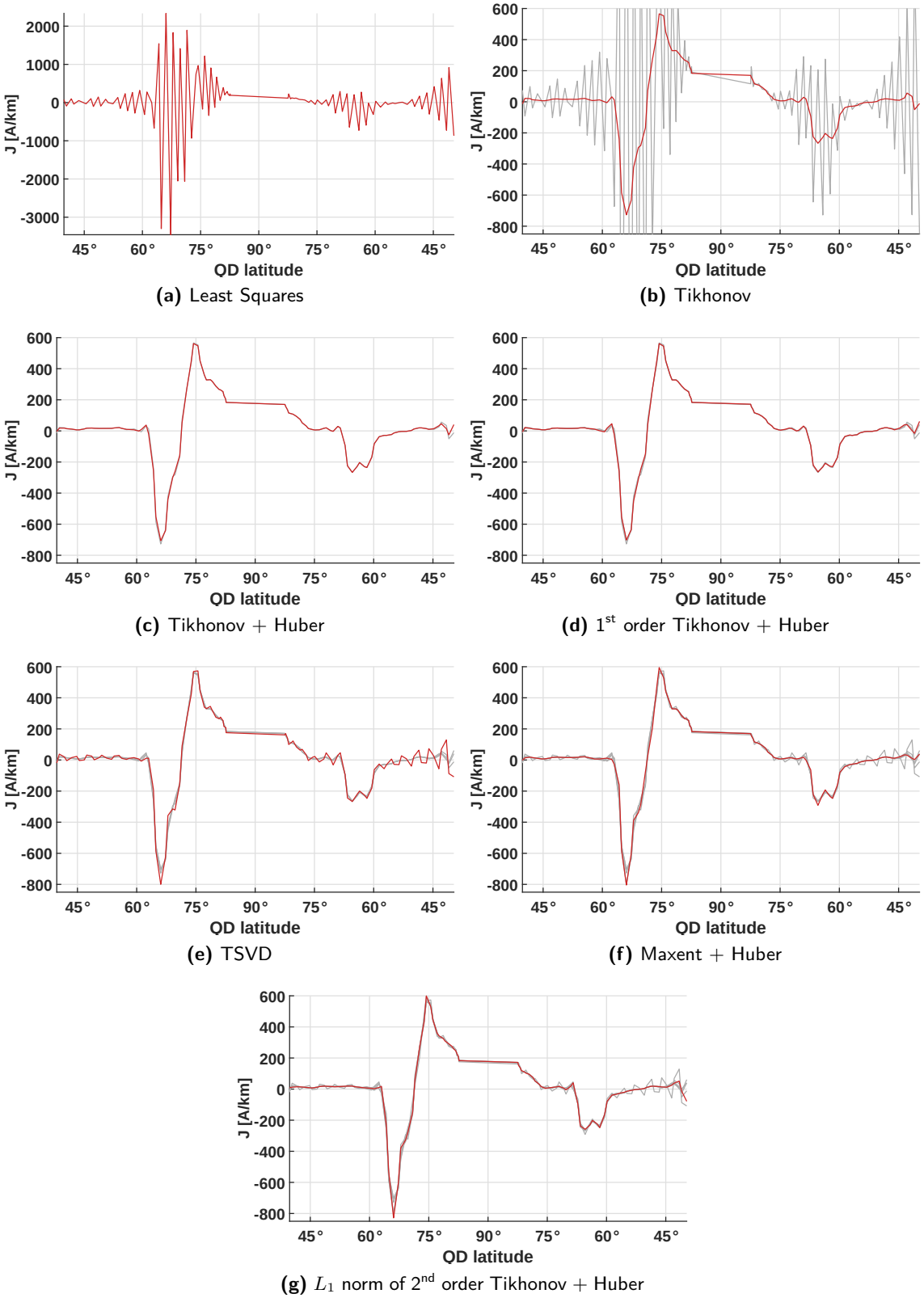

(a) Least Squares

(b) Tikhonov

(c) Tikhonov + Huber

(d) 1st order Tikhonov + Huber

(e) TSVD

(f) Maxent + Huber

(g) L_1 norm of 2nd order Tikhonov + Huber

Figure 7.2: Sheet current density along orbit 3334 on the 28th of June 2014 from 13:42 to 14:08 UT, with a corresponding MLT at $60°$ QD latitude of approximately 19:30, from seven different regularization methods as a function of QD latitude with a positive current in the sunward direction. Each plot contains estimates from previous panels in grey (with exeption of least squares solution from (c) and onwards), and estimates from the present regularization method in red.

Simple least squares (LS)

The simplest solution to the inverse problem is the non-regularized least squares solution (Equation 5.7),

$$\boldsymbol{m}^{\boldsymbol{LS}} = (\boldsymbol{G}^T\boldsymbol{G})^{-1}\boldsymbol{G}^T\boldsymbol{d}^{\boldsymbol{obs}}.$$

The highly fluctuating model parameters ($\boldsymbol{J}$) given in Figure 7.2(a) clearly shows the need for regularization. Although the data fits to a very high degree of accuracy (variance ratio between the variance of observations and variance of data misfit of $4.00 \cdot 10^{-7}$), large non-physical fluctuations in model parameters report a clear overfitting of data. We therefore conclude a need for regularization.

Zeroth-order Tikhonov solution (Tikhonov)

The amplitudes of the model parameters can be controlled through the regularization parameter, α^2, by applying a zeroth-order Tikhonov regularization, minimizing the sums of squares of the line current strength, and thereby restricting the structure of the model parameters. The solution of the inverse problem is found from Equation 5.8,

$$\boldsymbol{m}^{\boldsymbol{Tik}} = (\boldsymbol{G}^T\boldsymbol{G} + \alpha^2\boldsymbol{I})^{-1}\boldsymbol{G}^T\boldsymbol{d}^{\boldsymbol{obs}}.$$

The results given in Figure 7.2(b), presented with $\alpha^2 = 3.6 \cdot 10^{-27}\ \frac{\mathsf{nT}^2}{\mathsf{A}}$, show a clear improvement in structure of the model parameters, with solutions very close to the predefined requirements given in the enumeration on page 81. The improvement is furthermore found with only little decrease in variance ratio ($7.05 \cdot 10^{-6}$) compared to the least squares solution. The role and estimation of the regularization parameter, α^2, is discussed in Section 7.3. We find unwanted non-zero currents outside the polar region (approximately $\pm 30^\circ$ from the pole despite the in general physically acceptable sheet current densities).

Zeroth-order Tikhonov solution with a Huber weighted data misfit measure (Tikhonov + Huber)

The *Swarm* satellites provides smooth data with very few outliers. The presence of outliers, though, could be responsible for the small scale oscillations in the non-polar regions, present in the Tikhonov solution. We therefore implement a Huber weighted data misfit measure. Applying Huber weights, deals with non-Gaussian noise for least squares problems, and thereby a non-Gaussian distribution of the data misfit. The IRLS routine is added alongside the zeroth-order Tikhonov regularization, with the model parameter vector at (i+1)'th iteration determined by Equation 5.10,

$$\boldsymbol{m}_{i+1}^{Tik,W^d} = (\boldsymbol{G}^T\boldsymbol{W}_i^d\boldsymbol{G} + \alpha^2\boldsymbol{I})^{-1}\boldsymbol{G}^T\boldsymbol{W}_i^d\boldsymbol{d}^{\mathsf{obs}}.$$

The iterative process is run with 50 iteration, more than adequate for conversion for all tested orbits. Figure 7.2(c) shows the resultant current density distribution. The solution is almost identical ($V_R = 1.38 \cdot 10^{-5}$) to the zeroth-order Tikhonov solution given in (b). This indicates that outliers, as already expected, is not a key issue, dealing with *Swarm* data. The solution is found with the same α^2 ($3.6 \cdot 10^{-27}$). The assumed data error, σ, (used in the iterative process) is estimated from the Tikhonov solution model misfit, which also acts as the first

iteration of IRLS. A reasonable estimation of σ is of rather large importance in model fit. An initial choice too large, resulted in this case (not shown), in large enhancements of the non-physical oscillations outside the polar region, indicating, as expected that these are results of the inversion and not physical currents.

As an attempt to more directly control autocorrelation in the model parameter vector, we switch from a zeroth-order to a higher-order Tikhonov regularization - entailing a minimization of the first order differences, and thereby ensuring interdependence between neighbouring line currents (Equation 5.10, including $\boldsymbol{D}_1$, controlling the first order differences)

$$\boldsymbol{m}_{i+1}^{Tik,W^d,D_1} = (\boldsymbol{G}^T\boldsymbol{W}_i^d\boldsymbol{G} + \alpha^2\boldsymbol{D}_1^T\boldsymbol{D}_1)^{-1}\boldsymbol{G}^T\boldsymbol{W}_i^d\boldsymbol{d}^{\text{obs}}.$$

The solution is given in Figure 7.2(d). Implementation of $\boldsymbol{D_1}$ does, however, not have the desired effect on the small scale oscillations in the non-polar regions.

α^2 has so far been kept constant for the sake of comparison. A different choice in α^2 could be beneficial when introducing the minimization of first order differences. This has not been tested in detail, but preliminary investigations showed no significant improvements.

Truncated SVD solution (TSVD)

Since the previous improvements on the least squares solution did not meet all the predefined requirements, we tried with an alternative regularization approach, equal to the one presented for the 1D SECS method, namely the TSVD solution. The solution is found from Equation 5.15

$$\boldsymbol{m}^{\text{TSVD}} = \boldsymbol{X}\boldsymbol{\Lambda}^{-1}\boldsymbol{U}^T\boldsymbol{d}^{\text{obs}}.$$

The results presented in Figure 7.2(e) are found using a truncation value of $\varepsilon = 4 \cdot 10^{-3}$. Even though a non-truncated solution (not shown) shows improvements compared to the least squares solution, no significant improvement is found in the TSVD solution compared to the regularized LS solution. The resultant sheet current density profile shows increased unwanted small scale variations, which makes the solution unfit, despite an increased model fit ($V_R = 6.05 \cdot 10^{-6}$).

Maximum entropy solution (Maxent+Huber)

The previous regularization methods show how the observations can be re-estimated to a high degree of accuracy with variance ratios of the order of 10^{-5}. We do, however, find non-physical oscillations in the non-polar region which can only be damped satisfactory at the expense of damping the peak of the sheet current density profile, and thus decreasing the model fit to observations. We thus implement a maximum entropy solution which should minimize the small scale oscillation, while still allowing the large main peak. The balance in this regularization method is to find a solution that satisfies our demand of small or no oscillations near the boundary while keeping the main peak large enough. If α^2 is too high, it is not possible to fit the main peak, and if it is not high enough, we do not get rid of the unwanted oscillations. The solution is found from Equation 5.16,

$$\boldsymbol{m}_{i+1}^{Maxent} = (2 \cdot \boldsymbol{G}^T\boldsymbol{W}_i^d\boldsymbol{G} + \alpha^2\boldsymbol{Q}_i^A)^{-1} \cdot \left(2 \cdot \boldsymbol{G}^T\boldsymbol{W}_i^d\boldsymbol{d}^{\text{obs}} + \alpha^2(\boldsymbol{Q}_i^A\boldsymbol{m}_i) - 4\omega_s\alpha^2\boldsymbol{Q}_i^B\right).$$

Applying the maximum entropy regularization removes a large part of the small scale oscillations (Figure 7.2(f)), and in some ways it fulfils our predefined requirements for the model fit and distribution of model parameters. Presented with $\alpha^2 = 1.44 \cdot 10^{-26}$ and $\omega = 2 \cdot 10^{12}$, we find a model fit with a variance ratio of $1.28 \cdot 10^{-5}$. It does on the other hand also introduce a second regularization parameter, ω, and with that a sharp boundary between optimized model fit and a highly unstable solution, different for each specific orbit. This adapts very poorly with the desired automatic implementation, and we therefore searched for a more stable regularization approach, with the same effect.

L_1 model norm minimization of the second order along-track differences of model parameters and a Huber weighted data misfit measure on data (L_1 norm)

Based on the possibilities of minimizing the small scale oscillations with the maximum entropy solution, we adopted a different approach to choose the regularization method. Basically, we want a distribution of model parameters which is mostly zero, narrow (allowing only few values close to zero - minimizing small scale oscillations) and has a long tail (allowing few values far from zero - large peak sizes). Minimizing the L_2 norm of the model parameters, as in the zeroth- or higher-order Tikhonov regularizations assumes a Gaussian distribution of model parameters. Solutions with model parameter distributions closer to Gaussian are therefore preferred. The Gaussian distribution does, however, not fit within the previously stated desired characteristics for the model parameter distribution. A more correct choice would be the Laplace distribution, which can be implemented through an L_1 minimization of the model parameters.

Minimizing the first order differences of the model parameters introduces autocorrelation. Any slopes will, however, still contribute to the norm - favouring solutions where slopes are minimized. This is an undesired feature, since we aim at a solution with sharp boundaries between zero and peak. By minimizing the second order differences of the model parameters instead, we allow solutions with sharp peaks. The solution, including minimization of the second order differences of the L_1 norm of model parameters is found from Equation 5.13,

$$\boldsymbol{m} = (\boldsymbol{G}^T \boldsymbol{W}^d \boldsymbol{G} + \alpha^2 \boldsymbol{D}_2^T \boldsymbol{W}^m \boldsymbol{D}_2)^{-1} \boldsymbol{G}^T \boldsymbol{W}^d \boldsymbol{d}^{\text{obs}}.$$

Figure 7.2(g) shows the resultant sheet current density profile, found with $\alpha^2 = 6.4 \cdot 10^{-15}$. Introducing the regularization on model parameters, changes the ratio between the data and model regularization term in Equation 5.13, and we therefore need to adjust α^2 accordingly. Changes in model parameter distribution allows us to increase the dampening (α^2 increased from $3.6 \cdot 10^{-27}$ with L_2 to $6.4 \cdot 10^{-15}$ with L_1) of the small scale oscillations while keeping the main peak and a variance ratio ($6.46 \cdot 10^{-6}$) closer to the least squares solution.

Choosing the best regularization method

Most of the presented regularization approaches return data fits, describing almost all of the variance in the measurements (see Table 7.1). The low variance ratios are supported by residuals of less than 1 nT (not shown), corresponding to approximately 0.5% of the signal strength. We argue, however, still to apply the more complicated L_1 model regularization including a Huber weighted data misfit measure based on three arguments:

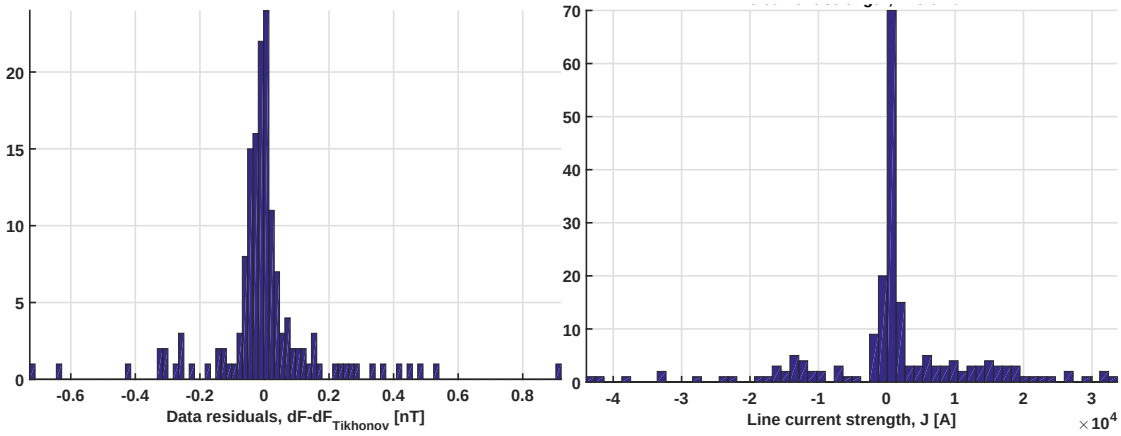

(a) Data residual distribution **(b)** Model parameter distribution

Figure 7.3: (a) Distribution of data residuals from orbit 6248 on the 4th of January 2015 and (b) the distribution of model parameters for orbit 3334 on the 28th of June 2014.

1. Non-Gaussian distribution of data residuals. Figure 7.3(a) shows the distribution of the data residuals for orbit 6248 on the 4th of January 2015, estimated from the Tikhonov regularization approach. The distribution clearly differs from Gaussian, arguing the need for implementation of the Huber weighted data misfit measures, dealing with non-Gaussian errors (outliers).

2. Non-Gaussian model parameter distribution. Figure 7.3(b) shows the distribution of the model parameters for orbit 3334 on the 28th of June 2014, estimated by minimization of the L_1 norm of the second order differences of the model parameters including a Huber weighted data misfit measure. The distribution reveals an equally clear deviation from a Gaussian distribution. Minimizing the L_2 norm of the model parameters is therefore not an adequate assumption. The distribution is more consistent to implementation of an L_1 regularization scheme.

3. Non-Gaussian model parameter distribution. Figure 7.3(b) shows the distribution of the model parameters for orbit 3334 on the 28th of June 2014, estimated by minimization of the L_1 norm of the second order differences of the model parameters including a Huber weighted data misfit measure. The distribution reveals an equally clear deviation from a Gaussian distribution. Minimizing the L_2 norm of the model parameters is therefore not an adequate assumption. The distribution is more consistent to implementation of an L_1 regularization scheme.

4. Increased regularization does not contribute significantly to the processing time.

The arguments are supported by a generally better description using the L_1 norm solution, with a mean variance ratio of $120 \cdot 10^{-6}$ compared to the L_2 norm solution with a mean variance ratio of $400 \cdot 10^{-6}$. The mean variance ratio is found considering the mean variance ratios of 1000 *Swarm* Alpha orbits (orbit nos. 6142 to 7142) between the 28th of December 2014 and the 3rd of March 2015. The low mean variance ratio furthermore shows that a good data fit is found, not only for the specific above presented orbit, but for all tested orbits, at least on average. All variance ratios are found less than $820 \cdot 10^{-6}$ for the L_1 norm solution and

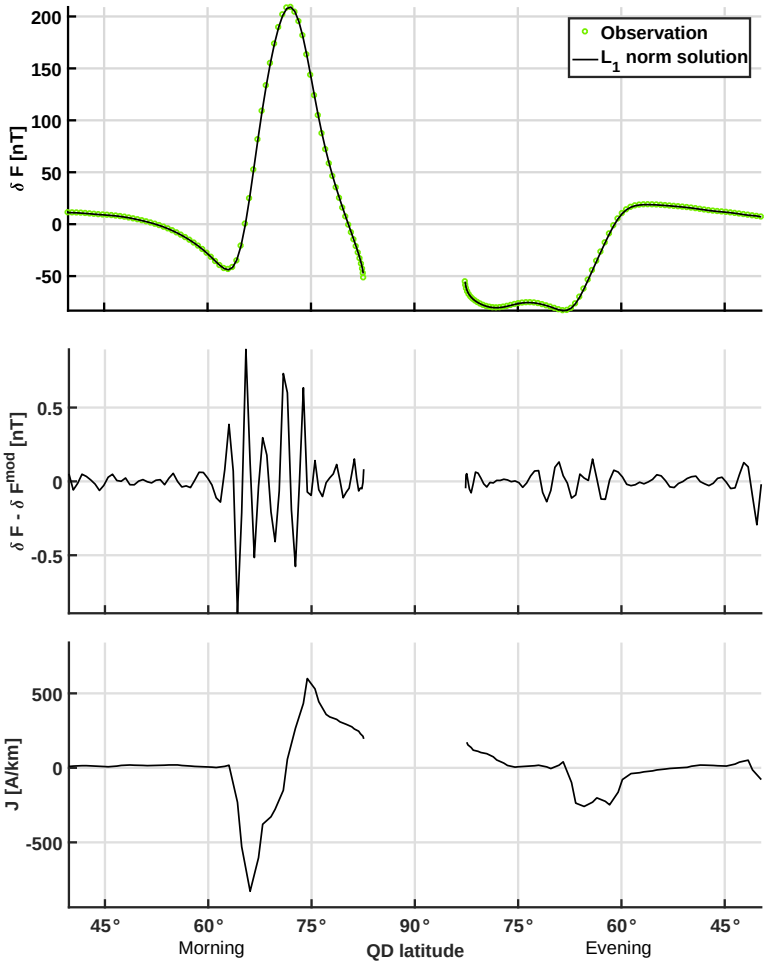

Figure 7.4: As Figure 7.1, but applied to *Swarm* Alpha orbit 3334 on the 28th of June 2014 13:42 to 14:08 UT. A positive current is in the direction from midnight to noon.

$2000 \cdot 10^{-6}$ for the L_2 norm solution. Thus, the method works very well even for the worst data fit. The largest variance ratios are mainly found for quiet orbits, where small errors results in a large increase in the signal to noise ratio.

Minimization of the L_1 norm of the model parameters will, in conclusion despite the good modelling results of the L_2 norm solution, provide the most reliable estimation of the model parameters, along with slightly lower variance ratios. The L_1 norm solution is therefore preferred. All results from here-on are presented using the minimization of the L_1 model norm of the second order differences of model parameters and a Huber-weighted data misfit measure, with the solution given by Equation 5.13. Figure 7.4 shows the results applying the preferred L_1 norm regularization method equal to the one presented in Aakjær et al. [2016] for *Swarm* Alpha orbit 3334 on the 28th of June 2014 (corresponding to results presented in Figure 7.2). The sheet current densities are presented with a positive current towards the sun. Observations are presented in green and the model fit of the magnetic field signature δF in black (top panel), corresponding model residuals in the middle panel, and the sheet current density, $\boldsymbol{J}$, in the bottom panel; all as a function of QD latitude.

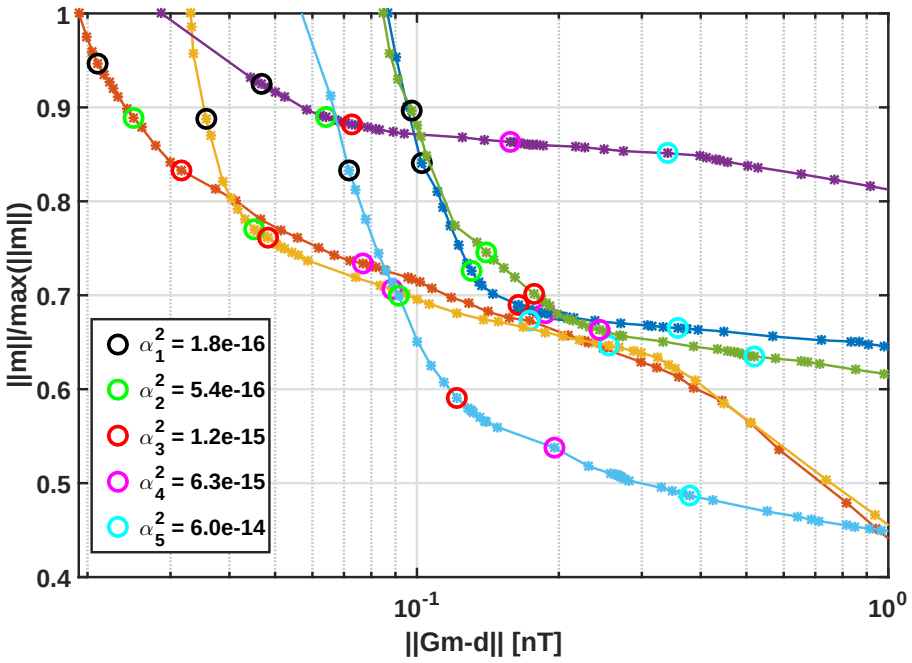

Figure 7.5: Normalized L-curve for six individual *Swarm* Alpha orbits: 200 (orange), 2000 (yellow), 3334 (dark blue), 6248 (light green), 6493 (light blue) and 8000 (purple), chosen to represent both disturbed and quiet times. Information about the orbits are given in Table 7.2. The L-curve compares individually normalized norm of the model parameters with data misfit and α^2 for six individual orbits, with α^2 logarithmically spaced in $[10^{-16}\ 10^{-12}]\mathrm{nT} \cdot \mathrm{A}^{-2}$. From Aakjær et al. [2016].

7.3 Estimating the regularization parameter and sensitivity to small scale variations

L_1 model norm minimization of the second order along track differences of model parameters requires specification of a regularization parameter, α^2 and ϵ. ϵ ensures a non-singular solution at $j_k = 0$ in the Ekblom measure. This is insensitive to orbit specific measures, and set to 0.1. Correct estimation of α^2, however, plays a central role in regularized inverse problems, with effects already shown for the 1D SECS method in Sections 6.2 and 6.4. The choice of α^2 is therefore very important, also for the line current method. α^2 can be estimated as described in Section 5.2 from an L-curve, showing the individually normalized norm of model parameters as a function of data misfit and α^2. The L-curve, equally presented in Aakjær et al. [2016] for six individual *Swarm* Alpha orbit nos. 200 (orange), 2000 (yellow), 3334 (dark blue), 6248 (light green), 6493 (light blue) and 8000 (purple), are given in Figure 7.5 representing both disturbed and quiet times. α^2 is logarithmically spaced in $[10^{-16}\ 10^{-12}]\ \frac{\mathrm{nT}^2}{\mathrm{A}}$, and information about crossing times and Kp level is given in Table 7.2. Five values of α^2 are highlighted as coloured circles to show the effect of changes in α^2 on the complexity of the model parameters: $\alpha_1^2 = 1.8 \cdot 10^{-16}\ \frac{\mathrm{nT}^2}{\mathrm{A}}$ (black), $\alpha_2^2 = 5.4 \cdot 10^{-16}\ \frac{\mathrm{nT}^2}{\mathrm{A}}$ (green), $\alpha_3^2 = 1.2 \cdot 10^{-15}\ \frac{\mathrm{nT}^2}{\mathrm{A}}$ (red), $\alpha_4^2 = 6.3 \cdot 10^{-15}\ \frac{\mathrm{nT}^2}{\mathrm{A}}$ (purple) and $\alpha_5^2 = 6.0 \cdot 10^{-14}\ \frac{\mathrm{nT}^2}{\mathrm{A}}$ (blue).

The optimal choice in α^2 is found as the corner value of orbit 6493 (light blue), $\alpha_3^2 = 1.2 \cdot 10^{-15} \frac{\mathrm{nT}^2}{\mathrm{A}}$ (marked by the red circle). This value provides a good balance between the

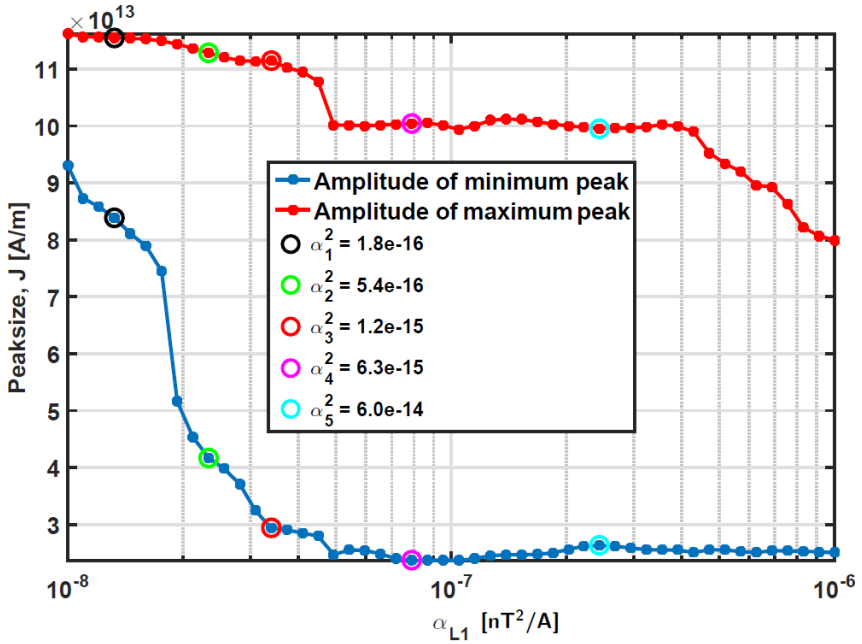

Figure 7.6: Peaksize as a function of α for orbit 6248 on the 4th of January 2015. Five different α^2 values are highlighted for easier comparison with Figure 7.5.

model misfit and complexity. Visual inspection of the data fit and current profile, however, reveals remaining unwanted small scale oscillations outside the polar region. We therefore increased the damping slightly to obtain the final choice of $\alpha^2 = 6.4 \cdot 10^{-15} \frac{\text{nT}^2}{\text{A}}$, corresponding approximately to the purple value ($\alpha_4^2 = 6.3 \cdot 10^{-15} \frac{\text{nT}^2}{\text{A}}$).

Our aim with the regularization is minimization of the non-physical complexity of model parameters without compromising the peak value and thereby the estimate of the western and eastern electrojet strength. We have therefore compared the L-curve with an analysis of the amplitude of the maximum and minimum peak with changing α^2. The amplitude of the minimum (blue) and maximum (red) peak, is given in Figure 7.6 for orbit 6248 (light blue) as a function of α^2 with five highlighted values, corresponding to the highlighted circles of Figure 7.5. The maximum peak corresponds to the amplitude of the eastward electrojet, and the minimum peak to the amplitude of the westward electrojet. The decrease in amplitude is especially rapid for the amplitude of the WAEJ in the low α^2 region, where large non-physical oscillations (as seen in the unregularized least squares solution of Figure 7.2 (a)) are damped by the increasing α^2 value ($\alpha_3^2 = 1.2 \cdot 10^{-15} \frac{\text{nT}^2}{\text{A}}$) and onwards. This decrease is slowed considerately for larger damping, with only little change in amplitude between α_3^2 and α_4^2. We therefore conclude that an increase in α^2 from α_3^2 to α_4^2 to avoid the small scale oscillations can be done without or with only little loss in physical signal.

It is important to note that the choice in α^2 will not only depend on regularization norm but also number of observations, since changing the size of $\boldsymbol{G}$ also affects the weight between the two terms in the parenthesis of Equation 5.13 and thereby the choice in α^2. We therefore need to be aware that orbits containing large data gaps might be over-damped by the common choice in α^2. Applied to *Swarm* data, this is, however, not of great concern.

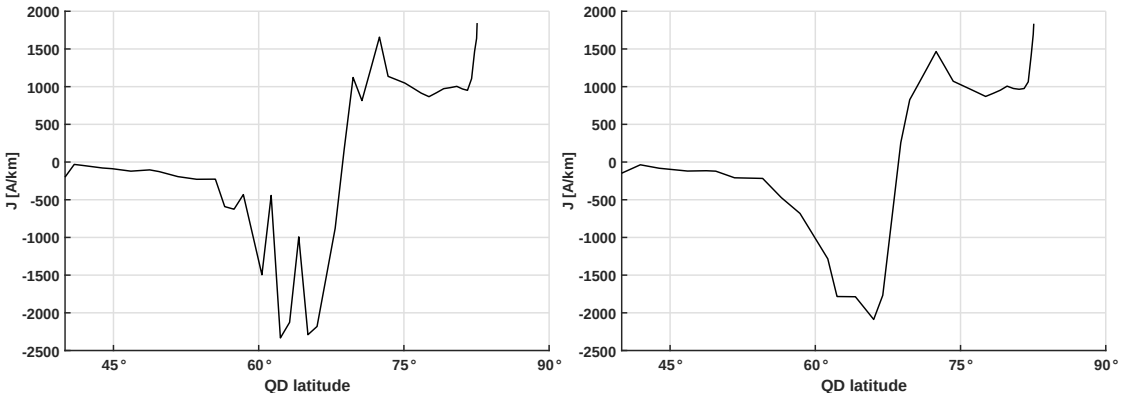

(a) $\alpha^2 = 6.4 \cdot 10^{-15}$ $\frac{\mathrm{nT}^2}{\mathrm{A}}$ **(b)** $\alpha^2 = 1.69 \cdot 10^{-14}$ $\frac{\mathrm{nT}^2}{\mathrm{A}}$

Figure 7.7: Sheet current densities for the 6th of November 2001 estimated with two different regularization parameters.

Individual adjustment of regularization parameters with visual interpretation of model misfit is not possible when applied in an automated algorithm. We therefore need a robust method, working for all (or almost all) orbits with a minimum of adjustments. Based on an almost constant placement of α_3^2 (red circle) presented in Figure 7.5, we conclude that the model is insensitive orbit specific variations such as disturbance level and that a common choice in α^2 is possible. All investigations in regularization parameter has been performed on *Swarm* data. Adjustment for application to CHAMP data might be needed. Figure 7.7 shows an example for the 6th of November 2001 with the same regularization parameter of Swarm data and with a slightly increased damping ($\alpha^2 = 1.69 \cdot 10^{-14}$). This test concludes that further investigation in the regularization parameter. The sensitivity of small variations in input data is further explored by an inter-satellite comparison of 1000 orbits from *Swarm* Alpha and Charlie, ranging from orbit no. 3000-4000 over a period between the 6th of June 2014 18:41 UT and the 11th of August 2014 00:47 UT. The comparison exposed that Charlie is able to describe 97% of the variance from Alpha. The low variance ratio supports the conclusion based on the regularization parameter analysis, of insensitivity towards small changes in input data, indicating a robust minimum for the inverse, and thereby a robust estimate of the model parameters.

Date	Orbit	Kp	time range	MLT
05.12.2013	200	1^-	15:14-15:40	14:32
02.04.2014	2000	1^+	12:26-12:52	14:50
28.06.2014	3334	3^-	13:42-14:08	19:26
04.01.2015	6248	4^-	13:37-14:03	14:26
20.01.2015	6493	0^+	12:38-13:04	12:59
28.04.2015	8000	1^-	15:23-15:49	16:36

Table 7.2: Orbit information for the orbits used in Figure 7.5.

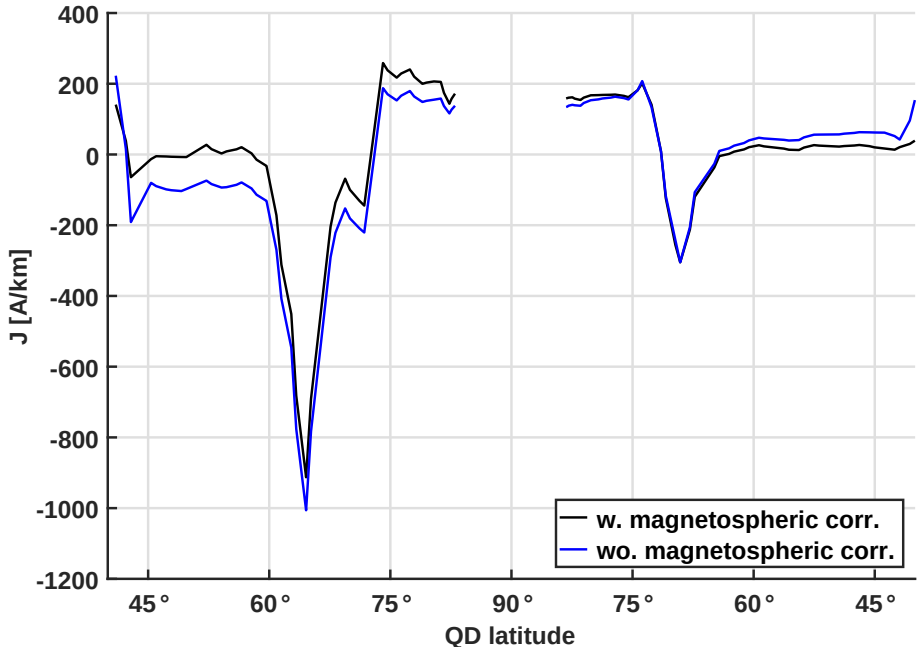

Figure 7.8: Sheet current densities as a function of QD latitude, estimated with (black) and without (blue) the magnetospheric correction applied for orbit 6248 on the 4th of January 2015 from 13:37 to 14:03 UT.

The time resolution of the CHAOS magnetospheric model is given by that of the hourly mean values of the *RC* index used to parametrize the ring current. The real currents may, however, change faster. We therefore need to be aware that the applied magnetospheric correction may be imperfect. In order to further investigate the effect of signatures from non-ionospheric origin, we have carried out tests of our modelling scheme with and without the magnetosphere correction applied. This tells us how possible non-removed magnetospheric signatures might map into the estimated sheet current density. Figure 7.8 shows the result for the moderately disturbed ($Kp = 4^+$) *Swarm* Alpha orbit 6248 on the 4th of January 2015. The black curve shows the results with magnetospheric correction applied, and the blue curve, without. We find that applying the correction does not affect the position or width of the inferred auroral electrojet currents. The model differs primarily in a long wavelength trend, consistent with the finding of Stolle et al. [2016]. We furthermore find that the non-corrected current distribution has non-zero sheet current densities in the low latitude regions, where no currents are expected. This is not the case when the magnetospheric correction is applied. Despite the possibility of an imperfect correction, we conclude that the method is capable of dealing with small contaminations of non-ionospheric sources.

7.4 Applying rotation of the line currents along constant QD latitude

The previous results have been presented with the assumption of line currents being perpendicular to the satellite track. To avoid a systematic underestimation of the line current strengths, we now apply the rotation along constant magnetic latitude, described in Equation 4.12 on page 38. This changes the direction of a positive current, such that positive indicates an

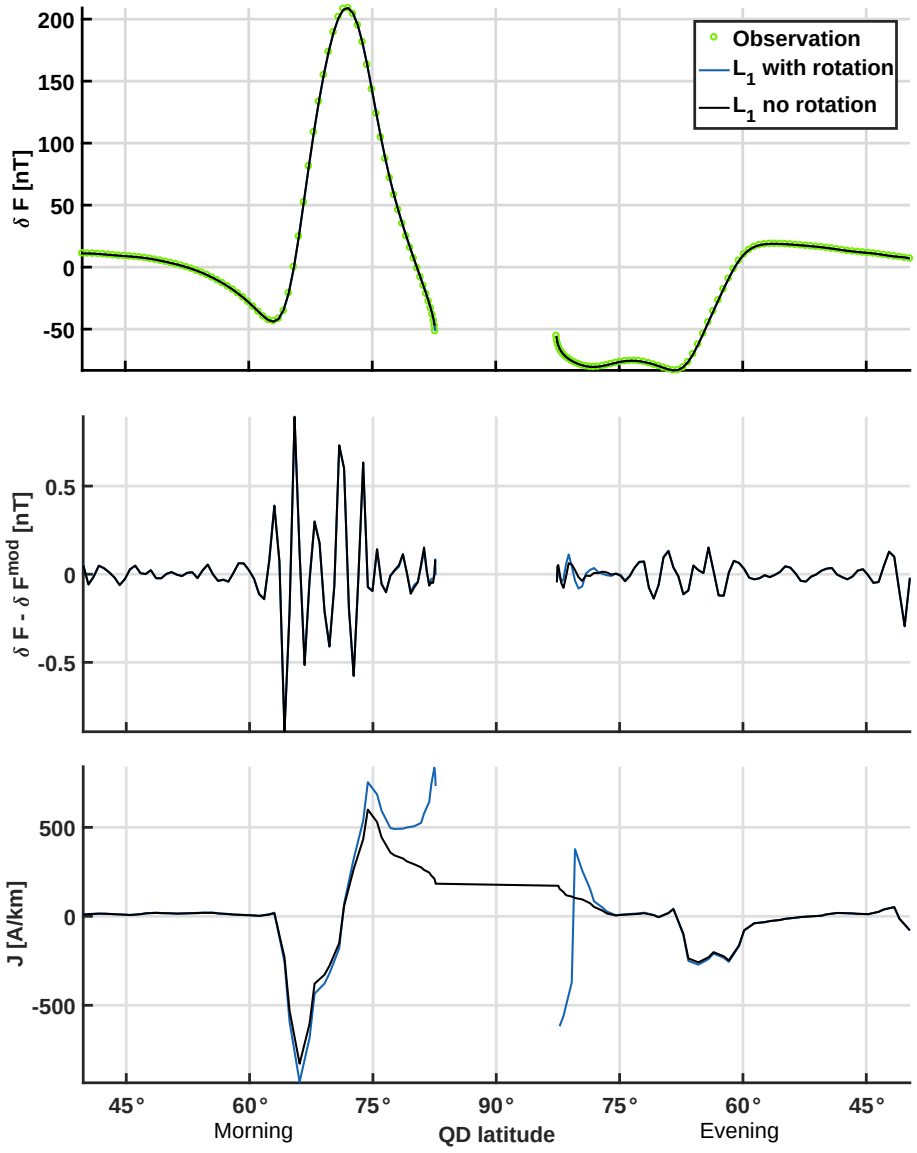

Figure 7.9: As figure 7.4, with (blue) and without (black) rotation applied for *Swarm* Alpha orbit 3334 on the 28th of June 2014.

eastward current, and negative, a westward current. Figure 7.9 shows an example with (blue) and without (black) the rotation for orbit 3334 on the 28th of June 2014, corresponding to the results presented in Figure 7.4 on page 87. The change in sign for the rotated currents is suppressed in Figure 7.9 to enable better comparison with the non-rotated currents.

The model fit, described by the top two panels, shows no real changes in sheet current densities (bottom panel) outside the polar region, and only small differences in the polar cap misfit (middle panel), undetectable in the model fit (top panel). Larger changes are, however, found in the auroral oval region $(60^\circ$ to $75^\circ)$ of the sheet current densities. The rotated currents are, as expected, found stronger in the polar regions, especially the WAEJ peak in the morning sector is affected. The effect of the rotation will be different for each orbit, and determined

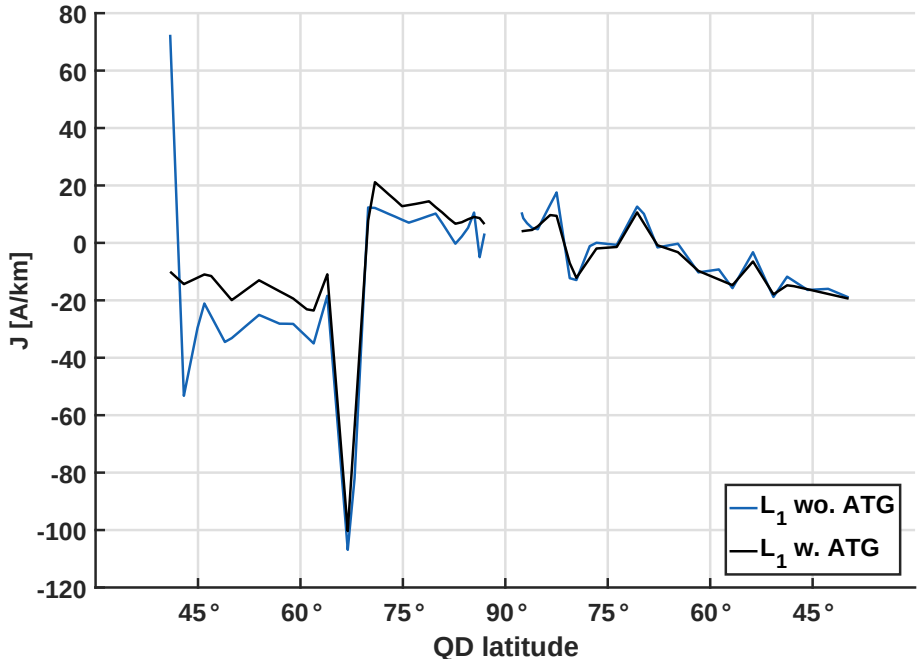

Figure 7.10: Sheet current densities with (black) and without (blue) ATG function applied for orbit 6450 on the 17th of January 2015.

by the satellite track in a QD coordinate system. The rotation also brings along instabilities in the polar cap region, presented by the non-physical spikes in sheet current densities around $\pm 80°$, consistent with the prediction of largest effects in the polar cap region. The instability is limited by the truncation of rotation, presented in Section 4.1. Inclusion of the rotation is, despite the instabilities in the polar cap region, preferred due to a physically more correct geometry of the currents in the auroral oval.

Despite the evidence that an imperfect magnetospheric correction does not alter the position and strength of the auroral electrojets, we have applied the along track first differences, approximating the *along track gradient* (ATG), of the magnetic input data to remove any remaining long term magnetospheric contamination. The result of the sheet current density with (black) and without (blue) the ATG applied is given in Figure 7.10 for orbit 6450 on the 17th of January 2015. Expectably, no significant changes are found to the peak position and strength. Changes are mainly found in lower latitude regions between $45°$ and $60°$ QD latitude, seen as minor smoothing of small scale oscillation outside the polar region. A series of tests, shows that changes due to application of ATG are mostly present during low activity periods, while highly disturbed orbits disguises the possible effect of the magnetospheric contamination.

As a final indication of the robustness of the method, we applied the method to all 10 years of CHAMP data along with 2 years of data from *Swarm* Alpha and Bravo for both the Northern and Southern Hemisphere. From these 148004 pole crossings, 189 ($\sim 0.13\%$) unstable orbits (99 on the Northern Hemisphere and 90 on the Southern Hemisphere) are identified as orbits with physically unrealistic peak values ($> 10^4$ A/km). The high performance ratio (99.87%) is concluded satisfactory for automatic implementation. The unstable orbits are all CHAMP orbits, which reveals a high possibility of an underestimated regularization parameter

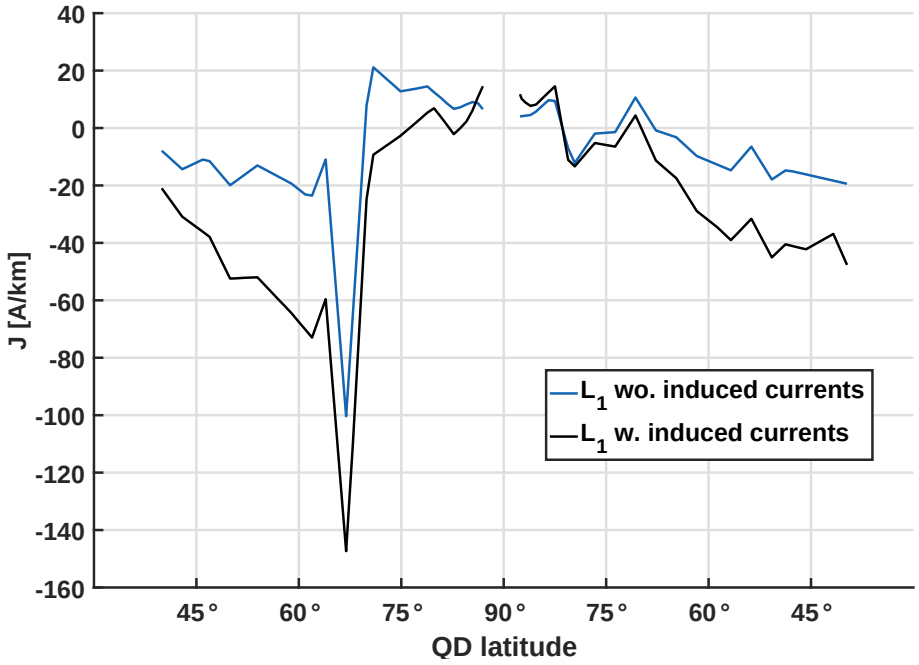

Figure 7.11: Sheet current densities, with (black) and without (blue) induced currents for orbit 6450 on the 17th of January 2015.

for CHAMP data. However, further investigations into the specific orbits is needed to provide a satisfactory reason for the instability.

Effect of induced currents

The effect of secondary Earth-induced currents have until now been ignored. Induced currents are implemented by placing a secondary layer of line currents at a depth of 250 km, as described in Section 4.1. Induced currents are of lesser importance at satellite altitude, due to the large distance to the currents, and we do therefore not expect large effects of the implementation of these in the model.

Figure 7.11 shows the sheet current density as a function of QD latitude with (black) and without (blue) including induced currents when applied to orbit 6450 on the 17th of January 2015 (Kp of 0^+). The figure shows how implementation of induced currents increases the instability in the inversion, shown by the undesired trend for non-polar regions. We have therefore decided not to include induced currents in further applications of the method. The effect of not inluding induced currents will be an underestimation of the ionospheric currents, also seen in the figure.

7.5 Inter model comparison and discussion on their differences

Chapter 6 and the first sections of the present chapter presents two very different methods for determining the auroral electrojet system. One represents the complicated, more physically correct set-up (1D SECS), and the other a simple, yet robust estimate (LCM). We will now

compare the two methods to reveal the strengths and weaknesses of them both.

The 1D SECS method provides, for the 40% days without strong 2D effects, an accurate description of the auroral electrojet system. The associated FACs were, however, somewhat flawed from an incorrect determination of adjustable parameters (d_{mod}, d_{obs}, $d\delta$, ε_c, ε_d, α_c^2 and α_d^2 described in Chapter 6). For the remaining 60% of the days, we were not able to obtain an acceptable model fit, and the method can therefore not be applied. With the large amount of inter-dependent adjustable parameters and unresolved 2D effects, we were unfortunately not able to obtain robust implementation of the method.

The LCM on the other hand provides a robust method for estimating the equivalent current system with a very high degree of data fit. If the two methods were to be compared on the performance level alone (measured on the percentage of working orbits and variance ratio of model fit), the choice would be very clear. The line current method further exploits the advantage of using the scalar field residuals as input which are less contaminated by other sources (such as FACs) compared to the full vector observations. Since FACs, at satellite altitude, are order of magnitudes larger (in situ measurements) than the signal of the auroral electrojet system, even small contaminations can produce large deviations. The LCM does, however, not provide a direct measure of the FACs.

All in all, the choice came down to the desired automatic estimation of the auroral electrojet system, and the possibility of providing a very large dataset (CHAMP and *Swarm* orbits) for statistical interpretation of the auroral electrojet system. We have therefore decided to proceed with the line current model.

Comparing the line current model with other estimates of the auroral electrojet system

Even though we do not choose the 1D SECS method as our preferred model for this study, it provides a valuable reference frame to which the line current model can be compared against. To ensure that possible discrepancies are not due to our implementation of the method, we compare with results provided by Liisa Juusola [Juusola, 2016]. The orbits are chosen to enable comparison with the 2D SECS method from IMAGE[1] ground observations. The results of the LCM are furthermore compared with the *intensity model* (IM) presented by Vennerstrom and Moretto [2013], briefly explained in Chapter 1. Results of the IM is provided by Ashley Smith [Smith, 2017]. The IM is only compared on position since their peak intensity measurements are not directly comparable.

Figure 7.12 and 7.13 shows the auroral sheet current densities estimated by the divergence-free part of the 1D SECS method (a), LCM (b) and the 2D SECS method (c) for two *Swarm* Alpha orbits. The two orbits, represent a western electrojet crossing on the 1$^{\text{st}}$ of January 2015 (orbit 6194) at 01:10 to 01:36 UT (Figure 7.12) and an eastern electrojet crossing on the 4$^{\text{th}}$ of January 2015 (orbit 6248) at 13:37 to 14:03 UT (Figure 7.13). Both crossings were during active magnetic conditions, with Kp values of 2^+ and 4^-, accordingly. Figure 7.12(a)

[1] IMAGE is an array of 35 magnetometer stations with the prime objective to study moving two-dimensional current systems such as the auroral electrojet system IMAGE [2017]

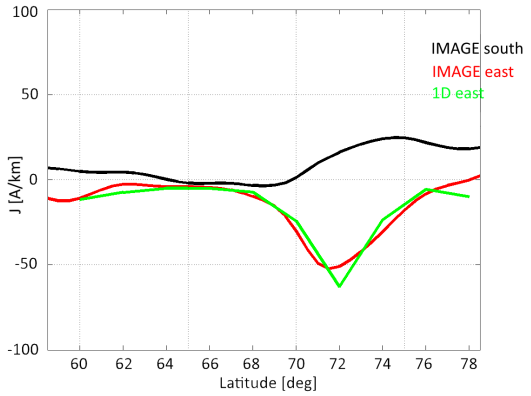

(a) Source: Juusola [2016]

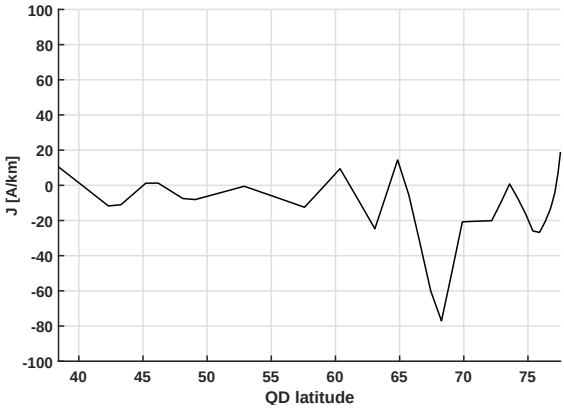

(b) Source: Juusola [2016]

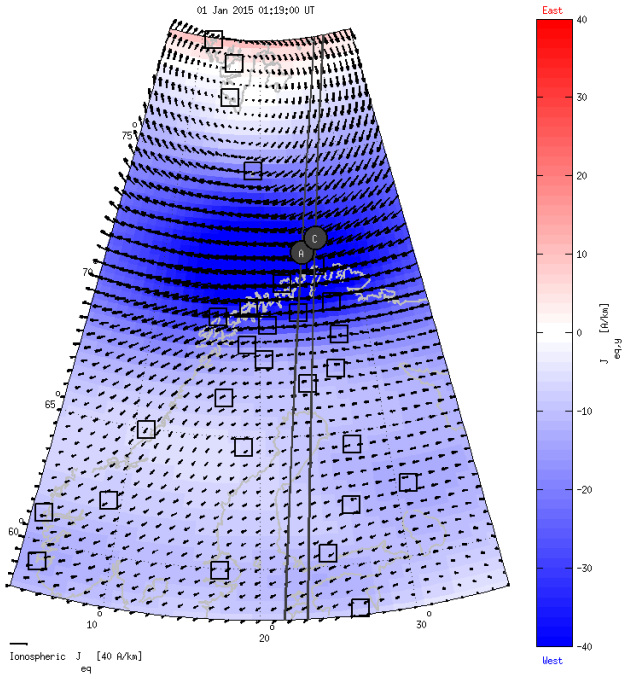

(c)

Figure 7.12: Auroral sheet current densities for a western electrojet crossing, estimated by (a) 1D SECS method. The plot is provided by Liisa Juusola [Juusola, 2016], (b) LCM and (c) 2D SECS method, also provided by Liisa Juusola [Juusola, 2016] for the 1st of January 2015 from 01:10 to 01:36 UT (orbit 6194). The polar crossing was during relatively quiet conditions with a Kp value of 2^+. The green line in (a) marks the 1D SECS solution, the red, the estimated 2D SECS solution along the satellite track, and the black, the magnetic field residuals. (b) is found using a minimization of the second order difference of the L_1 norm including a Huber weighted data misfit measure. The last figure (c) gives the full 2D SECS solution with the satellite track of A and C marked by the black lines, and the sheet current density given in colour. Red marks an eastern current, and blue, a western current, and black arrows the strength and direction of the sheet currents. A reference arrow is printed in the bottom left corner of the figure, and squares marks magnetometer stations. Estimates given in (a) and (b) are based on *Swarm* A observations of the magnetic residual field.

Date	Position				Strength		
	1D	2D	LCM	IM	1D	2D	LCM
01.01.2015	$69°$	$69°$	$69°$	$69°$	-65 A/km	-55 A/km	-77 A/km
04.01.2015	$68°$	$69°$	$68°$	$67°$	385 A/km	215 A/km	223 A/km
06.11.2001	$68°$	$67°$	$66°$	$65°$	-3350 A/km	-2931 A/km	-2090 A/km
24.01.2015	$76°$	$76°$	$75°$	$70°$	219 A/km	83 A/km	106 A/km

Table 7.3: Position (QD latitude) and strengths of the eastward and westward electrojet estimated from the 1D SECS, 2D SECS, LCM and IM method (position only) for 4 different orbits.

gives the 1D SECS solution as the divergence-free part of the solution $\boldsymbol{J}^{df}$ described by Equation 4.25 in green, and the 2D SECS solution from IMAGE ground observations along the satellite track in red. The magnetic field residuals are given as reference in black. (c) gives the full 2D SECS estimation of the sheet current densities from ground observations in colour, with the satellite track of Alpha and Charlie marked by the black lines. Estimates based on the intensity model are given in Appendix D, Figure D.1 and D.2. Estimates of peak position and strength for the three methods are provided in Table 7.3 along with estimates for two additional orbits (Appendix D, Figure D.3-D.6). All positions have been converted to QD latitude for ease of comparison. The two additional orbits present a westward and eastward pole crossing with orbit nos. 7383 (CHAMP) and 6254 (*Swarm* Alpha) on the 6$^{\text{th}}$ of November 2001 04:47 to 05:13 and the 24$^{\text{th}}$ of January 2015 11:48 to 13:22 UT. The regularization parameter α^2 has been slightly increased for the CHAMP crossing to $\alpha^2 = 1.69 \cdot 10^{-14}\ \frac{\text{nT}^2}{\text{A}}$ Peak values and positions of the 1D and 2D SECS methods are estimated from the figure alone.

The position of the eastern and western electrojet is found to agree within two degrees QD latitude. A two degree separation is within the expected error of margin due to the quite large model spacing ($2°$) of the 1D SECS method. The peak sheet current densities show larger inter-model discrepancies. The largest differences between the LCM and the two SECS estimates are found with the satellite based 1D SECS estimate from the 24$^{\text{th}}$ of January 2015, where a discrepancy of more than 100% of the LCM signal strength is found. The ground based 2D SECS estimates are in general found in better agreement, with differences between 28.6% (01.01.2015 and 06.11.2001) and 3.5% (04.01.2015) of the signal strength. In conclusion we find that the LCM estimates from the four tested orbits are not in disagreement with the results of peak position and strength estimated by the three other methods.

Summary of the LCM application to satellite magnetic data

The line current model has proven to provide a robust measure of the auroral electrojet system, both in terms of choice in regularization parameter and handling of possible data noise, important for automatic implementations. A simple test on CHAMP data revealed, however, the need for further investigations on regularization parameter. Through a test of a series of regularization methods, we have argued the need for implementing a rather complex regularization method (Minimization of an L_1 model norm of the second order differences of model parameters along with a Huber-weighted data misfit measure), along with along track gradient as input data. We have shown, how the LCM provides data fits for 1000 orbits with very high

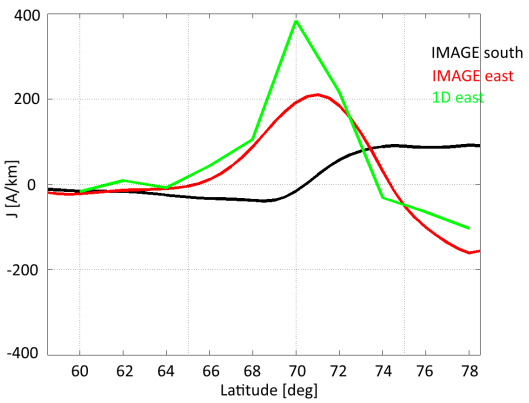

(a) Source: Juusola [2016]

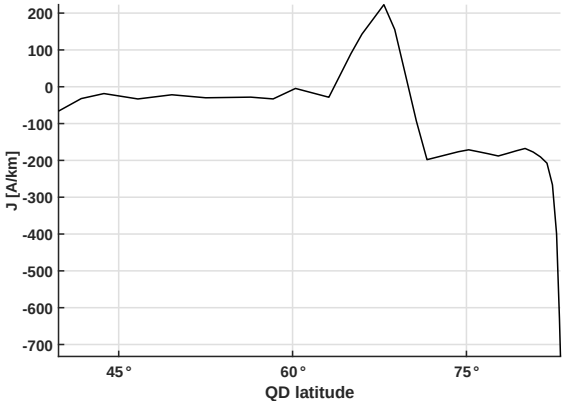

(b) Source: Juusola [2016]

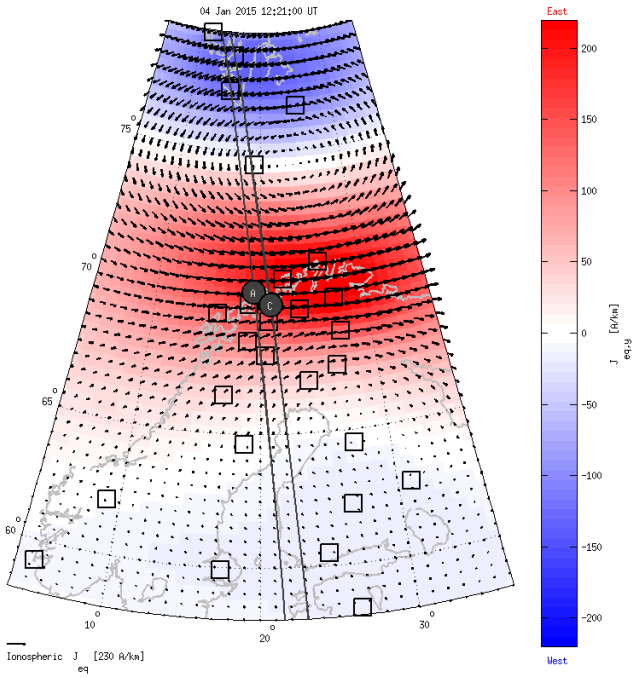

(c)

Figure 7.13: As Figure 7.12, for an eastern electrojet crossing on the 4th of January 2015 (orbit 6247) from 13:37 to 14:03 UT. The polar crossing was during moderately disturbed magnetic activity with a Kp value of 4^-.

accuracy (mean variance ratio of $120 \cdot 10^{-6}$), indicating a reliable estimate of the sheet current densities. Comparison with results of the 1D and 2D SECS method, furthermore revealed that the estimates of peak position and strength is not in disagreement with other model results. Based on the very high variance and performance ratios (99.87% of the LCM) and the desire of automatic implementation, we prefer to continue our investigations with the LCM over the 1D SECS method.

Chapter 8

Statistical analyses of the auroral electrojet system estimated from satellite observations

Statistical investigations provide a powerful tool for general investigations of the currents [e.g. Friis-Christensen et al., 1985b; Weimer, 2001; Vennerstrom and Moretto, 2013; Weimer, 2013; Laundal et al., 2016b]. Most of the geomagnetic activity is powered by energy input from the solar wind. With the polar ionospheric region being where most of the solar wind energy is dissipated, it is important to study and understand how the auroral electrojet system reacts to various conditions of solar activity. The solar wind interaction with the magnetosphere can at any given moment be described by a simple set of plasma parameters, concerning the solar wind, such as it's density, it's velocity and it's direction of the magnetic field. One well established indicator for geomagnetic activity, is the *Kp* index, described in Section 2.6. The following chapter show a few examples of possible applications to the sheet current density dataset, determined by the LCM ATG model including rotation of the line current along constant QD latitude, applying a minimization of an L_1 norm of the second order differences of model parameters along with a Huber-weighted data misfit measure regularization approach (see Section 7.2 for further detail on the model).

8.1 Space-time development of auroral electrojets in a three week period around Equinox

In Aakjær et al. [2016] we presented the temporal development of the current system around the Saint Patrick's day storm 2015 along with the same period for the preceding year, 2014, measured by *Swarm* Alpha. This section reports a similar analysis based on an updated version of the line current model. The results in the article are found without the application of ATG to the input data and rotation of the line currents along constant QD contours. The specific periods were chosen, because they represent equinox conditions. At equinox, both hemispheres are affected in the same way, with equal amount of sunlight and darkness, giving a period optimal for interhemispherical comparisons. See Section 8.2 for further discussion about the effect of sunlight on the ionospheric currents. Secondarily the periods are chosen to exemplify how the current system acts during both geomagnetic disturbed and quiet times. Plotting the individual orbits next to each other enables investigations of the space-time evolution of the auroral electrojet system, which is not possible, when analysing individual orbits. Figure 8.1

gives the sheet current density (colour) as a function of QD latitude and time for the three week period from the 10th to 31st of March 2014. The example covers a change in MLT by approximately 1.5 hour during the three week period. At QD latitude 60° it shifts from approximately 20:30 to 19:00 on the evening side. The results are presented for the Southern Hemisphere in the bottom panel, and for the Northern Hemisphere in the middle panel. Each plot is divided into an evening sector (19.00 MLT to 20.30 MLT) and a morning sector (07.30 MLT to 09.00 MLT), to distinguish between the westward and eastward electrojet signal. The sign of the current is, as previously stated, negative for a westward current, and positive for an eastward current. The top panel shows the intensity level, represented by the AE and *Kp* index for reference.

The inclination of the satellite orbits creates a gap around the pole, which in geographical coordinates is of constant size since the satellite orbits are oriented after the geographical pole. In QD latitudes, this gap will be of oscillating size, shown in the figure as a white gap around 90°, not to be confused with a zero sheet current density. The resultant sheet current densities reveal an electrojet system confined to the region of the auroral oval, approximately 70° to 80° QD latitude. The strength of the current system should therefore be evaluated within this region.

The results within the polar cap should be treated with care, since the rotation of the line currents in this region may produce unrealisticly large currents. To avoid the largest instabilities in the polar cap, we have truncated the rotation along constant QD latitude (grey area on graph), where the angle between the QD latitude contours and the perpendicular line current is larger than 60°, $\cos\delta > 0.5$, (see Section 7.3 for further description). The currents south of the auroral oval are as expected found very small, but not zero. The largest deviation from zero is found during disturbed periods. As stated in the top panel, and by the estimated relatively weak sheet current densities, the period presents quiet times, with Kp values below 4. There is, however, found three moderately active periods around the 13th, 21st and between the 25th and 28th of March 2014. The visual agreement between geomagnetic activity (Kp and AE) values and the corresponding sheet current density strengths is in general good.

The space-time development provides a good measure for studying the development of the intensity of the current system during a storm event (disturbed conditions). An example is the period around the 13th of March, where we see a sudden intensification of the current, corresponding with an increase in both AE and *Kp* index. The intensification is accompanied by an equatorward expansion of the auroral oval, presented by a wider band of strong sheet current densities. An event like this is consistent with the onset of a substorm, as described in Section 2.4 [Akasofu, 1964; McPherron, 1991]. This shows, how figures like this, can be used to estimate the identification and progress of storm events. The figure, furthermore, provides, as previously stated, a basis for interhemispheric comparisons. We do not expect a perfect fit between the sheet current densities due to the time difference of approximately 45 minutes between the measurements at different hemispheres. The overall picture is, however, a very good visual correlation between the two hemispheres - strong sheet current densities are found at the same time in both hemispheres.

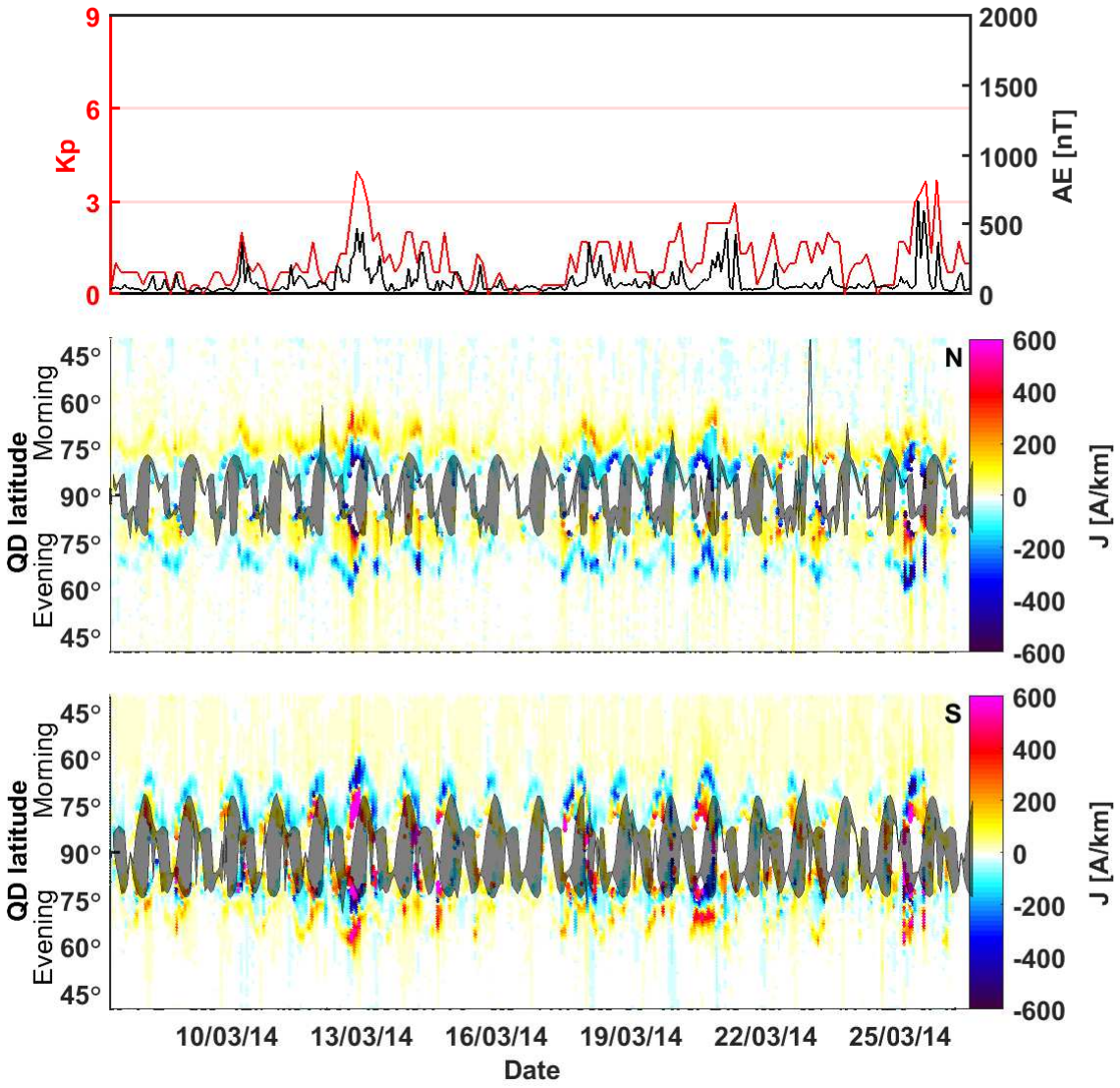

Figure 8.1: Top panel: Kp and AE index for a three week period (8th to 31st of March) around 2014 Equinox. AE is given in black on the left, and Kp in red (right). Middle and bottom panel: space-time development of the sheet current densities (colour) shown as a function of QD latitude and time for the Northern (middle) and Southern (bottom) Hemisphere. Sheet current densities are estimated from *Swarm* Alpha measurements with positive current towards east.

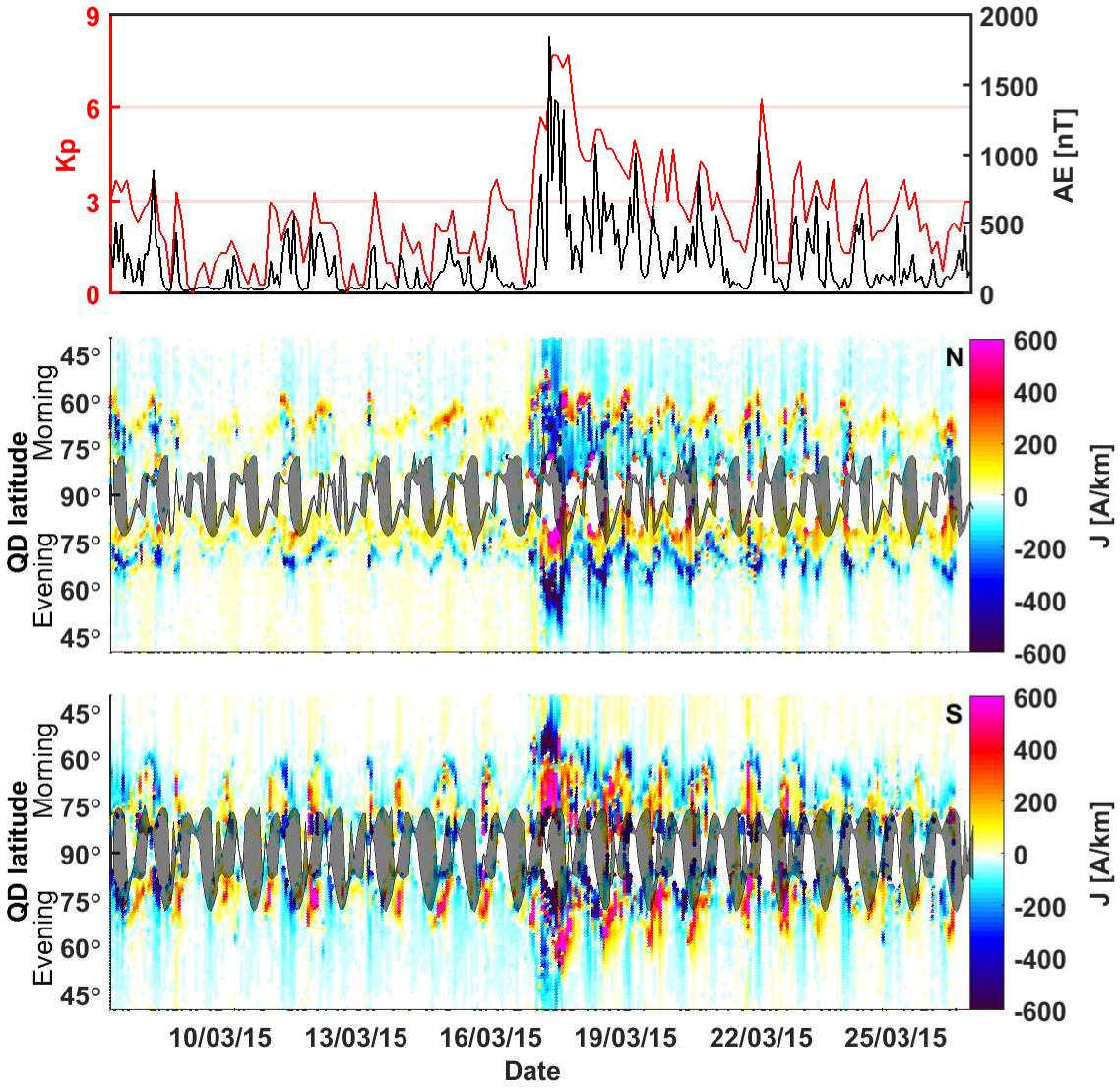

Figure 8.2: Similar to Figure 8.1, for a three week period (8th to 31st of March) around the Saint Patrick's day storm (17th of March) at Equinox, 2015.

An example of a much more disturbed period is given in Figure 8.2. The figure shows the sheet current density (colour) as a function of QD latitude and time for the three week period (10th to 31st of March 2015) around the Saint Patrick's day storm on March 17th 2015 for the Northern (middle panel) and Southern (bottom panel) Hemisphere. The Saint Patrick's day storm, which was the most severe storm of solar cycle 24, lasted for approximately 18 hours with *Kp* values as high as 8^-. The first part of the period, leading up to the storm, is relatively quiet with $Kp < 4$, and only little variation in the sheet current densities are found.

The onset of the Saint Patrick's day storm is marked by a sudden increase in sheet current densities on the 17th of March. The exact time is, however, difficult to determine due to the arrival of a smaller *coronal mass ejection* (CME) prior to the main eruption, clouding the observations in the times leading up to the storm. The intensification of the sheet current densities are accompanied by an expansion of the auroral oval down to approximately $45°$N, indicated by the southward movement of the high intensity region of the sheet current densities. The very large southward expansion of the auroral oval is consistent with aurora observations as far south as France. Higher sheet current densities in the period after the storm reveals how the current system is affected long time after the storm has subsided, without (or only little) southward expansion of the auroral oval seen during the storm.

Inter-hemispherical and AE correlation for a three week period in March 2015

The previous space-time presentation of the sheet current densities does not support a direct comparison between the sheet current density strengths and the well established intensity indicators, such as *Kp* and AE index. The total polar current, J^{tot}, is therefore calculated to enable correlation analysis

$$J^{\text{tot}} = r_I \int_{-50°}^{50°} |\boldsymbol{J}| d\beta \approx \Delta\beta \cdot r_I \sum_k |J_k|. \tag{8.1}$$

β and $\boldsymbol{J}$ follow the same definitions as presented in Section 4.1. Figure 8.3 shows an example of the space-time development of the total polar current (red) for the period presented in Figure 8.2 (10th to 31st of March 2015) together with the corresponding mean AE index (black) for the satellites polar crossing. $\boldsymbol{J}^{tot}$ follows primarily the AE index closely. There are, however periods around the 12th and 15th of March, where the satellite derived index is much lower than the AE index. The AE index is derived across different magnetic local times, and will always present the disturbance level of the most disturbed magnetic local time (often $1-4$ MLT). The satellite derived index depend on the other hand on MLT, and present only the disturbance level of the magnetic local times covered by the satellite tracks. Satellite orbits going through 'quiet' local times will therefore have a lower index value relative to the AE index. The MLT dependence of the electrojet system is elaborated in Section 8.2.

The visual correlation of $\boldsymbol{J}^{\text{tot}}$ and AE is supported by a squared coherence analysis in dependence of frequency, f, and corresponding period, $\mathcal{T} = 1/f$. The AE and total current in the frequency domain ($\boldsymbol{AE}(f)$ and $\boldsymbol{J}^{\text{tot}}(f)$) is determined from a Fourier Transformation. These are then used as input to estimate the coherence between the two datasets as a function of $\mathcal{T}$. The analysis, presented in Figure 8.4, is found considering 400 orbits (7200 to 7799) in the period between 7th of March and 1st of April 2015. The coherence is found between the

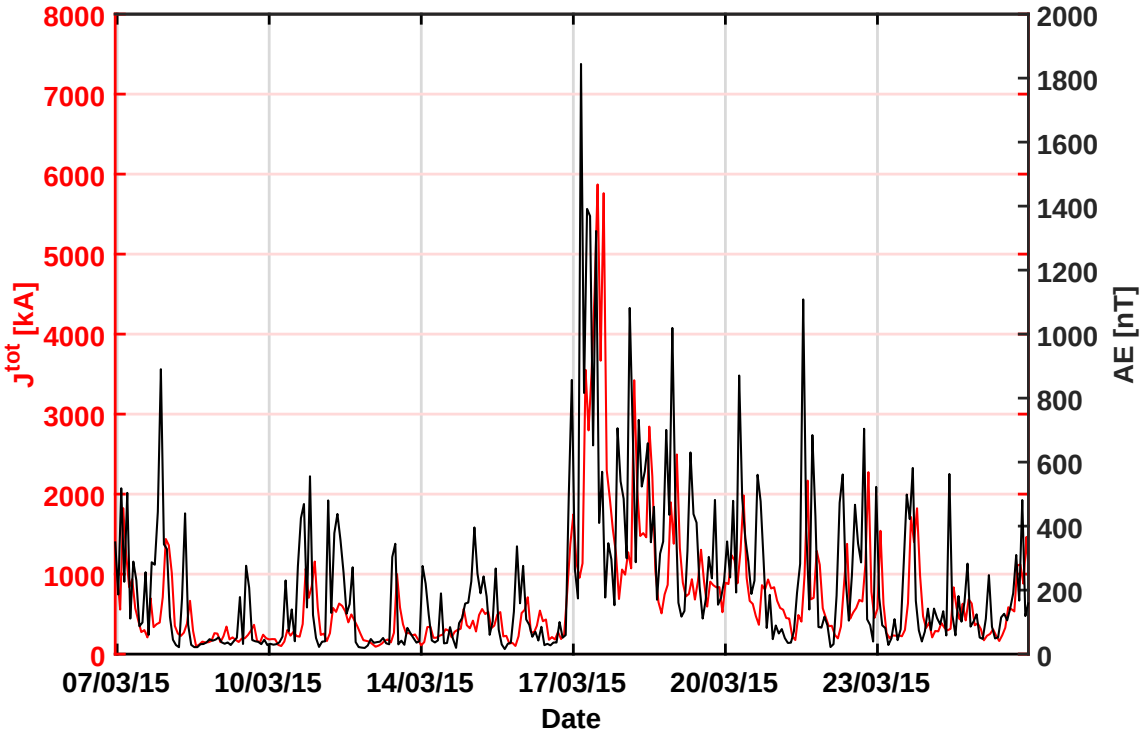

Figure 8.3: Time series of the total ionospheric current, $\boldsymbol{J}^{\text{tot}}$ (left, red) and AE index (right, black) for a period of 400 *Swarm* Alpha orbits (orbit number 7200 on the 7$^{\text{th}}$ of March to orbit 7799 on the 1$^{\text{st}}$ of April) around the Saint Patrick's day storm on the 17$^{\text{th}}$ of March 2015.

AE and the Northern (black) and Southern (red) Hemisphere as a function of, $\mathcal{T}$. Coherence for the Northern and Southern Hemispheres with AE are found very similar with a squared coherence above 0.9 for periods longer than two days. We estimate that a squared coherence above 0.9 supports the conclusion from the visually inspected high correlation between the sheet current densities and the AE index found in Figure 8.2. The blue line in Figure 8.4 gives the interhemispheric squared coherence, representing the correlation between the sheet current densities in the two hemispheres. The coherence is in general a little higher compared to the coherence with the AE index, indicating a clear connection between the currents in the two hemispheres. A more detailed study of the general interhemispherical differences can be found in Section 8.3.

Investigations of the longitudinal differences between *Swarm* Alpha and Bravo

The automatic implementation and robustness of the LCM invites for a new type of index of auroral electrojet intensities. The already established AE index provides a good indicator of geomagnetic activity. Longitudinal dependencies are removed when calculating the index. Figure 8.3 and 8.4 shows how the total ionospheric current, $\boldsymbol{J}^{\text{tot}}$, from satellite measurements are able to produce results very similar to the AE index, while maintaining the possibility to investigate longitudinal dependence. This possibility is exploited through the unique constellation of the *Swarm* satellites, by a direct comparison of simultaneous measurements of the sheet current densities at different longitudes by comparing *Swarm* Alpha/Charlie with Bravo. The top panel of Figure 8.5 shows the total polar current $\boldsymbol{J}^{\text{tot}}$ found by Alpha and Bravo for

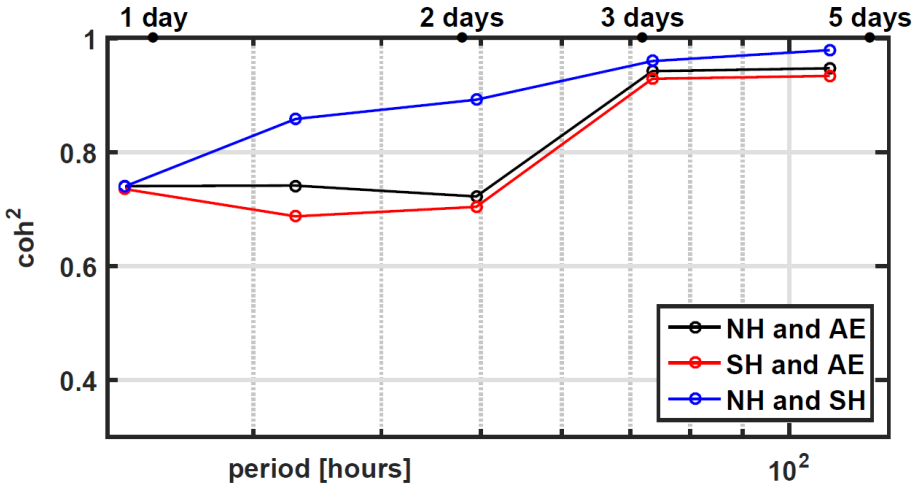

Figure 8.4: Correlation between the total polar current and the AE index as a function of period of the signal for 400 orbits (orbit number 7200 to 7799 on the 7th of March to 1st of April), corresponding to the time series, presented in Figure 8.3. The coherence is presented between the AE index and the Northern Hemisphere in black, between the AE index and the Southern Hemisphere in red, and between the Northern and Southern Hemisphere in blue.

the three week period around the Saint Patrick's day storm 2015 for the Northern Hemisphere as a function of time. The middle panel is a replica of the middle panel of Figure 8.2, showing the space-time development of the sheet current densities for *Swarm* Alpha as a function of QD latitude and time. The bottom panel gives the space-time development of the differences between the sheet current densities measured by Alpha and Bravo (Alpha - Bravo). A positive difference indicates stronger sheet current densities measured by Alpha. A high visual correlation between $\boldsymbol{J}^{\text{tot}}$ from the two satellites (top plot) is supported by a correlation coefficient of 0.81. The high correlation between the satellites is expected, since the sheet current density in general is high during disturbed conditions and lower during quiet conditions. We do, however, find some larger small scale differences, presented in the bottom panel. These indicate a possible longitudinal or MLT dependence of the intensity of the auroral electrojet system, not available by the AE index. The longitudinal equatorial separation was on the 17th of March 2015 $24.5°$, indicating that even smaller longitudinal length scales might be important for ionospheric currents during high activity times. A comparison with the ionospheric sheet current density space-time development presented in the middle plot reveals that the highest differences are found during disturbed conditions. The differences are mainly positive inside the auroral oval, consistent with a generally higher AE index during Alpha crossings, compared to Bravo crossings (not shown in thesis). Furthermore, we find differences of comparable size to the sheet current densities.

Investigations performed in the previous section adds to the conclusion of a robust measure, able to provide both a more detailed presentation of the space-time development of the sheet current densities and a simple intensity index, provided by the total current, $\boldsymbol{J}^{tot}$.

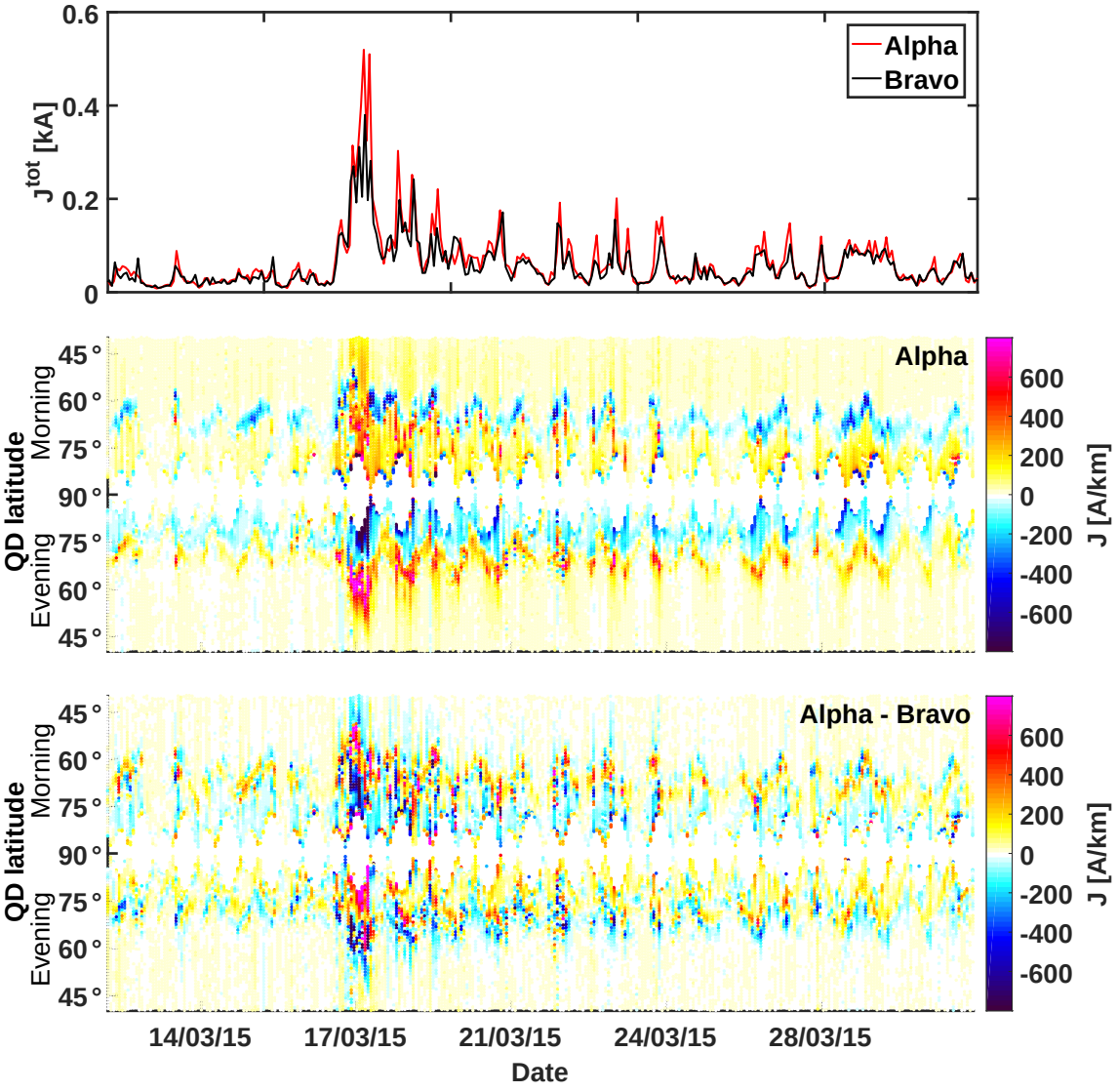

Figure 8.5: Space-time development of the sheet current densities and their differences for *Swarm* Alpha and Bravo on the Northern Hemisphere around the Saint Patrick's day storm (17th of March) for 300 orbits in the period from the 11th to the 31st of March 2015. Top panel: Time series of the total polar current, $\boldsymbol{J}^{tot}$, for *Swarm* Alpha (red) and Charlie (black). Middle and bottom panel: Sheet current densities (colour) as a function of QD latitude and time for *Swarm* Alpha (middle panel) and difference between *Swarm* Alpha and Bravo (bottom panel). A positive difference follows times with largest sheet current densities estimated by *Swarm* Alpha.

8.2 Geomagnetic and solar wind activity

This section uses estimates of the ionospheric sheet current densities to investigate how the current system reacts on changes in intensity and direction of the IMF. The importance of solar irradiation and tilt angle is investigated through statistical presentations of the sheet current densities during the four seasons of the year.

Variation with geomagnetic activity monitored by the *Kp* index

Figure 8.6 shows the ionospheric sheet current densities presented as the robust mean in bins of 1 h in MLT and 2° in QD latitude for various geomagnetic activity (*Kp*) levels along with the corresponding robust estimate of the standard deviation (σ) for *Swarm* Alpha and Bravo in 2015. The results are presented for both the Northern (left) and Southern (right) Hemisphere. The top row shows the results using data for all values of *Kp*, while for the other three rows, the data have been divided according to *Kp* ($Kp \leq 1^o$, $1^o < Kp \leq 2^o$ and $Kp > 2^o$), with approximately one third of the data in each bin.

Increased geomagnetic activity results in a clear westward electrojet (WEAJ) in the evening sector, and an eastward electrojet (EAEJ) in the morning sector, corresponding to existing statistical models of the auroral electrojet system [*e.g.* Friis-Christensen et al., 1985b; Untiedt and Baumjohann, 1993]. The maximum of the WAEJ is found in the MLT region between 01 and 05, and the maximum of the EAEJ between 15 and 18 for both the Southern and Northern Hemisphere, consistent with the findings of *e.g.* Juusola et al. [2009]; Vennerstrom and Moretto [2013]. The strength of the electrojet currents are, as expected, highly correlated with the *Kp* index. Growing strengths are found for increasing *Kp* along with an equatorward motion of the location of maximum current strength, consistent with findings of *e.g.* Weimer [2013]. An important observation is, how not only the strength, increases with *Kp*, but also the scatter of the data for the individual bins, confirming an equatorward expanding auroral oval during substorm activity. The movement is more profound the more disturbed the current system is, aligning with the results presented in the figure. Since sample sizes are almost the same in the different bins, we have a larger Kp range in the last bin. This will obviously result in much larger natural variance in especially the strength, but also locality of the electrojet system, presented by a larger variation in the last bin. Despite of this, we deduce that disturbed conditions result in much more variety in place and strength, compared to the quiet conditions. The data in the polar cap should be treated with care, since the rotation of the currents along constant QD latitude may introduce current spikes, as described in Section 4.1. These will affect the mean values. Although the influence is minimized by using a robust mean measure, it cannot be expected to be fully removed.

Dependence on solar wind activity

Present knowledge of the auroral electrojet system explains how the shape of the system depends on the relationship between the direction and strength of the y and z component of the IMF in GSM coordinates (see further details in Section 2.3). As with the dependence on *Kp*, the robust mean of the sheet current density is estimated within bins of 1 hour MLT and 2 degree magnetic co-latitude. The results are presented in Figure 8.7 for the Southern Hemisphere on the right and the Northern Hemisphere on the left.

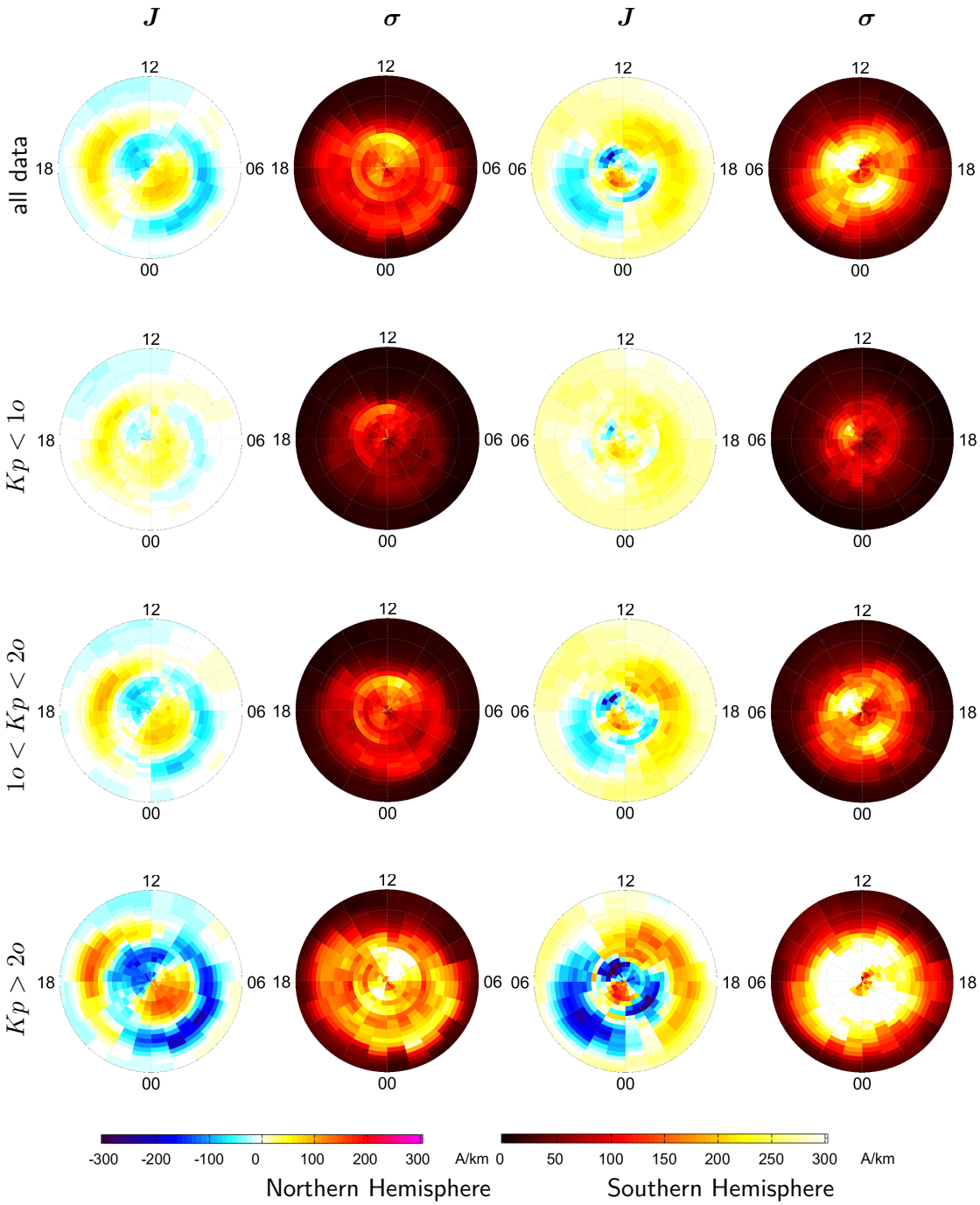

Figure 8.6: Sheet current densities (first and third column, left colourbar) and their respective error estimates, σ (second and fourth column, right colourbar) binned in 1 hour MLT and 2° QD windows according to activity (Kp) level for the Northern (left) and Southern (right) Hemisphere. The low-latitude boundary is at $\pm 60^\circ$. The top row presents mean values of the sheet current densities from one year (2015) of *Swarm* Alpha observations, the second row, including only data at times with $Kp < 1^o$, the third row including data at times with $1^o < Kp < 2^o$, and the bottom row, mean values where $Kp > 2^o$.

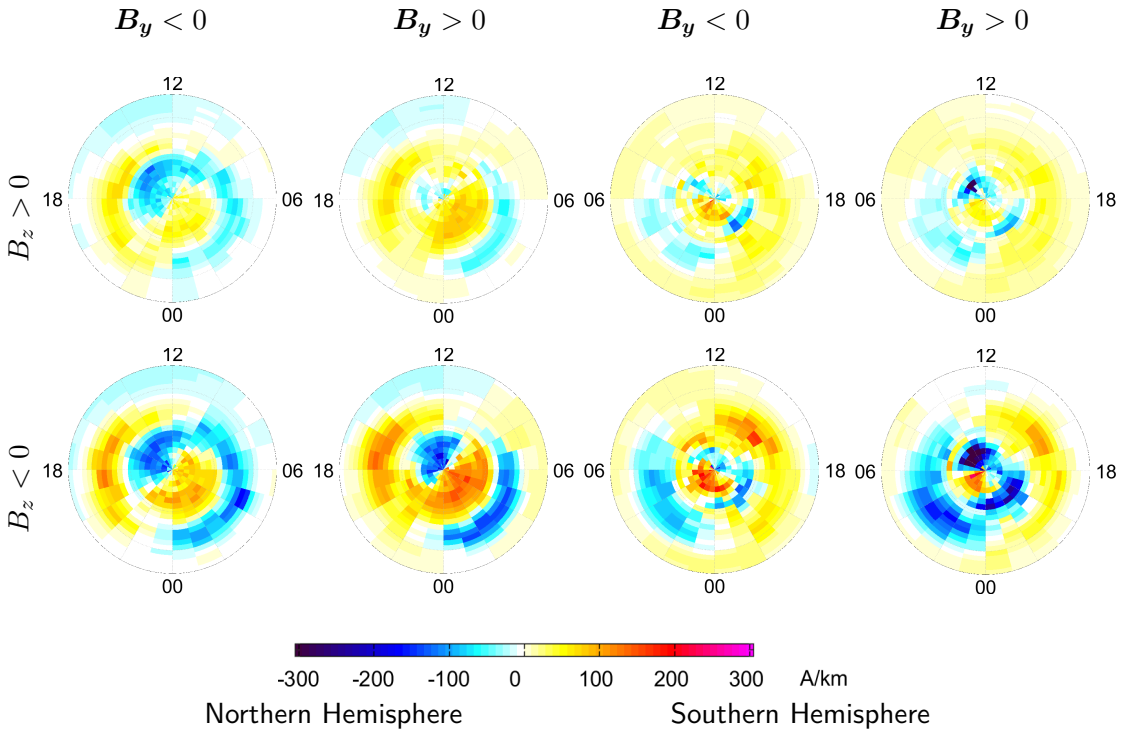

Figure 8.7: As Figure 8.6, binned according to the y and z component of IMF in GSM coordinates. The top row presents mean values of the sheet current densities with $\boldsymbol{B_z} > 0$ and the bottom row, for $\boldsymbol{B_z} < 0$. The first and second column presents the mean values at times of $\boldsymbol{B_y} < 0$, and the second and third at $\boldsymbol{B_y} > 0$.

The results correlate well with the present understanding [*e.g.* Friis-Christensen et al., 1985b; Weimer, 2001] of how the currents react to different states of the IMF. As an example, we find significantly larger sheet current densities for a Southward IMF (*i.e.* negative $\boldsymbol{B_z}$) compared to a northward IMF (positive $\boldsymbol{B_z}$) for both the Southern and Northern Hemisphere. The figure also indicates a slight difference in intensity for positive and negative $\boldsymbol{B_y}$, consistent with the findings of Juusola et al. [2007]. This difference is slightly larger in the Southern Hemisphere, indicating a stronger vulnerability in the symmetry with direction of $\boldsymbol{B_y}$. The presence of a $\boldsymbol{B_y}$ component of the IMF results in an asymmetry between the Northern and Southern Hemisphere (see Section 2.3). This anticlockwise rotation on the Northern Hemisphere and clockwise on the Southern Hemisphere presented as an example in Cowley et al. [1991]; Friis-Christensen et al. [1985b] and Juusola et al. [2014], is however not clearly present in our data.

Dependence on season selection

The seasonal differences can, in the same way as the *Kp* and IMF dependence, be estimated by dividing data from *Swarm* Alpha and Bravo, 2015, into the four seasons: spring, March to May (September to November), summer, June to August, autumn, September to November, (March to May) and winter, December to February on the Northern (Southern) Hemisphere. The resulting robust mean sheet current density is presented in Figure 8.8 as a function of magnetic co-latitude and MLT.

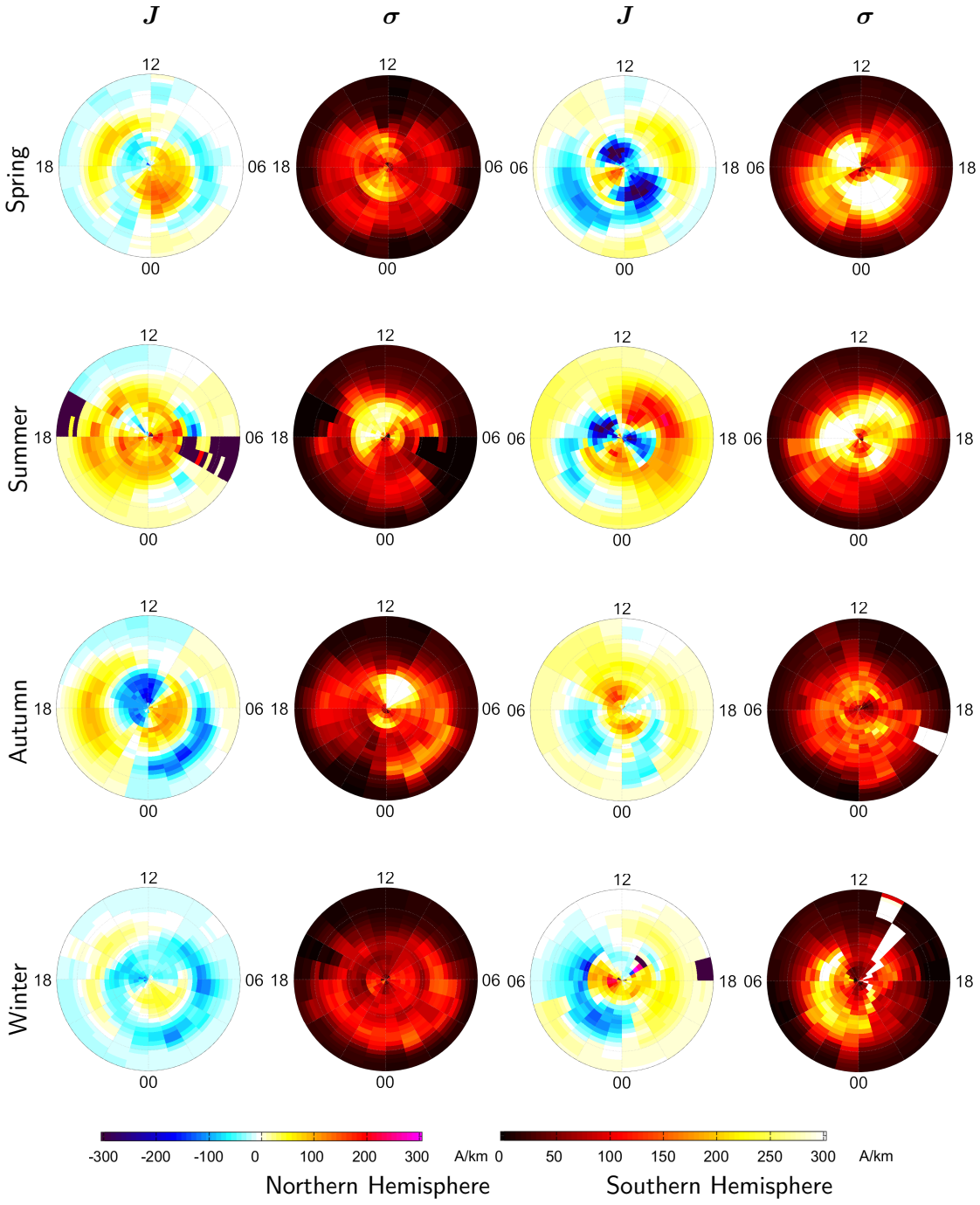

Figure 8.8: As Figure 8.6, binned according to local seasons, Spring (top row), Summer (second row), Autumn (third row) and Winter (bottom row).

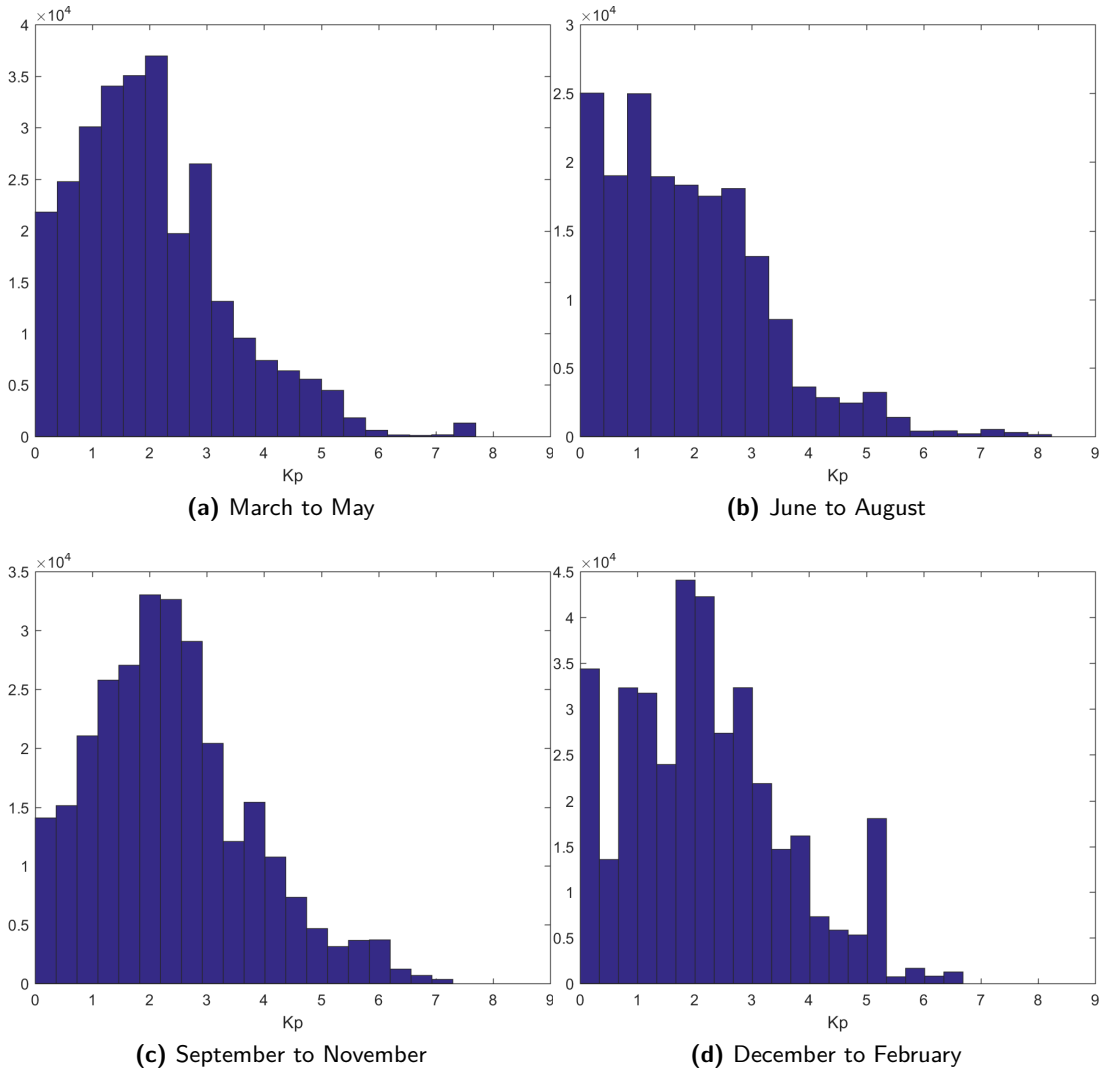

Figure 8.9: Histograms of Kp values divided into four seasons, March to May (a), June to August (b), September to November (c) and December to February (d).

The first and third row of the figure show clear differences between the hemispheres, with largest sheet current densities during southern spring and northern autumn. Some of the difference is attributed natural variability in the IMF conditions. Figure 8.9 therefore presents a histogram of the *Kp* values for each 3 month period to estimate the effect of the IMF variability. The figure reveals a higher mean intensity for the northern autumn and winter (September to February), compared to summer and spring. This will cause a bias in the intensities measured in this period, and fits well with the results of a relatively stronger sheet current density in the northern autumn and southern spring. It is therefore difficult to say whether the found differences are due to seasonal differences or differences in disturbance level of the solar wind.

Other studies of the seasonal differences report an increase in currents between a factor of 1.35 [Papitashvili et al., 2002] and 1.8 [Christiansen et al., 2002] between summer and winter in the FACs. Consistent with the findings of Juusola [2009]; Fujii et al. [1981] and Vennerstrom

and Moretto [2013], we estimate the dayside/nightside differences to be strongest in summer, with only little difference during winter. The largest enhancements in eastward currents is observed between 12 and 18 MLT. This day/night difference results in strongest currents on the nightside during winter, and on the dayside during summer. The dayside enhancement is found strongest in the Southern Hemisphere, which could be due to the increase in disturbance levels during these months. The increase in disturbance levels is likely also the reason for the slight increase in the westward flowing currents during winter in the morning sector, Northern Hemisphere.

A study of the impact of sunlight on high-latitude equivalent currents [Laundal et al., 2016a,b] shows a large difference between the sunlit and dark part of the ionosphere. The sunlit part is found with high resemblance to the statistical two-cell opposite convection pattern [*e.g.* Heppner and Maynard, 1987; Weimer, 2005], while the dark side is dominated by a strong current cell in the dawn sector. This corresponds well with our findings in Figure 8.8. where we clearly see a dawn-dominated current distribution during winter, which is not present during summer. This feature is present for both hemispheres, but stronger for the Southern. The interhemispherical difference could be due to natural variability, since only one year of data is presented.

Since the sunlight seems to affect both the intensity and the distribution of currents, we argue that the best period for examining interhemispheric differences is around equinox (spring and autumn) since both hemispheres will be affected by the same amount of sunlight. From the histograms of Kp (Figure 8.9), we would expect the southern spring to be slightly stronger than the northern, and opposite at autumn, which is consistent with the findings of Figure 8.8. The Russel-McPherron effect (Section 2.3) states how the IMF-geomagnetic field configuration causes stronger currents around equinox. The currents are found strongest during northern autumn, consistent with this theory. The pattern can, however not be deemed significant due to the short statistical period.

Average position and strength of the electrojet

The results presented in Figure 8.6 can be expressed more simply as the average position and strength of the electrojet ($\boldsymbol{J}^{\text{peak}}$) as described briefly in Section 1. There is little doubt that this is a simplification of the previous results. It does, however, provide a simple presentation of the current system particularly well suited for analysing the behaviour of the auroral oval and strength of the sheet current densities according to intensity level.

The outcome of this analysis is presented in Table C.1 and C.2 on page 186 and in Figure 8.10, showing the median latitude of the peak sheet current density ($\boldsymbol{J}^{\text{peak}}$) as a function of MLT and geomagnetic activity (Kp value). The median latitude is found from a dataset comprising data from all 10 years of CHAMP data along with data from *Swarm* Alpha and Bravo in the period November 2013 to December 2015. The number of data points used to estimate the medians are presented in Table C.3 and C.4 on page 187 for the Northern and Southern Hemisphere respectively. It is clear from this table how most of the orbits fall in the category of quiet or moderately disturbed days. The results presented in Figure 8.10 clearly support the theory of a southward expansion of the auroral oval for increasing Kp for both the Northern and Southern Hemisphere [*e.g.* Feldstein and Starkov, 1967; Akasofu et al., 1973; Burch, 1974].

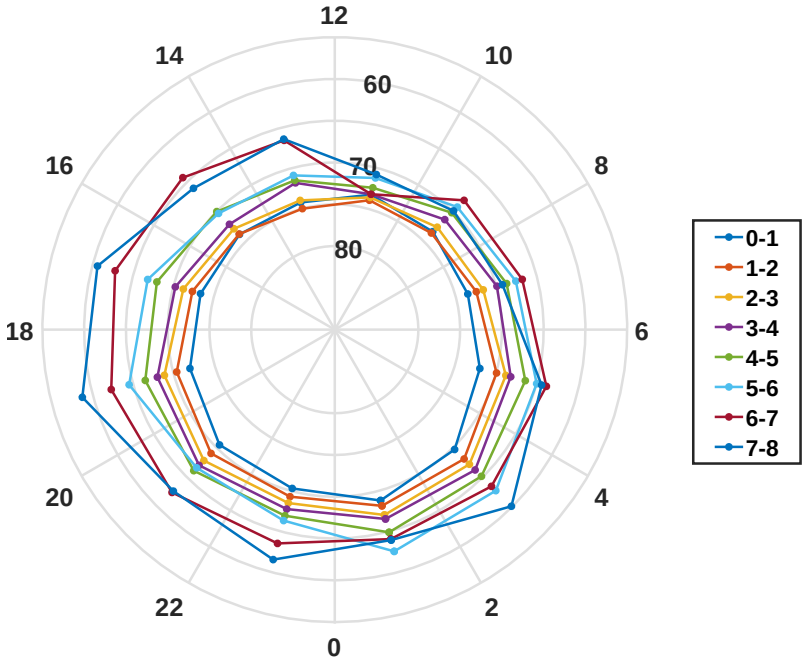

(a) Northern Polar cap

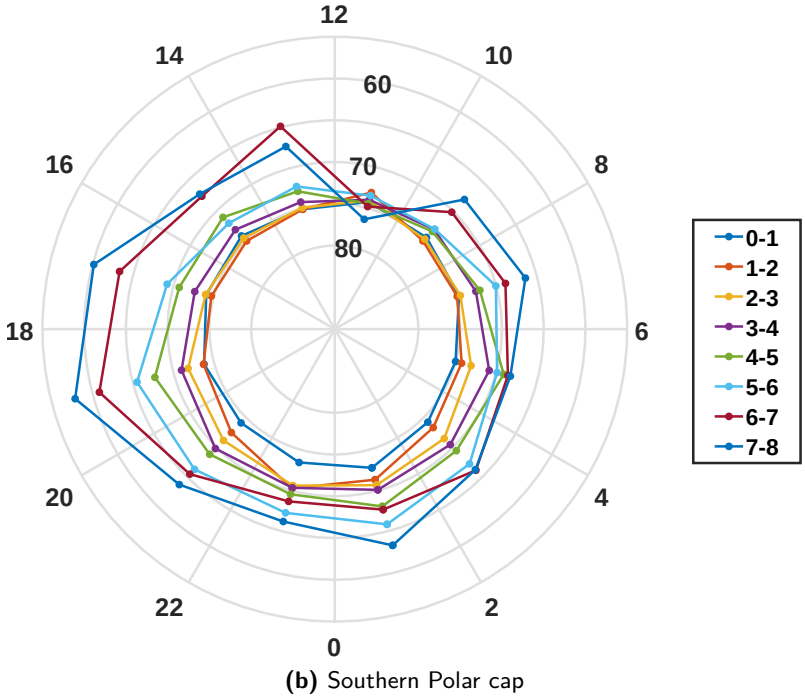

(b) Southern Polar cap

Figure 8.10: Median QD latitude of the peak sheet current density, $\boldsymbol{J}^{\text{peak}}$, as a function of activity level, Kp, and MLT, estimated from 10 years of CHAMP data and *Swarm* Alpha and Bravo measurements in the period between November 2013 and December 2015 (both months included). One line represents the median position at the Northern (a) and Southern (b) Hemisphere in a given Kp interval.

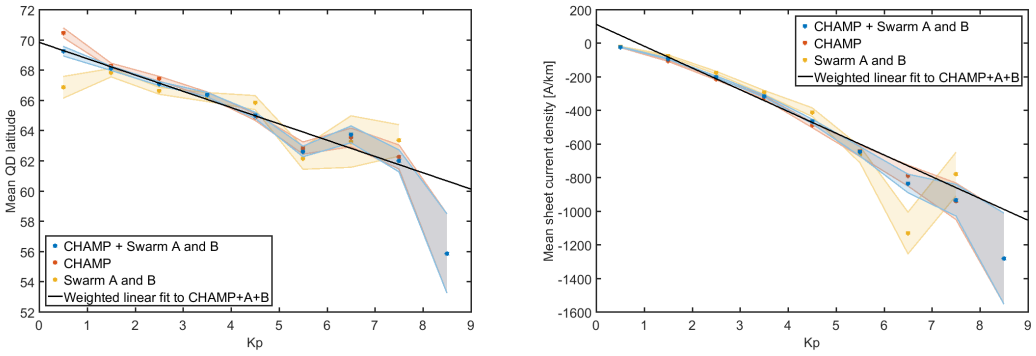

(a) Mean Position of $\boldsymbol{J}^{\text{peak}}$ **(b)** Mean strength of $\boldsymbol{J}^{\text{peak}}$

Figure 8.11: Mean position (a) and strength (b) of $\boldsymbol{J}^{\text{peak}}$ as a function of Kp for three datasets. Blue shows results using all provided data (CHAMP + *Swarm* Alpha and Bravo 2013-2015), red gives the results based on CHAMP data alone, and the yellow, results estimated from Swarm Alpha and Bravo 2013-2015. Error estimates (MAD) are given as shaded contours for each line estimated separately for the position and strength.

The shape of the oval is found more non-symmetric for the Southern Hemisphere, compared to the Northern, where the shape is close to circular at all intensity levels, and more profound for high-intensity data. The deviating shape of the outermost contour (*Kp* 7 to 8^-) of both the Northern and Southern Hemisphere is attributed to the sparse data distribution for these intensity levels (see Table C.3 and C.4).

It is also worth to notice the larger movement of the oval in the Southern Hemisphere. The oval during quiet times is considerately smaller than that in the Northern Hemisphere, but expands down to similar latitudes during disturbed times, where also the shape of the oval becomes less circular. The cause for this has not been investigated further, but could be due to the difference in the distance between the magnetic and the geographic pole in the two hemispheres. The inter-hemispherical differences are discussed in further detail in Section 8.3.

A pattern similar to Figure 8.10 is found, when presenting the estimated sheet current densities as the mean strength and position for the WAEJ at MLT 01 and 03 as a function of *Kp*. These results are presented in Figure 8.11 for three different datasets. (a) gives the mean latitude of the WAEJ and (b) the mean strength of $\boldsymbol{J}^{\text{peak}}$. Shown in blue is the dataset corresponding to the results given in the figures above (CHAMP + *Swarm* Alpha and Bravo 2013-2015), red is results from CHAMP alone, and the yellow line, results based on two years of *Swarm* Alpha and Bravo data (2013-2015). From the two years of *Swarm* data it was not possible to provide enough data for highly disturbed times ($Kp > 8$) to calculate the median position and strength, and the last entry is therefore omitted. The shaded areas gives the associated joined error estimates of the median position and strength of $\boldsymbol{J}^{\text{peak}}$ from *median absolute deviation* (MAD[1]). The joined error estimates are found from propagation of errors [Emery and Thomson, 2004]

$$\sigma = \sqrt{\sigma_1^2 + \sigma_2^2 ... + \sigma_n^2}. \tag{8.2}$$

[1] a robust measure of the variability of the data sample

Kp/parameter	$\mathcal{A}$	$\mathcal{B}$	r_0	ϑ_0	γ
0-1	17.44	18.59	2.43	0.11	0.16
1-2	18.36	19.23	3.24	0.10	-0.28
2-3	19.21	20.42	3.37	0.05	-0.22
3-4	20.17	21.36	3.06	0.08	-0.15
4-5	21.04	23.20	3.11	0.04	-0.28
5-6	21.91	24.70	3.68	0.19	-0.40
6-7	23.10	27.08	3.04	-0.60	-0.31
7-8	23.30	28.16	4.24	-0.70	-0.34

Table 8.1: Results from the elliptic fit to median positions (Figure 8.10) presented in Figure 8.12(a), for the Northern Hemisphere. $\mathcal{A}$ gives the semi minor axis and $\mathcal{B}$, the semi major axis, both represented in $90-$QD latitude. (r_0, ϑ_0) gives the position of the centre of the fit, also in 90 - QD latitude, and γ the rotation of the ellipse in radians.

The black line gives a weighted linear fit to the estimate based on CHAMP + Swarm Alpha + Bravo 2013-2015 of $y = -(1.1 \pm 0.1)x + 69.9 \pm 0.3$ for the position and $y = -(96.7 \pm 6.7)x + 33 \pm 9$ for the strength of the westward electrojet. The *Kp* index is a logarithmic index, with a fixed upper boundary and limited in the lower end by the always present auroral oval, even during very quiet times. The linear dependence found here aligns very well with this, and the fact that the oval and absolute strength of the westward electrojet is positively correlated with *Kp* level. The sheet current densities does, however, not seem to follow the linear trend for $Kp > 5$. A exponential or quadratic dependence of the sheet current densities with Kp would fit data better. Due to lack of physical explanation, this dependence has not been investigated further. Using the results from the linear fit, we find an increase of approximately 97 A/km per Kp level. Comparing low activity data ($Kp = 1$) with high activity ($Kp = 5$) data, reveals an increase in $\boldsymbol{J}^{\text{peak}}$ by approximately 385 A/km, corresponding to a factor of 7.1. Correspondingly, Juusola [2009] finds a factor of 7 increase between $Kp = 0$ and $Kp \geq 5$ for the FACs and Vennerstrom and Moretto [2013] a factor of 4 increase between $Kp < 2$ and $Kp \geq 5$ for the auroral electrojet system.

In stead of representing the size and position of the auroral oval from the position of the WAEJ at MLT at 01 and 03, we can give an estimate of the auroral oval size and shape by estimating an elliptic fit, using a general equation of the ellipsis in polar coordinates (r, ϑ),

$$1 = \frac{((r\cos\vartheta - r_0\cos\vartheta_0)\cos\gamma + (r\sin\vartheta - r_0\sin\vartheta_0)\sin\gamma)^2}{\mathcal{A}^2} + \frac{((r\cos\vartheta - r_0\cos\vartheta_0)\sin\gamma - (r\sin\vartheta - r_0\sin\vartheta_0)\cos\gamma)^2}{\mathcal{B}^2}$$

to the median positions with MLT. Here (r_0, ϑ_0) is the centre of the ellipsis and γ is the angle of rotation of the ellipsis. $\mathcal{A}$ gives the semi minor axis, and $\mathcal{B}$ the semi major axis. The eccentricity of the ellipsis is found as

$$\Upsilon = \sqrt{1 - \frac{\mathcal{B}^2}{\mathcal{A}^2}}.$$

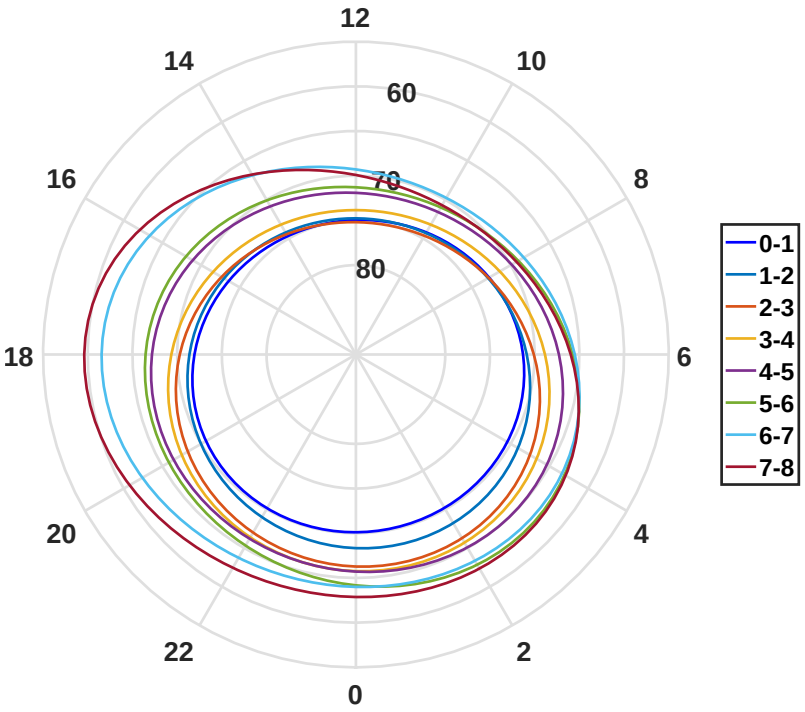

(a) Northern Polar cap

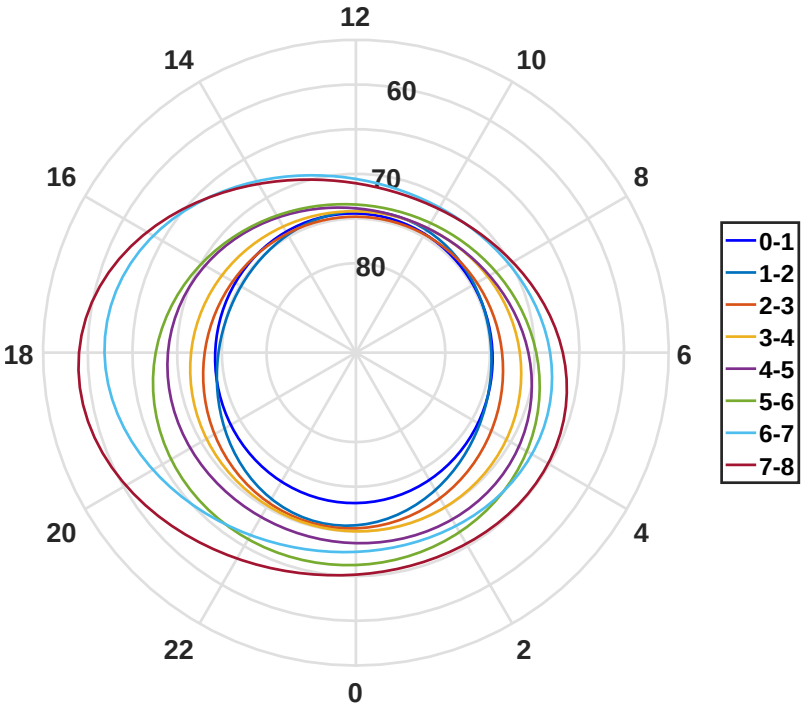

(b) Southern Polar cap

Figure 8.12: Elliptic fit to median positions of the peak sheet current density, $\mathbf{J}^{peak}$, represented in Figure 8.10. One line represents the fit for a given Kp interval for the Northern (a) and Southern (b) Hemisphere.

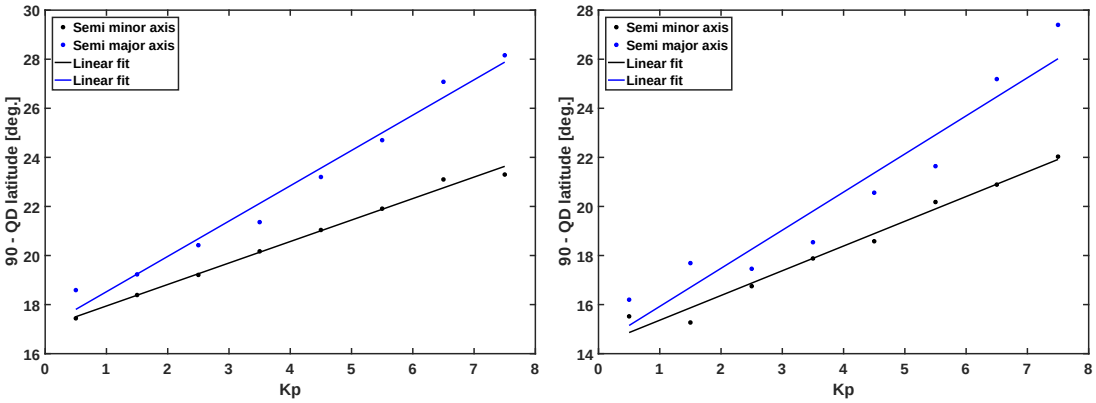

(a) Auroral oval size, North

(b) Auroral oval size, South

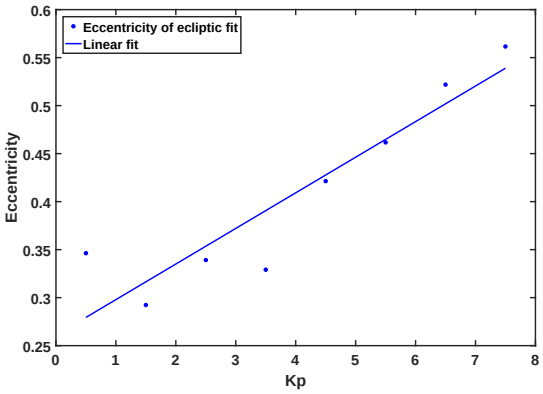

(c) Eccentricity, North

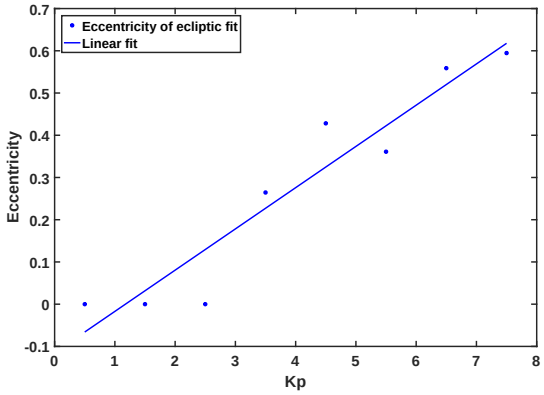

(d) Eccentricity, South

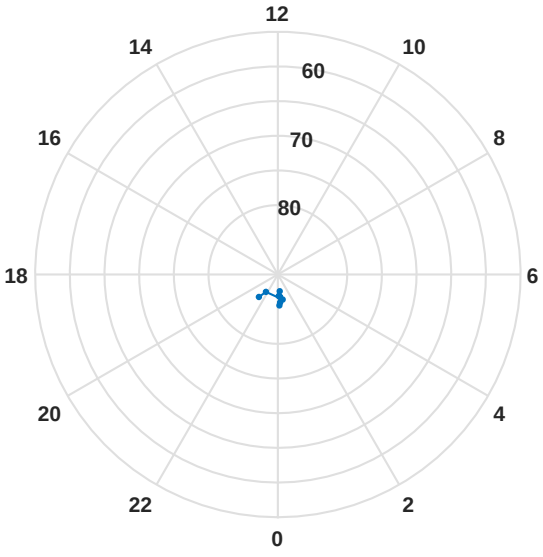

(e) Centre position, North

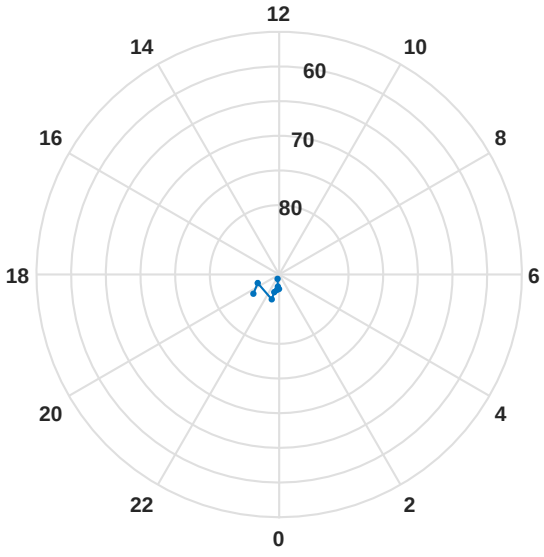

(f) Centre position, South

Figure 8.13: Elliptic fit to median positions of the peak sheet current density, $\mathbf{J}^{peak}$, represented in Figure 8.10. One line represents the fit for a given Kp interval for the Northern (a) and Southern (b) Hemisphere.

$\boldsymbol{Kp}$/parameter	$\mathcal{A}$	$\mathcal{B}$	r_0	ϑ_0	γ
0-1	15.52	16.20	0.67	-0.35	0.027
1-2	15.28	17.69	1.76	-0.11	-0.19
2-3	16.75	17.46	2.25	-0.14	-0.18
3-4	17.88	18.53	2.09	-0.011	0.19
4-5	18.58	20.56	2.64	-0.27	-0.31
5-6	20.18	21.64	3.74	-0.29	-0.076
6-7	20.89	25.19	3.33	-1.19	-0.20
7-8	22.03	27.40	4.64	-0.93	-0.13

Table 8.2: As Table 8.1 for the Southern Hemisphere.

The results of the elliptic fit, corresponding to the positions given in Figure 8.10 are given in Figure 8.12 for the Northern (a) and the Southern (b) Hemisphere. One line represents the fit for a given Kp interval. The fit to individual Kp levels are given in Figures C.1 and C.2 for the Northern Hemisphere, and in Figures C.3 and C.4 for the Southern Hemisphere. The corresponding fit values are given in Table 8.1 for the Northern Hemisphere, and Table 8.2 for the Southern Hemisphere. Figures similar to Figure 8.11(a), are presented in Figure 8.13, where the size of the oval is represented by the semi major and minor axis (a and b), and the shape of the oval by the eccentricity (c and d) for the Northern (left column) and Southern (right column) Hemisphere, accordingly. The semi major (blue) and in particular the semi minor (black) axis shows an increased linear dependence with Kp compared to Figure 8.11(a) (visual comparison). The non-symmetric shape found in Figure 8.11(a) is presented in the elliptic fit by a flattening of the ellipsis for increasing Kp. This is supported by a linear increasing eccentricity with Kp. Only little variation in the position of the centre (e and f) is found for increasing Kp.

Figure 8.14 to 8.17 shows the median position and strength of $\boldsymbol{J}^{\text{peak}}$ for the full dataset comprising 10 years of CHAMP and two years of *Swarm* Alpha and Bravo as a function of MLT. The first two figures shows results for the Northern Hemisphere and the last two for the Southern Hemisphere. Plots for the 2 hour intervals 8 to 9^- have not been included due to insufficient data in many ranges of MLT. The peak position of the WAEJ is plotted in the morning sector (MLT between 00 and 12), and the EAEJ in the evening sector (MLT between 12 and 24). The estimate of the WAEJ is added in the Harang discontinuity region, for the 2 hour interval around 23. The black dot gives the position of the electrojet, while the size and colour of the circle gives the intensity of the sheet current density. The figures show an increasing strength and equatorward motion of the auroral oval for increasing intensity consistent with the previous analysis. The strongest WAEJ is found between 0 and 6 MLT, while the strongest EAEJ is found between 16 and 20 MLT. This corresponds very well to the result found in Figure 8.6, Vennerstrom and Moretto [2013] and Juusola et al. [2007].

As was the case in the analysis presented in Figure 8.10(a) and (b), we find deviating shapes of the auroral oval for high activity periods. This is attributed to the fewer data points and larger spread (Figure 8.6) for these intervals. We have therefore presented the data in a larger *Kp* bin, ranging from *Kp* 6 to *Kp* 9^+, see Figure 8.15(e) and 8.17(e). Due to the few data from the very disturbed periods Kp > 7, we see how the shape and strength is highly depicted

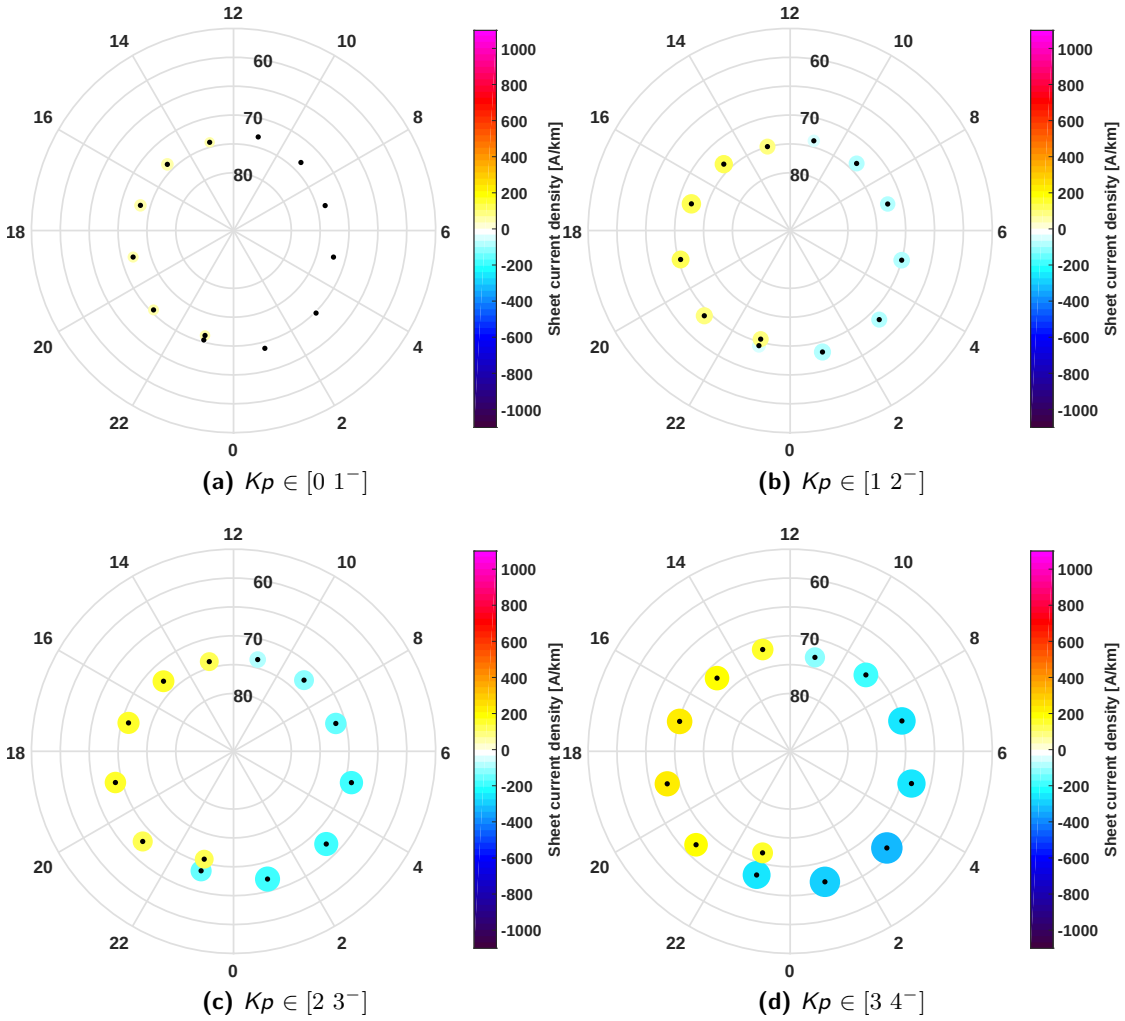

(a) $Kp \in [0\ 1^-]$ **(b)** $Kp \in [1\ 2^-]$

(c) $Kp \in [2\ 3^-]$ **(d)** $Kp \in [3\ 4^-]$

Figure 8.14: Median position and strength of the peak current density strength $\boldsymbol{J}^{\text{peak}}$, from 10 years of Northern Hemisphere CHAMP data and 2 years of *Swarm* Alpha and Bravo data (November 2013 to December 2015) binned in 2 hour MLT window. The position is given by the black dots, and the strength as the size and colour of the surrounding area. The morning sector (MLT between 0 and 12) presents position and strength of the western electrojet (blue), and the evening sector (MLT between 12 and 24), the position and strength of the eastern electrojet (red). An additional estimate of the western electrojet has been placed at MLT 23 to mark the Harang discontinuity region. The errors in the Harang discontinuity region refers to the WAEJ estimates. The data are divided into four Kp intervals.

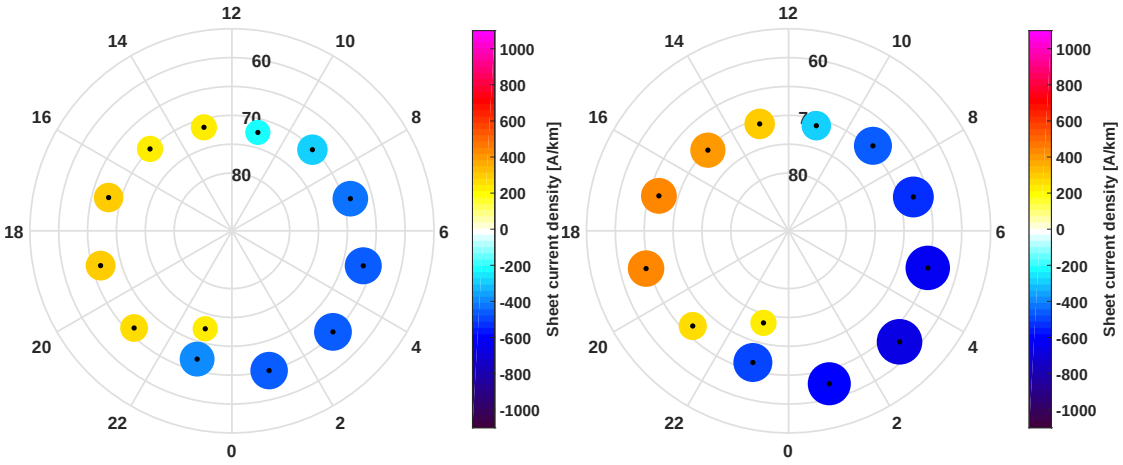

(a) $Kp \in [4\ 5^{-}]$ **(b)** $Kp \in [5\ 6^{-}]$

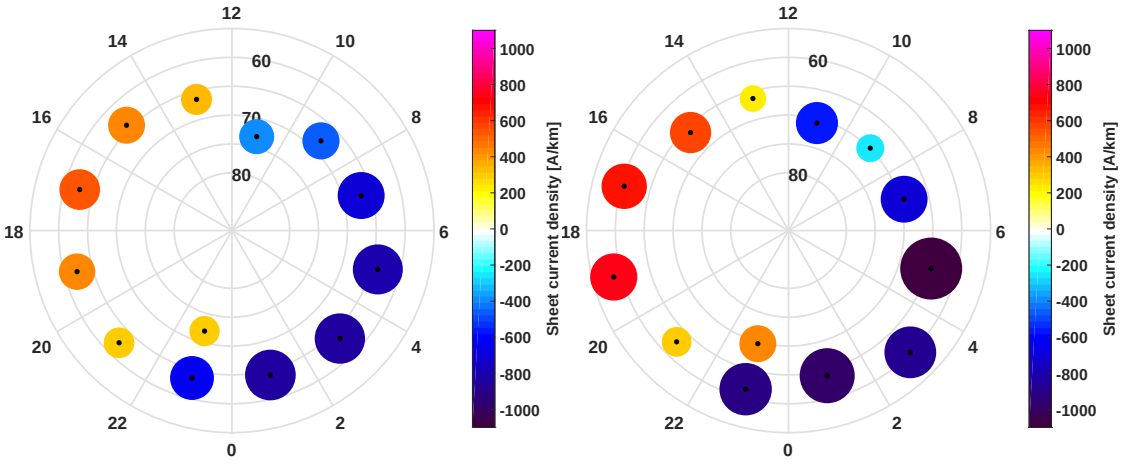

(c) $Kp \in [6\ 7^{-}]$ **(d)** $Kp \in [7\ 8^{-}]$

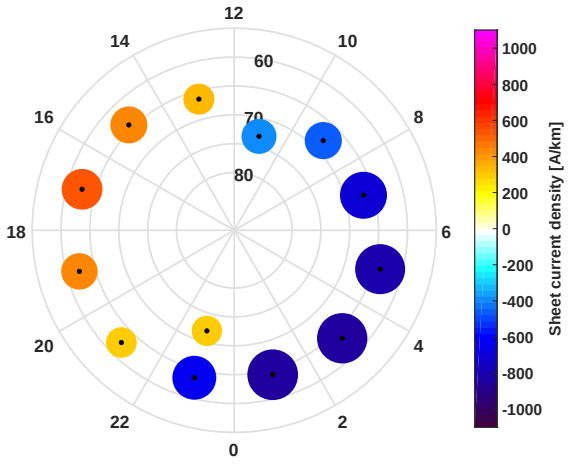

(e) $Kp \in [6\ 9^{+}]$

Figure 8.15: Figure 8.14, continued with five additional Kp ranges.

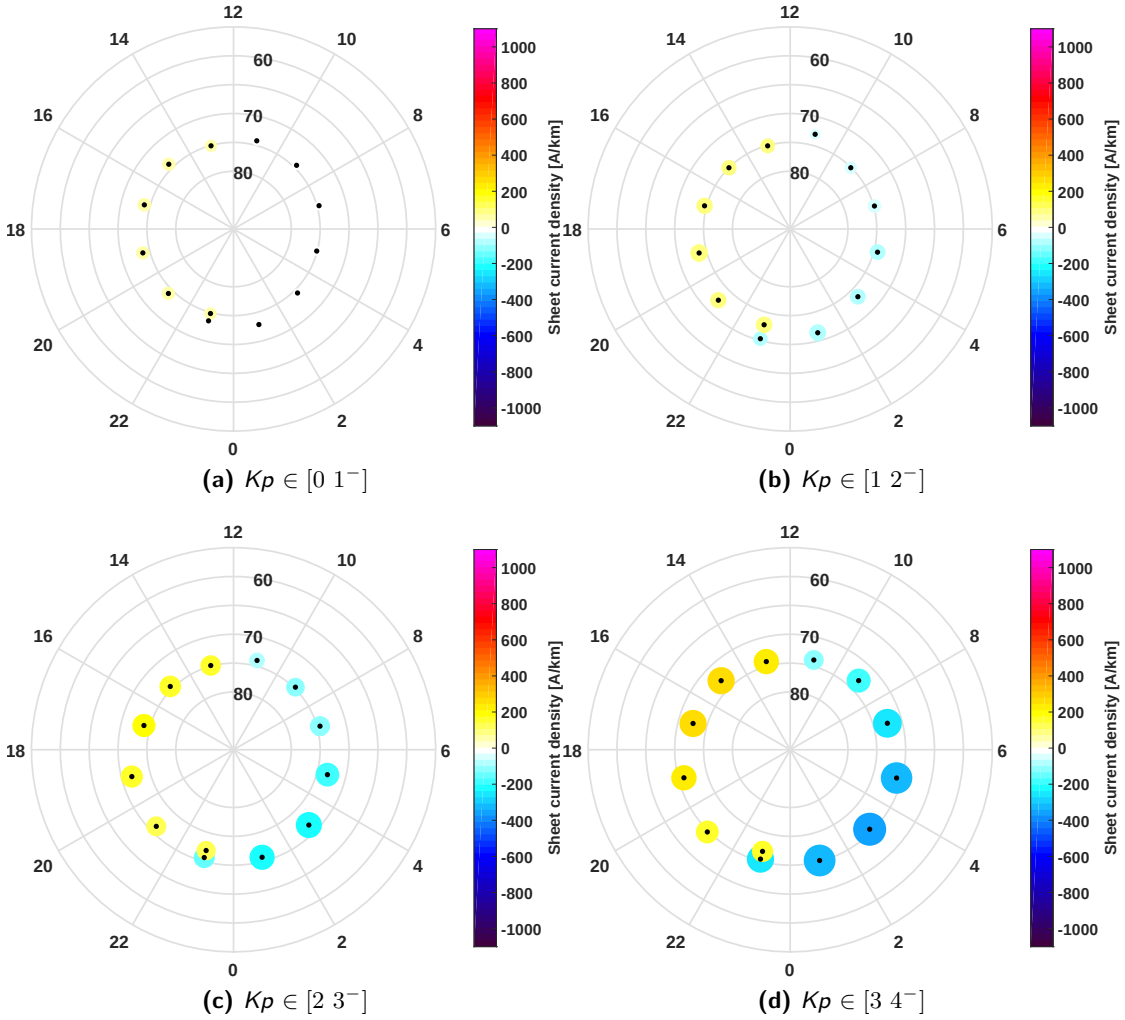

(a) $Kp \in [0\ 1^-]$ **(b)** $Kp \in [1\ 2^-]$

(c) $Kp \in [2\ 3^-]$ **(d)** $Kp \in [3\ 4^-]$

Figure 8.16: As Figure 8.14, but for the Southern Hemisphere.

by $6 <$ Kp < 7 (8.15(c) and 8.17(c)).

For low activity data ($Kp < 2$), we find that the placement of the WAEJ and EAEJ for MLT$= 23$ is almost identical, indicating a weak Harang discontinuity. The strength of the current densities increases with the displacement between the WAEJ and EAEJ, indicating a strengthening of the discontinuity, along with a strengthening of the substorm electrojet. The presence of the substorm electrojet is mainly seen in a amplification of the westward sheet current density across the midnight sector. Another notable example of the presence and strengthening of the substorm electrojet is the growing difference in strength between the westward and eastward electrojet with increasing *Kp*. An example of this can be seen in the difference between Figure 8.14(a,b) and Figure 8.14(b).

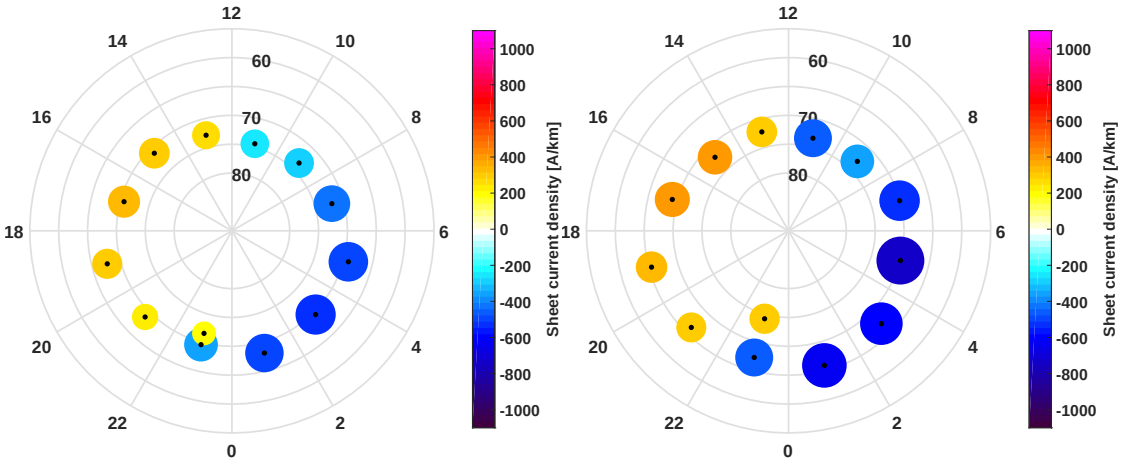

(a) $Kp \in [4\ 5^{-}]$ **(b)** $Kp \in [5\ 6^{-}]$

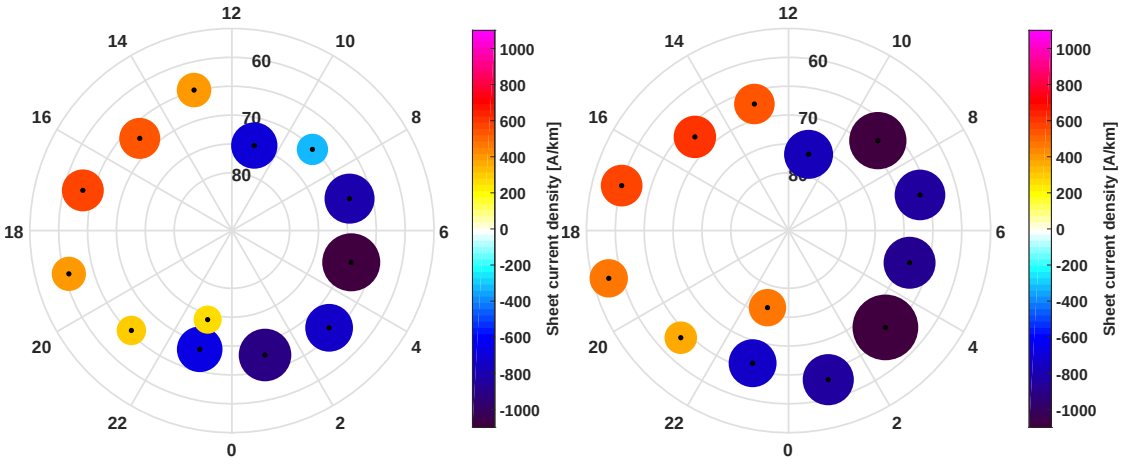

(c) $Kp \in [6\ 7^{-}]$ **(d)** $Kp \in [7\ 8^{-}]$

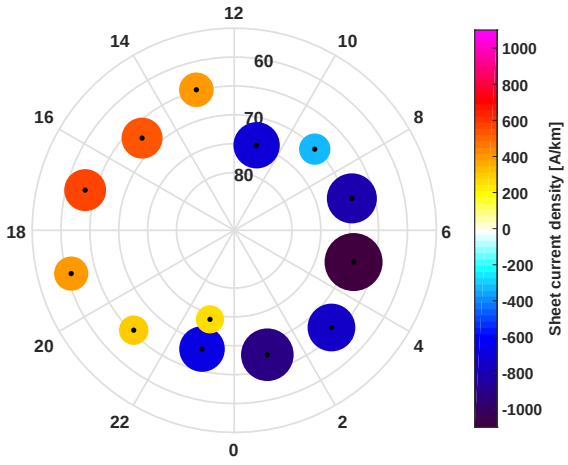

(e) $Kp \in [6\ 9^{+}]$

Figure 8.17: Figure 8.16, continued with five additional Kp ranges.

8.3 Hemispherical differences

We have looked into statistical differences due to variations in the solar wind conditions, such as activity level and direction of the IMF for the Northern Hemisphere. In this section, we will investigate the interhemispherical differences. In the theory section (Section 2.3) we use symmetry arguments to state how the two hemispheres should behave in similar matters, and hence show similar, if not equal, current distributions during equal IMF conditions. To evaluate this statement, we looked at the statistical patterns for the Northern and Southern Hemisphere separately. The results of this is illustrated in the following figures.

Figure 8.18(a) and (b) gives the median position in QD latitudes of the peak intensity of the WAEJ and EAEJ as a function of MLT for the Northern and Southern Hemisphere estimated from CHAMP and *Swarm* data separately. Results for the Northern Hemisphere are given in blue, and for the Southern Hemisphere in red. MLT 23 to 11 shows the average position of the WAEJ, while MLT 13 to 21 shows the average position of the EAEJ. One immediately obvious feature is the larger oval in the Northern Hemisphere, also found when binned according to *Kp* (Figure 8.10). A consistently larger oval is found from both data samples (CHAMP and *Swarm*), indicating a significant difference. The cause has, as previously mentioned, not been investigated further. The difference could, however, be due to a non-symmetric distribution of the B_y component of the IMF, since this causes an asymmetry between the two hemispheres. A positive $\boldsymbol{B}_y$ gives a stronger WAEJ in the Northern Hemisphere, while a negative $\boldsymbol{B}_y$ results in a stronger WAEJ in the Southern Hemisphere [Friis-Christensen et al., 2017].

The study of the oval size in the Northern Hemisphere by Meng [1979] (see Section 2.3) has revealed a dependence of oval size on the distance to the magnetic pole, with a smaller oval when the northern geomagnetic pole is close to local noon (see Section 2.4). This effect can be attributed to the conductivity configuration being dependent on the position of the sun. With a larger magnetic pole displacement on the Southern Hemisphere, this effect is likely larger (we have not found similar investigations on the southern auroral oval size). The interhemispherical differences in auroral oval size could likely be caused by the larger difference in solar illumination and thereby EUV conductivity. Statistical investigations binned according to longitude (proximity to the magnetic pole) could show the significance of the pole displacement in both Hemispheres. These could be a step in the direction to find the cause of the smaller southern oval, but have not been investigated further.

Figure 8.18(c) shows the corresponding sheet current densities as a function of MLT for the Southern (red) and Northern (blue) Hemisphere with error estimate (± 1 MAD) marked by the shaded area. MLT 23 to 11 shows the median strength of the sheet current densities of the WAEJ, and MLT 13 to 21, the strength of the EAEJ, explaining the change in sign between 11 and 13, and again between 21 and 23. The maximum strength of the WAEJ is found for both Hemispheres for $0 <$ MLT < 4, and the maximum strength of the EAEJ for $16 <$ MLT < 20. The strength of the EAEJ is almost identical (~ 150 A/km) in the two hemispheres, with the only exception of MLT $= 15$. The differences for the WAEJ are, however, much larger, especially for the region $6 <$ MLT < 12, where we find differences of up to 60 nT. The difference between the maximum and minimum in WAEJ for $0 <$ MLT < 10 is small (~ 40 nT), while the Southern Hemisphere shows larger variations (~ 100 nT) in strength within the same MLT range.

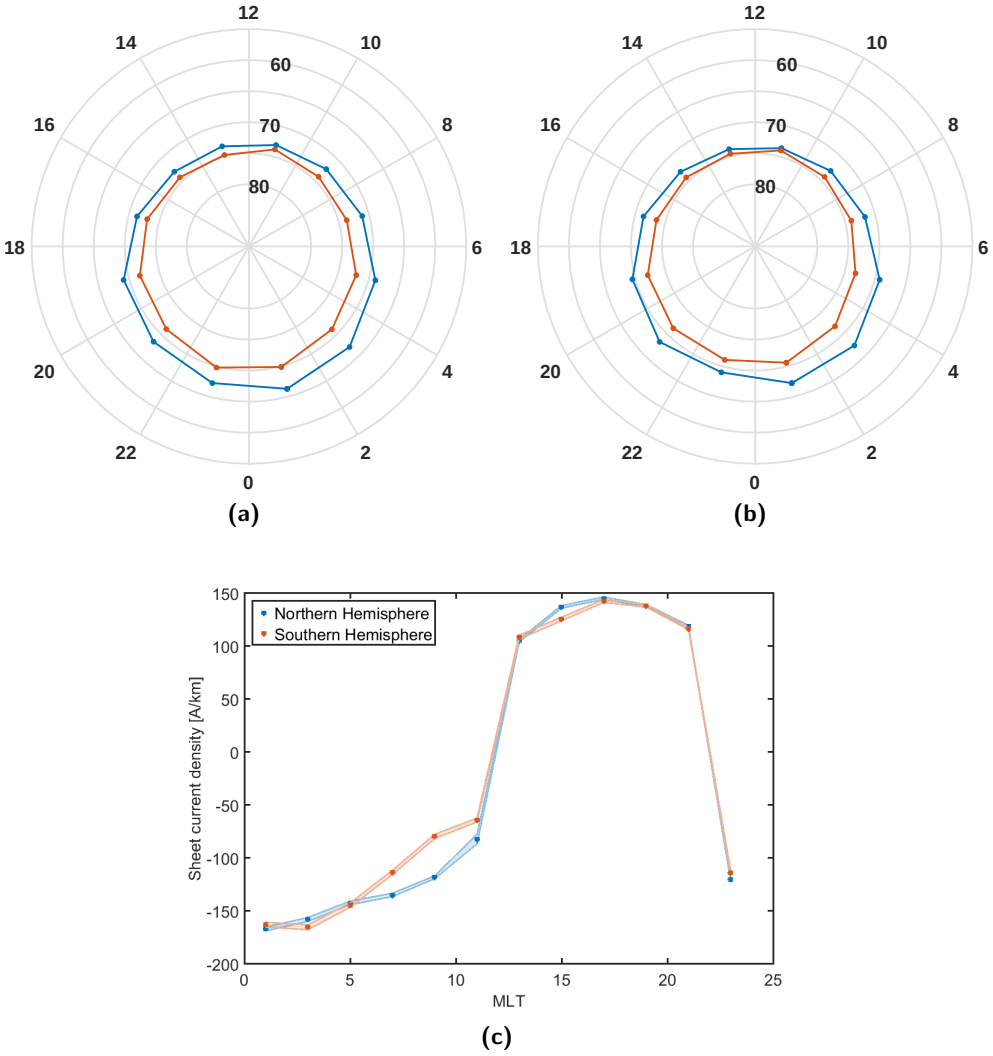

Figure 8.18: Median position of the peak intensity of the WAEJ and EAEJ as a function of MLT for (a) *Swarm* Alpha and Bravo 2013-2015 data and (b) CHAMP data. Shown in blue is results from the Northern Hemisphere, and in red, the Southern Hemisphere results. MLT 23 to 11 shows the average position of the WAEJ, while MLT 13 to 21 shows the average position of the EAEJ. (c) similar to (a) and (b), but for peak intensity in stead of median position estimated from CHAMP and *Swarm* data.

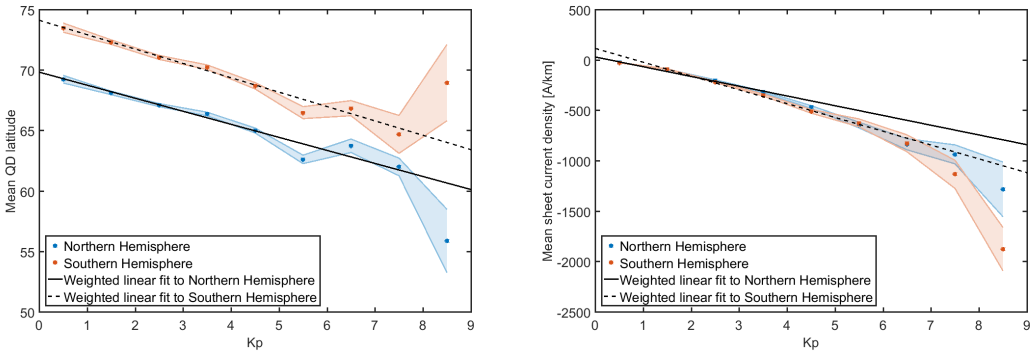

(a) Position of $\boldsymbol{J}^{\text{peak}}$ **(b)** Strength of $\boldsymbol{J}^{\text{peak}}$

Figure 8.19: Mean position (a) and strength (b) of $\boldsymbol{J}^{\text{peak}}$ as a function of Kp for the Northern (blue) and Southern (red) Hemisphere. Error estimates (± 1 MAD) are given in the shaded areas. The solid black line gives a linear fit to the Northern Hemisphere data, and the dashed black line to Southern Hemisphere data. The blue lines are equal to the blue lines in Figure 8.11.

A similar analysis, binned for different geomagnetic activity levels, is presented in Figure 8.19 with the Northern Hemisphere given in blue and the Southern in red. (a) shows the median position of the electrojet and (b) the median strength, both as a function of *Kp*, along with shaded error estimates. The blue line in both subfigures are identical to the blue line in Figure 8.11(a) and (b). As was found when binned according to MLT, we see significant higher QD latitudes for the southern hemisphere, resulting in a much smaller oval, compared to the average oval found for the Northern Hemisphere. The weighted linear fit to the position $y^{NH} = -(1.1 \pm 0.1)x + 69.9 \pm 0.3$ (Northern Hemisphere) and $y^{SH} = -(1.2 \pm 0.1)x + 74,1 \pm 0.3$ (Southern Hemisphere), return a very similar linear Kp dependence for both hemispheres, shifted approximately 4 degrees closer to the magnetic pole on the Southern Hemisphere. Taking the error estimates into account, we perform a significance test on the interhemispherical differences in slope (a in $y = ax + b$) and offset (b). This is done by performing a student's t-test of a null hypothesis. For the offset residual ($b(NH) - b(SH)$), the null hypothesis states that $b(NH) - b(SH)$ is not significantly different from zero. A joint error estimate of $\sigma = 0.42$ results in a t-value of

$$t = \frac{|b(NH) - b(SH)|}{\sigma} = \frac{4.2}{0.42} = 10.0 \tag{8.3}$$

Table lookup from Taylor [1982] reveals that the null hypothesis is rejected with a probability well within the normal accepted 95% confidence bounds [von Storch and Zwiers, 1999; Cowan, 1998], with a probability of 99.9994 for a t value of 5.0. A t-value of 1.0 for the slope residual reveals on the other hand only a probability of 68.27% that the two estimates of the slopes are different. We therefore conclude that the two estimates of a are not significantly different. To test the significance of the slope itself, we test the null hypothesis that $a(NH)$ is not significantly different from zero. This returns a t-value of 11, well within the accepted 95% confidence bounds.

The position of the ovals are within the ranges presented by Vennerstrom and Moretto [2013] and supported by results by Juusola et al. [2009] and Ahn et al. [2005]. The mean sheet current

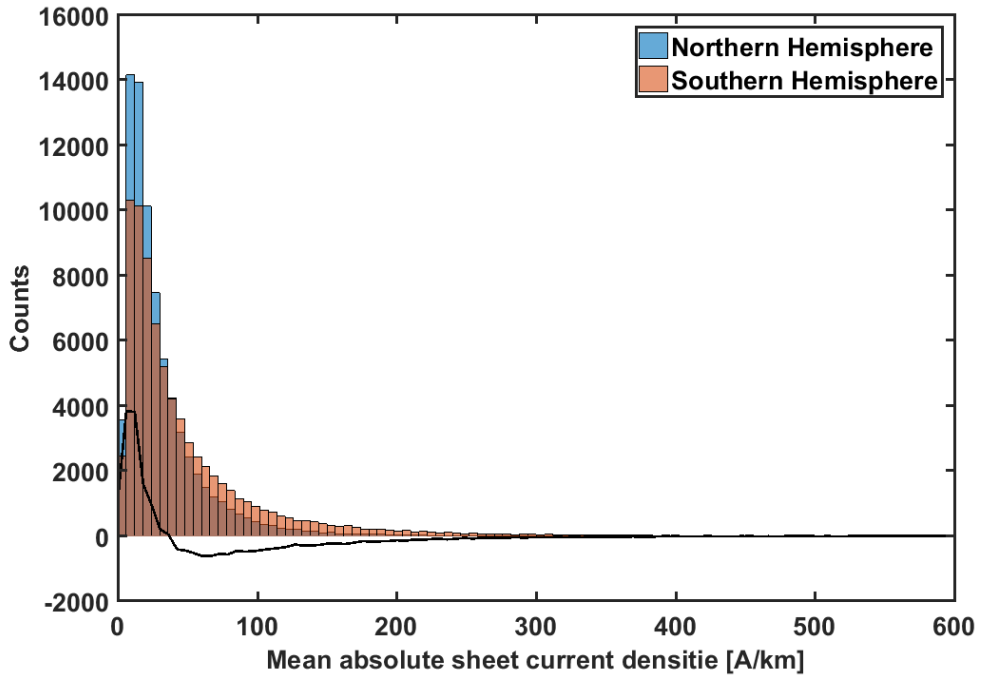

Figure 8.20: Histogram of the total polar current, $\boldsymbol{J}^{\text{tot}}$, for the Northern (blue) and Southern (red) Hemisphere. The black line gives the interhemispherical difference.

densities as a function of Kp, presented in Figure 8.19(b) supports the large interhemispherical similarities presented in Figure 8.18, with the exception of the highly disturbed Kp interval [8 9]. The lack of fit in this range is attributed the sparse data. Weighted linear fits of the sheet current density strength with Kp, $y^{NH} = -(97\pm7)x+33\pm9$ and $y^{SH} = -(101\pm9)x+35\pm12$ are, as also presented in Figure 8.11 not found to provide a satisfactory description of the Kp dependence in any of the hemispheres. t-values of 0.35 and 0.12 states that the slope and offset differences are different with 27.37% and 9.55% probability, revealing no significant difference in Kp dependence of the sheet current density strength between the two hemispheres.

If, in stead, we estimate the intensity of the currents as the total polar current ($\boldsymbol{J}^{\text{tot}}$), presented in Equation 8.1, we see a very different representation of the interhemispherical differences. The results are presented as a histogram of $\boldsymbol{J}^{\text{tot}}$ in Figure 8.20 and a bar plot of $\boldsymbol{J}^{\text{tot}}$ as a function of *Kp* in Figure 8.21. The last figure corresponds directly to Figure 8.19(b) found from the peak value, $\boldsymbol{J}^{\text{peak}}$, from each orbit. The histogram shows that both Hemispheres have mostly low auroral electrojet activity orbits, with a peak at approximately 12 A/km. Results for the Northern hemisphere are, however, more skewed towards lower intensities, than for the Southern Hemisphere, which has a smaller peak, and wider distribution.

The indication from Figure 8.20 of stronger sheet current densities in the Southern Hemisphere is supported by the bar plot in Figure 8.21, showing significantly stronger median sheet current densities for the southern hemispheres for all *Kp* values. This is in contradiction to the results presented in Figure 8.19, where only very small interhemispherical differences where found. A possible explanation is an insufficient removal of the unstable polar cap currents. For

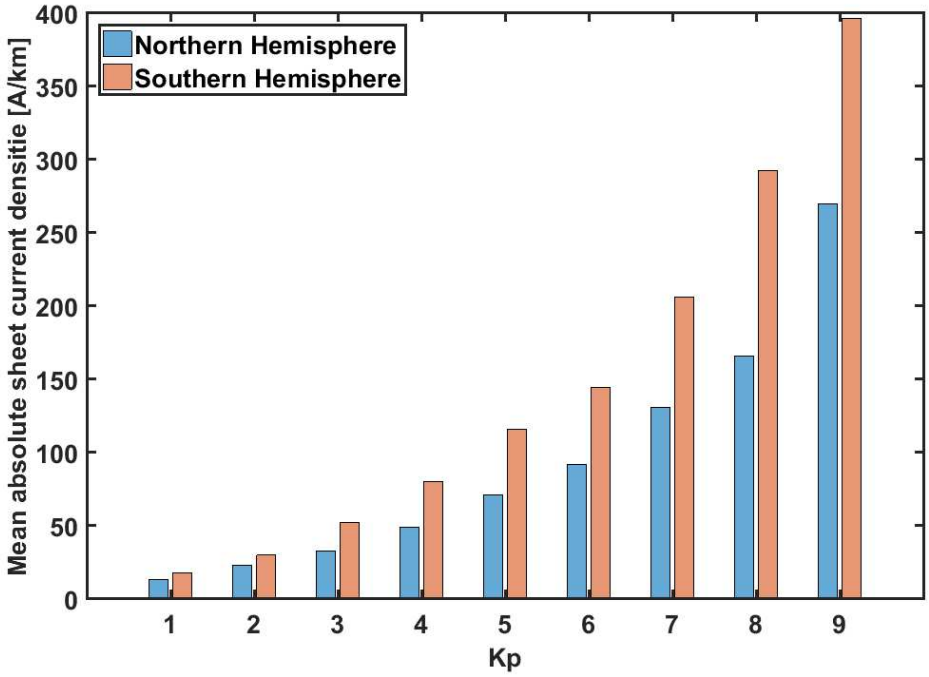

Figure 8.21: Median total polar current, $\boldsymbol{J}^{\text{tot}}$, binned according to Kp for the Northern (blue) and Southern (red) Hemisphere.

the peak value, this removal is of lesser importance, but cannot be ignored when estimating the total current. Stronger polar cap currents (or larger instabilities in the polar cap from the rotation of the line currents) in the Southern Hemisphere is needed for this explanation to hold.

Other studies, such as Vennerstrom and Moretto [2013], find that the overall statistical inter-hemispherical differences in both position and strength disappear when ordering the data in magnetic coordinates. One other study is found of the statistical inter-hemispherical differences in the strength of the electrojets. Coxon et al. [2016] uses measurements from the Active Magnetosphere and Planetary Electrodynamics Response Experiment (AMPERE) satellite project to give the total FAC for both Hemispheres. They find contradictory to our estimates stronger currents in the Northern Hemisphere. It is, however, important to note that their results are based on estimates of FACs and not the auroral electrojet currents.

When all of this is said, a stronger current in the Southern Hemisphere could be explained by an increase in solar intensity on the dayside, resulting in an increase in conductivity over the Northern Hemisphere. We do, however, find the differences too large to be adequately explained by this effect alone. Assuming that the total current is in fact larger in the Southern Hemisphere, and the polar cap instabilities have successfully been removed, the width of the current peak must be larger for the Southern Hemisphere, since the peak intensity (Figure 8.18) is found of similar size for both the Northern and Southern Hemisphere. This hypothesis could be tested by estimating the width of the peak, along with the peak intensity. The questions raised by this study warrant further investigations of a possible hemispherical bias in the total current estimates.

8.4 Further applications

From the results given in the previous section, it is reasonable to conclude that the data set comprised of 12 years (approximately 75000 orbits) of sheet current densities provides a good basis for investigating features of both statistical and space-time behaviour of the auroral electrojet system. The analyses paves the way for further research possibilities, not all possible to fit within the limits of this thesis. The following provides a short presentation of some of these possible applications.

- Combination of height integrated current density estimates with electric field measurements [*e.g.* Archer et al., 2015; Juusola et al., 2016], deriving height-integrated Hall conductivities.

- Closer investigation of the currents in comparisons with statistical estimations of the conductivity. Interhemispherical comparisons, normalized according to solar intensity and ionospheric conductivity, could reduce the conductivity based bias in the interhemispherical differences and highlight any magnetic deduced differences between the Southern and Northern Hemisphere.

- The intensity indices derived ($\boldsymbol{J}^{\text{tot}}$ and $\boldsymbol{J}^{\text{peak}}$) in the previous sections paves the way for a new way of selecting quiet time data for satellite derived internal field modelling, where very accurate input data (disturbance free) is crucial. Indices, such as the AE index, provide a measure of the disturbance level of the most disturbed local time. This is, however, not always a good measure of the disturbance of a specific orbit. Potential useful data are excluded from the field modelling, reducing the statistics and thereby accuracy and scale size of the results. An example of the potential is described in Figure 8.3 where we clearly find periods with high AE index and low intensity of $\boldsymbol{J}^{\text{peak}}$. Tests of this possible application has already been set in motion.

- An important validation of the estimated sheet current densities would be a comparison with ground observations. Since our model also applies to ground observations, it should be possible to use satellite derived sheet current densities to predict the ground level magnetic disturbance. Such comparison would provide a more independent measure of the inversion method, since the validating data is different from the input data. Induced currents will expectedly play a more important role, compared to investigations at satellite height, and this comparison would therefore furthermore provide a measure of the importance of induced currents. Regions with poor data fit could reveal regions of more diverse distributions of conductivities, due to the assumed constant conductivity in the introduction of induced currents.

- Further investigations of individual sheet current density profiles could provide additional information about the auroral electrojet system. Examples of this is the estimation of the width of the westward and eastward electrojets. The width of the current profile would be useful in understanding the interhemispherical differences, but also give an estimate of the width of the auroral oval. This could in turn be used to investigate how the current system maps to the magnetosphere. An estimation of the slope of the sheet current profile could give an estimate of the FAC, with a stronger FAC for steeper current profiles. The FACs are expected to lie in the region on each side of

the electrojet peaks (see Section 2.3). Determining the boundaries of the peaks would therefore give an estimate of the positions of Region 1 and 2 FACs. In this sense it could also be fruitful to compare FACs estimated from *Swarm* magnetic data, provided by the *Swarm* L2 FAC-single product [Ritter et al., 2013; He et al., 2012; ESA, 2017e] to both magnitudes determined by the slopes and in particular the position found by the boundaries of the current peaks.

- Improvement of model with partial D_1 and D_2 regularization of model parameters for better interpretation of the polar cap currents. We have in the method presented in this thesis focused on the currents in the auroral oval and lower latitudes. The regularization optimization has therefore focused on returning a model fit suitable in this region. This may, however, not be the optimum choice in regularization for the polar cap currents, which follow a different (flat) along track distribution. The flat distribution of the polar cap currents could be favoured by introducing a minimization of the first order differences of the model parameters inside the polar cap, and a minimization of the second order differences outside. The implementation should not be difficult, and we recommend to test this in further analysis of the method.

Chapter 9

Summary and conclusions

With the aim of developing a reliable automatic method, capable of returning sheet current density profiles of the auroral electrojet currents, the LCM and the 1D SECS methods were applied to magnetic field residual observations by CHAMP and *Swarm* satellites. The two methods were compared in a thorough validation of both synthetic case examples and application to satellite data. Tests of the impact of regularization methods furthermore provided important insight into the reaction of the methods to small variations. This gave an estimate of the reliability of the methods. We created a dataset from optimum values of regularization method and parameters consisting of the sheet current density profiles for nearly all 10 years of CHAMP data and two years of *Swarm* Alpha and Bravo crossings of the South and North Pole. Along with these, indices of the peak strength and position of the western and eastern electrojet, $\boldsymbol{J}^{peak}$, and the total sheet current density, $\boldsymbol{J}^{tot}$, were estimated for statistical purposes.

Summarizing the main results, the following is concluded

- The 1D SECS method was tested for estimation of the sheet current densities from synthetic and satellite magnetic field observations. Several issues were raised, including a high sensitivity to a set of adjustable parameters: model and observation spacing ($\delta\theta^{\text{mod}}$ and $\delta\theta^{\text{obs}}$), width of box function ($d\delta$), truncation parameters for the TSVD solution (ε_c and ε_d) and observation and model range. Variations in the adjustable parameters were shown in the synthetic case to have the largest impact on the estimate of the FACs. When applied to magnetic satellite observations, only a few days returned acceptable model fits. Several tests with the aim of improving the method were conducted, though none of them allowed the method to work for all the tested days. The poor model fit was attributed a breakdown of the 1D assumption, in approximately 60% of the orbits. In conclusion, we were not able to obtain robust implementation of the 1D SECS method.

- Application of the line current method to satellite magnetic observations was found to provide a robust measure of the auroral electrojet system. Assumption of electrojet alignment along constant QD contours was implemented in the method by applying a rotation of the line currents along $\hat{\boldsymbol{f}}_1$. This ensured a physically more correct estimate of the auroral electrojets along with an improvement over previous applications of the LCM. The method is found to return a robust measure of the sheet current densities both in

terms of choice in regularization parameter and the ability to handle possible data noise. Illustrating the inversion method through examples of different regularization methods, we argued the need for a rather complex regularization method on the along track first differences on input data: minimization of an L_1 model norm of the second order along track differences of model parameters along with a Huber-weighted data misfit measure.

- The robustness of the line current method was illustrated through variations in regularization parameter and input data. A study of the L-curve for six randomly chosen *Swarm* Alpha orbits showed that a common choice in regularization parameter, α^2, was possible. However, further investigations of a possible modification to the regularization parameter for CHAMP data are needed. Comparing the sheet current density profiles from 1000 *Swarm* Alpha orbits with orbit profiles from the side-by-side flying Charlie, revealed that Charlie is able to describe 97% of the variance from Alpha. The sheet current density profile was found only slightly affected by a removal of the magnetospheric correction. This indicates, together with the common choice in regularization parameter, a robust model insensitive to orbit sensitive factors, such as activity level.

- The line current method was able to return model fits to a high degree of accuracy. Variance ratios for 1000 *Swarm* Alpha orbits were found below $820 \cdot 10^{-6}$ and with a mean of $120 \cdot 10^{-6}$, indicating that even the worst orbits return acceptable model fits. The largest variance ratios were found for quiet days, where even small misfits result in a large increase of the signal to noise ratio. The reliability is furthermore explored by applying the method to 10 years of CHAMP data and two years of *Swarm* Alpha and Bravo data. From these 148004 pole crossing, 189 unstable orbits are detected from physically unrealistic peak values ($> 10^4$ A/km). The unstable orbits are all CHAMP orbits, and most likely a result of an underestimated regularization parameter for the CHAMP orbits. The reliability or performance ratio of 99.87% is concluded satisfactory for automatic implementation.

- Comparisons of sheet current densities for four single pole crossings estimated from the 1D SECS, 2D SECS, LCM and IM revealed a consistency in position within 2°. This is within the error of margin due to the 2° model spacing of the 1D SECS method. Larger differences are, however, found in the strength of the electrojet with discrepancies of up to 100% with the 1D SECS results and 28.6% with the 2D SECS results.

- Despite the additional information about FACs provided by the 1D SECS method, the high performance ratio of the line current method makes this a better candidate for automatic implementation. The LCM was therefore preferred in the remaining investigations of the auroral electrojet system.

- The line current method was applied to 10 years of CHAMP data and two years of *Swarm* Alpha and Bravo data to create a dataset consisting of the orbit-by-orbit sheet current densities for the region $\pm 40^\circ \beta$ from the northern and southern geomagnetic pole. The large dataset allowed large scale space-time and statistical studies of the auroral electrojet system on both hemispheres. Three orbit specific geomagnetic activity indices were furthermore found, representing the peak intensity, $\boldsymbol{J}^{\text{peak}}$, of the westward and eastward electrojet along with an estimate of the total polar current, $\boldsymbol{J}^{\text{tot}}$. These indices provide, contrary to other presented indices, a direct measure of the disturbance

level of each orbit, important for quiet time data selection. A squared coherence with the AE index of more than 0.9 for periods larger than two days, provided validation for the sheet current estimates, while differences highlighted the use of an orbit specific index.

- Space-time development of the auroral electrojet system was illustrated through two examples around Northern Hemisphere spring equinox 2014 and 2015. Presenting the sheet current densities in this way, was shown to be a good way to present the full lifetime of a magnetic storm, including the preceding and following period. The examples showed a clear difference between high and low geomagnetic activity level, along with a high visual consistency between the hemispheres. Largest differences were found during disturbed conditions and attributed to the fast changes in the auroral electrojet system during high geomagnetic activity. The high visual correlation is supported by a squared coherence of more than 0.9 for periods longer than two days.

- Longitudinal dependence of the auroral electrojet system was investigated by inter-satellite comparison between *Swarm* Alpha and Bravo. A correlation coefficient of 0.81 between estimates of $\boldsymbol{J}^{\text{tot}}$ supports that large sheet current densities in general are found during high activity periods. Some larger small-scale variations in the space-time development indicate, however, a presence of longitudinal dependence of the auroral electrojet system. The equatorial, longitudinal separation was on the 17$^{\text{th}}$ of March 2015 24.5°, indicating together with the large differences that even smaller longitudinal length scales might be important for the auroral electrojet system during geomagnetically disturbed conditions.

- Investigations of the sheet current density variation with solar activity showed a clear dependence of IMF direction, with stronger currents for a southward $\boldsymbol{B}_z$. A weaker $\boldsymbol{B}_y$ dependence was found, while expected hemispherical asymmetries were unclear - both attributed a limited data use. Seasonal differences were in a similar manner difficult to estimate due to the use of only one year of *Swarm* Alpha and Bravo observations.

- Variations with geomagnetic activity were investigated through dependence on Kp index. Sheet current densities presented as the robust mean in bins of 1 h MLT and 2° QD latitude for three ranges of Kp, showed an increasing westward and eastward electrojet current strength for increasing Kp. Maximum intensity of the westward electrojet was found between 01 and 05 MLT, and of the eastward electrojet in the MLT region between 15 and 18. A general equatorward expansion and increasing scatter was furthermore found for growing Kp, consistent with an expansion of the polar cap.

- Equatorward motion of the auroral electrojet system for increasing Kp was supported by an investigation of the average position of the peak intensity of the westward and eastward electrojet. Furthermore, consistently smaller oval was found for the Southern Hemisphere. Additional investigations are needed to provide a better understanding of the origin of the asymmetry. Displacement of the magnetic pole and the following asymmetrical conductivity was suggested as contributing factors. No significant differences where found in the strength of the sheet current densities.

- Investigation of the position and strength of $\boldsymbol{J}^{peak}$ revealed a similar dependence of Kp for Northern and Southern Hemisphere. A weighted linear fit to the position gave a significant linear dependence of $y^{NH} = -(1.1 \pm 0.1)x + 69.9 \pm 0.3$ for the Northern

Hemisphere and $y^{SH} = -(1.2 \pm 0.1)x + 74, 1 \pm 0.3$ for the Southern. The 4° difference in offset between the two hemispheres was found well within the accepted 95% confidence limit. However, a linear fit to the strength of $\boldsymbol{J}^{peak}$, was not found to provide a satisfactory description of the Kp dependence.

- Besides aforementioned applications of the model, a future lowering of the *Swarm* satellites would provide more detailed observations of the sheet current densities. Longitudinal differences estimated from the side-by-side flying Alpha and Charlie is presently not possible due to the distance between the satellites compared to the ionosphere. A lowering of the satellite pair or increased distance between the satellites would provide an observation spacial structure capable of estimating the instantaneous longitudinal dependence.

In conclusion, the work of this thesis presented a clear candidate for automatic application and near-real-time monitoring of the auroral electrojet system capable of returning robust estimates of the sheet current densities. We furthermore created a large dataset of the auroral region sheet current densities for the Northern and Southern Hemisphere with many future possible applications. The associated indices, $\boldsymbol{J}^{\text{tot}}$ and $\boldsymbol{J}^{\text{peak}}$ provide *e.g.* important information adaptive to data selection in internal field modelling.

Bibliography

Aakjær, Cecilie Drost, C., Olsen, N., and Finlay, C. (2016). Determining polar ionospheric electrojet currents from Swarm satellite constellation magnetic data. *Earth, Planets and Space*, 68(1). doi: 10.1186/s40623-016-0509-y.

Ahn, B.-H., Chen, G. X., Sun, W., Gjerloev, J. W., Kamide, Y., Sigwarth, J. B., and Frank, L. A. (2005). Equatorward expansion of the westward electrojet during magnetically disturbed periods. *Journal of Geophysical Research: Space Physics*, 110(A1). A01305.

Akasofu, S.-I. (1964). The development of the auroral substorm. *Planetary and Space Science*, 12:273–282.

Akasofu, S.-I., Perreault, P. D., Yasuhara, F., and Meng, C.-I. (1973). Auroral substorms and the interplanetary magnetic field. *Journal of Geophysical Research*, 78(31):7490–7508.

Amm, O. (1997). Ionospheric Elementary Current Systems in Spherical Coordinates and Their Application. *Journal of geomagnetism and geoelectricity*, 49(7):947–955.

Amm, O. (2001). The elementary current method for calculating ionospheric current systems from multisatellite and ground magnetometer data. *Journal of Geophysical Research: Space Physics*, 106(A11):24843–24855.

Amm, O. and Viljanen, A. (1999). Ionospheric disturbance magnetic field continuation from the ground to the ionosphere using spherical elementary current systems. *Earth, Planets and Space*, 51(6):431–440.

Angelopoulos, V., Baumjohann, W., Kennel, C. F., Coroniti, F. V., Kivelson, M. G., Pellat, R., Walker, R. J., Lühr, H., and Paschmann, G. (1992). Bursty bulk flows in the inner central plasma sheet. *Journal of Geophysical Research: Space Physics*, 97(A4):4027–4039.

Angelopoulos, V., Kennel, C. F., Coroniti, F. V., Pellat, R., Kivelson, M. G., Walker, R. J., Russell, C. T., Baumjohann, W., Feldman, W. C., and Gosling, J. T. (1994). Statistical characteristics of bursty bulk flow events. *Journal of Geophysical Research: Space Physics*, 99(A11):21257–21280.

Anger, C. D., Lui, A. T. Y., and Akasofu, S.-I. (1973). Observations of the auroral oval and a westward traveling surge from the Isis 2 satellite and the Alaskan meridian all-sky cameras. *Journal of Geophysical Research*, 78(16):3020–3026.

Archer, W. E., Knudsen, D. J., Burchill, J. K., Patrick, M. R., and St.-Maurice, J. P. (2015). Anisotropic core ion temperatures associated with strong zonal flows and upflows. *Geophysical Research Letters*, 42(4):981–986. 2014GL062695.

Ashour-Abdalla, M. (2015). *A Simulation Study of the Relationship Between Tail Dynamics and the Aurora*, chapter 5, pages 109–127. Springer International Publishing. Editor: SWH. Cowley, D. Southwood and S. Mitton.

Aster, R. C., Borchers, B., and Thurber, C. H. (2005). *Parameter Estimation and Inverse Problems*. Elsevier, 1. edition.

Baker, D. N., Pulkkinen, T. I., Angelopoulos, V., Baumjohann, W., and McPherron, R. L. (1996). Neutral line model of substorms: Past results and present view. *Journal of Geophysical Research: Space Physics*, 101(A6):12975–13010.

Bartels, J. (1932). Terrestrial-magnetic activity and its relations to solar phenomena. *Terrestrial Magnetism and Atmospheric Electricity*, 37(1):1–52.

Bartels, J. (1957). The geomagnetic measures for the time variations of solar corpuscular radiation, described for use in correlation studies in other geophysical fields. *Ann. Int. Geophys. Year 4, part 4*, 127.

Bartels, J., Heck, N. H., and Johnston, H. F. (1939). The three-hour-range index measuring geomagnetic activity. *Terrestrial Magnetism and Atmospheric Electricity*, 44:411–454.

Baumjohann, W. and Treumann, R. A. (2012). *Basic Splace Plasma Physics*. Imperial College Press, revised edition edition. ISBN-13: 976-1-84816-895-4.

BBC (2016). Iron 'jet stream' detected in Earth's outer core. URL: http://www.bbc.com/news/science-environment-38372342.

Belian, R. D., Cayton, T. E., and Reeves, G. D. (2013). *Quasi-Periodic Global Substorm Generated Flux Variations Observed at Geosynchronous Orbit*, pages 143–148. American Geophysical Union. Edited by M. Ashour-Abdalla, T. Chang and P. Dusenber.

Birkeland, K. (1908). *The Norwegian Aurora Polaris Expedition 1902-1903*, volume 1. H. Aschehoug, Christiania/Oslo.

Borowski, J. E. (2016). *Solar Wind-Magnetosphere Interaction*, chapter 4, pages 48–73. Taylor & Francis Group. Edited by V . Khazanov Georgev.

Burch, J. L. (1974). Observations of interactions between interplanetary and geomagnetic fields. *Reviews of Geophysics*, 12(3):363–378.

Burch, J. L., Goldstein, J., and Sandel, B. R. (2004). Cause of plasmasphere corotation lag. *Geophysical Research Letters*, 31(5):n/a–n/a. L05802.

Burch, J. L., Torbert, R. B., Phan, T. D., Chen, L.-J., Moore, T. E., Ergun, R. E., Eastwood, J. P., Gershman, D. J., Cassak, P. A., Argall, M. R., Wang, S., Hesse, M., Pollock, C. J., Giles, B. L., Nakamura, R., Mauk, B. H., Fuselier, S. A., Russell, C. T., Strangeway, R. J., Drake, J. F., Shay, M. A., Khotyaintsev, Y. V., Lindqvist, P.-A., Marklund, G., Wilder, F. D.,

Young, D. T., Torkar, K., Goldstein, J., Dorelli, J. C., Avanov, L. A., Oka, M., Baker, D. N., Jaynes, A. N., Goodrich, K. A., Cohen, I. J., Turner, D. L., Fennell, J. F., Blake, J. B., Clemmons, J., Goldman, M., Newman, D., Petrinec, S. M., Trattner, K. J., Lavraud, B., Reiff, P. H., Baumjohann, W., Magnes, W., Steller, M., Lewis, W., Saito, Y., Coffey, V., and Chandler, M. (2016). Electron-scale measurements of magnetic reconnection in space. *Science*.

Campbell, W. H. (2003). *Introduction to geomagnetic fields*. Cambridge University Press, 2. edition edition.

Christiansen, F., Papitashvili, V. O., and Neubert, T. (2002). Seasonal variations of high-latitude field-aligned currents inferred from Ørsted and Magsat observations. *J. Geophys. Res.*, 107(A2):1029.

Colomb, F., Alonso, C., Hofmann, C., and Nollmann, I. (2004). SAC-C mission, an example of international cooperation . *Advances in Space Research*, 34(10):2194 – 2199. Space Science Education and Promoting North-South Partnership in Space Research.

Constable, C. G. (1988). Parameter estimation in non-gaussian noise. *Geophys. J.*, 94:131–142.

Cowan, G. (1998). *Statistical Data Analysis*. Oxford Science Publications.

Cowley, S. and Lockwood, M. (1992). Excitation and decay of solar wind-driven flows in the magnetosphere-ionophere system. In *Annales Geophysicae*, volume 10, pages 103–115. Copernicus.

Cowley, S. W. H., Morelli, J. P., and Lockwood, M. (1991). Dependence of convective flows and particle precipitation in the high-latitude dayside ionosphere on the X and Y components of the interplanetary magnetic field. *Journal of Geophysical Research: Space Physics*, 96(A4):5557–5564.

Coxon, J. (2015). *The role of Birkeland currents in the Dungey cycle*. PhD thesis, University of Leicester.

Coxon, J. C., Milan, S. E., Carter, J. A., Clausen, L. B. N., Anderson, B. J., and Korth, H. (2016). Seasonal and diurnal variations in AMPERE observations of the Birkeland currents compared to modeled results. *Journal of Geophysical Research: Space Physics*, 121(5):4027–4040. 2015JA022050.

DEMA (2017). Nationalt Risikobillede - National risk assesment. Published by Danish emergency management agency (DEMA) http://brs.dk/viden/publikationer/Documents/Nationalt-Risikobillede-2017.pdf.

DeMets, C., Gordon, R. G., Argus, D. F., and Stein, S. (1994). Effect of recent revisions to the geomagnetic reversal time scale on estimates of current plate motions. *Geophysical Research Letters*, 21(20):2191–2194.

Dungey, J. W. (1961). Interplanetary Magnetic Field and the Auroral Zones. *Phys. Rev. Lett.*, 6:47–48.

EASA (2012). Effects of Space Weather on Aviation. EASA Safety Information Bulletin - http://www.skybrary.aero/bookshelf/books/1803.pdf.

Ekblom, H. (1987). The L1-estimate as limiting case of an Lp-or Huber-estimate. *Statistical data analysis based on the L1-norm and related methods*, pages 109–116.

Elphinstone, R. D., Murphree, J. S., and Cogger, L. L. (1996). What is a global auroral substorm? *Reviews of Geophysics*, 34(2):169–232.

Emery, W. J. and Thomson, R. E. (2004). *Data Analysis Methods in Physical Oceanography*. Elsevier B.V, 2. edition.

ESA (2016). Orbit Evolution of the Swarm Mission. https://earth.esa.int/documents/10174/1568455/Orbit-Evolution-of-the-Swarm-Mission. Assessed online 03.04.2017.

ESA (2017a). Space in images. http://www.esa.int/spaceinimages/Images/. Website assesed on 31.03.2017.

ESA (2017b). Supersonic plasma jets discovered. http://www.esa.int/Our_Activities/Observing_the_Earth/Swarm/Supersonic_plasma_jets_discovered. Assessed online 18.04.2017.

ESA (2017c). Swarm. http://www.esa.int/Our_Activities/Observing_the _Earth/Swarm/. Website assesed on 31.03.2017.

ESA (2017d). Swarm detects asymmetry. http://www.esa.int/Our_Activities/Observing_the _Earth/Swarm/Swarm_detects_asymmetry. Assessed online 18.04.2017.

ESA (2017e). Swarm Level 2 Processing Facility Product specification for L2 Products and Auxiliary Products (SW-DS-DTU-GS-0001). Doc. no. SW-DS-GFZ-GS-0001, review 2T, date: 2017-01-19. https://earth.esa.int/documents/10174/1514862/Swarm_L2_Product_Specification. Assessed online 25.01.2017.

Farquharson, C. G. and Oldenburg, D. W. (1998). Non-linear inversion using general measures of data misfit and model structure. *Geophysical Journal International*, 134(1):213–227.

Feldstein, Y. and Starkov, G. (1967). Dynamics of auroral belt and polar geomagnetic disturbances. *Planetary and Space Science*, 15(2):209 – 229.

Finlay, C., Lesur, V., Thébault, E., Vervelidou, F., Morschhauser, A., and Shore, R. (2016a). Challenges Handling Magnetospheric and Ionospheric Signals in Internal Geomagnetic Field Modelling. *Space Science Reviews*, 206(1):1–33.

Finlay, C. C., Olsen, N., Kotsiaros, S., Gillet, N., and Tøffner-Clausen, L. (2016b). Recent geomagnetic secular variation from Swarm and ground observatories as estimated in the CHAOS-6 geomagnetic field model. *Earth, Planets and Space*, 68(1):112.

Finlay, C. C., Olsen, N., and Tøffner-Clausen, L. (2015). DTU candidate field models for IGRF-12 and the CHAOS-5 geomagnetic field model. *Earth, Planets and Space*, 67(1):1–17.

Forbes, A. (1987). General instrumentation. *Geomagnetism*, 1:51–142. Edited by J. A. Jacobs.

Frankel, R. B. (1984). Magnetic guidance of organisms. *Annual review of biophysics and bioengineering*, 13(1):85–103.

Friis-Christensen, E., Finlay, C. C., Hesse, M., and Laundal, K. M. (2017). Magnetic Field Perturbations from Currents in the Dark Polar Regions During Quiet Geomagnetic Conditions. *Space Science Reviews*, pages 1–17.

Friis-Christensen, E., Kamide, Y., Richmond, A. D., and Matsushita, S. (1985a). Interplanetary magnetic field control of high-latitude electric fields and currents determined from Greenland Magnetometer Data. *Journal of Geophysical Research: Space Physics*, 90(A2):1325–1338.

Friis-Christensen, E., Kamide, Y., Richmond, A. D., and Matsushita, S. (1985b). Interplanetary magnetic field control of high-latitude electric fields and currents determined from Greenland Magnetometer Data. *Journal of Geophysical Research: Space Physics*, 90(A2):1325–1338.

Friis-Christensen, E., Lühr, H., and Hulot, G. (2006). Swarm: A constellation to study the Earth's magnetic field. *Earth, Planets and Space*, 58:351–358.

Friis-Christensen, E., Lühr, H., Knudsen, D., and Haagmans, R. (2008). Swarm – An Earth Observation Mission investigating Geospace. *Advances in Space Research*, 41(1):210 – 216.

Friis-Christensen, E. and Wilhjelm, J. (1975). Polar cap currents for different directions of the interplanetary magnetic field in the $Y - Z$-plane. *J. Geophys. Res.*, 80:1248–1260.

Fujii, R., Iijima, T., Potemra, T. A., and Sugiura, M. (1981). Seasonal dependence of large-scale Birkeland currents. *Geophysical Research Letters*, 8(10):1103–1106.

Fukushima, N. (1976). Generalized theorem for no ground magnetic effect of vertical currents connected with Pedersen currents in the uniform-conductivity ionosphere. *Report of Ionosphere and Space Research in Japan, vol. 30, no. 1-2, June 1976, p. 35-40.*, 30:35–40.

Fung, S. F., Tepper, J. A., and Cai, X. (2016). Magnetospheric state of sawtooth events. *Journal of Geophysical Research: Space Physics*, 121(8):7860–7869. 2016JA022693.

Gauss, C. F. (1839). *Allgemeine Theorie des Erdmagnetismus*. 1838. Göttinger Magnetischer Verein.

GFZ (2017). Kp index archive. ftp://ftp.gfz-potsdam.de/pub/home/obs/kp-ap/tab/. Assesed online 28.02.2017.

Gilbert, W. (1958). *De magnete*. Courier Corporation.

Gjerloev, J. W. and Hoffman, R. A. (2014). The large-scale current system during auroral substorms. *Journal of Geophysical Research: Space Physics*, 119(6):4591–4606. doi: 10.1002/2013JA019176.

Glassmeier, K.-H. and Tsurutani, B. T. (2014). Carl Friedrich Gauss; General Theory of Terrestrial Magnetism; a revised translation of the German text. *History of Geo- and Space Sciences*, 5(1):11–62.

Griffiths, D. J. (1981). *Introduction to electrodynamics*. Prentice-Hall International, 3. edition.

Grocott, A. and Milan, S. E. (2014). The influence of IMF clock angle timescales on the morphology of ionospheric convection. *Journal of Geophysical Research: Space Physics*, 119(7):5861–5876.

Guo, J., Pulkkinen, T. I., Tanskanen, E. I., Feng, X., Emery, B. A., Liu, H., Liu, C., and Zhong, D. (2014). Annual variations in westward auroral electrojet and substorm occurrence rate during solar cycle 23. *Journal of Geophysical Research: Space Physics*, 119(3):2061–2068.

Haaland, S. E., Paschmann, G., Förster, M., Quinn, J. M., Torbert, R. B., Mcilwain, C. E., Vaith, H., Puhl-Quinn, P. A., and Kletzing, C. A. (2007). High-latitude plasma convection from Cluster EDI measurements: method and IMF-dependence. *Annales Geophysicae*, 25(1):239–253.

Hansen, P. and O'Leary, D. (1993). The use of the L-curve in the regularization of discrete ill-posed problems. *SIAM Journal on Scientific Computing*, 14(6):1487–1503.

Hansen, P. C. (1992). Analysis of Discrete Ill-Posed Problems by Means of the L-Curve. *SIAM Review*, 34(4):pp. 561–580.

Hansen, P. C. (1999). *The L-curve and its use in the numerical treatment of inverse problems*. IMM, Department of Mathematical Modelling, Technical University of Denmark.

Hansen, P. C. (2010). *Discrete Inverse Problems*. Society for Industrial and Applied Mathematics SIAM.

He, M., Vogt, J., Lühr, H., Sorbalo, E., Blagau, A., Le, G., and Lu, G. (2012). A high-resolution model of field-aligned currents through empirical orthogonal functions analysis (MFACE). *Geophysical Research Letters*, 39(18):n/a–n/a. L18105.

Heppner, J. P. and Maynard, N. C. (1987). Empirical high-latitude electric field models. *Journal of Geophysical Research: Space Physics*, 92(A5):4467–4489.

Huber, P. J. (1964). Robust Estimation of a Location Parameter. *Ann. Math. Statist.*, 35(1):73–101.

Hughes, W. (1995). The magnetopause, magnetotail, and magnetic reconnection. *Introduction to Space Physics*, pages 227–287.

Hulot, G., Eymin, C., Langlais, B., Mandea, M., and Olsen, N. (2002). Small-scale structure of the geodynamo inferred from Oersted and Magsat satellite data. *Nature*, 416. doi:10.1038/416620a.

IMAGE (2017). International Monitor for Auroral Geomagnetic Effects. http://space.fmi.fi/image/beta/?page=home. Weside assessed on 22.04.2017.

Jackson, A., Constable, C., and Gillet, N. (2007). Maximum entropy regularization of the geomagnetic core field inverse problem. *Geophysical Journal International*, 171(3):995–1004.

Jackson, A., Jonkers, A. R., and Walker, M. R. (2000). Four centuries of geomagnetic secular variation from historical records. *Philosophical Transactions of the Royal Society of London A: Mathematical, Physical and Engineering Sciences*, 358:957–990.

Juusola, L. (2009). *Observations of the solar wind-magnetosphere-ionosphere coupling*. PhD thesis, Department of Physics, Faculty of Science, University of Helsinki, Finland.

Juusola, L. (2016). Personal correspondance. Finnish Meteorological Institute, P.O.Box 503, FI-00101 Helsinki, Finland.

Juusola, L., Amm, O., Kauristie, K., and Viljanen, A. (2007). A model for estimating the relation between the Hall to Pedersen conductance ratio and ground magnetic data derived from CHAMP satellite statistics. *Annales Geophysicae*, 25(3):721–736.

Juusola, L., Amm, O., and Viljanen, A. (2006). One-dimensional spherical elementary current systems and their use for determining ionospheric currents from satellite measurements. *Earth Planet Space*, 58.

Juusola, L., Archer, W. E., Kauristie, K., Burchill, J. K., Vanhamäki, H., and Aikio, A. T. (2016). Ionospheric conductances and currents of a morning sector auroral arc from Swarm-A electric and magnetic field measurements. *Geophysical Research Letters*, 43(22):11,519–11,527. 2016GL070248.

Juusola, L., Kauristie, K., Amm, O., and Ritter, P. (2009). Statistical dependence of auroral ionospheric currents on solar wind and geomagnetic parameters from 5 years of CHAMP satellite data. *Annales Geophysicae*, 27(3):1005–1017.

Juusola, L., Milan, S., Lester, M., Grocott, A., and Imber, S. (2014). Interplanetary magnetic field control of the ionospheric field-aligned current and convection distributions. *Journal of Geophysical Research: Space Physics*, 119(4):3130–3149.

Kamide, Y., Richmond, A. D., and Matsushita, S. (1981). Estimation of ionospheric electric fields, ionospheric currents, and field-aligned currents from ground magnetic records. *Journal of Geophysical Research: Space Physics*, 86(A2):801–813.

Kauristie, K., Pulkkinen, T. I., Pellinen, R. J., and Opgenoorth, H. J. (1997). What can we tell about global auroral-electrojet activity from a single meridional magnetometer chain? *Annales Geophysicae*, 14(11):1177–1185.

Kim, H., Clauer, C. R., Engebretson, M. J., Matzka, J., Sibeck, D. G., Singer, H. J., Stolle, C., Weimer, D. R., and Xu, Z. (2015). Conjugate observations of traveling convection vortices associated with transient events at the magnetopause. *Journal of Geophysical Research: Space Physics*, 120(3):2015–2035. doi: 10.1002/2014JA020743.

Kisabeth, J. L. and Rostoker, G. (1974). The expansive phase of magnetospheric substorms: 1. Development of the auroral electrojets and auroral arc configuration during a substorm. *Journal of Geophysical Research*, 79(7):972–984. doi: 10.1029/JA079i007p00972.

Kivelson, M. G. and Russell, C. T. (1995). *Introduction to space physics*. Cambridge University Press, Cambridge.

Kother, L., Hammer, M. D., Finlay, C. C., and Olsen, N. (2015). An equivalent source method for modelling the global lithospheric magnetic field. *Geophysical Journal International*, 203(1):553.

Langel, R., Ousley, G., Berbert, J., Murphy, J., and Settle, M. (1982). The MAGSAT mission. *Geophysical Research Letters*, 9(4):243–245.

Laundal, K. M. (2010). *Auroral Imaging as a Tracer of Global Magntospheric Dynamics*. PhD thesis, Universty of Bergen.

Laundal, K. M., Finlay, C. C., and Olsen, N. (2016a). Sunlight effects on the 3D polar current system determined from low Earth orbit measurements. *Earth, Planets and Space*, 68(1):142.

Laundal, K. M. and Gjerloev, J. W. (2014). What is the appropriate coordinate system for magnetometer data when analyzing ionospheric currents? *Journal of Geophysical Research: Space Physics*, 119(10):8637–8647.

Laundal, K. M., Gjerloev, J. W., Østgaard, N., Reistad, J. P., Haaland, S., Snekvik, K., Tenfjord, P., Ohtani, S., and Milan, S. E. (2016b). The impact of sunlight on high-latitude equivalent currents. *Journal of Geophysical Research: Space Physics*, 121(3):2715–2726. 2015JA022236.

Laundal, K. M. and Richmond, A. D. (2017). Magnetic Coordinate Systems. *Space Science Reviews*, 206(1):27–59.

Lesur, V., Wardinski, I., Hamoudi, M., and Rother, M. (2010). The second generation of the GFZ reference internal magnetic model: GRIMM-2. *Earth, Planets and Space*, 62:765–773.

Lühr, H., Park, J., Gjerloev, J. W., Rauberg, J., Michaelis, I., Merayo, J. M. G., and Brauer, P. (2015). Field-aligned currents' scale analysis performed with the Swarm constellation. *Geophysical Research Letters*, 42(1):1–8. 2014GL062453.

Liu, H. and Lühr, H. (2005). Strong disturbance of the upper thermospheric density due to magnetic storms: CHAMP observations. *Journal of Geophysical Research: Space Physics*, 110(A9).

Livermore, P. W., Hollerbach, R., and Finlay, C. C. (2016). An accelerating high-latitude jet in Earth's core. *Nature Geoscience*.

Lockwood, M. (2013). Reconstruction and Prediction of Variations in the Open Solar Magnetic Flux and Interplanetary Conditions. *Living Reviews in Solar Physics*, 10(1):4.

Lopez, R. E. (2000). The current sheet disruption model for substorm expansion phase onset: Background, arguments, and relationship to global substorm evolution. *Advances in Space Research*, 25(7):1667 – 1677.

Lopez, R. E., Goodrich, C. C., Reeves, G. D., Belian, R. D., and Taktakishvili, A. (1994). Midtail plasma flows and the relationship to near-Earth substorm activity: A case study. *Journal of Geophysical Research: Space Physics*, 99(A12):23561–23569.

Mareschal, M. (1986). Modelling of natural sources of magnetospheric origin in the interpretation of regional induction studies: A review. *Surveys in Geophysics*, 8(3):261–300.

Maule, C. F. (2005). *Geophysical interpretation of the magnetic field models*. PhD thesis, University of Copenhagen.

McIntosh, D. H. (1959). On the Annual Variation of Magnetic Disturbance. *Philosophical Transactions of the Royal Society of London A: Mathematical, Physical and Engineering Sciences*, 251(1001):525–552.

McPherron, R. L. (1970). Growth phase of magnetospheric substorms. *Journal of Geophysical Research*, 75(28):5592–5599.

McPherron, R. L. (1991). Physical processes producing magnetospheric substorms and magnetic storms. In Jacobs, J. A., editor, *Geomagnetism*, pages 593–739.

McPherron, R. L., Russell, C. T., and Aubry, M. P. (1973). Satellite studies of magnetospheric substorms on August 15, 1968: 9. Phenomenological model for substorms. *Journal of Geophysical Research*, 78(16):3131–3149.

Meng, C.-I. (1979). Diurnal variation of the auroral oval size. *Journal of Geophysical Research: Space Physics*, 84:5319–5324.

Menke, W. (2012). *Geophysical Data Analysis: Discrete Inverse Theory, Matlab edition*. Elsevier, 3. edition.

Merrill, R. T. and McFadden, P. L. (1999). Geomagnetic polarity transitions. *Rev. Geophys.*, 37(2):201–226.

Milan, S. E., Clausen, L. B. N., Coxon, J. C., Carter, J. A., Walach, M.-T., Laundal, K., Østgaard, N., Tenfjord, P., Reistad, J., Snekvik, K., Korth, H., and Anderson, B. J. (2017). Overview of Solar Wind–Magnetosphere–Ionosphere–Atmosphere Coupling and the Generation of Magnetospheric Currents. *Space Science Reviews*, pages 1–27.

Milan, S. E., Provan, G., and Hubert, B. (2007). Magnetic flux transport in the Dungey cycle: A survey of dayside and nightside reconnection rates. *Journal of Geophysical Research: Space Physics*, 112(A1):n/a–n/a. A01209.

Moretto, T., Olsen, N., Ritter, P., and Lu, G. (2002). Investigating the auroral electrojets with low altitude polar orbiting satellites. *Annales Geophysicae*, 20(7):1049–1061.

Moretto, T., Sibeck, D. G., and Watermann, J. F. (2004). Occurrence statistics of magnetic impulsive events. *Annales Geophysicae*, 22(2):585–602.

Mosegaard, K. and Hansen, T. M. (2016). *Inverse Methods*, pages 7–27. John Wiley & Sons, Inc.

Neubert, T., Mandea, M., Hulot, G., von Frese, R., Primdahl, F., Joergensen, J. L., Friis-Christensen, E., Stauning, P., Olsen, N., and Risbo, T. (2001). Ørsted satellite captures high-precision geomagnetic field data. *EOS Trans. AGU*, 82(7):81–88.

Nishida, A. and Maezawa, K. (1971). Two basic modes of interaction between the solar wind and the magnetosphere. *Journal of Geophysical Research*, 76(10):2254–2264.

Olsen, N. (1996). A new tool for determining ionospheric currents from magnetic satellite data. *Geophysical Research Letters*, 23(24):3635–3638.

Olsen, N. (2007). Ørsted. In Gubbins, D. and Herrero-Bervera, E., editors, *Encyclopedia of Geomagnetism and Paleomagnetism*, pages 743–745. Springer, Heidelberg.

Olsen, N. (2016). *Earth's Magnetic Field*, chapter 3, pages 35–45. Taylor & Francis Group. Edited by V . Khazanov Georgev.

Olsen, N., Friis-Christensen, E., Floberghagen, R., Alken, P., Beggan, C. D., Chulliat, A., Doornbos, E., da Encarnac, J. T., Hamilton, B., Hulot, G., van den IJssel, J., Kuvshinov, A., Lesur, V., Luehr, H., Macmillan, S., Maus, S., Noja, M., Olsen, P. E. H., Park, J., Plank, G., Puethe, C., Rauberg, J., Ritter, P., Rother, M., Sabaka, T. J., Schachtschneider, R., Sirol, O., Stolle, C., Thebault, E., Thomson, A. W. P., Toeffner-Clausen, L., Velimsky, J., Vigneron, P., and Visser, P. N. (2013). The Swarm Satellite Constellation Application and Research Facility (SCARF) and Swarm Data Products. *Earth, Planets and Space*, 65:1189–1200.

Olsen, N., Lühr, H., Finlay, C. C., Sabaka, T. J., Michaelis, I., Rauberg, J., and Tøffner-Clausen, L. (2014). The CHAOS-4 geomagnetic field model. *Geophysical Journal International*, 197(2):815–827.

Olsen, N., Moretto, T., and Friis-Christensen, E. (2002). New approaches to explore the Earth's magnetic field. *Journal of Geodynamics*, 33(1–2):29 – 41. Earth's Gravity and Magnetic Fields from Space.

Olsen, N. and Stolle, C. (2012). Satellite geomagnetism. *Annual Review of Earth and Planetary Sciences*, 40:441–465.

Papitashvili, V. O., Christiansen, F., and Neubert, T. (2002). A new model of field-aligned currents derived from high-precision satellite magnetic field data. *Geophysical Research Letters*, 29(14):28–1–28–4.

Pirjola, R., Kauristie, K., Lappalainen, H., Viljanen, A., and Pulkkinen, A. (2005). Space weather risk. *Space Weather*, 3(2).

Pirjola, R., Viljanen, A., Pulkkinen, A., and Amm, O. (2000). Space weather risk in power systems and pipelines. *Physics and Chemistry of the Earth, Part C: Solar, Terrestrial & Planetary Science*, 25(4):333 – 337.

Poedjono, B., Beck, N., Buchanan, A., Borri, L., Maus, S., Finn, C. A., Worthington, E. W., White, T., et al. (2013). Improved Geomagnetic Referencing in the Arctic Environment (Russian). In *SPE Arctic and Extreme Environments Technical Conference and Exhibition*. Society of Petroleum Engineers.

Prölss, G. W. (2010). *Physics of the Earth's Space Environment - An Introduction*. Springer. Translated by Michael Bird.

Pulkkinen, A., Amm, O., Viljanen, A., Group, B. W., et al. (2003). Separation of the geomagnetic variation field on the ground into external and internal parts using the spherical elementary current system method. *Earth, planets and space*, 55(3):117–129.

Pulkkinen, A., Lindahl, S., Viljanen, A., and Pirjola, R. (2005). Geomagnetic storm of 29–31 October 2003: Geomagnetically induced currents and their relation to problems in the Swedish high-voltage power transmission system. *Space Weather*, 3(8):n/a–n/a. S08C03.

Pulkkinen, T. I., Partamies, N., McPherron, R. L., Henderson, M., Reeves, G. D., Thomsen, M. F., and Singer, H. J. (2007). Comparative statistical analysis of storm time activations and sawtooth events. *Journal of Geophysical Research: Space Physics*, 112(A1):n/a–n/a. A01205.

Reigber, C., Lühr, H., and Schwintzer, P. (2002). CHAMP mission status. *Adv. Space Res.*, 30:129–134.

Richmond, A., Lu, G., Emery, B., and Knipp, D. (1998). The {AMIE} procedure: Prospects for space weather specification and prediction. *Advances in Space Research*, 22(1):103 – 112. Solar-Terrestrial Relations: Predicting the Effects on the Near-Earth Environment.

Richmond, A. D. (1974). The computation of magnetic effects of field-aligned magnetospheric currents. *J. Atmos. Terr. Phys.*, 36:245–252.

Richmond, A. D. (1995). Ionospheric Electrodynamics Using Magnetic Apex Coordinates. *Journal of geomagnetism and geoelectricity*, 47(2):191–212.

Ritter, P. and Lühr, H. (2006). Search for magnetically quiet CHAMP polar passes and the characteristics of ionospheric currents during the dark season. *Annales Geophysicae*, 24(11):2997–3009.

Ritter, P., Lühr, H., and Rauberg, J. (2013). Determining field-aligned currents with the Swarm constellation mission. *Earth, Planets and Space*, 65(11):9.

Ritter, P., Lühr, H., Viljanen, A., Amm, O., Pulkkinen, A., and Sillanpää, I. (2004). Ionospheric currents estimated simultaneously from CHAMP satelliteand IMAGE ground-based magnetic field measurements: a statisticalstudy at auroral latitudes. *Annales Geophysicae*, 22(2):417–430.

Ritter, P., Viljanen, A., Lühr, H., Amm, O., and Olsen, N. (2003). Ionospheric currents from champ magnetic field data — comparison with ground based measurements. In Reigber, C., Lühr, H., and Schwintzer, P., editors, *First CHAMP Mission Results for Gravity, Magnetic and Atmospheric Studies*, pages 347–352. Springer Berlin Heidelberg.

Rostoker, G. (1972). Geomagnetic indices. *Reviews of Geophysics*, 10(4):935–950.

Rostoker, G., Akasofu, S.-I., Foster, J., Greenwald, R., Kamide, Y., Kawasaki, K., Lui, A., McPherron, R., and Russell, C. (1980). Magnetospheric substorms—definition and signatures. *Journal of Geophysical Research: Space Physics*, 85(A4):1663–1668.

Russell, C. T. and McPherron, R. L. (1973). Semiannual variation of geomagnetic activity. *Journal of Geophysical Research*, 78(1):92–108.

Sabaka, T. J., Olsen, N., and Langel, R. A. (2000). A comprehensive model of the near-earth magnetic field: Phase 3. NASA GSFC, Greenbelt, MD 20771.

Sabaka, T. J., Olsen, N., and Purucker, M. E. (2004). Extending comprehensive models of the Earth's magnetic field with Ørsted and CHAMP data. *Geophys. J. Int.*, 159:521–547.

Sabaka, T. J., Olsen, N., Tyler, R. H., and Kuvshinov, A. (2015). CM5, a pre-*Swarm* comprehensive magnetic field model derived from over 12 years of CHAMP, Ørsted, SAC-C and observatory data. *Geophys. J. Int.*, 200:1596–1626.

Sabaka, T. J., Tøffner-Clausen, L., and Olsen, N. (2013). Use of the Comprehensive Inversion Method for Swarm satellite data analysis. *Earth, Planets and Space*, 65:1201–1222.

Shea, M., Smart, D., McCracken, K., Dreschhoff, G., and Spence, H. (2006). Solar proton events for 450 years: The Carrington event in perspective. *Advances in Space Research*, 38(2):232 – 238. The Great Historical Geomagnetic Storm of 1859: A Modern Look.

Singh, A. K., Rawat, R., and Pathan, B. M. (2013). On the UT and seasonal variations of the standard and SuperMAG auroral electrojet indices. *Journal of Geophysical Research: Space Physics*, 118(8):5059–5067.

Smith, A. (2017). Personal correspondence. University of Edinburgh, Grant Institute, The King's Buildings, James Hutton Road, Edinburgh EH9 3FE.

Østgaard, N. and Laundal, K. M. (2013). *Auroral Asymmetries in the Conjugate Hemispheres and Interhemispheric Currents*, pages 99–112. American Geophysical Union.

Stolle, C., Michaelis, I., and Rauberg, J. (2016). The role of high-resolution geomagnetic field models for investigating ionospheric currents at low Earth orbit satellites. *Earth, Planets and Space*, 68(1):110.

Sugiura, M. (1964). Hourly values of equatorial Dst for IGY. *Ann. Int. Geophys. Year*, 35:49.

Sugiura, M. and Davis, T. (1966). Auroral electrojet activity index AE and its universal time variations. *J. Geophys. Res*, 71:785–801.

Tanaka, T. (2001). Interplanetary magnetic field B y and auroral conductance effects on high-latitude ionospheric convection patterns. *Journal of Geophysical Research: Space Physics*, 106(A11):24505–24516.

Tanskanen, E. I., Viljanen, A., Pulkkinen, T. I., Pirjola, R., Häkkinen, L., Pulkkinen, A., and Amm, O. (2001). At substorm onset, 40% of AL comes from underground. *Journal of Geophysical Research: Space Physics*, 106(A7):13119–13134.

Taylor, J. R. (1982). *An Introduction to Error Analysis - The study of uncertainties in physical Measurements*. University Science Books, 2. edition edition.

Thébault, E., Finlay, C. C., Beggan, C. D., Alken, P., Aubert, J., Barrois, O., Bertrand, F., Bondar, T., Boness, A., Brocco, L., Canet, E., Chambodut, A., Chulliat, A., Coïsson, P., Civet, F., Du, A., Fournier, A., Fratter, I., Gillet, N., Hamilton, B., Hamoudi, M., Hulot, G., Jager, T., Korte, M., Kuang, W., Lalanne, X., Langlais, B., Léger, J.-M., Lesur, V., Lowes, F. J., Macmillan, S., Mandea, M., Manoj, C., Maus, S., Olsen, N., Petrov, V., Ridley, V., Rother, M., Sabaka, T. J., Saturnino, D., Schachtschneider, R., Sirol, O., Tangborn, A., Thomson, A., Tøffner-Clausen, L., Vigneron, P., Wardinski, I., and Zvereva, T. (2015).

International Geomagnetic Reference Field: the 12th generation. *Earth, Planets and Space*, 67(1):79.

Thorup, K. (2007). Solving the mystery of bird migration: Tracking small birds from space. Bird Ringing Centre, Zoological Museum, University of Copenhagen. URL: http://www.dtusat.dtu.dk/fileadmin/docs/payload/Bird_proposal.pdf.

Tikhonov, A. N. (1963). Solution of incorrectly formulated problems and the regularization method. *Soviet Math. Dokl.*, 4:1035–1038. English translation of Dokl. Akad. Nauk. SSSR, 151 (1963), pp. 501–504.

Untiedt, J. and Baumjohann, W. (1993). Studies of polar current systems using the IMS Scandinavian magnetometer array. *Space Science Reviews*, 63(3-4):245–390.

Vanhamäki, H., Amm, O., and Viljanen, A. (2003). One-dimensional upward continuation of the ground magnetic field disturbance using spherical elementary current systems. *Earth, planets and space*, 55(10):613–625.

Vennerstrom, S. and Moretto, T. (2013). Monitoring auroral electrojets with satellite data. *Space Weather*, 11(9):509–519.

Viljanen, A. (2012). Description of the magnetospheric/ionospheric sources. In *The Magnetotelluric Method - Theory and practice*. Cambridge University Press. Edited by: Alan D. Chave and Alan G. Jones.

Viljanen, A., Amm, O., and Pirjola, R. (1999). Modeling geomagnetically induced currents during different ionospheric situations. *Journal of Geophysical Research: Space Physics*, 104(A12):28059–28071.

Viljanen, A. and Pirjola, R. (1994). Geomagnetically induced currents in the Finnish high-voltage power system. *Surveys in Geophysics*, 15(4):383–408.

von Storch, H. and Zwiers, F. W. (1999). *Statistical Analysis in Climate Research.* Cambridge University Press, 2. edition edition.

WDCG (2015). World Data Center for Geomagnetism (WDCG), Kyoto University, http://wdc.kugi.kyoto-u.ac.jp/aeasy/index.html.

Weimer, D. R. (2001). Maps of ionospheric field-aligned currents as a function of the interplanetary magnetic field derived from Dynamics Explorer 2 data. *Journal of Geophysical Research: Space Physics*, 106(A7):12889–12902.

Weimer, D. R. (2005). Improved ionospheric electrodynamic models and application to calculating Joule heating rates. *Journal of Geophysical Research: Space Physics*, 110(A5):n/a–n/a. A05306.

Weimer, D. R. (2013). An empirical model of ground-level geomagnetic perturbations. *Space Weather*, 11(3):107–120.

Weimer, D. R., Clauer, C. R., Engebretson, M. J., Hansen, T. L., Gleisner, H., Mann, I., and Yumoto, K. (2010). Statistical maps of geomagnetic perturbations as a function of the interplanetary magnetic field. *Journal of Geophysical Research: Space Physics*, 115(A10):n/a–n/a. A10320.

Weygand, J. M., Amm, O., Angelopoulos, V., Milan, S. E., Grocott, A., Gleisner, H., and Stolle, C. (2012). Comparison between SuperDARN flow vectors and equivalent ionospheric currents from ground magnetometer arrays. *Journal of Geophysical Research: Space Physics*, 117(A5):n/a–n/a. A05325.

Wiltschko, W. and Wiltschko, R. (2005). Magnetic orientation and magnetoreception in birds and other animals. *Journal of Comparative Physiology A*, 191(8):675–693.

Appendix A

Determining polar ionospheric electrojet currents from Swarm satellite constellation magnetic data

The following presents the conference and peer reviewed contributions.

Swarm Science meeting, Copenhagen, June 2014
Cecilie Drost Aakjær, Nils Olsen and Christopher C. Finlay, *Modelling the magnetic field of the polar electrojet* - Poster presentation

IAGA, Prague, June 2015
Cecilie Drost Aakjær, Nils Olsen and Christopher C. Finlay, *Investigating the polar electrojet using Swarm satellite magnetic data* - Poster presentation

ESA Living Planet, Prague, May 2016
Cecilie Drost Aakjær, Nils Olsen and Christopher C. Finlay, Investigating the polar electrojet using *Swarm* satellite magnetic data - Poster presentation

Journal article, June 2016
Cecilie Drost Aakjær, Nils Olsen and Christopher C. Finlay, *Determining polar ionospheric electrojet currents from Swarm satellite constellation magnetic data*, Earth, Planets and Space. The article is appended in the following pages.

Swarm data quality workshop, September 2016
Cecilie Drost Aakjær, Nils Olsen and Christopher C. Finlay, *Determining polar ionospheric currents from Swarm magnetic data* - Oral presentation

Aakjær *et al. Earth, Planets and Space* (2016) 68:140
DOI 10.1186/s40623-016-0509-y

Earth, Planets and Space

FULL PAPER

Open Access

Determining polar ionospheric electrojet currents from *Swarm* satellite constellation magnetic data

Cecilie Drost Aakjær*, Nils Olsen and Christopher C. Finlay

Abstract

We determine the strength and location of the ionospheric currents responsible for the polar electrojets from magnetic data collected by the *Swarm* satellite constellation on an orbit-by-orbit basis. The ionospheric currents are modelled using a simple, yet robust, method by a series of line currents at 110 km altitude (corresponding to the ionospheric E-layer) perpendicular to the satellite orbit, separated by 1° (about 113 km). We assess the reliability of our method, with the aim of a possible near-real-time application. A study of the effect of different regularization methods is therefore carried out. An L_1 model regularization of the second-order spatial differences, and robust treatment of the data (to account for non-Gaussian error distributions), yields the most encouraging results. We apply our approach to two three-weekly data periods in March 2014 (geomagnetic quiet conditions) and March 2015 (more disturbed conditions), respectively. Our orbit-by-orbit approach also allows the temporal evolution of the polar electrojets to be investigated. We find remarkable agreement of the ionospheric activity in Northern and Southern polar regions, with correlation exceeding 0.9 for periods longer than two days. Reliability of the approach is shown by three key results: (1) a common regularization parameter for all orbits with enough data coverage, (2) 0.95 squared coherence with the Auroral Electrojet index, and (3) 0.97 squared coherence is found between the side-by-side flying satellites, Alpha and Charlie, indicating a method invariant to small changes in data input. All these results indicate a possible automated near-real-time application.

Keywords: Geomagnetism, Field modelling, Ionosphere, *Swarm*

Introduction

Geomagnetic reference models provide a good description of the main parts of Earth's magnetic field, including contributions from the core and crust, as well as the large-scale magnetospheric (e.g. Finlay et al. 2016; Lesur et al. 2010; Olsen et al. 2014). Non-ionospheric field (e.g. Sabaka et al. 2004, 2015) contributions are also well described by modern models. The situation is, however, different in the polar regions, where the large temporal and spatial variability of electric currents in the polar ionosphere makes their description difficult, and their prediction almost impossible.

These ionospheric currents give rise to a variety of important space weather effects, influencing the performance and reliability of spaceborn and ground-based technological systems. Problems in ground-based systems occur for instance due to the secondary, Earth-induced, electric fields and corresponding currents. For directional drilling in polar regions disturbances in the magnetic field caused by strong ionospheric currents may hamper accurate well positioning (Poedjono et al. 2013). Ionospheric currents may also lead to increased drag on low-altitude spacecraft (Liu and Lühr 2005; Pirjola et al. 2005). Better understanding of the time–space structure of polar ionospheric currents and in particular their improved modelling are therefore of great importance, not only for advances in fundamental space research but also regarding practical applications.

*Correspondence: cda@space.dtu.dk
Division of Geomagnetism, DTU Space, Technical University of Denmark, Diplomvej 371, Kongens Lyngby, Denmark

There are two major constituents to magnetic disturbance fields at polar latitudes: (1) electrical currents in the ionospheric E-layer (at an altitude of about 110 km) form the *polar electrojets* (PEJs) and (2) currents flowing along field lines of the ambient magnetic field feeding the PEJs by connecting the ionosphere and the magnetosphere. These so-called *field-aligned currents* (FACs) result in large magnetic field disturbances at satellite altitude, in particular in the east-west magnetic field component.

The PEJs have been successfully estimated from ground magnetic data (e.g. Amm 1997; Friis-Christensen et al. 1985; Kamide et al. 1981; Richmond et al. 1998). Indices monitoring the electrojet activity, such as the *Auroral Electrojet* (AE) index (Sugiura and Davis 1966) have been developed. These indices provide important information on the state of the polar ionosphere, but are restricted by the positions of the magnetometer stations. Since primarily stations from the Northern Hemisphere are used, the resulting indices mainly reflect PEJ activity in that hemisphere.

From magnetic ground observations it is only possible to estimate the equivalent currents, e.g. (hypothetic) horizontal ionospheric currents that would cause the same magnetic field disturbance as the observed one. Magnetic observations taken at satellite height in addition allow the estimation of the FACs, which is a clear advantage compared to ground observations. Furthermore, satellites allow access to the entire, mainly north-south-directed, current density profile, in contrast to what is possible from ground observations, and thereby provide a better description of the currents position and magnitude as a function of latitude. The global coverage of satellite data also enables interhemispheric comparisons. With these advantages in mind, several studies of ionospheric currents have been conducted using satellite measurements from, e.g., the *Magsat*, *Ørsted*, and *CHAMP* satellites (Olsen 1996; Ritter et al. 2003).

The magnetic field produced by an electric current is, at least in the vicinity of the current, always perpendicular to the current direction. This means that the magnetic field caused by FACs is perpendicular to the field line and hence not observable in the magnetic component parallel to the field line. As a consequence, the magnetic field intensity, $F = |\mathbf{B}|$, which by definition is the field component parallel to the magnetic field, is only marginally affected by FACs. Field intensity, F, is, however, sensitive to contributions from the horizontal currents in the ionospheric E-layer that form the PEJs. Observations of F collected by satellites can therefore be used to determine these currents.

A model study of the PEJ's using *Magsat* scalar magnetic satellite data and a current model consisting of a series of line currents perpendicular to the satellite track was presented by Olsen (1996) and later applied to *CHAMP* satellite data by Ritter et al. (2003) and Ritter et al. (2004). The use of scalar magnetic satellite data is a simplification compared to using the full vector data, resulting in similar results to a ground magnetic chain. The line current method has been applied to multi-satellite data by Olsen et al. (2002) and Moretto et al. (2002).

Juusola et al. (2006) proposed an alternative approach for monitoring the auroral activity from magnetic satellite data. They worked with a 1D version of the 2D *Spherical Elementary Current System* (SECS) method developed by Amm (1997) for application to *CHAMP* satellite vector data. By using vector data they were able to estimate not only the horizontal currents but also the FACs. The use of vector data in the 1D SECS method may, however, introduce both a complication in computation and an error source due to stronger contamination by unwanted sources such as the FAC in the radial magnetic vector component compared to only using measurements of the magnetic field intensity.

A simple approach to determine the location and strength of the PEJs from magnetic satellite data was presented by Vennerstrom and Moretto (2013). Their method corresponds roughly to finding the position and amplitude of the PEJs in the current profiles determined using the line current model of Olsen (1996).

With the aim of a possible near-real-time monitoring of the time–space structure of polar electrojet activity, we aim at developing a reliable and simple approach, while still estimating entire current profile along the satellite tracks. We therefore applied the line current model of Olsen (1996) to *Swarm* satellite magnetic data and investigated how different regularization methods affect the model results. By applying the method to *Swarm* magnetic data, we do not only gain new insights concerning the current system in the ionosphere, but also have the opportunity to explore previously unavailable results regarding longitudinal variations of the PEJs thanks to the unique constellation of the *Swarm* satellites.

The trio of *Swarm* satellites (e.g. Friis-Christensen et al. 2008) has been in orbit since 22 November 2013. Two of the satellites, called Alpha and Charlie, fly side by side at an altitude of about 450 km (as of January 2016) in a near-polar orbit of inclination 87.4° with an east-west separation of 1.4° in longitude (corresponding to about 160 km at the equator). The third satellite, Bravo, has an orbital inclination of 88° and is flying at an altitude of approximately 520 km. The different orbital inclination of the satellites results in different drift rates in local time (LT). The Bravo satellite in November 2015 (i.e. two years after launch) measured the magnetic field at a local time 2.6 h ahead of the lower satellite pair Alpha and Charlie.

Each of the three satellites carry, amongst other instruments, an absolute scalar magnetometer (ASM) for measuring the magnetic field intensity F, a vector fluxgate magnetometer (VFM) measuring the three vector components of the magnetic field, and a triple-head star imager to determine orientation.

The first part of the paper presents the chosen model parametrization along with a description of the model estimation scheme and an exploration of various regularization methods. Next we present results from a single orbit crossing and then move on to consider time dependence in three weeks of data for both the Northern and Southern Hemisphere. We also compare our results with the Auroral Electrojet index, a ground-based measure of PEJ activity. Finally, results obtained with data from all three *Swarm* satellites are compared, and the effects of secondary, Earth-induced, currents are discussed.

Model parameterization

We describe the polar ionospheric currents by a series of line currents placed at an altitude of 110 km in the ionospheric E-layer, perpendicular to the satellite track and separated in horizontal (along-track) direction by $\Delta = 113$ km corresponding to 1°. The geometry of the model is shown in Fig. 1. The magnetic field due to ionospheric E-layer currents is a Laplacian potential field at satellite altitude, and thus the strength of the magnetic field, and the spatial structure of the ionospheric currents, depends on the distance to the measurements. A typical rule of thumb in this case is that one cannot resolve structure of scale smaller than half the distance to the measurements. Since the *Swarm* satellites measure at a height of minimum 340 km above the ionosphere, it is hardly possible to distinguish between a continuous current distribution and a series of discrete line currents separated by 1° (corresponding to about 113 km). We therefore use a series of discrete line current separated by 1°.

As mentioned previously, electric currents at satellite altitudes are predominantly confined to flow parallel to the field lines of the ambient magnetic field $\mathbf{B}_0$ due to the nearly vanishing transverse electrical conductivity in this region. These FACs do, at least to first order, not contribute to the magnetic field component $F = B_{||}$ parallel to the ambient field $\mathbf{B}_0$. In the ionospheric E-layer, however, the transverse conductivity is comparably large, resulting in horizontal currents causing magnetic signatures that do not contribute to $F = B_{||}$. The magnetic field intensity F can therefore be used to investigate the horizontal currents flowing in the ionospheric E-layer. Although this is strictly true only for a uniform ambient field $\mathbf{B}_0$, FACs give, even for a real distribution of currents, only a very small contribution to F.

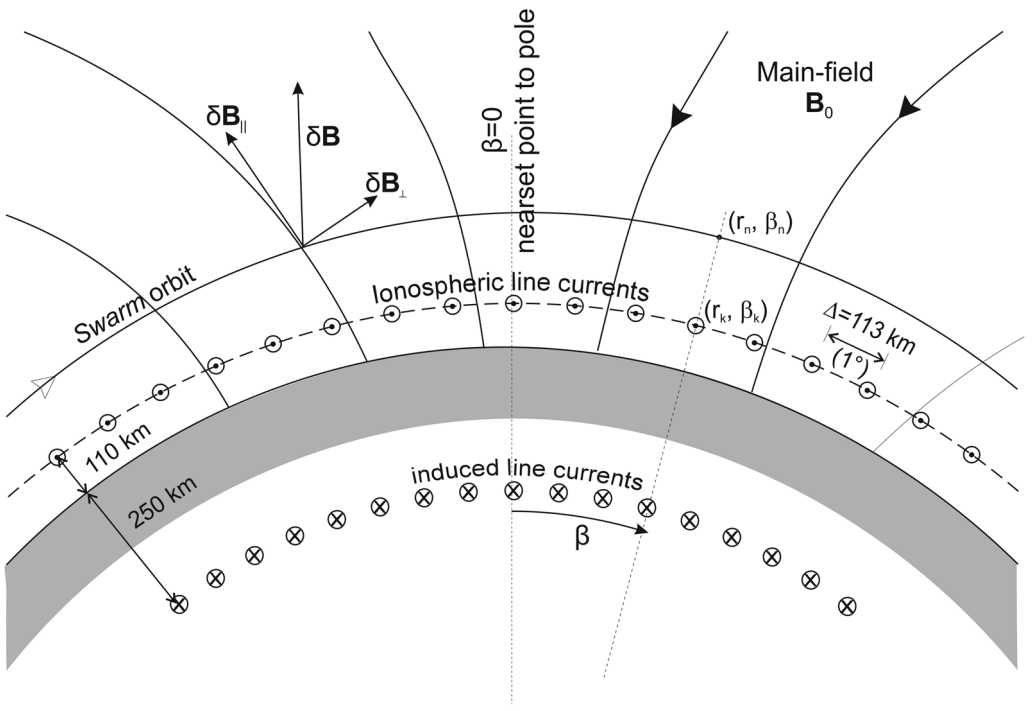

Fig. 1 Geometry of the model

As input data we use field intensity anomaly values $\delta F = F^{\text{obs}} - F^{\text{mod}}$ obtained from satellite observations of the Mag LR 1 Hz L1b magnetic field intensity, F^{obs} downsampled to 10 s, after removal of model values, F^{mod}, given by the CHAOS-5 field model (Finlay et al. 2015). This model provides estimates for the core and crustal field contributions as well as the contributions from the large-scale magnetospheric field, the time dependence of which is given by the *RC* index, which describes the strength of the magnetospheric ring current (Olsen et al. 2014).

The contribution from one single line current to the magnetic field intensity δF is given, following Olsen (1996), by

$$\begin{aligned} \delta F_n &= \frac{\mu_0}{2\pi} \frac{\xi_{n,k} \cos I_n + \eta_{n,k} \sin I_n}{\xi_{n,k}^2 + \eta_{n,k}^2} \cdot j_k \\ \eta_{n,k} &= r_k \sin(\beta_n - \beta_k) \\ \xi_{n,k} &= r_n - r_k \cos(\beta_n - \beta_k) \end{aligned} \tag{1}$$

where $\mu_0 = 4\pi \cdot 10^{-7}$ Vs/Am is vacuum magnetic permeability, I_n is the magnetic inclination of the main field model, $\mathbf{B}_0$, at the satellite location (r_n, β_n), and j_k is the amplitude of the kth line current at location (r_k, β_k). η_n and ξ_n measure the radial and horizontal distance, respectively. β_n and β_k are along-track arc parameters describing the distance from the closest approach to the magnetic North geomagnetic pole (or South geomagnetic pole) for the observation locations and line current locations, respectively, as shown in Fig. 1.

The magnetic field disturbance caused by a superposition of the contributions from single line currents described by Eq. (1) results in a model of the form

$$\boldsymbol{d} = \boldsymbol{G}\boldsymbol{m} \tag{2}$$

where $\boldsymbol{d}$ is the data vector consisting of the N observations, δF_n, with $n = 1, \ldots, N$, $\boldsymbol{m}$ is the vector of the M model parameters (the line current amplitudes), j_k, with $k = 1, \ldots, M$, and $\boldsymbol{G}$ is the design matrix of size $N \times M$ with elements

$$g_{n,k} = \frac{\mu_0}{2\pi} \frac{\xi_{n,k} \cos I_n + \eta_{n,k} \sin I_n}{\xi_{n,k}^2 + \eta_{n,k}^2}. \tag{3}$$

The sheet current density $J(\beta_k)$ is estimated from the model parameters by dividing the line current amplitudes j_k (the model parameters) by the distance, $\Delta\beta = 113$ km, between the line currents that corresponds to 1° at 110 km altitude. Since the spacing is equidistant in β, the sheet current density is simply found as

$$J(\beta_k) = \frac{j_k}{\Delta\beta} = \frac{j_k}{113 \text{ km}} \tag{4}$$

Model estimation

The M model parameters j_k are estimated by solving the linear inverse problem described in Eq. (2). An *iteratively reweighted least squares* (IRLS) approach with Huber weights (Constable 1988; Huber 1964) is used in order to handle a possibly non-Gaussian data error distribution. Although formally overdetermined (since $N > M$), the problem is ill-conditioned, and thus, the use of unconstrained least squares results in huge variations of the amplitudes of neighbouring line currents. In order to avoid this instability, we adopt a regularization approach (Aster et al. 2005; Menke 2012).

We carried out tests on a range of different regularization norms including: zeroth-order Tikhonov regularization (Tikhonov 1963), i.e. minimizing the sum of the squares of the line current strengths; higher-order Tikhonov regularization (Aster et al. 2005) considering finite differences of the line current strengths in the along-track direction; maximum entropy regularization (Jackson et al. 2007) as well as the use of L1 rather than L2 norms (Farquharson and Oldenburg 1998). Below we focus on the two following approaches that were found to perform well:

1 Minimization of an L_2 norm of the model parameters [i.e. zeroth-order Tikhonov regularization, see Aster et al. (2005)] and a Huber-weighted misfit measure. This is implemented through an IRLS technique, where the model at the $(i+1)$th iteration is determined by

$$\boldsymbol{m}_{i+1}^{L_2} = (\boldsymbol{G}^T \boldsymbol{W}_i^d \boldsymbol{G} + \alpha^2 \boldsymbol{I})^{-1} \boldsymbol{G}^T \boldsymbol{W}_i^d \boldsymbol{d}. \tag{5}$$

Here $\boldsymbol{I}$ is the identity matrix of size $M \times M$, α^2 is a parameter controlling the strength of the regularization, and $\boldsymbol{W}_i^d$ is the data weight matrix. α^2 is adjusted to achieve the desired trade-off between data misfit and model complexity. Its value and choice thereof is discussed further in the section "Choice of regularization parameter, α^2". The Huber-weighted misfit approach allows non-Gaussian errors to be handled by applying small weights to outliers through a series of iterations. $\boldsymbol{W}_i^d$ is the Huber weight matrix for the i'th iteration with diagonal elements $w_{i,n} = \min\left(\frac{c\sigma_i}{|\Delta\delta F|}\right)$. c is here a constant typically 1.5, σ is the standard deviation of the model residuals $\Delta\delta F = \delta F^{obs} - \delta F^{\text{mod}}$, where δF^{mod} are the model predictions of the observations. This solution will be referred to below as the L_2 norm solution.

2 Minimization of an L_1 norm of the second-order differences of model parameters and a Huber-weighted

misfit measure. This is also implemented via IRLS via the scheme

$$\boldsymbol{m}_{i+1}^{\boldsymbol{L_1}} = (\boldsymbol{G}^T \boldsymbol{W}_i^d \boldsymbol{G} + \alpha^2 \boldsymbol{D}^T \boldsymbol{W}_i^m \boldsymbol{D})^{-1} \boldsymbol{G}^T \boldsymbol{W}_i^d \boldsymbol{d}. \quad (6)$$

$\boldsymbol{D}$ is the second-order finite-difference operator, controlling the second-order difference minimization of the model parameters (Aster et al. 2005), and $\boldsymbol{W}_i^m$ is a reweighting matrix implementing the L_1 minimization of the model parameters (Farquharson and Oldenburg 1998). The elements of the diagonal matrix $\boldsymbol{W}_i^m$ are found using Ekbloms measure, where $(W_{kk}^m = (j_k^2 + \epsilon^2)^{-1/2}$ Ekblom (1987). ϵ ensures a non-singular solution at $j_k = 0$. A sufficiently small value of ϵ compared to the magnitude of the model parameters was chosen. Note that $\boldsymbol{D}^T \boldsymbol{W}_i^m \boldsymbol{D}$ is non-dimensionless and α^2 in Eq. 6 will therefore have a different unit than in Eq. 5. This solution will be referred to below as the L_1 norm solution.

Results and discussion

Examples of geomagnetically quiet and disturbed periods

We first illustrate our approach with a few examples, representing geomagnetic quiet and disturbed conditions, respectively. We have chosen *Swarm* Alpha orbit no. 6248 on 4 January 2015 13:36 to 14:01 UT, corresponding to a *magnetic local time* (MLT) of midnight around 60° *Quasi-Dipole* (QD) latitude. Since ionospheric conductivity and currents are guided by the geometry of Earth's main field, it is advantageous to describe the currents using magnetic coordinates like the QD latitude (Richmond 1995). This was a moderately disturbed period, with index of global geomagnetic activity $\mathrm{Kp} = 4^+$. As an example of quiet-time conditions, we have chosen orbit no. 6493 from 20 January 12:37 to 13:02 UT, at a similar MLT but with a Kp index of 0^+.

The top row of Fig. 2 shows the observations of magnetic field intensity F, and the obtained data fit, the middle row shows the corresponding model residuals, and the bottom row presents the estimated sheet current density, J, for the disturbed day (left), and the quiet day (right).

Shown in green is the observed magnetic field signature δF (after removal of core, crust, and magnetospheric contributions), along with model predictions obtained using L_1 (black) and L_2 (red) norm regularization. A simple least squares solution with zeroth-order Tikhonov regularization is given in blue for comparison. Both regularization schemes, with $\alpha^2 = 6.4 \cdot 10^{-15} \mathrm{nT} \cdot \mathrm{A}^{-2}$ (L_1) and $\alpha^2 = 3.6 \cdot 10^{-27} \mathrm{nT} \cdot \mathrm{A}^{-2} (L_2)$, are able to produce an extremely good fit to the observed field intensity. The chosen values of α^2 are discussed in the section "Choice of regularization parameter, α^2".

The variance ratios,

$$\frac{\sigma^2_{\Delta\delta F}}{\sigma^2_{\delta F}}, \quad (7)$$

where $\Delta\delta F$ are the residuals between observations and the model predictions for the L_1 or for the L_2 solution are found to: $4.1 \cdot 10^{-6}$ (L_1) and $9.2 \cdot 10^{-6}$ (L_2) for the disturbed day (orbit 6248), and $39 \cdot 10^{-6}$ (L_1) and $67 \cdot 10^{-6}$ (L_2) during quiet conditions (orbit 6493). This reveals that L_1 regularization results in slightly lower misfit than L_2 regularization, although both approaches describe almost all of the variance in the measurements. The small model residuals, $\Delta\delta F$, given in the middle row of Fig. 2 support the very low variance ratios with residuals lower than 1 nT (≈0.5 % of the signal strength) for the disturbed day.

Considering the mean variance ratios for 1000 orbits between 28 December 2014 to 3 March 2015 (orbit nos. 6142 to 7142) for satellite *Swarm* Alpha, we find that the L_1 solution in general gives a better description (mean variance ratio of $120 \cdot 10^{-6}$) compared to the L_2 solution $(400 \cdot 10^{-6})$. This tells us that the model gives a very good data fit not only for the single orbits presented above, but for all tested orbits at least on average. The largest values of the variance ratio of the 1000 tested orbits was $820 \cdot 10^{-6}$ for the L_1 solution and $2000 \cdot 10^{-6}$ for the L_2 solution. Thus even for the orbits with the worst data fits (highest variance ratios), the model still performs very well. The orbits with highest variances are mainly from quiet days, since on disturbed days the signal amplitude is larger compared to the noise level.

The sheet current densities, J, are presented in the bottom row of Fig. 2 for both the L_1 (black) and L_2 (red) norm inversions as a function of QD latitude. A positive current is defined as a current flowing from midnight to noon (sunward). Compared to the reference least squares zeroth-order Tikhonov solution (blue curve), there are no major differences between the sheet current densities from L_1 (black curve) and L_2 (red curve) norm regularization. We expect that the sheet current densities are weak or absent where there are no currents (e.g. in non-polar regions) and not wildly fluctuating. The L_1 solution correctly estimates the currents outside the polar region (auroral oval) to be zero, or very close to zero, while the L_2 solution displays non-physical small-scale oscillations around zero. These cannot be damped sufficiently by increasing α^2 without also reducing the amplitude of the peak of the sheet current density. The results obtained

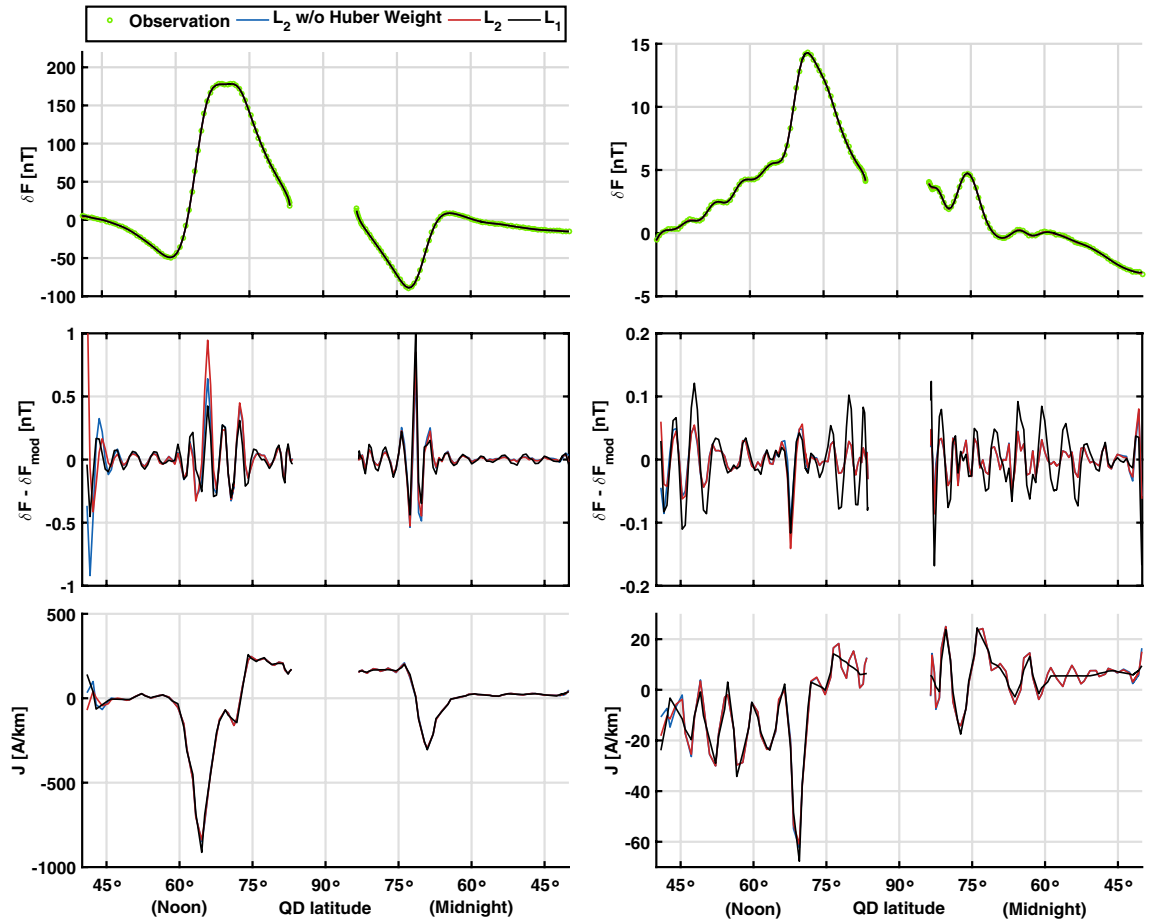

Fig. 2 *Top row* shows observations, δF, in *green* along with the model predictions, δF^{mod}, for three solution methods, L_1 norm (*black*), L_2 norm (*red*), and L_2 norm without Huber-weighted misfit (*blue*). The *middle row* shows the model residuals, $\Delta\delta F$, for the same inversion methods, and the *bottom row* shows the corresponding sheet current densities, J, again for all three methods. Data are from satellite Alpha for 2 days: (*left column*) orbit 6248 on 04.01.2015 13:36 to 14:01 UT, corresponding to a magnetic local time (MLT) of midnight around 60° magnetic latitude (disturbed, $\text{Kp} = 4^-$) and (*right column*) orbit 6493 on 20.01.2015 12:37 to 13:02 UT, a similar MLT (quiet, $\text{Kp} = 0^+$). The sheet current densities are found using $\alpha^2 = 6.4 \cdot 10^{-15} \frac{\text{nT}^2}{\text{A}}$ for the L_1 norm solution and $\alpha^2 = 3.6 \cdot 10^{-27} \frac{\text{nT}^2}{\text{A}^2}$ for the L_2 norm solutions. A positive current flows from midnight to noon (sunward)

with the L_1 norm, therefore, give a representation of the model parameters slightly closer to what we expect on physical grounds, compared to the results found in the L_2 norm solution.

The simple least square zeroth-order Tikhonov regularization solution (blue curve in Fig. 2) gives a rather similar solution as the L_2 norm solution for these orbits, which also involves a Huber-weighted misfit measure. We prefer, however, to use the latter since the distribution of residuals (data minus model predictions) is non-Gaussian.

A similar argument also applies on going from L_2 to L_1 norm regularization. When solving with an L_2 regularization norm, we assume that the model parameters are Gaussian distributed. The distribution of the obtained model parameters is highly non-Gaussian, in particular shown in long tails; in this case it is more consistent to use an L_1 norm regularization scheme.

Choice of regularization parameter, α^2

Both the L_2 and L_1 norm regularization methods require specification of a regularization parameter α^2. The choice is a trade-off between goodness of data fit and model complexity. Too small values of α^2 will result in interpretation of non-physical noise, while a value too large leads to a model for which the desired signal is suppressed, resulting in a decreased data fit. So the question is: when does damping regularization of a non-physical noise become damping of a physical signal?. One way to objectively choose α^2 is by plotting the norm of the

model vector, $||\boldsymbol{m}||/\max(||\boldsymbol{m}||)$ (individually normalized to the range between 0 and 1 for better comparison between different orbits) versus the norm of data misfit, $||\boldsymbol{Gm} - \boldsymbol{d}^{\mathbf{obs}}||$ for various values of the regularization parameter α^2.

The individually normalized norm of the model vector as a function of α^2 and data misfit is shown in a so-called L-curve (Hansen 1992) in Fig. 3 for the six example orbits. The L-curves are based on the model parameters obtained using the L_1 norm solution. The chosen orbits (nos. 200 (orange), 2000 (yellow), 3334 (dark blue), 6248 (light green), 6493 (light blue), and 8000 (purple)) represent orbit crossings for both disturbed and quiet times.

The range of α^2 was chosen between $10^{-16}\text{nT} \cdot \text{A}^{-2}$ and $10^{-12}\text{nT} \cdot \text{A}^{-2}$. According to Hansen (1992), the optimal choice of α^2 is in, or near, the corner of the L-curve. The corner value of $\alpha^2 = 1.2 \cdot 10^{-15}\text{nT} \cdot \text{A}^{-2}$ (red) seems to provide a good balance between the model misfit and complexity, but a visual inspection of the data fit and current profile revealed unwanted small-scale oscillations. This value was therefore increased slightly to obtain the final choice of $\alpha^2 = 6.4 \cdot 10^{-15}\text{nT} \cdot \text{A}^{-2}$ (approximately the purple marked value, $6.3 \cdot 10^{-15}\text{nT} \cdot \text{A}^{-2}$). The fact that the chosen α^2 stays in almost the same position of the L-curve for different classes of Kp indicates that a common choice in α^2 is possible for different geomagnetic activity conditions.

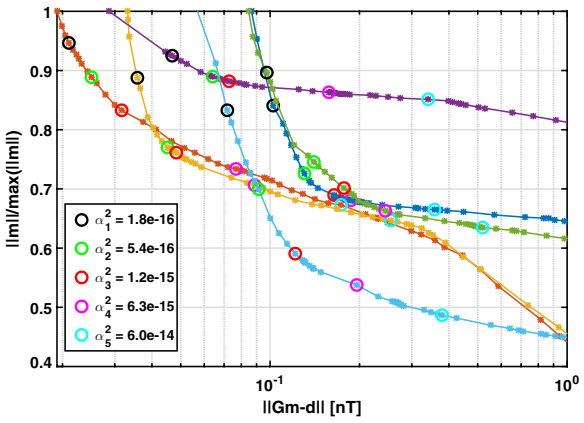

Fig. 3 Normalized L-curves for 6 individual orbits: orbit no. 200 with Kp index of 1^- (*orange*), orbit no. 2000 with Kp index of 1^+ (*yellow*), orbit no. 3334 with Kp index of 3^- (*dark blue*), orbit no. 6248 with Kp index of 4^- (*light green*), orbit no. 6493 with Kp index of 0^+ (*light blue*), and orbit no. 8000 with Kp index of 1^+ (*purple*). Five different $\boldsymbol{\alpha}^2$s are highlighted to show how changes in complexity and model fit change with changing values of $\boldsymbol{\alpha}^2$, $\alpha_1^2 = 1.8 \cdot 10^{-16}\,\frac{\text{nT}^2}{\text{A}}$, $\alpha_2^2 = 5.4 \cdot 10^{-16}\,\frac{\text{nT}^2}{\text{A}}$, $\alpha_3^2 = 1.2 \cdot 10^{-15}\,\frac{\text{nT}^2}{\text{A}}$, $\alpha_4^2 = 6.3 \cdot 10^{-15}\,\frac{\text{nT}^2}{\text{A}}$, and $\alpha_5^2 = 6.0 \cdot 10^{-14}\,\frac{\text{nT}^2}{\text{A}}$

The preferred α^2 will not only depend on the choice of regularization norm, but also on the number of observations, since a change in the size of $\boldsymbol{G}$ will result in a change in the weight between the two terms in the parenthesis of Eq. 5, and hence affect the choice in α^2. Therefore, we need to be aware that orbits with large data gaps might need a different choice in α^2.

Temporal variations

By looking at periods of several weeks, one can investigate the space–time evolution of ionospheric currents during both disturbed and quiet periods. Studying variations as a function of QD latitude, we can estimate where the currents are located, and whether the location changes with time and/or disturbance level. Figure 4 shows the sheet current densities as a function of time and QD latitude for a period of three weeks around spring equinox 2015 (10 to 31 March 2015). The top plot shows the Kp and AE indices; the Northern (middle panel), respectively, Southern (bottom panel) Hemisphere. Each plot is divided into a morning and an evening side. The sign of the current is defined as positive if directed from midnight to noon (sunward).

The oscillating gap around QD latitude 90 is not zero current, but comes from the satellite orbit inclination compared to the geographical pole and not the magnetic pole. The satellite will therefore only sometimes cross the magnetic pole. We find that the ionospheric electrojet current system is confined to the auroral oval (≈70° to 80° QD latitude), and the strengths of the electrojets may therefore be estimated from the sheet current densities in this region. Densities of approximately 1 kA/km near the pole reveal polar cap currents, while the sheet current densities equatorward of the auroral oval are expected to be small. From the temporal development, we can see that deviations from zero at lower latitudes are largest during disturbed periods.

MLT changes by about 1.5 h at non-polar latitudes during the three weeks under consideration; at QD latitude 60° it drifts on the evening side from approximately 20:30 to 19:00 for the example shown in Fig. 4. The period in question is mainly quiet, with low Kp and AE index values (see top plot), but indicates three more active intervals, around 13, 21, and 25 to 28 March 2015. Corresponding higher values of Kp are found for these periods.

Figure 4 reveals a large degree of consistency between the two hemispheres—strong sheet current densities are found in the Northern Hemisphere at the same times as in the Southern Hemisphere, as expected. The small interhemispheric differences may be due to the time difference of 45 min between the pole crossings. This will mainly be an issue during substorms, where changes in the current system can happen very rapidly.

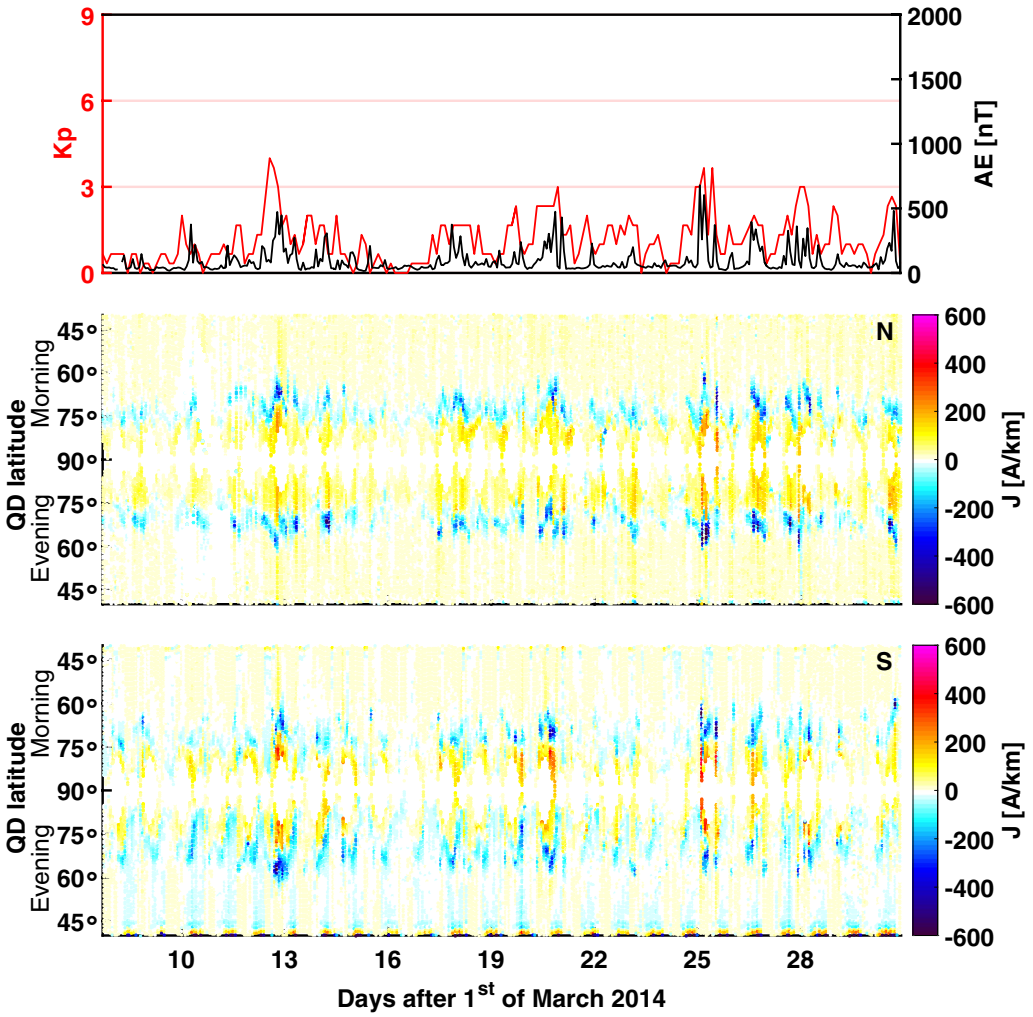

Fig. 4 Temporal development of the sheet current densities measured from satellite Alpha as a function of QD latitude and time (*bottom two panels*) along with the corresponding Kp and AE index values (*top panel*). The *middle panel* shows the temporal development for the Northern Hemisphere, while the *bottom panel* shows the temporal development for the Southern Hemisphere. The results are given for the period 8 to 31 March 2015 for satellite Alpha. A positive current is defined in the sunward direction

The intensities of the ionospheric currents estimated from this type of plot are a good way to show the development of a substorm event. We see, for example, how quiet periods are followed by a sudden intensification of the currents, and expansion of the auroral oval. An event like this marks the onset of a substorm (Akasofu 1964; McPherron 1991), here showing how plots like these can be used identify substorm events. Despite the rapid changes, especially during disturbed times, and the time of about 20 min that it takes for the satellite to cross one polar hemisphere, we still get a clear picture of the state of the ionospheric current system.

Figure 5 shows an example of a much more disturbed period, namely the period around the St. Patrick's day storm on 17 March 2015. This was the most severe geomagnetic storm of solar cycle 24, with Kp indices as large as 8^-, lasting for approximately 18 h. Figure 5 clearly shows how the ionosphere is not only affected during the storm, but also for a long period thereafter. The onset of the storm is difficult to identify due to the effects of a smaller CME ejected from the sun just three days prior to the very large eruption that caused the storm on 17. We see, however, how the oval expands very far south during the storm, consistent with observations of aurora as far south as France.

The interhemispheric differences are larger for the period shown in Fig. 5, compared to that of Fig. 4. This might be due to the more rapid changes during disturbed times but could also indicate interhemispheric

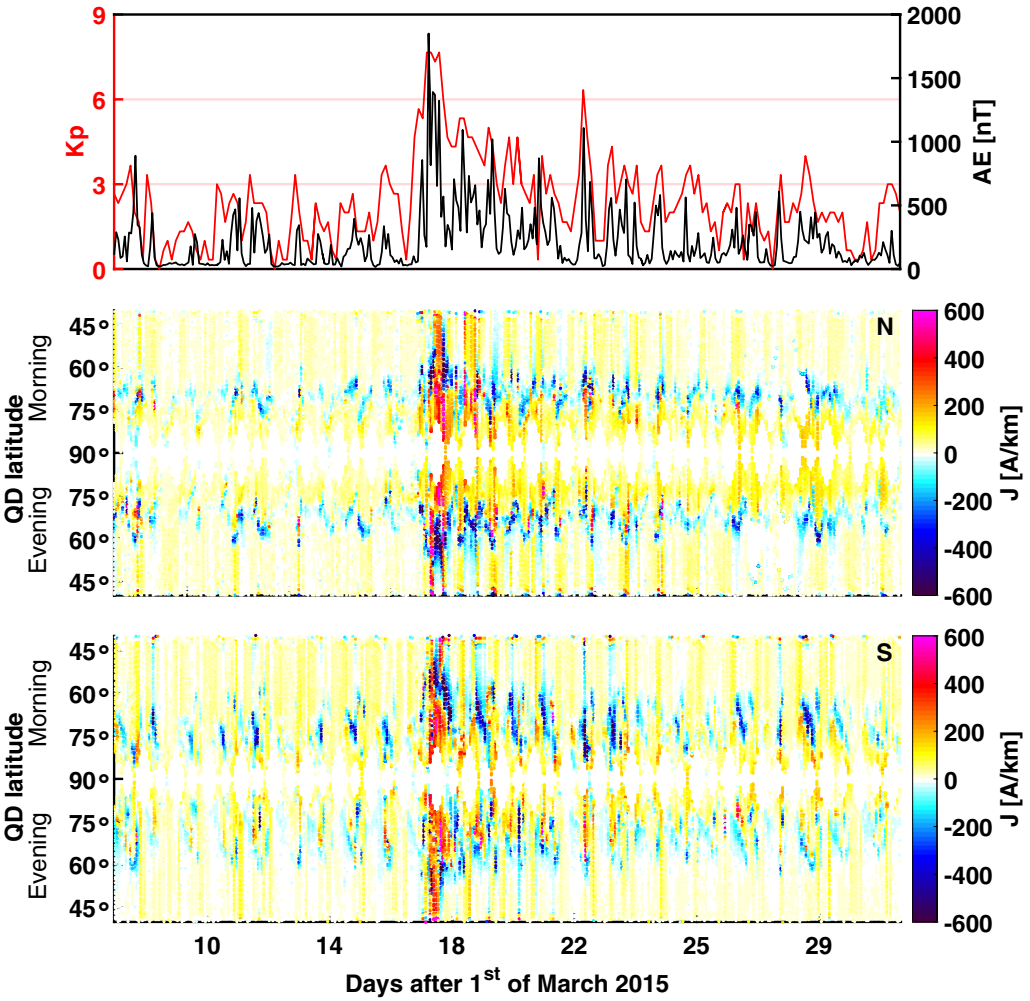

Fig. 5 Temporal development of the sheet current densities measured from satellite Alpha as a function of QD latitude and time (*bottom two panels*) along with the corresponding Kp and AE index values (*top panel*). The *middle panel* shows the results for the Northern Hemisphere, and the *bottom panel* shows the results for the Southern Hemisphere. The results are given for the period around the St. Patrick's day storm on 17 March 2015 (8 to 31 March 2015). A positive current corresponds to a sunward current

asymmetries. Nevertheless, in both cases we find very similar developments of the sheet current densities.

Auroral Electrojet index

We now compare our estimated sheet current densities with the AE index (Sugiura and Davis 1966). It is derived from geomagnetic variations in the horizontal component at 12 observatories along the northern auroral zone and aims at monitoring auroral electrojet activity (Baker 1985). AE provides an estimate of the combined strengths of Eastward and Westward electrojets. Data are found at the *World Data Center for Geomagnetism* (WDCG 2015).

Here, we compare AE with the total polar current, $\boldsymbol{I}$,

$$\boldsymbol{I} = \Delta\beta \int_{-50^\circ}^{50^\circ} |\boldsymbol{J}| d\beta \tag{8}$$

To enable comparison to the sheet current densities, we find the corresponding mean AE index for the period of the selected orbit. An example of this comparison is given in Fig. 6 for the Northern (top) and Southern (bottom) Hemisphere. The AE index is given in red (left y-axis), and the sheet current densities in black (right y-axis). An overall good correlation is found by visual inspection. The total polar current in black follows the AE index very nicely for both the Southern and Northern Hemisphere, despite the fact that they were derived using different methods and data sets (ground-based and spaceborn)

To give an idea of how well the two data series $\boldsymbol{AE}(t)$ and $\boldsymbol{I}(t)$ are correlated, we estimated the squared coherence of the two data series in dependence on frequency, f, and

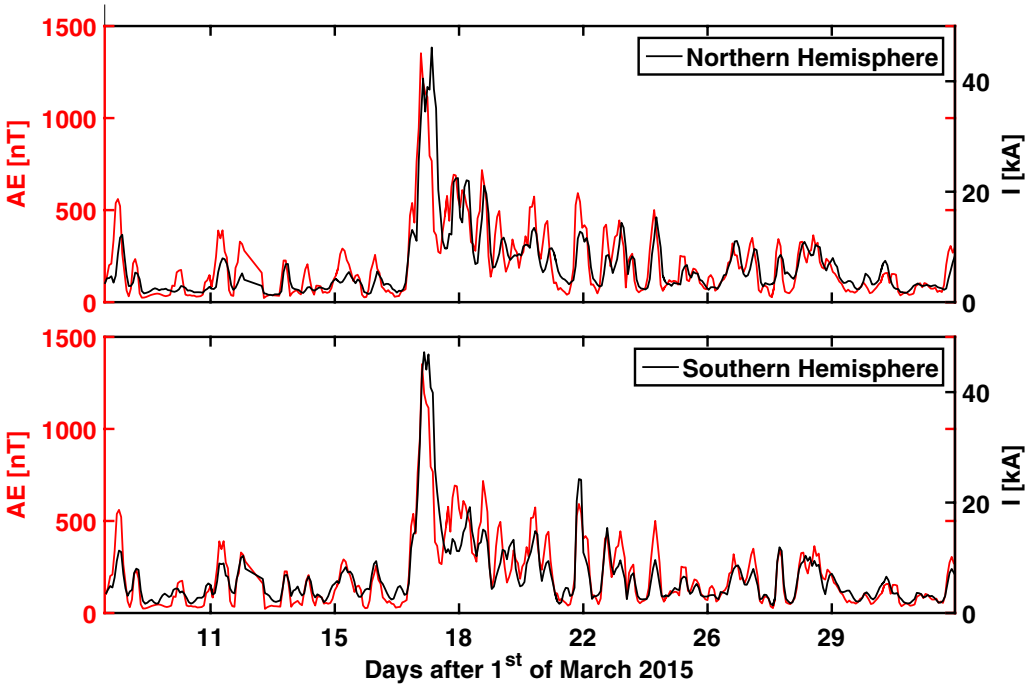

Fig. 6 Time series of AE index and the total polar current, *I*, for a period of 400 orbits (orbit number 7200 to 7799) from 7 March to 1 April 2015. The time series are smoothed with a 3-point running mean boxcar window for better comparison. The AE index is compared to the integrated time series of the sheet current densities for the Northern (*top*) and Southern (*bottom*) Hemisphere, respectively

corresponding period, $T = 1/f$, considering the 400 orbits (orbit number 7200 to 7799) from 7 March to 1 April 2015 given in Fig. 7. The black curve shows the coherence between the Northern Hemisphere sheet current densities and the AE index. The red curve shows the coherence between the Southern Hemisphere sheet current densities and the AE index, and the blue curve shows the coherence between the sheet current densities for the Northern and Southern Hemisphere. The interval studied here corresponds to a small selection of that presented in Fig. 5.

A Fourier transformation is used to determine $\boldsymbol{AE}(f)$ and the total polar currents ($\boldsymbol{I}(f)$) in the frequency domain. Squared coherence between the two data series are found as a function of T. For all three cases, we find

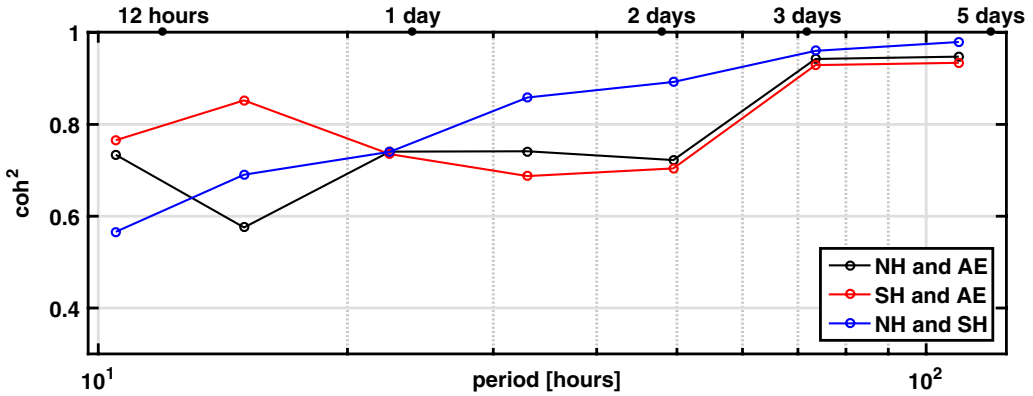

Fig. 7 Correlation between AE index and the total polar current, *I*, as a function of period. The correlation is found for the period of 400 orbits from 7 March to 1 April 2015. The *black curve* shows the coherence of the AE index with the Northern Hemisphere, the *red* shows the coherence of the AE index with the Southern Hemisphere, and the *blue curve* shows the coherence of the Northern and Southern Hemisphere time series as a function of the period of the signal

that the squared coherency for daily variations, and all periods smaller than this, is relatively low, while the squared coherency for periods longer than two days is above 0.9. The interhemispheric coherency is in general a little higher than the coherency with the AE index. The high interhemispheric coherency shows a clear connection between the sheet current densities in the Northern and Southern Hemisphere confining the findings in Fig. 5.

The large coherence values between the total current and the AE index (black and red curve) supports the conclusion from the visual inspection of Figs. 4 and 5 of high correlation between currents (Northern and Southern Hemisphere) and the AE index.

Intersatellites comparison

The AE index provides a good measure of the auroral activity despite some limitations. Summing over longitudes removes any longitudinal dependence of the electrojet activity (see, e.g., Sugiura and Davis 1966). We show here how the integrated absolute values of the sheet current densities measured by satellite give comparable results to the AE index. With the *Swarm* satellite constellation it is not only possible to obtain a result comparable to the AE index, but also to estimate the longitudinal dependence of the electrojets by comparing the satellites Alpha/Charlie and Bravo. An example of the difference between satellite Alpha and Bravo is given in Fig. 8.

Visual inspection of the individual integrated time series of $J(\beta)$ for satellite Alpha and Bravo (top panel) shows high correlation between the two satellites. There are, however, also larger differences mainly during disturbed times. The longitudinal separation between satellites Alpha and Bravo was 24.5° on 17 March 2015 at the equator. The differences are shown in the bottom panel as a function of both magnetic (QD) latitude and time. A positive difference indicates a stronger current for satellite Alpha. Comparing with the temporal development of *Swarm* Alpha (middle plot), we see that the largest differences are found in the auroral oval and during disturbed times (e.g. around 17 March). During disturbed periods, the differences (middle plot) are of comparable size to the sheet current densities found by *Swarm* Alpha (bottom plot). This, together with the longitudinal separation, shows that even smaller longitudinal length scales might be important in auroral electrojet currents during disturbed times.

Sheet current densities from 1000 orbits (orbit number 3000–4000) from Charlie are found to describe 97 % of the variance from Alpha. This indicates that our technique is robust and insensitive to small changes in the data set.

Induced currents

Secondary, induced, currents in the electrically conducting Earth's upper mantle and lithosphere have until now been ignored. They can, however, easily be considered in our current model, by assuming a superconductor at depth, d, acting as a mirror for the primary, ionospheric, currents, placing the induced currents at radius, $r_k = a - 2d$. Induced currents are especially important for observations at ground level, such as directional drilling. The induced currents are implemented in the model by including an additional term (with opposite sign and a different radius of the currents) in the design matrix elements, $g_{n,k}$, presented in Eq. 3. d is set to 125 km, corresponding to a depth of the induced currents of 250 km. The revised design matrix, including the effects of induction, has elements:

$$g_{n,k} = \frac{\mu_0}{2\pi}\left[\frac{\xi_{n,k}\cos I_n + \eta_{n,k}\sin I_n}{\xi_{n,k}^2 + \eta_{n,k}^2} - \frac{(\xi_{n,k})_j \cos I_n + (\eta_{n,k})_j \sin I_n}{(\xi_{n,k})_j^2 + (\eta_{n,k})_j^2}\right]. \tag{9}$$

$$(\eta_{n,k})_j = (a - 2d)\sin(\beta_n - \beta_k) \tag{10}$$

$$(\xi_{n,k})_j = r_n - (a - 2d)\cos(\beta_n - \beta_k). \tag{11}$$

Figure 9 shows the magnetic field estimation (top), the residual magnetic field (middle), and the sheet current density (bottom) for orbit 6493 on 20 January 12:37 to 13:02 UT if induced currents are considered. Comparisons with Fig. 2 (without induced currents) reveal no significant changes in position or in the strength of the sheet current densities.

Conclusions and outlook

The magnetic perturbations due to ionospheric auroral electrojet current system were estimated by applying the line current model of Olsen (1996) to magnetic observations taken by the three satellites Alpha, Bravo, and Charlie of the *Swarm* satellite constellation. Sheet current densities were obtained using two different inversion methods: (1) minimization of an L_2 norm of the model parameters and a Huber-weighted misfit measure and (2) minimization of an L_1 norm of the second-order spatial differences of model parameters and a Huber-weighted misfit measure. The method is illustrated with examples from single orbits with model predictions that match very well the observations for both L_1 and L_2 norm models.

The L_1 norm solution is preferred since it leads to current profiles with weaker currents in non-polar regions. In addition, the distribution of model parameters possessed long tails, favouring the L_1 norm approach.

A study of the regularization parameter, α^2, revealed that a common choice was possible for all tested orbits. This indicates a robust model, not sensitive to disturbance level or other orbit sensitive factors. The tests also indicate that the results are fairly insensitive to the exact

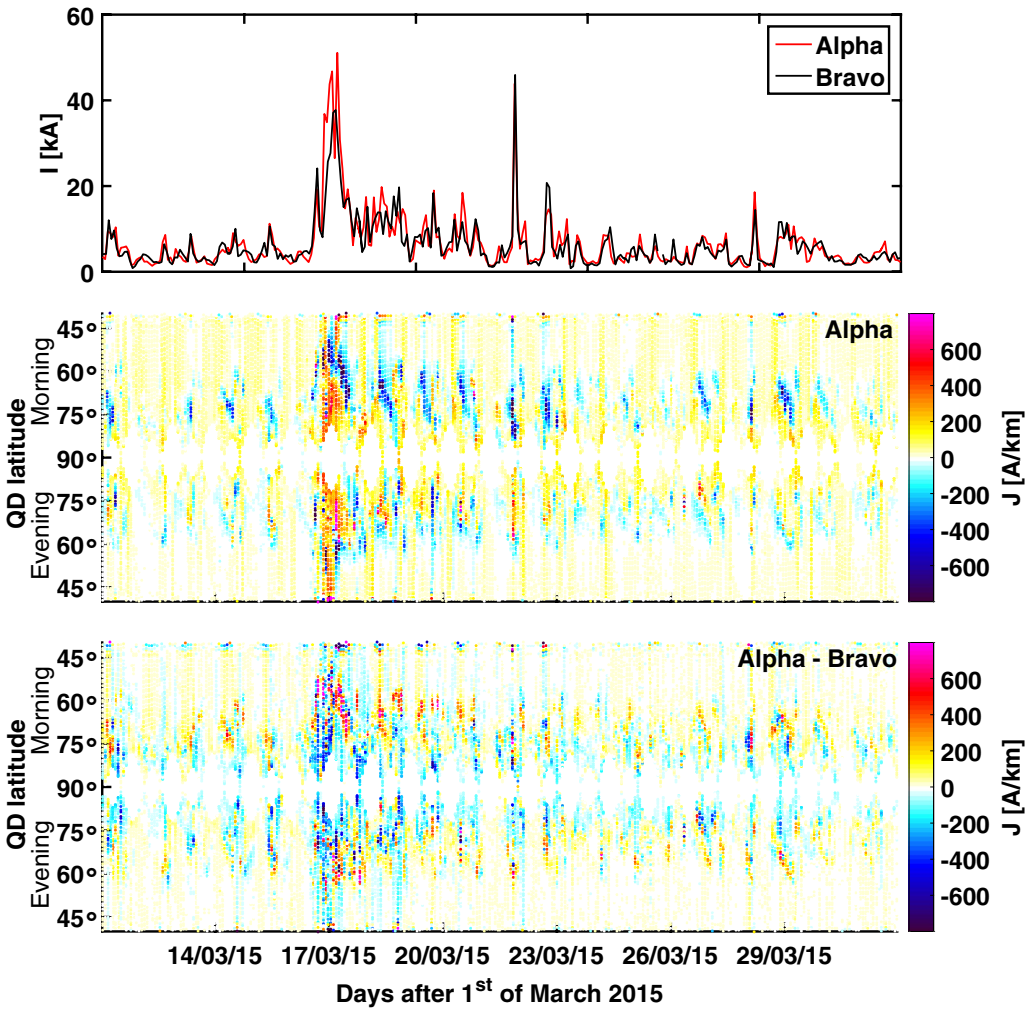

Fig. 8 Temporal development of the sheet current densities and their differences for satellite Alpha and Bravo for the Northern Hemisphere in the period 11 to 31 March 2015. The *top panel* shows the integrated time series of the sheet current densities for satellite Alpha and Bravo for 300 orbits. The *middle panel* shows the sheet current densities of *Swarm* Alpha as a function of magnetic latitude and time (corresponding to middle plot of Fig. 5), and the *bottom panel*, the temporal development of their differences. Positive difference follows times with largest sheet current densities found by *Swarm* Alpha

choice of α^2. Model robustness was tested by comparing results obtained with data from the side-by-side flying satellites Alpha and Charlie: currents derived with Charlie describe more than 97 % of those derived from Alpha.

Investigations of the time dependence of the sheet current densities for the two hemispheres showed a clear difference between disturbed and quiet times. They also revealed a very high consistency between the two hemispheres, with largest differences occurring during disturbed periods which are attributed to the fast changes in the ionospheric current system during these times. The visual consistency is backed up by a squared coherence analysis that revealed a value of more than 0.9 for periods larger than two days.

Comparison to the AE index also showed a very high squared coherence value (≈0.9) for periods longer than two days for the Northern and Southern Hemisphere.

The line currents in this study are placed perpendicular to the satellite track. This can lead to a systematic underestimation of the sheet current densities, dependent on the angle with the actual current. The effect will therefore be largest in the region around the poles, though it will differ from orbit to orbit, dependent on the satellite track. A more accurate approach would be to assume the currents to be parallel to magnetic latitude.

The results pave the way for further research possibilities, such as combining the height-integrated current density estimates with measurements from the Swarm

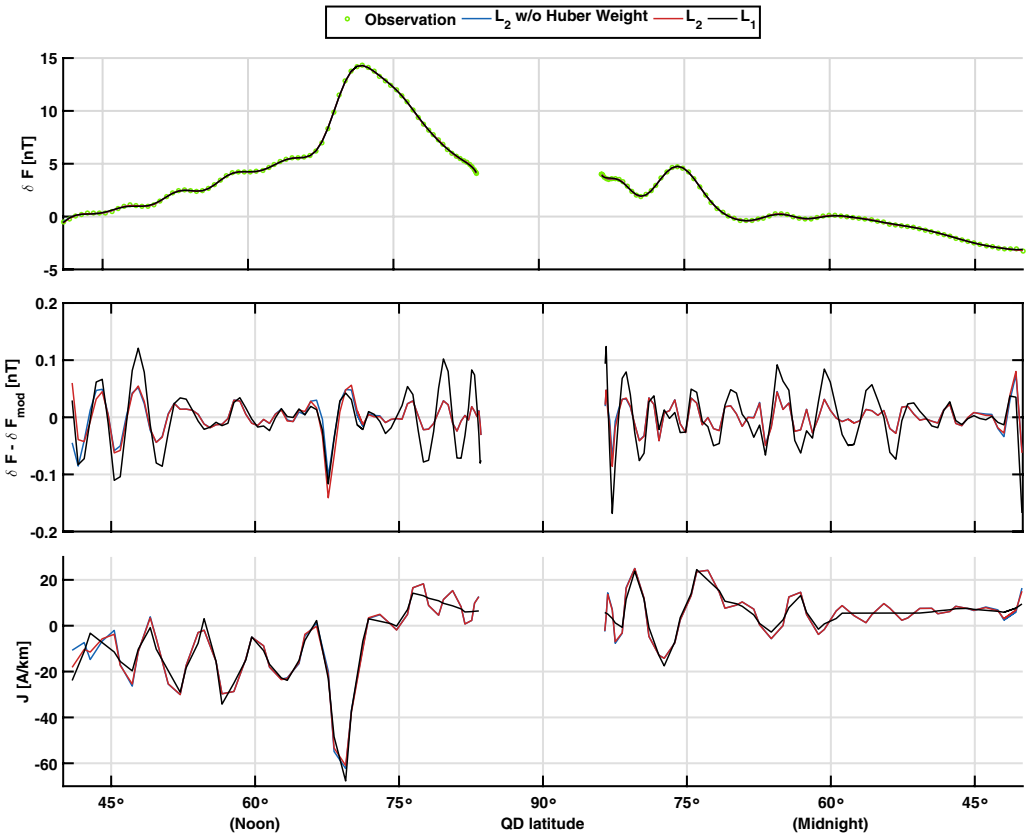

Fig. 9 Corresponding to Fig. 2 for *Swarm* Alpha, orbit 6493 on 20.01.2015 12:37 to 13:02 UT, including induced currents. The *top panel* shows observations, δF, in *green* along with the model predictions, δF^{mod}, for three solution methods, L_1 norm (*black*), L_2 norm (*red*), and L_2 norm without Huber-weighted misfit (*blue*). The *middle panel* shows the model residuals, $\Delta\delta F$, for the same inversion methods, and the *bottom panel* shows the corresponding sheet current densities, J, again for all three methods. The sheet current densities are found using $\alpha^2 = 6.5 \cdot 10^{-15} \frac{\text{nT}^2}{\text{A}}$ for the L_1 norm solution and $\alpha^2 = 1 \cdot 10^{-26} \frac{\text{nT}^2}{\text{A}^2}$ for the L_2 norm solutions. A positive current flows from midnight to noon (sunward)

Electric Field Instrument to derive height-integrated Hall conductivities.

Overall, we found that the line current model provides useful estimates of the polar ionospheric sheet current densities. The robustness of the method and the fact that the method worked for all tested orbits reveal a clear opportunity for automatic application and near-real-time estimations of the ionospheric sheet current densities.

Authors' contributions

CDAa coded the model, carried out the data analysis, and drafted the manuscript. NO and CCF participated in key discussions of the model and data analysis. All authors read and approved the final manuscript.

Acknowledgements

We would like to thank ESA for providing prompt access to the *Swarm* L1b data. This project was supported by The Research Council of Norway through the PETROMAKS research programme. The financial support is gratefully acknowledged.

Competing interests

The authors declare that they have no competing interests.

Received: 8 February 2016 Accepted: 6 July 2016
Published online: 05 August 2016

References

Akasofu S-I (1964) The development of the auroral substorm. Planet Space Sci 12(4):273–282. doi:10.1016/0032-0633(64)90151-5

Amm O (1997) Ionospheric elementary current systems in spherical coordinates and their application. J Geomagn Geoelectr 49(7):947–955

Aster RC, Borchers B, Thurber CH (2005) Parameter estimation and inverse problems, 1st edn. Elsevier, Amsterdam

Baker D (1985) Statistical analyses in the study of solar wind–magnetosphere coupling. In: Technical report, Los Alamos National Laboratory, NM (USA)

Constable CG (1988) Parameter estimation in non-Gaussian noise. Geophys J 94:131–142

Ekblom H (1987) The L_1-estimate as limiting case of an L_p-or Huber-estimate. In: Dodge Y (ed) Statistical data analysis based on the L_1-norm and related methods. Elsevier, Amsterdam, pp 109–116

Farquharson CG, Oldenburg DW (1998) Non-linear inversion using general measures of data misfit and model structure. Geophys J Int 134(1):213–227. doi:10.1046/j.1365-246x.1998.00555.x

Finlay CC, Olsen N, Tøffner-Clausen L (2015) DTU candidate field models for IGRF-12 and the CHAOS-5 geomagnetic field model. Earth Planets Space 67(1):1–17

Finlay CC, Olsen N, Kotsiaros S, Gillet N, Tøffner-Clausen L (2016) Recent geomagnetic secular variation from Swarm and ground observatories in the CHAOS-6 geomagnetic field model. Earth Planets Space. doi:10.1186/s40623-016-0486-1

Friis-Christensen E, Kamide Y, Richmond AD, Matsushita S (1985) Interplanetary magnetic field control of high-latitude electric fields and currents determined from greenland magnetometer data. J Geophys Res Space Phys 90(A2):1325–1338. doi:10.1029/JA090iA02p01325

Friis-Christensen E, Lühr H, Knudsen D, Haagmans R (2008) Swarm—an earth observation mission investigating geospace. Adv Space Res 41(1):210–216. doi:10.1016/j.asr.2006.10.008

Hansen PC (1992) Analysis of discrete ill-posed problems by means of the L-curve. SIAM Rev 34(4):561–580

Huber PJ (1964) Robust estimation of a location parameter. Ann Math Stat 35(1):73–101. doi:10.1214/aoms/1177703732

Jackson A, Constable C, Gillet N (2007) Maximum entropy regularization of the geomagnetic core field inverse problem. Geophys J Int 171(3):995–1004. doi:10.1111/j.1365-246X.2007.03530.x

Juusola L, Amm O, Viljanen A (2006) One-dimensional spherical elementary current systems and their use for determining ionospheric currents from satellite measurements. Earth Planet Space 58:667–678

Kamide Y, Richmond AD, Matsushita S (1981) Estimation of ionospheric electric fields, ionospheric currents, and field-aligned currents from ground magnetic records. J Geophys Res 86(A2):801–813. doi:10.1029/JA086iA02p00801

Lesur V, Wardinski I, Hamoudi M, Rother M (2010) The second generation of the GFZ reference internal magnetic model: GRIMM-2. Earth Planets Space 62:765–773. doi:10.5047/eps.2010.07.007

Liu H, Lühr H (2005) Strong disturbance of the upper thermospheric density due to magnetic storms: CHAMP observations. J Geophys Res Space Phys 110(A9). doi:10.1029/2004JA010908

McPherron RL (1991) Physical processes producing magnetospheric substorms and magnetic storms. In: Jacobs JA (ed) Geomagnetism. Academic Press Ltd, London, pp 593–739

Menke W (2012) Geophysical data analysis: discrete inverse theory, MATLAB edition, 3rd edn. Elsevier, Amsterdam

Moretto T, Olsen N, Ritter P, Lu G (2002) Investigating the auroral electrojets with low altitude polar orbiting satellites. Ann Geophys 20(7):1049–1061

Olsen N (1996) A new tool for determining ionospheric currents from magnetic satellite data. Geophys Res Lett 23(24):3635–3638. doi:10.1029/96GL02896

Olsen N, Moretto T, Friis-Christensen E (2002) New approaches to explore the earth's magnetic field. J Geodyn 33(1–2):29–41 (**earth's Gravity and Magnetic Fields from Space**)

Olsen N, Lühr H, Finlay CC, Sabaka TJ, Michaelis I, Rauberg J, Tøffner-Clausen L (2014) The CHAOS-4 geomagnetic field model. Geophys J Int 197(2):815–827

Pirjola R, Kauristie K, Lappalainen H, Viljanen A, Pulkkinen A (2005) Space weather risk. Space Weather 3(2). doi:10.1029/2004SW000112

Poedjono B, Beck N, Buchanan A, Borri L, Maus S, Finn CA, Worthington EW, White T et al (2013) Improved geomagnetic referencing in the arctic environment (russian). In: SPE arctic and extreme environments technical conference and exhibition, society of petroleum engineers

Richmond A, Lu G, Emery B, Knipp D (1998) The AMIE procedure: prospects for space weather specification and prediction. Adv Space Res 22(1):103–112. doi:10.1016/S0273-1177(97)01108-3 (**solar-Terrestrial Relations: Predicting the Effects on the Near-Earth Environment**)

Richmond AD (1995) Ionospheric electrodynamics using magnetic apex coordinates. J Geomagn Geoelectr 47(2):191–212. doi:10.5636/jgg.47.191

Ritter P, Viljanen A, Lühr H, Amm O, Olsen N (2003) Ionospheric currents from champ magnetic field data comparison with ground based measurements. In: Reigber C, Lühr H, Schwintzer P (eds) First CHAMP mission results for gravity, magnetic and atmospheric studies. Springer, Berlin, pp 347–352. doi:10.1007/978-3-540-38366-6_50

Ritter P, Lühr H, Viljanen A, Amm O, Pulkkinen A, Sillanpää I (2004) Ionospheric currents estimated simultaneously from champ satelliteand image ground-based magnetic field measurements: a statistical study at auroral latitudes. Ann Geophys 22(2):417–430. doi:10.5194/angeo-22-417-2004

Sabaka TJ, Olsen N, Purucker ME (2004) Extending comprehensive models of the Earth's magnetic field with Ørsted and CHAMP data. Geophys J Int 159:521–547. doi:10.1111/j.1365-246X.2004.02421.x

Sabaka TJ, Olsen N, Tyler RH, Kuvshinov A (2015) CM5, a pre-Swarm comprehensive magnetic field model derived from over 12 years of CHAMP, Ørsted, SAC-C and observatory data. Geophys J Int 200:1596–1626. doi:10.1093/gji/ggu493

Sugiura M, Davis T (1966) Auroral electrojet activity index AE and its universal time variations. J Geophys Res 71:785–801

Tikhonov AN (1963) Solution of incorrectly formulated problems and the regularization method. In: Soviet Math. Dokl., vol 4, pp 1035–1038, english translation of Dokl. Akad. Nauk. SSSR, 151 (1963), pp 501–504

Vennerstrom S, Moretto T (2013) Monitoring auroral electrojets with satellite data. Space Weather 11(9):509–519. doi:10.1002/swe.20090

WDCG (2015) World Data Center for Geomagnetism (WDCG), Kyoto University. http://wdc.kugi.kyoto-u.ac.jp/aeasy/index.html

Appendix B

Synthetic test case of the 1D SECS method

This appendix provides a thorough test of a synthetic test case of the 1D SECS method, investigating the influence of a set of adjustable parameters, , model and observation spacing ($\delta\theta^{\text{mod}}$ and $\delta\theta^{\text{obs}}$), width of box function ($d\delta$), truncation parameters for the divergence free and curl free part of the solution (ε_c and ε_d) along with model and observation range.

From synthetic estimates of sheet current densities, synthetic magnetic observations and modelled estimates of both are found, according to the flow chart in Figure 6.2 on page 63. The resulting sheet current densities and magnetic field perturbations are given in Figure B.1 as a function of latitude. The left column shows the magnetic field components, and the right column, the sheet current densities. Shown in blue are the virtual observations, and the re-estimated modelled values are given by the dashed red line. Results are obtained using a model parameter spacing, $\delta\theta^{\text{mod}}$, of 0.5°, observation spacing, $\delta\theta^{\text{obs}}$, of 1° and truncation values of 10^{-10} for both inversions. The figure shows a nearly perfect fit between all modelled and synthetic data, with differences below 10^{-8} for the magnetic field components, and 10^{-12} for the sheet current densities for the majority of the orbit, see Figure B.2. The blue line gives the differences for the radial component, the black line for the theta component and the black line for the phi component of the magnetic field (a) and sheet current densities (b), accordingly, as a function of latitude. The differences for the sheet current densities, especially for J_r, are at the boundaries somewhat larger, with values up to 10^{-8}, though still significantly smaller than the signal strengths. These results correspond well with the variance ratios between the residuals of observations and model estimates, $\boldsymbol{d}^{\text{mod}} - \boldsymbol{d}^{\text{obs}}$ and the observations, $\boldsymbol{d}^{\text{obs}}$ (Equation 5.20 on page 59), ranging between 10^{-15} and 10^{-34} given in Table B.1.

ε_A	ε_M	$\delta\theta^{\text{mod}}$	$\delta\theta^{\text{obs}}$	$d\delta$	B_r	B_θ	B_ϕ	J_r	J_θ	J_ϕ
10^{-10}	10^{-10}	0.5	1		10^{-34}	10^{-20}	10^{-20}	10^{-15}	10^{-25}	10^{-30}
10^{-3}	$5 \cdot 10^{-12}$	0.5	1		10^{-17}	10^{-17}	10^{-29}	0.05	10^{-11}	10^{-30}
10^{-3}	$5 \cdot 10^{-12}$	1	1	2.3°	10^{-25}	10^{-25}	10^{-30}	0.09	10^{-11}	10^{-30}
10^{-3}	$5 \cdot 10^{-12}$	1	0.5	2.3°	10^{-24}	10^{-25}	10^{-30}	0.07	0.008	0.008

Table B.1: Variance ratios for various values of ε_A, ε_M, $\delta\theta^{\text{mod}}$ and $\delta\theta^{\text{obs}}$.

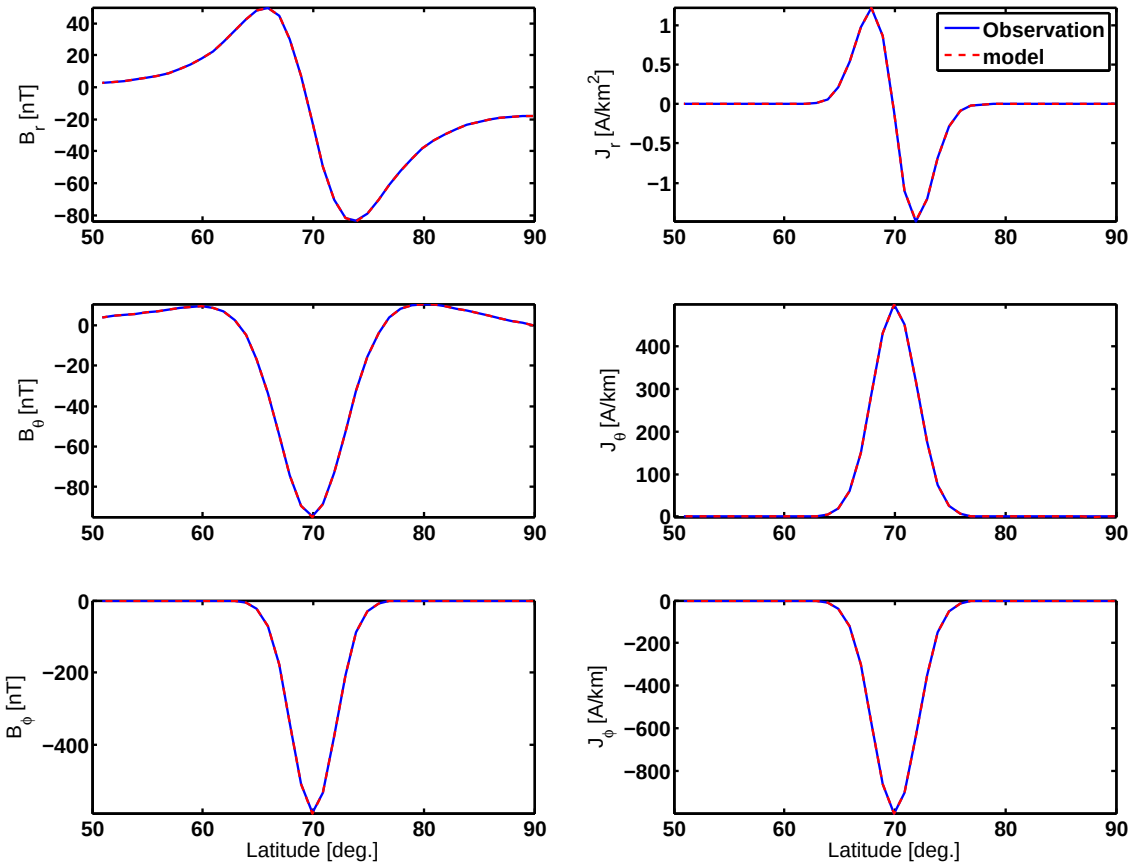

Figure B.1: Magnetic field, $\boldsymbol{B}^{\text{obs}}$ and $\boldsymbol{B}^{\text{mod}}$ (first column), and sheet current density, $\boldsymbol{J}^{\text{obs}}$ and $\boldsymbol{J}^{\text{mod}}$ (second column), components. Virtual observations are given in blue, and in red, the corresponding model fit, as a function of latitude. The results are are found using truncation values $\varepsilon_A = \varepsilon_M = 10^{-10}$, model spacings of $\delta\theta^{\text{mod}} = 0.5^\circ$ and observation spacing of $\delta\theta^{\text{obs}} = 1^\circ$ (*i.e.* underdetermined problem).

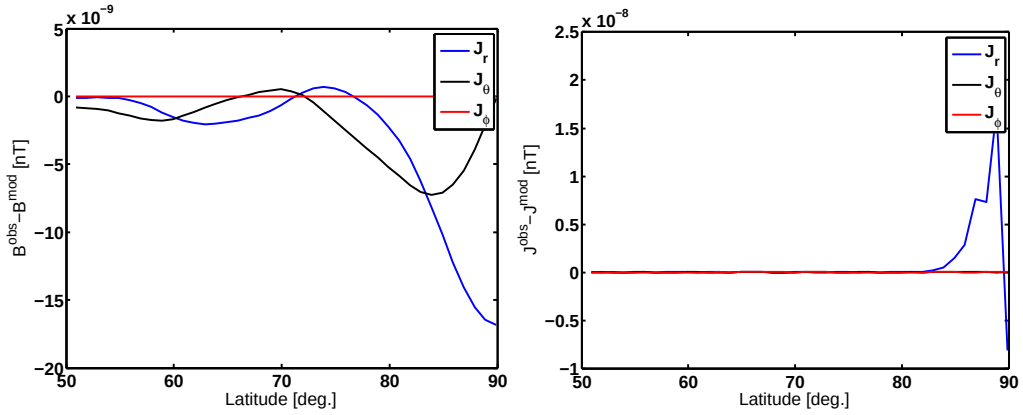

(a) Magnetic field differences

(b) Sheet current density differences

Figure B.2: Differences between virtual observed magnetic field (a) and sheet current densities (b) for the individual components as a function of latitude. The differences are found, corresponding to Figure B.1 using $\varepsilon_A = \varepsilon_M = 10^{-10}$, $\delta\theta^{\text{mod}} = 0.5^\circ$ and $\delta\theta^{\text{obs}} = 1^\circ$.

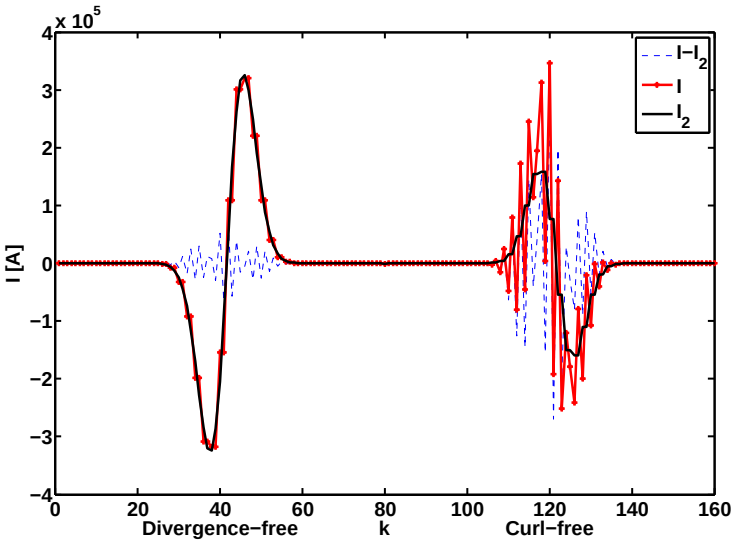

Figure B.3: Model parameters found from sheet current density $\mathcal{I}$ (red) and from magnetic field observations $\mathcal{I}_2$ (black) along with their differences marked by the dashed blue line. The first part of the graph corresponds to the divergence-free part and the second to the curl-free part of the model parameters. Parameters are found with corresponding values of $\varepsilon_A = \varepsilon_M = 10^{-10}$, $\delta\theta^{\text{obs}} = 1^\circ$ and $\delta\theta^{\text{mod}} = 0.5^\circ$ as in Figure B.1.

Choice of SVD Truncation parameter

The need for regularization in the synthetic case is less important, compared to dealing with real data, since the input data are noise free. We do not therefore expect the truncation parameter of $\boldsymbol{M}$, ε_M and $\boldsymbol{A}$, ε_A, to be of great importance. The results in Figure B.3 reveals, however, the results given in Figure B.1 return an unstable solution to the inverse problem. The figure shows the model parameters, corresponding to the current amplitudes, as a function of singular value number, k (see Section 5.2 on page 57). The size of $\boldsymbol{\mathcal{I}}$ will, as a result of how the inverse problem is stated (Equation 4.51 and Equation 4.55), be $2M$, where the first part corresponds to the divergence-free model parameters, $\boldsymbol{\mathcal{I}}_{df}$, and the last part to the curl-free model parameters, $\boldsymbol{\mathcal{I}}_{cf}$. Given in red is the model parameters, $\boldsymbol{\mathcal{I}}$, found by inverting $\boldsymbol{A}$, and in black the model parameters, $\boldsymbol{\mathcal{I}}_2$, found from inversion of $\boldsymbol{M}$. The dashed blue line shows the difference between the two. The two model parameter vectors would be the same for perfect inversions. The figure shows, however, that this is not the case, with especially the curl-free part showing large differences. The correlation coefficient between the two vectors is found to 0.87. From our physical understanding on how the sheet current amplitudes are distributed across the ionosphere, we expect a certain amount of autocorrelation in the sheet current amplitudes. The highly fluctuating signal in $\boldsymbol{\mathcal{I}}$, is therefore attributed to numerical noise added by the inversion, since the synthetic data are noiseless, indicating a fit of the re-estimated current densities to a degree not permitted by the data. We therefore feel it necessary to further regularize the solutions, by increasing the truncation value, ε_A, for the inversion of $\boldsymbol{A}$. The effect of the regularization parameter and method is discussed in the following section.

A more correct value of the truncation parameters (ε_A and ε_M) can be estimated from a plot of the singular values spectrum. This is for the model parameters given in Figure B.1 presented in

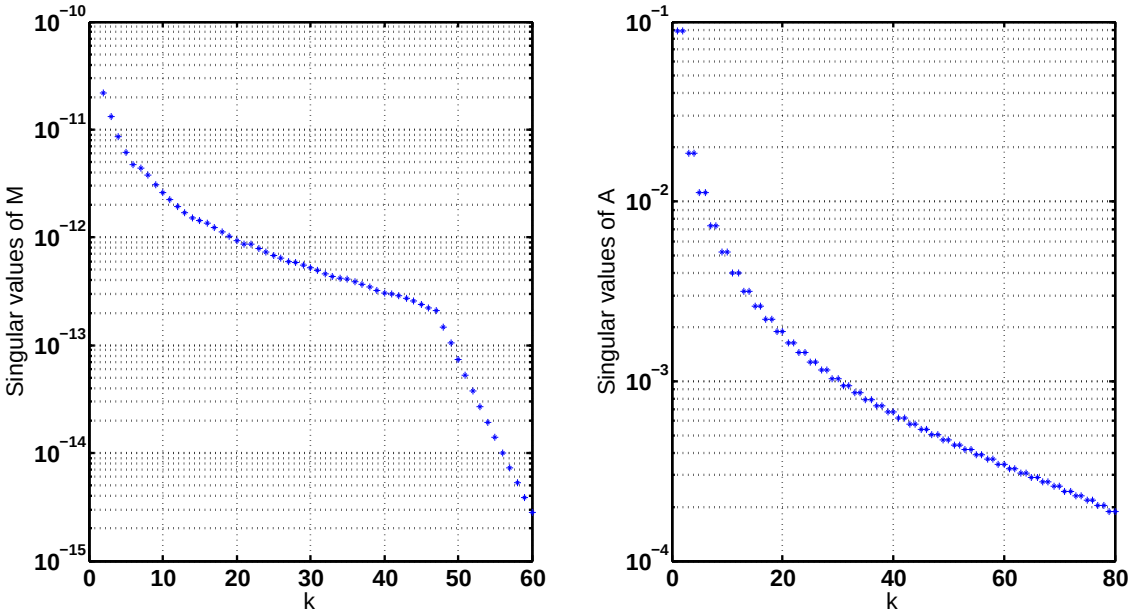

Figure B.4: Singular value spectrum using $\varepsilon_A = \varepsilon_M = 10^{-10}$, $\delta\theta^{\text{obs}} = 1^\circ$ and $\delta\theta^{\text{mod}} = 0.5^\circ$ corresponding to Figure B.1.

Figure B.4. We find, as expected from theory of SVD, singular values decreasing with increasing k. Figure B.4 shows how truncation parameters $\varepsilon_M = 10^{-3}$ and $\varepsilon_A = 5 \cdot 10^{-12}$ represents a better trade-off between the variance explained and the number of small eigenvalues retained. Recalculated results of magnetic field and sheet current densities with these values are given in Figure B.5 as a function of latitude. The virtual observations are displayed in blue and the modelled in the dashed red line, corresponding to Figure B.1. The corresponding model parameters and differences are shown in Figure B.6 and B.7 accordingly. From Figure B.6 we see how the model parameters behave much more as expected, compared to the model parameters presented in Figure B.3, and with a higher correlation (0.99 compared to 0.87) between $\boldsymbol{\mathcal{I}}$ and $\boldsymbol{\mathcal{I}_2}$. The effect of the change in truncation values was largest in the fit to $\boldsymbol{J}_r$, where a decrease in variance ratio from 10^{-15} to 10^{-2} was observed and differences of up to 0.4 A/km^2(Figure B.7(b)) is found. Remaining components of $\boldsymbol{J}$ and $\boldsymbol{B}$ are not significantly affected, with variance ratios still not significantly different from zero. This is supported by the differences found in Figure B.7, showing values up to 10^{-7} for the magnetic field components and 10^{-3} and 10^{-11} for the θ and ϕ component respectively of the sheet current density. All variance ratios are collected in the second row of Table B.1.

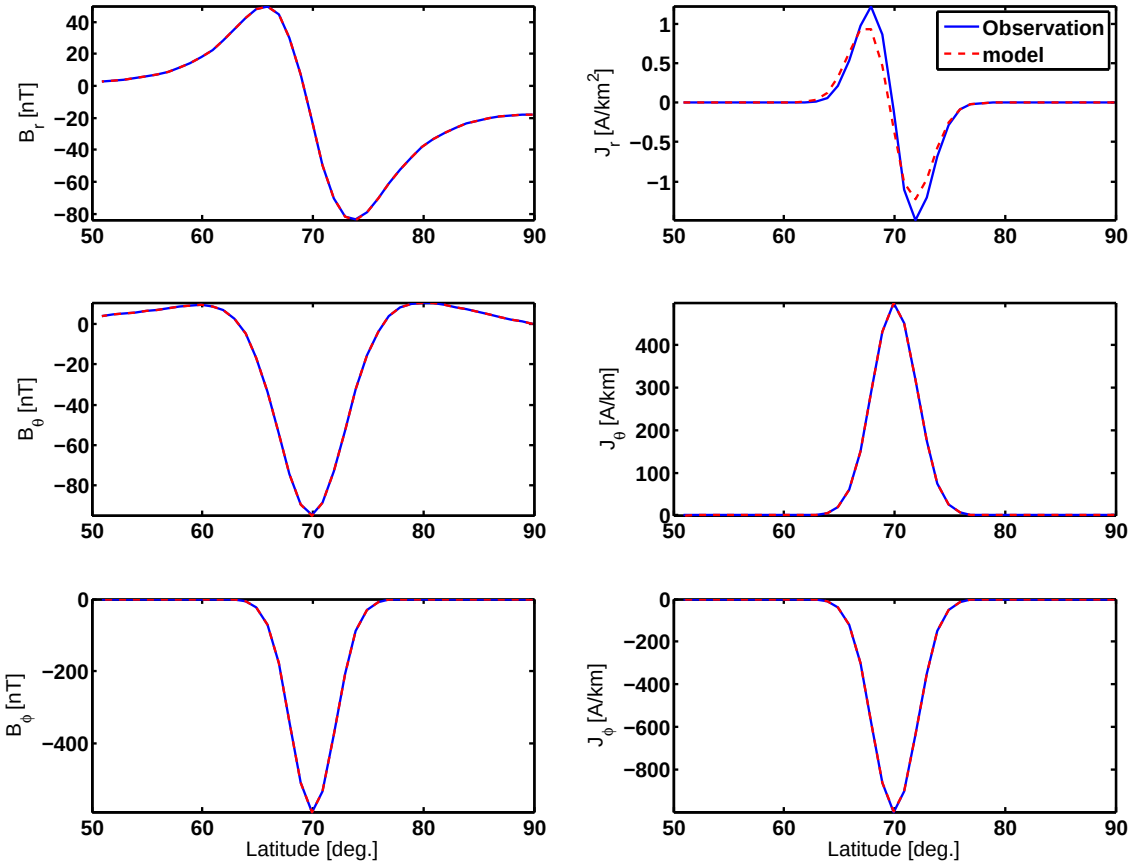

Figure B.5: As Figure B.1 found using truncation values $\varepsilon_A = 10^{-3}$, $\varepsilon_M = 5 \cdot 10^{-12}$, model spacings of $\delta\theta^{\text{mod}} = 0.5^\circ$ and observation spacing of $\delta\theta^{\text{obs}} = 1^\circ$ (underdetermined inverse problem).

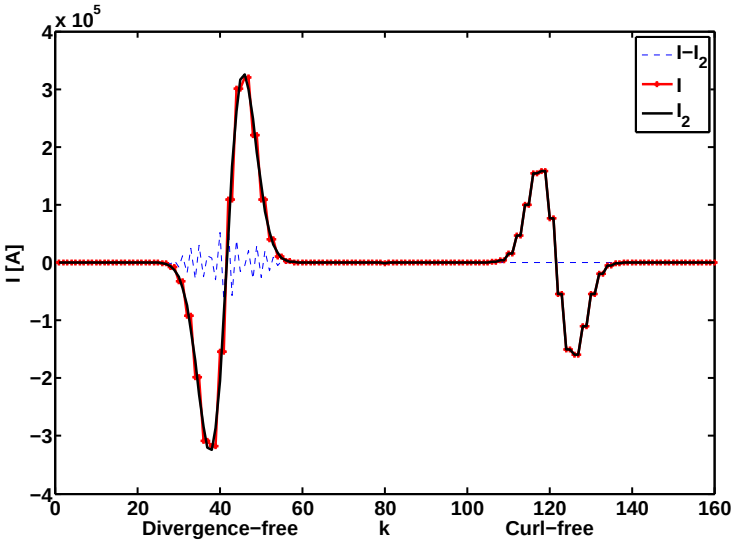

Figure B.6: As Figure B.3. Found with ε_A, ε_M, $\delta\theta^{\text{obs}}$ and $\delta\theta^{\text{mod}}$ corresponding to Figure B.5.

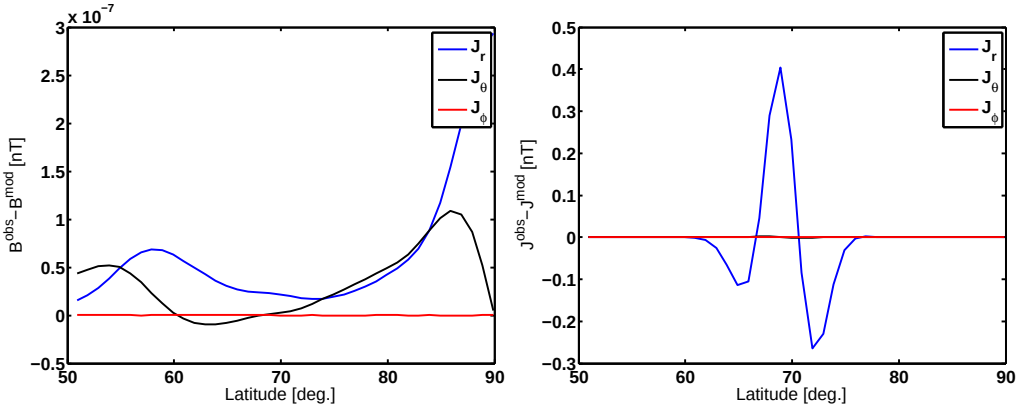

(a) Magnetic field differences **(b)** Sheet current density differences

Figure B.7: As Figure B.2. Found with the same model as presented in Figure B.5 using $\varepsilon_A = 10^{-3}$, $\varepsilon_M = 5 \cdot 10^{-12}$, $\delta\theta^{\text{mod}} = 0.5°$ and $\delta\theta^{\text{obs}} = 1°$.

Choice of regularization method

The inverse problem presented above was for grids spacing $\delta\theta^{\text{obs}} = 1°$ and $\delta\theta^{\text{mod}} = 0.5°$, *i.e.* it was an underdetermined problem. TSVD inversion should, however, be able to handle this. We test a possible improvement in the fit to $\boldsymbol{J}_r$, by turning the problem into an exact inverse problem, setting $\delta\theta^{\text{obs}} = \delta\theta^{\text{mod}} = 1$. The change in the ratio $\delta\theta^{\text{mod}}/\delta\theta^{\text{obs}}$, left us unable to model the radial component of the sheet current densities. We therefore tested (Figure B.8) the influence of the inversion method by comparing non-regularized least squares, SVD and TSVD solutions. The model parameters were now estimated using $\delta\theta^{\text{obs}} = \delta\theta^{\text{mod}} = 0.2$. Figure B.8(a) shows how an unregularized least squares solution returns very noisy model parameters, especially for the divergence free part of model parameters found from the inversion of $\boldsymbol{M}$. A simple SVD inversion, Figure B.8(b), shows large improvements compared to the least squares solution, however it is still dominated by unacceptable fluctuations in the divergence free part of the model parameters. The truncated SVD version ($\varepsilon_A = \varepsilon_M = 10^{-13}$) presented in Figure B.8(c) returns model parameters with very low complexity. We therefore conclude, that regularization by truncating the singular value spectrum is needed, even in the synthetic case. This could indicate that a correct solution to the inverse problem is difficult to find, when applied to real data, where the need for regularization is of much greater importance.
The definite need for regularization, opens a discussion about the choice in regularization method. Figure B.9, includes a least squares solution constructed using Tikhonov regularization, estimated with a regularization parameter of $\alpha^2 = 10^{-10}$ and TSVD parameters corresponding to Figure B.5. This shows a nearly perfect fit, with a correlation coefficient of 0.9997, between the Tikhonov and TSVD estimates of $\boldsymbol{J}_r$, indicating that the error is not due to the choice iof regularization, but more likely a problem in the numerical calculations of the curl-free part of the design matrix, $\boldsymbol{Acr}$, and more precisely the implementation of the delta function given in Equation 4.57. We, therefore, find no need for further tests of regularization methods in this specific case. Tests (not shown) revealed, how the error arose where $\delta\theta^{\text{mod}}/\delta\theta^{\text{obs}} \neq 0.1$, 0.25 or 0.5, indicating that the conversion of a continuous problem into a discrete one results in a singularity problem in the delta function. To avoid singularity problems when $\theta^{\text{obs}} \bigcap \theta^{\text{mod}}$ is empty, we substituted the delta function with a box function with a non-singular width, $d\delta$. This should help ensure that the influence of the FACs not only affect measurements at one

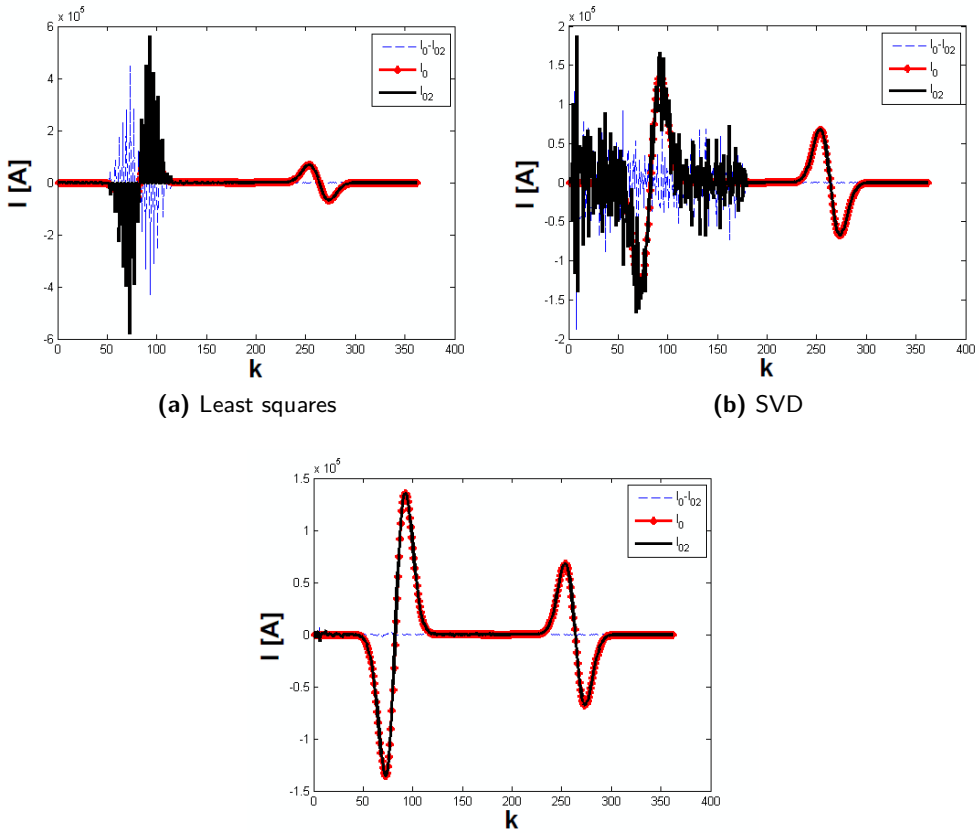

(a) Least squares

(b) SVD

(c) TSVD

Figure B.8: Model parameters using (a) Least squares inversion, (b) SVD inversion and (c) TSVD inversion with $\varepsilon_A = \varepsilon_M = 10^{-13}$. All are model parameters are found using $\delta\theta^{\text{obs}} = \delta\theta^{\text{mod}} = 0.2°$.

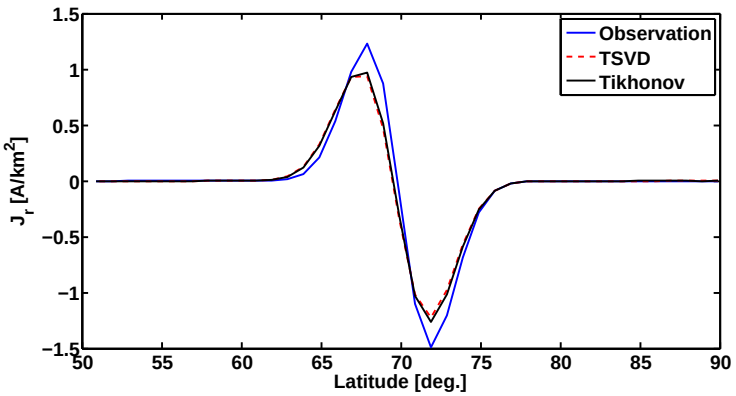

Figure B.9: Corresponding to Figure B.5 along with a Tikhonov solution added, using regularization parameter $\alpha^2 = 10^{-10}$.

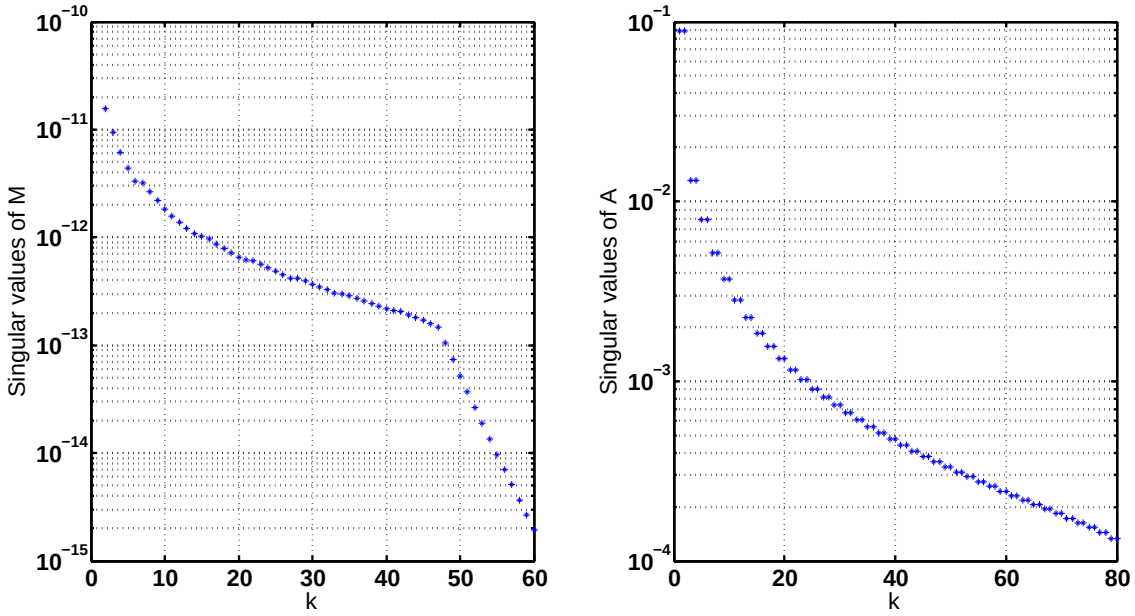

Figure B.10: Singular value spectrum for an exact determined problem. Solution is found with the truncation values similar to Figure B.5.

specific latitude, but also measurements in the proximity, depending on the width of the box function.

Equation 4.26 states that $\boldsymbol{J}_r(r_n, \theta_n, \theta_k) = \frac{\mathcal{I}}{r_k^2}\left(\frac{1}{2} - \frac{1}{\sin\boldsymbol{\theta}_k}\right)$, where $\boldsymbol{\theta}_n = \boldsymbol{\theta}_k$, and $\frac{\mathcal{I}}{2r_k^2}$ at $\boldsymbol{\theta}_n \neq \boldsymbol{\theta}_k$. Implementing the box function, this equation is adjusted to $\boldsymbol{J}_r = \frac{\mathcal{I}}{r_k^2}\left(\frac{1}{2} - \frac{1}{\sin\boldsymbol{\theta}_k}\frac{1}{d\delta}\right)$, where $\boldsymbol{\theta_k} \in [\boldsymbol{\theta_n} - \frac{d\delta}{2}; \boldsymbol{\theta_n} + \frac{d\delta}{2}]$ and $\frac{\mathcal{I}}{2r_k^2}$ elsewhere. The box function solution goes towards the delta function solution for $d\delta \to 0$. Introducing the box function, introduces an additional adjustable parameter, $d\delta$. The effect of this will be evaluated later.

Over- and under-determined problems

The influence of a change in the virtual observation spacings ($\delta\theta^{\text{obs}} = 1°$) to turn the problem into an exact determined problem is presented in Figure B.10 to B.13 with $d\delta = 2.3°$. Figure B.10 shows that no adjustment of the truncation values are needed, even though the size of the design matrices has changed. A nearly perfect fit between the model parameter vectors, $\mathcal{I}$ and $\mathcal{I}_2$, with a correlation coefficient of 1.0 (to 16$^{\text{th}}$ decimal) and differences smaller than $5 \cdot 10^{-6}$ is presented in Figure B.12. No noteworthy improvement was found in the fit of $\boldsymbol{J}_r$, with variance ratios going from 0.05 to 0.09 and differences from 0.4 A/km to 0.6 A/km (Figure B.13(b)). Figure B.11 shows how the amplitude is corrected, however, with a shift of the currents towards lower latitudes, resulting in a slightly larger variance ratio. The shift is also present in the non-zero centred differences for J_r (Figure B.13(b)). No noteworthy change is found in the other components. This is supported by Figure B.11, B.13 and the variance ratios given in the third row of Table B.1.

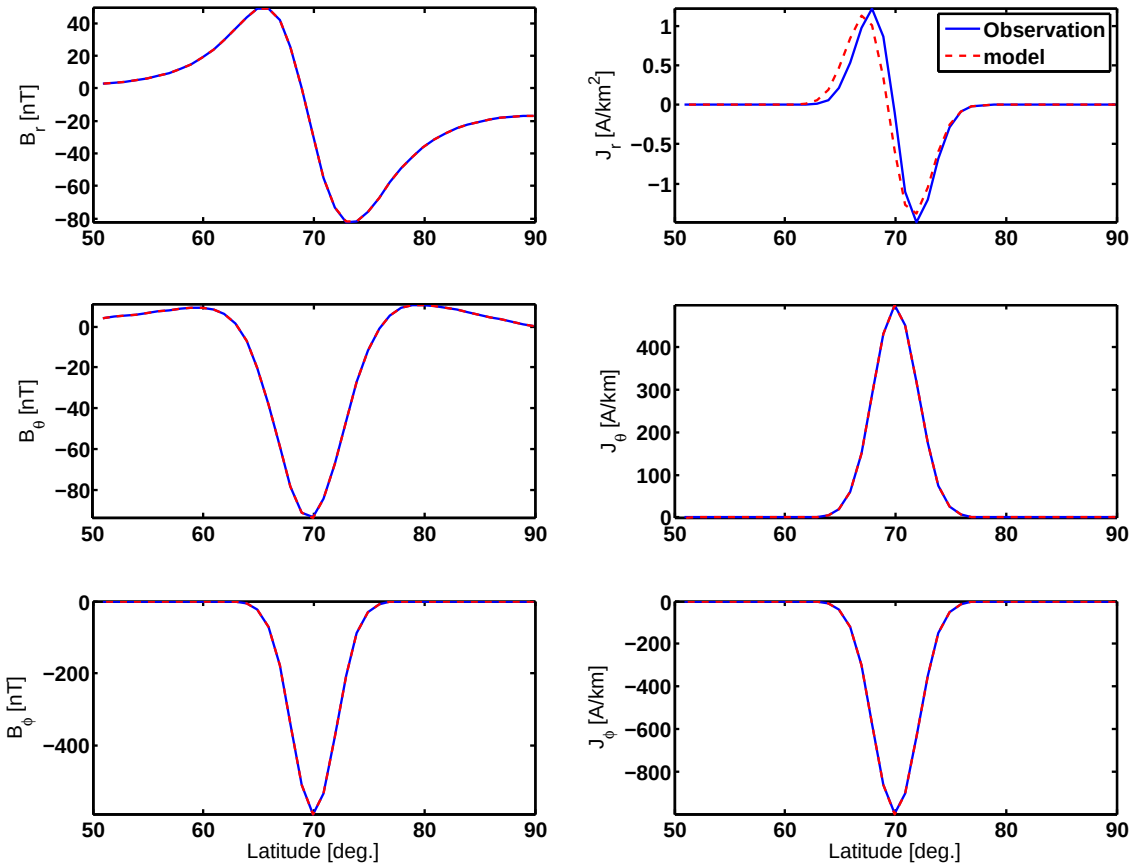

Figure B.11: As Figure B.1, but found using a truncation values $\varepsilon_A = 10^{-3}$, $\varepsilon_M = 10^{-10}$, and model and observations spacings of $\delta\theta^{\text{mod}} = \delta\theta^{\text{obs}} = 1^\circ$.

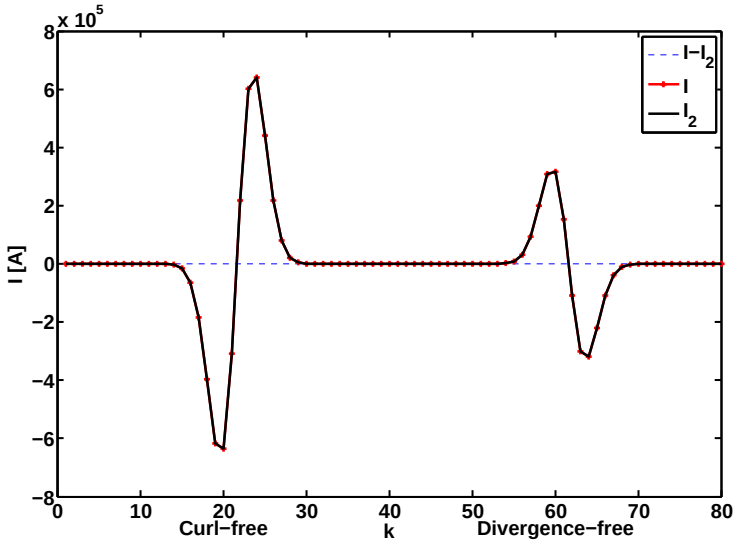

Figure B.12: Model parameters found similar to Figure B.3. Parameters are found with corresponding values of ε_A, ε_M, $\delta\theta^{\text{obs}}$ and $\delta\theta^{\text{mod}}$ as given in Figure B.11.

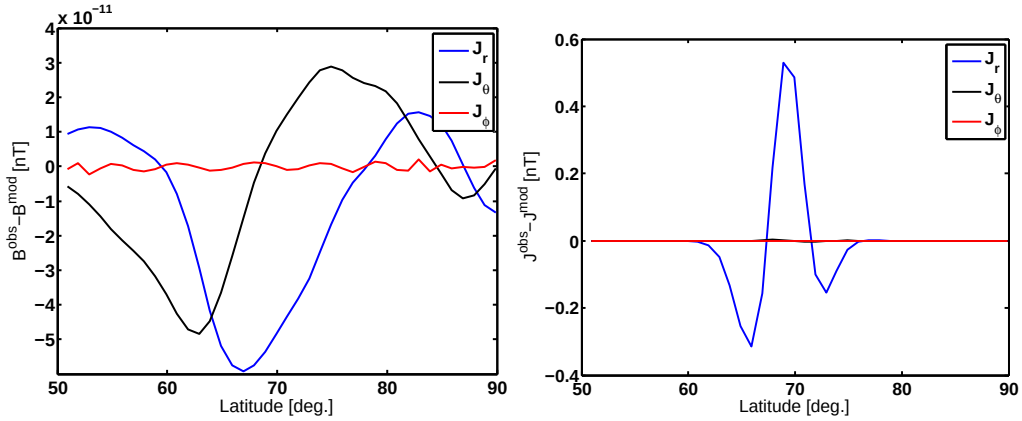

(a) Magnetic field differences **(b)** Sheet current densities

Figure B.13: Differences between virtual observed magnetic field (a) and sheet current densities (b) for the individual components as a function of latitude. The differences are found, corresponding to Figure B.11 using $\varepsilon_A = 10^{-3}$, $\varepsilon_M = 10^{-10}$, $\delta\theta^{\text{mod}} = \delta\theta^{\text{obs}} = 1^\circ$.

If we instead turn the problem into a more realistic overdetermined problem, using twice as many observation points as model parameters, $\delta\theta^{\text{obs}} = 0.5$ and $\delta\theta^{\text{mod}} = 1$, we get the results presented in Figure B.14 to B.16. The singular values have not changed, and the singular value spectrum figure has therefore been left out. The results presented in Figure B.14, differences presented in Figure B.16 and the variance ratios presented in the fourth row of Table B.1 show how the magnetic field components can be recovered to a very high degree of precision. The fit for the sheet current densities has on the other hand decreased significantly with variance ratios for J_θ and J_ϕ decreasing from 10^{-11} and 10^{-30} to 0.08. The change in the ratio $\delta\theta^{mod}/\delta\theta^{obs}$ to an overdetermined problem apparently introduces an instability in the inversion of $\boldsymbol{A}$. This is of less importance when applied to real data, where this inversion is not needed. It does, however, in the synthetic case influence the calculations of the ϕ-component of the virtual magnetic field perturbations, due to the inaccurately assessed curl-free model parameters, which display a piecewise structure, rather than smooth.

Effect of changing the box-car function

In the above, we have presented results, using a box function width of 2.3°. To test the significance of this value, we have in Figure B.17 estimated $\boldsymbol{J}_r$ for various values of $d\delta$. All other components are left out, since only $\boldsymbol{J}_r$ is affected, not including the virtual observations of $\boldsymbol{B}_\phi$. Values for $\delta\theta^{\text{mod}}$, $\delta\theta^{\text{obs}}$, ε_A and ε_M are kept the same as in Figure B.10 to B.13. Figure B.17 shows how the model fit of $\boldsymbol{J}_r$ changes with increasing $d\delta$. The tested box function widths are (a) $d\delta = 1.5^\circ$, (b) $d\delta = 2.0^\circ$, (c) $d\delta = 2.1^\circ$, (d) $d\delta = 2.2^\circ$, (e) $d\delta = 2.3^\circ$, (f) $d\delta = 2.5^\circ$, (g) $d\delta = 3.0^\circ$ and (h) $d\delta = 4.0^\circ$. Changing the box function width does not remove the agreement of the modelled estimates of $\boldsymbol{J}_r$ with the virtual observations, but it greatly affects the amplitude of the modelled $\boldsymbol{J}_r$ signal, so the chosen value of $d\delta$ can therefore not be ignored.

Small values of $d\delta$ might result in loss of signal if no, or only few values of θ_k, fall within the range $[\boldsymbol{\theta_n} - \frac{d\delta}{2}; \boldsymbol{\theta_n} + \frac{d\delta}{2}]$. This may be the case in the results for $d\delta \leq 2$. If the width of the box function, on the other hand, is too wide the smoothing will be too large, resulting in a

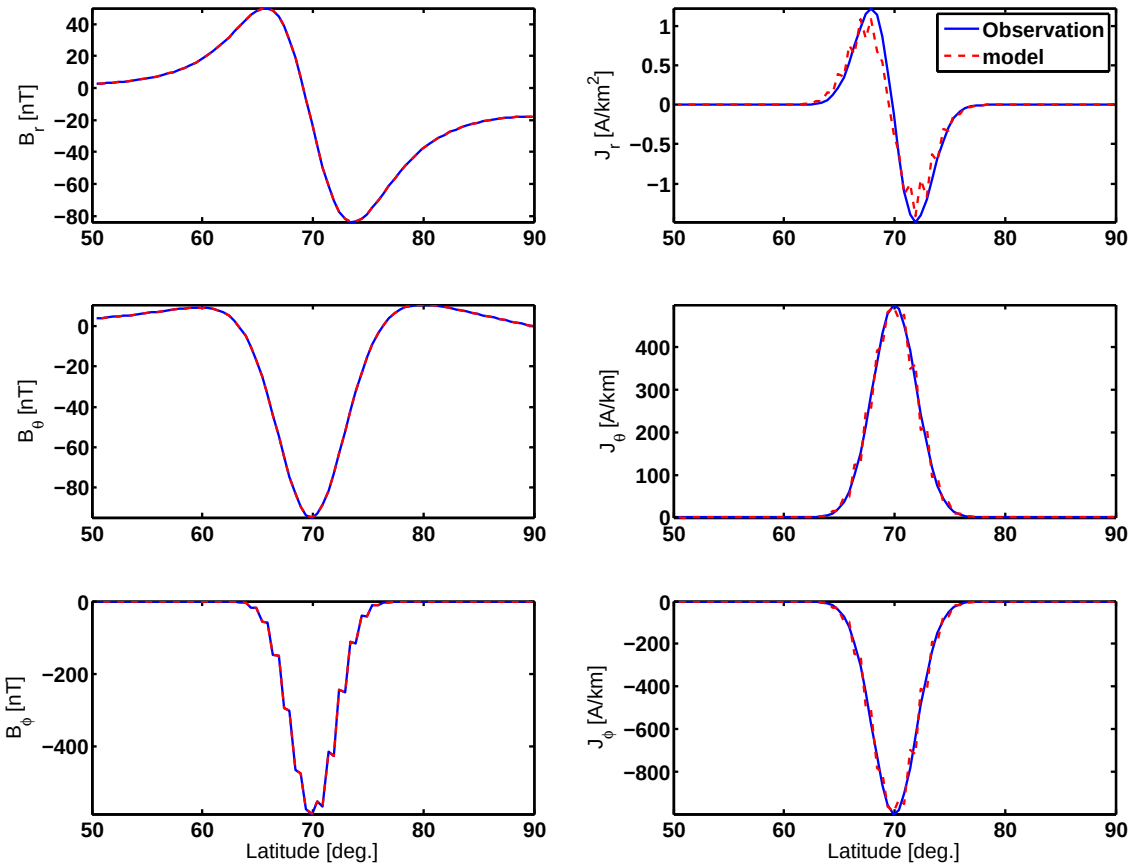

Figure B.14: As Figure B.1 but found using truncation values $\varepsilon_A = 10^{-3}$, $\varepsilon_M = 5 \cdot 10^{-12}$, model and observations spacings of $\delta\theta^{\text{mod}} = 1$ and $\delta\theta^{\text{obs}} = 0.5°$.

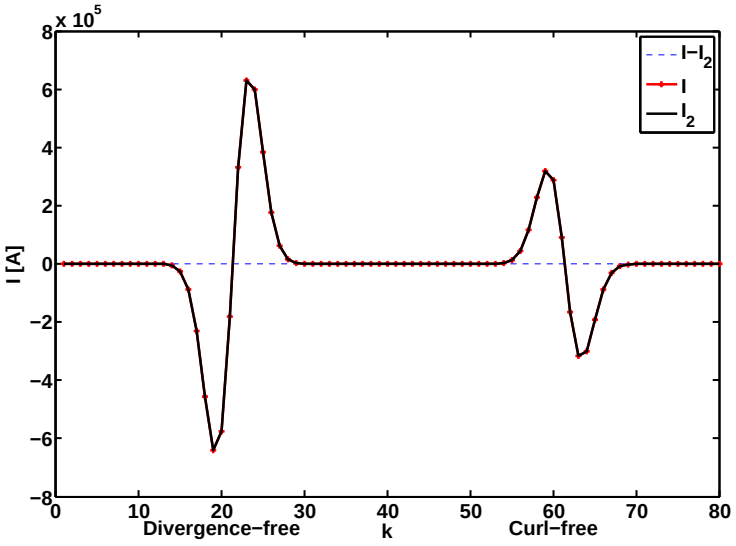

Figure B.15: Model parameters found similar to Figure B.3. Parameters are found with corresponding values of ε_A, ε_M, $\delta\theta^{\text{obs}}$ and $\delta\theta^{\text{mod}}$ as given in Figure B.14.

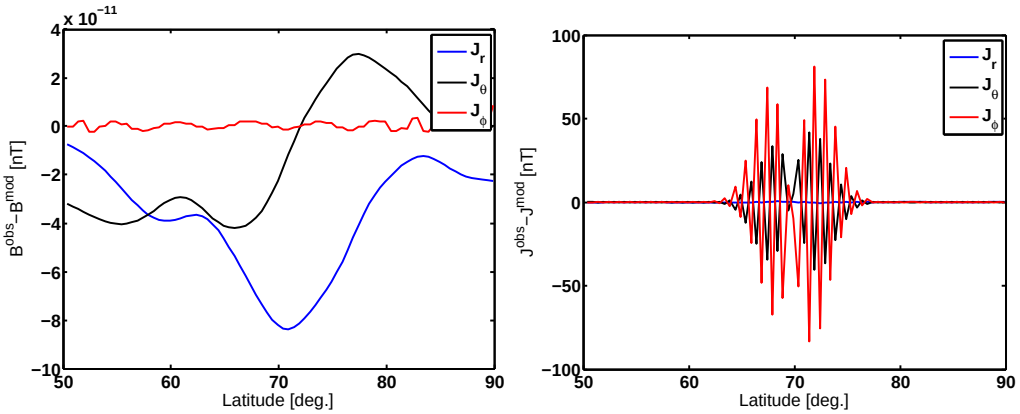

(a) Magnetic field differences **(b)** Sheet current densities

Figure B.16: Differences between virtual observed magnetic field (a) and sheet current densities (b) for the individual components as a function of latitude. The differences are found, corresponding to Figure B.5 using $\varepsilon_A = 10^{-3}$, $\varepsilon_M = 5 \cdot 10^{-12}$, $\delta\theta^{\text{mod}} = 1^\circ$ and $\delta\theta^{\text{obs}} = 0.5^\circ$.

broader, smaller peak, as is seen for results with $d\delta \geq 2.5^\circ$. A spacing of 2.1° is found to best satisfy a large peak and no loss of signal, and will therefore be used in further investigations.

Effect of model parameter and observation grid spacings

Changing the spacing between the model parameters and virtual observations, greatly alters the resultant model fit of $\boldsymbol{J}_r$, as seen when comparing between Figure B.5, B.11 and B.14. We therefore specifically tested the influence of this, keeping the SVD truncation parameters fixed at $\varepsilon_M = 10^{-10}$ and $\varepsilon_A = 10^{-10}$ and the box function width, $d\delta = 2.1^\circ$, constant. The results are presented in Figure B.19 and B.18. The first column of Figure B.19 shows results of $\boldsymbol{J}_r$ for overdetermined cases ($\delta\theta^{\text{obs}} > \delta\theta^{\text{mod}}$), and the second column for underdetermined cases ($\delta\theta^{\text{obs}} < \delta\theta^{\text{mod}}$). The tested spacings are: (a) $\delta\theta^{\text{obs}} = 0.1^\circ$ and $\delta\theta^{\text{mod}} = 0.2^\circ$, (b) $\delta\theta^{\text{obs}} = 0.2^\circ$ and $\delta\theta^{\text{mod}} = 0.1^\circ$, (c) $\delta\theta^{\text{obs}} = 0.1^\circ$ and $\delta\theta^{\text{mod}} = 1^\circ$, (d) $\delta\theta^{\text{obs}} = 1^\circ$ and $\delta\theta^{\text{mod}} = 0.1^\circ$, (e) $\delta\theta^{\text{obs}} = 0.2^\circ$ and $\delta\theta^{\text{mod}} = 1^\circ$, (f) $\delta\theta^{\text{obs}} = 1^\circ$ and $\delta\theta^{\text{mod}} = 0.2^\circ$, (g) $\delta\theta^{\text{obs}} = 0.5^\circ$ and $\delta\theta^{\text{mod}} = 1^\circ$ and (h) $\delta\theta^{\text{obs}} = 1^\circ$ and $\delta\theta^{\text{mod}} = 0.5^\circ$. The figures reveal that the solutions for the overdetermined problem introduce noise into the solution, corresponding to the results given in Figure B.14. This indicates that the numerical noise is not only present in the case of $\delta\theta^{\text{mod}} = 1^\circ$, $\delta\theta^{\text{obs}} = 0.5^\circ$, presented in Figure B.14, but for all overdetermined problems. Results for the underdetermined cases (presented in the second column) return a much less noisy model fit, but with too low amplitudes for $\boldsymbol{J}_r$. Therefore, this is not only the case for $\delta\theta^{\text{obs}} = \delta\theta^{\text{mod}} = 0.5^\circ$ as presented in Figure B.5 and Figure B.19(h).

The exact determined solutions ($\delta\theta^{\text{obs}} = \delta\theta^{\text{mod}}$) are presented in Figure B.18 with (a) $\delta\theta^{\text{obs}} = \delta\theta^{\text{mod}} = 0.1^\circ$, (b) $\delta\theta^{\text{obs}} = \delta\theta^{\text{mod}} = 0.2^\circ$, (c) $\delta\theta^{\text{obs}} = \delta\theta^{\text{mod}} = 0.5^\circ$, (d) $\delta\theta^{\text{obs}} = \delta\theta^{\text{mod}} = 1^\circ$. The shift towards lower latitudes, also found in Figure B.11, is minimized as $\delta\theta^{\text{mod}}$ and $\delta\theta^{\text{obs}}$ decreases, and for $\delta\theta^{\text{obs}} = \delta\theta^{\text{mod}} = 0.1^\circ$ is almost gone. The amplitude of the modelled $\boldsymbol{J}_r$, however, is also decreased with decreasing model and observations spacing, degrading the fit. The underestimated amplitudes man indicate that the solution has been overregularized. Decreasing the truncation value, ε_A to numerically zero, does however, not change the model

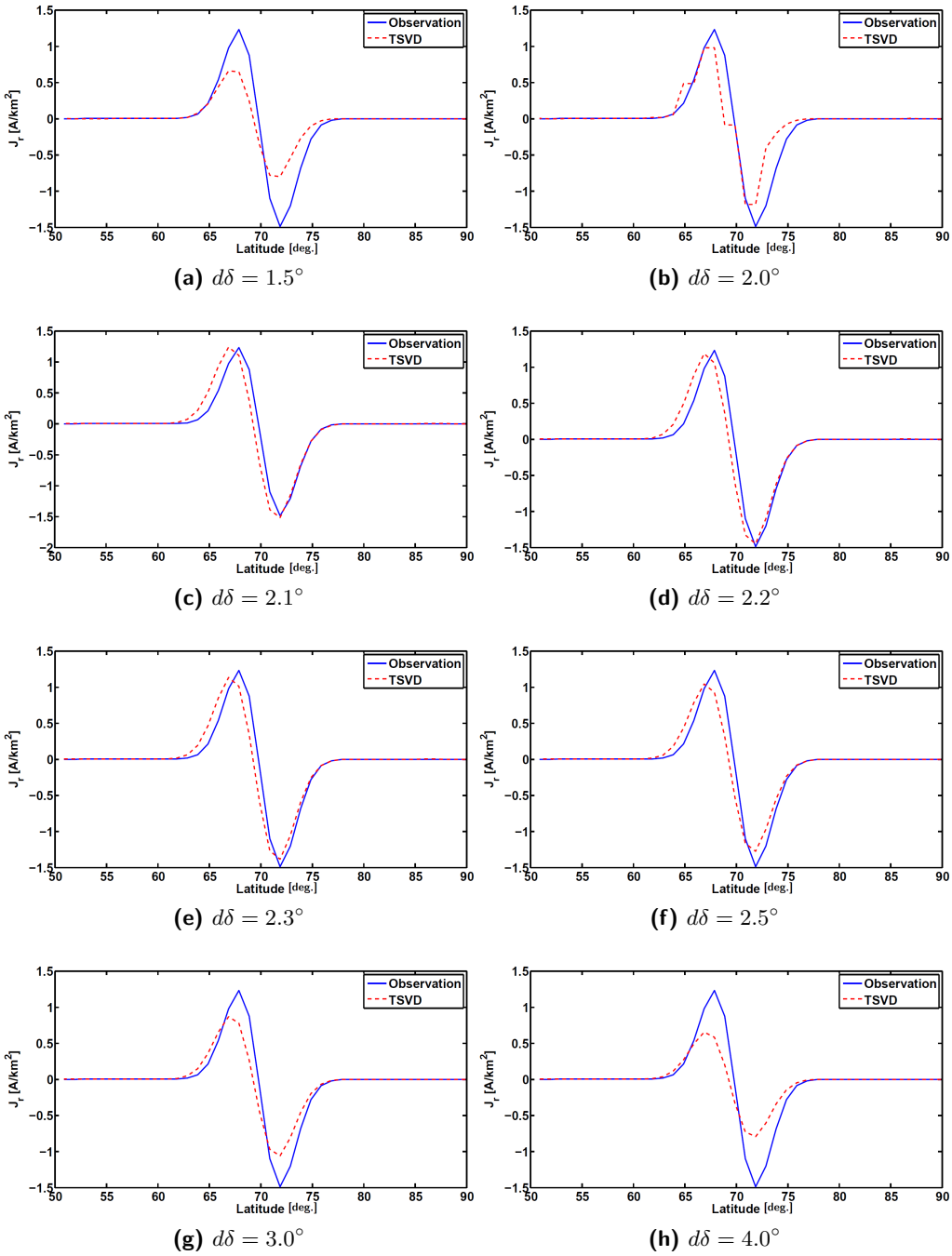

(a) $d\delta = 1.5^\circ$ **(b)** $d\delta = 2.0^\circ$

(c) $d\delta = 2.1^\circ$ **(d)** $d\delta = 2.2^\circ$

(e) $d\delta = 2.3^\circ$ **(f)** $d\delta = 2.5^\circ$

(g) $d\delta = 3.0^\circ$ **(h)** $d\delta = 4.0^\circ$

Figure B.17: Radial component of sheet current density, $\boldsymbol{J}_r$, as a function of latitude for various box function widths, $d\delta$. The sheet current densities are found for constant $\delta\theta^{\text{mod}}$, $\delta\theta^{\text{obs}}$, ε_A and ε_M with values corresponding to Figure B.10.

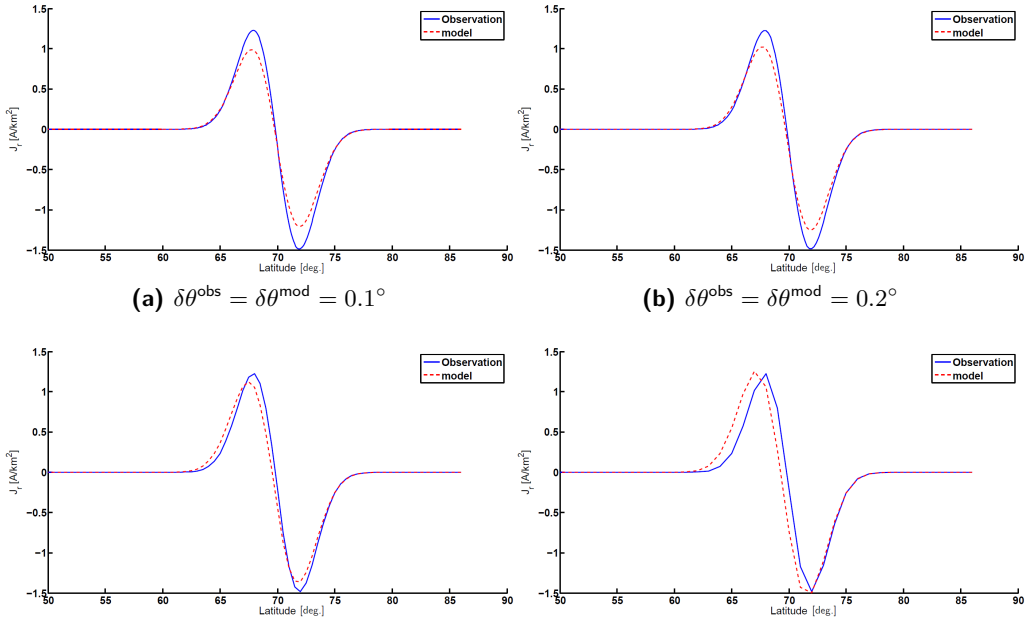

(a) $\delta\theta^{\text{obs}} = \delta\theta^{\text{mod}} = 0.1°$ **(b)** $\delta\theta^{\text{obs}} = \delta\theta^{\text{mod}} = 0.2°$

(c) $\delta\theta^{\text{obs}} = \delta\theta^{\text{mod}} = 0.5°$ **(d)** $\delta\theta^{\text{obs}} = \delta\theta^{\text{mod}} = 1°$

Figure B.18: Figure B.19, continued, showing results for exact determined cases.

fit, and we therefore conclude that the underestimated amplitude is not an issue due to over-regularization.

Figure B.17 previously presented how the box function width $d\delta$ had a large influence on $\boldsymbol{J}_r$. Since a different model and observation spacing could influence the choice of $d\delta$, we repeated the analysis presented in Figure B.17 for $\delta\theta^{\text{obs}} = \delta\theta^{\text{mod}} = 0.2°$. The results presented in Appendix C show, however, that changes to the box-function width is not able to remedy the underestimated amplitudes.

The best choice in model and observation spacing is not obvious from these tests. We were not able to find a solution with both correct amplitude and zero shift. Visual inspection of the model estimates given in Figure B.19 give that the best fits (from the tested model and observation spacings) are found in the underdetermined cases, in particular using $\delta\theta^{\text{obs}} = 1°$ and $\delta\theta^{\text{mod}} = 0.5°$, which will be used in following investigations.

Effect of model and data range

The influence of a point source on the magnetic field will, as previously mentioned, vary with distance according to it's Greens function. This is presented in a very simplified way in Figure B.21. If only a section of the influenced area is selected, $[\theta_1, \theta_2]$, a part of the influence will be excluded, represented by the grey areas, A and B, in the figure. This can introduce a poorly conditioned matrix with associated errors in the inversion. This effect could be part of the reason why regularization is needed, even for the noise-free, synthetic data examples.

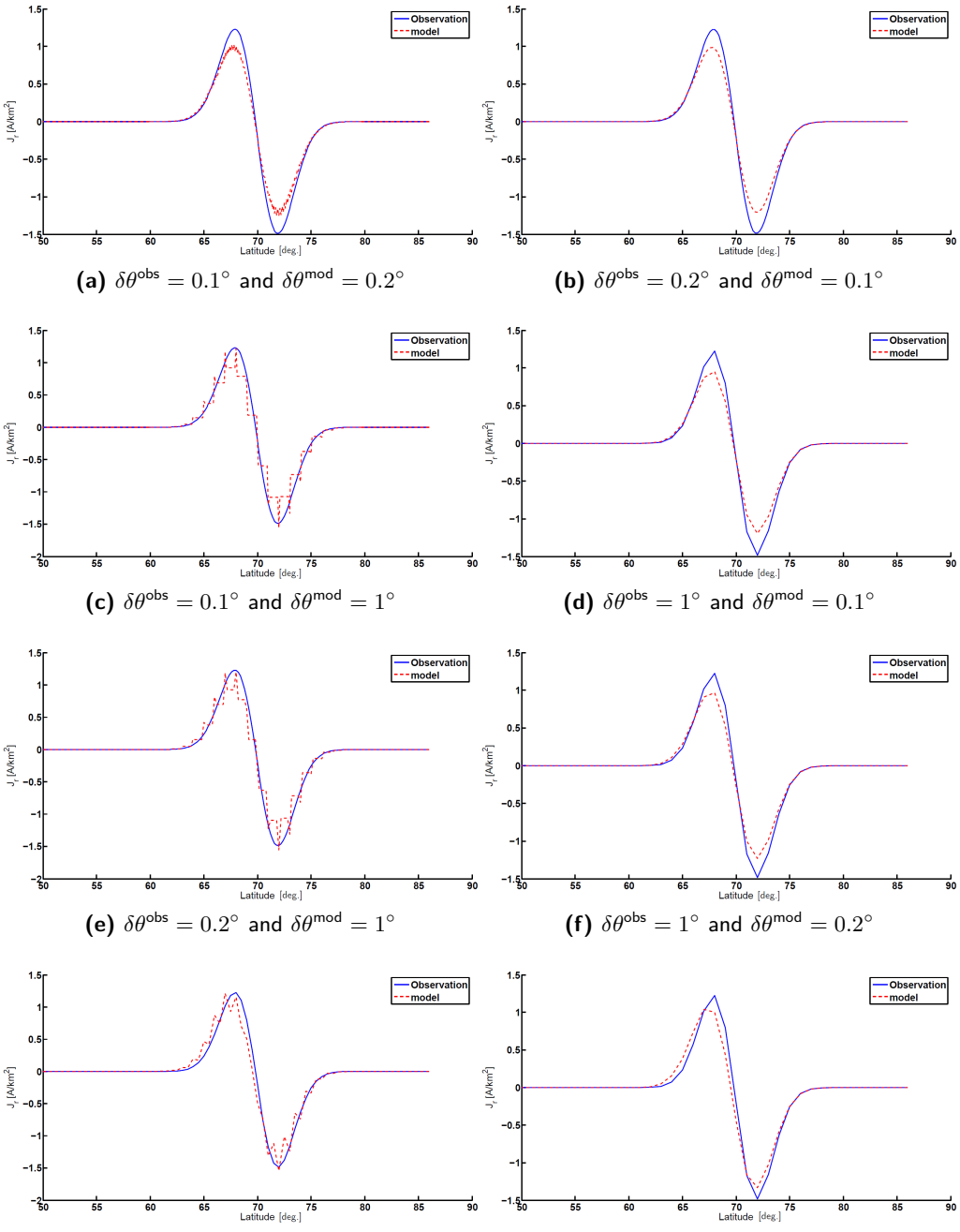

(a) $\delta\theta^{\text{obs}} = 0.1^\circ$ and $\delta\theta^{\text{mod}} = 0.2^\circ$

(b) $\delta\theta^{\text{obs}} = 0.2^\circ$ and $\delta\theta^{\text{mod}} = 0.1^\circ$

(c) $\delta\theta^{\text{obs}} = 0.1^\circ$ and $\delta\theta^{\text{mod}} = 1^\circ$

(d) $\delta\theta^{\text{obs}} = 1^\circ$ and $\delta\theta^{\text{mod}} = 0.1^\circ$

(e) $\delta\theta^{\text{obs}} = 0.2^\circ$ and $\delta\theta^{\text{mod}} = 1^\circ$

(f) $\delta\theta^{\text{obs}} = 1^\circ$ and $\delta\theta^{\text{mod}} = 0.2^\circ$

(g) $\delta\theta^{\text{obs}} = 0.5^\circ$ and $\delta\theta^{\text{mod}} = 1^\circ$

(h) $\delta\theta^{\text{obs}} = 1^\circ$ and $\delta\theta^{\text{mod}} = 0.5^\circ$

Figure B.19: Radial component of sheet current densities, J_r, as a function of latitude for various observation and model spacings. The sheet current densities are found with constant $\varepsilon_M = 10^{-10}$, $\varepsilon_A = 10^{-10}$ and $d\delta = 2.1^\circ$. Left column presents overdetermined cases, and the right column, underdetermined cases.

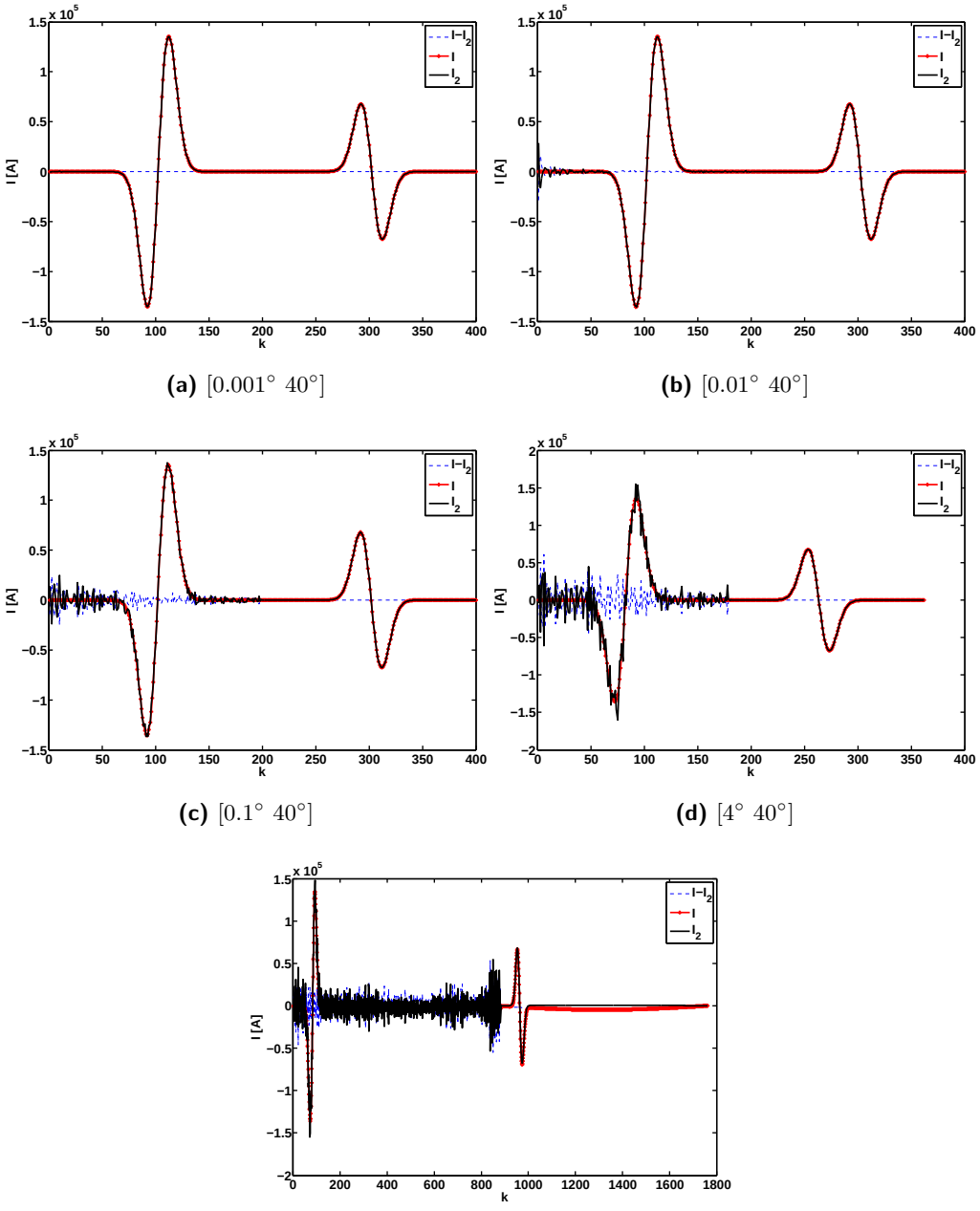

(a) $[0.001^\circ \ 40^\circ]$ **(b)** $[0.01^\circ \ 40^\circ]$

(c) $[0.1^\circ \ 40^\circ]$ **(d)** $[4^\circ \ 40^\circ]$

(e) $[4^\circ \ 180^\circ]$

Figure B.20: Model parameters as a function of index for various model and data range found from sheet current densities, similar to Figure B.3. The results are found with a $\varepsilon_A = \varepsilon_M = 10^{-20}$ and $d\delta = 2.3^\circ$.

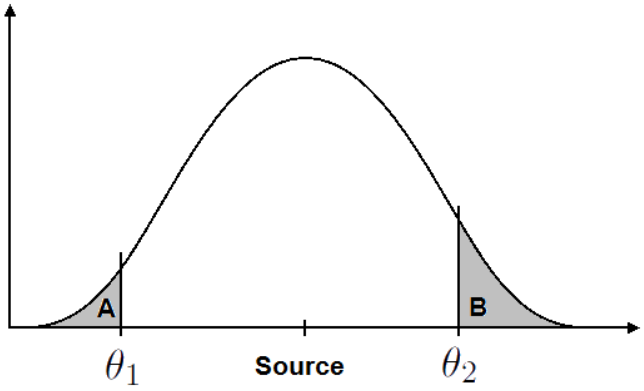

Figure B.21: A schematic presentation of the influence from a point source with co-latitude. A and B indicate the lost influence due to a co-latitude range being too small $[\theta_1\ \theta_2]$.

In search of a more correct estimation of $\boldsymbol{J}_r$, we tested this effect (Figure B.20) by choosing different regions of latitude for both model parameters and virtual observations. The different ranges are (a) 0.001° to 40°, (b) 0.01° to 40°, (c) 0.1° to 40° (d) 4° to 40° (e) 4° to 180°. All figures are found using regularization parameters, $\varepsilon_A = \varepsilon_M = 10^{-20}$ and $d\delta = 2.3^\circ$. The figure is a very clear example of how the range alters the fluctuations of the model parameters and thereby the need for regularization. The previous presented results are found using the range given in (d), which shows that the chosen truncation parameter in this case is a clearly unstable solution. Expanding the range equatorward (higher co-latitudes) as presented in (e) does not change the need for regularization. It is however minimized by a poleward expansion as presented in (a) to (c). The need for regularization seems to be directly correlated with the inclusion of area closer to the magnetic pole, with no need for further regularization for the range 0.001 to 40. This indicates that problems related to truncation of the Green's function are present for ranges starting more than 0.01° away from the pole. It does, however, not improve the fit for $\boldsymbol{J}_r$ (not shown).

Appendix C

Positions of peak sheet current density

The following pages presents table values of the median QD latitudes of the peak sheet current density, $\boldsymbol{J}^{\text{peak}}$, with activity level, Kp, and MLT for 10 years of CHAMP data and two years of Swarm Alpha and Bravo data. The values are presented in Figure 8.10. Table C.3 and C.4 give the number of measurements in each bin.

MLT/$\boldsymbol{Kp}$	**0-1**	**1-2**	**2-3**	**3-4**	**4-5**	**5-6**	**6-7**	**7-8**
01	21.17	21.83	22.96	23.46	25.11	27.47	25.95	26.07
03	20.28	21.89	22.78	23.75	24.82	27.25	26.52	29.89
05	17.97	20.04	21.19	21.80	23.60	25.01	26.21	25.63
07	16.48	17.54	18.39	20.09	21.29	22.43	23.22	20.77
09	16.58	16.35	17.34	18.62	19.79	20.74	21.88	20.09
11	16.72	16.03	16.38	16.77	17.58	18.79	16.78	19.21
13	15.76	14.99	16.01	18.18	18.49	19.11	23.45	23.60
15	16.13	16.18	17.07	17.83	19.98	19.67	25.72	23.92
17	16.63	17.65	18.77	19.76	22.04	23.18	27.22	29.40
19	17.95	19.58	21.11	21.98	23.48	25.48	27.69	31.28
21	19.51	20.95	22.16	22.97	23.87	23.38	27.55	27.32
23	19.67	20.69	21.48	22.23	23.05	23.66	26.48	28.49

Table C.1: Mean $\boldsymbol{J}^{\text{peak}}$ as a function of MLT and Kp corresponding to Figure 8.10 for the Northern Heimsphere.

MLT/Kp	0-1	1-2	2-3	3-4	4-5	5-6	6-7	7-8
01	17.18	18.65	19.33	19.91	21.96	24.18	22.36	26.79
03	15.75	16.66	18.52	19.54	20.58	22.81	23.88	23.79
05	14.97	15.72	16.89	19.13	20.93	20.11	21.45	21.75
07	15.39	15.16	15.56	17.48	17.97	19.96	21.14	23.62
09	15.51	14.92	15.24	16.85	16.52	16.92	19.79	21.94
11	15.75	16.92	15.94	16.03	15.55	16.54	15.18	13.61
13	14.85	14.84	15.04	15.74	17.08	17.67	25.13	22.63
15	15.78	14.92	15.41	16.83	18.92	17.93	22.49	22.86
17	15.93	15.29	16.00	17.35	19.28	20.78	26.66	29.86
19	16.19	16.26	18.17	18.99	22.29	24.50	29.17	32.17
21	15.87	17.50	18.84	20.21	21.18	23.73	24.54	26.31
23	16.52	19.73	19.38	19.66	20.46	22.76	21.34	23.83

Table C.2: As Table C.1 for the Southern Hemisphere.

MLT/Kp	0-1	1-2	2-3	3-4	4-5	5-6	6-7	7-8
1	3366	3111	2735	1498	554	186	60	47
3	3447	3248	2351	1342	547	204	72	29
5	3636	3143	2423	1381	524	199	54	10
7	3643	3205	2449	1451	520	188	69	29
9	3620	3440	2573	1437	553	202	40	18
11	3811	3355	2561	1412	536	194	54	28
13	3421	3240	2430	1342	521	205	67	28
15	3783	3113	2350	1340	527	198	59	9
17	3523	3243	2507	1406	528	180	68	25
19	3736	3438	2492	1448	534	180	42	22
21	3857	3334	2480	1411	549	200	52	28
23	3409	3115	2695	1532	563	202	65	49

Table C.3: Number of data points used to estimate the median QD latitude of the peak sheet current densities, given in Figure 8.10 for the Northern Hemisphere. The first column gives the MLT, and the Kp intervals are given in the first row.

MLT/Kp	0-1	1-2	2-3	3-4	4-5	5-6	6-7	7-8
1	3430	3174	2615	1499	549	188	65	53
3	3483	3148	2462	1390	522	206	70	29
5	3780	3246	2318	1290	544	211	56	4
7	3567	3263	2493	1397	538	166	63	21
9	3766	3404	2459	1489	516	191	43	28
11	3775	3282	2558	1438	551	205	48	32
13	3522	3215	2355	1355	562	211	66	30
15	3566	3253	2385	1400	526	184	54	12
17	3701	3215	2512	1409	517	193	57	29
19	3549	3398	2633	1474	576	209	53	20
21	3724	3259	2607	1428	512	192	49	20
23	3455	3213	2661	1405	537	182	80	42

Table C.4: As Table C.3 for the Southern Hemisphere.

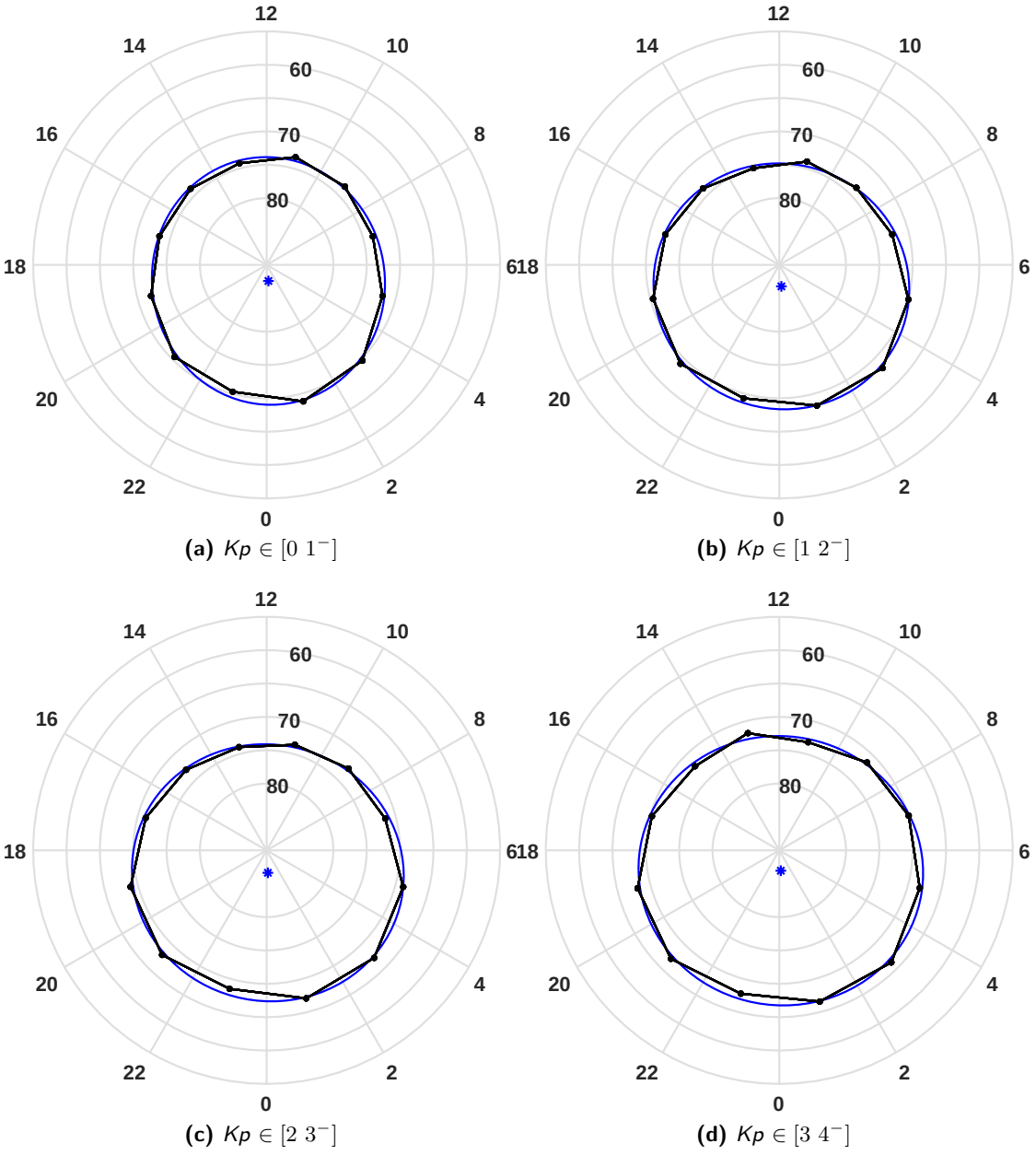

(a) $Kp \in [0\ 1^-]$ **(b)** $Kp \in [1\ 2^-]$

(c) $Kp \in [2\ 3^-]$ **(d)** $Kp \in [3\ 4^-]$

Figure C.1: Elliptic fit (blue) to median QD latitude (black) of the peak sheet current density, $\boldsymbol{J}^{\text{peak}}$, in the Northern Hemisphere, as a function of MLT for four different Kp intervals. Positions correspond to Figure 8.10(a). Fit values are listed in Table 8.1.

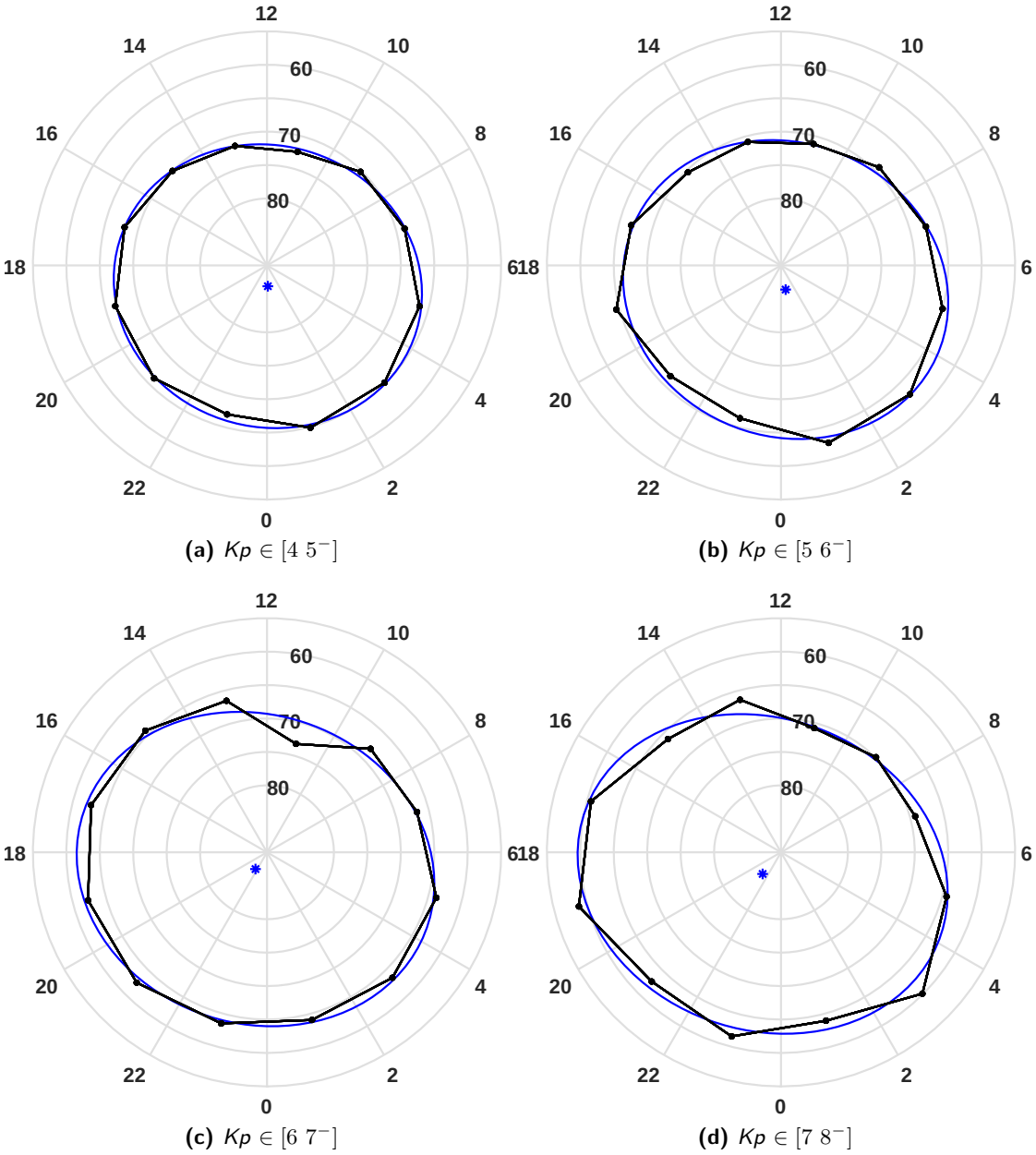

(a) $Kp \in [4\ 5^{-}]$ **(b)** $Kp \in [5\ 6^{-}]$

(c) $Kp \in [6\ 7^{-}]$ **(d)** $Kp \in [7\ 8^{-}]$

Figure C.2: Figure C.1, continued with five additional Kp ranges.

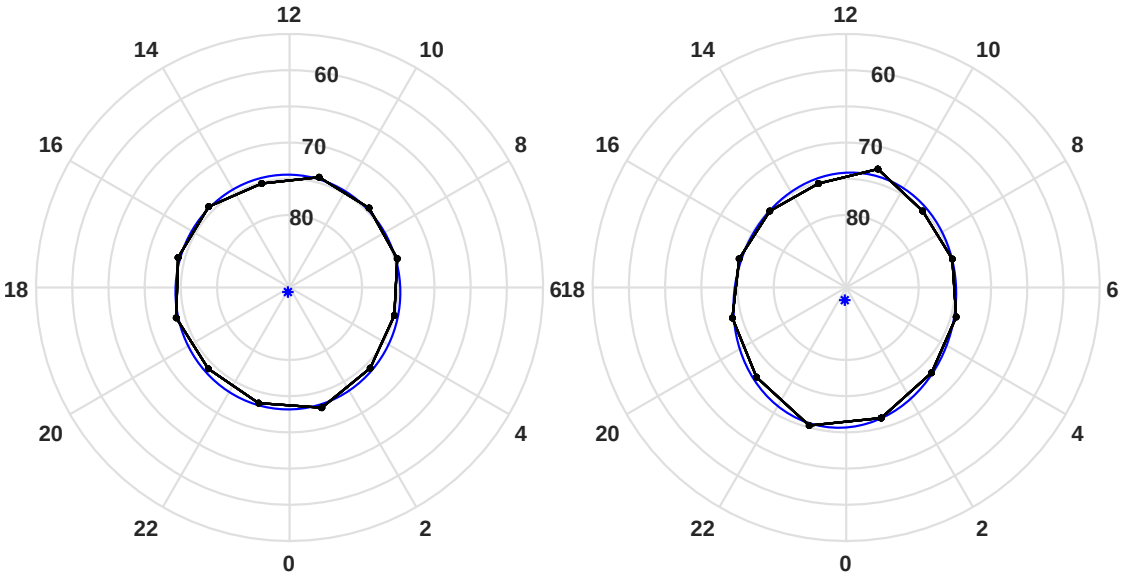

(a) $Kp \in [0\ 1^-]$ **(b)** $Kp \in [1\ 2^-]$

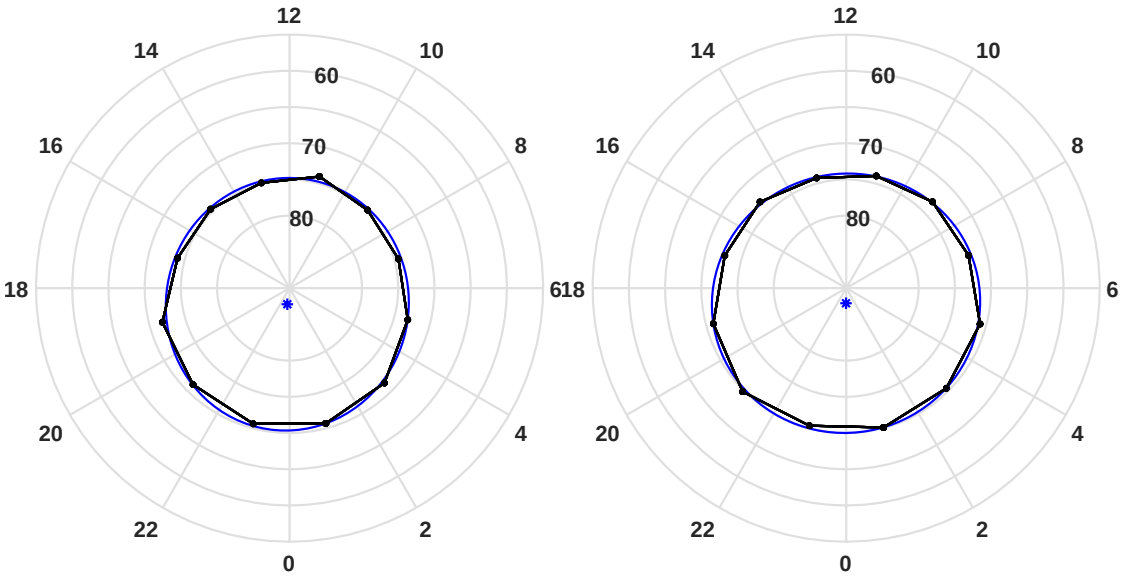

(c) $Kp \in [2\ 3^-]$ **(d)** $Kp \in [3\ 4^-]$

Figure C.3: As Figure C.1, for the Southern Hemisphere. Fit values are listed in Table 8.2.

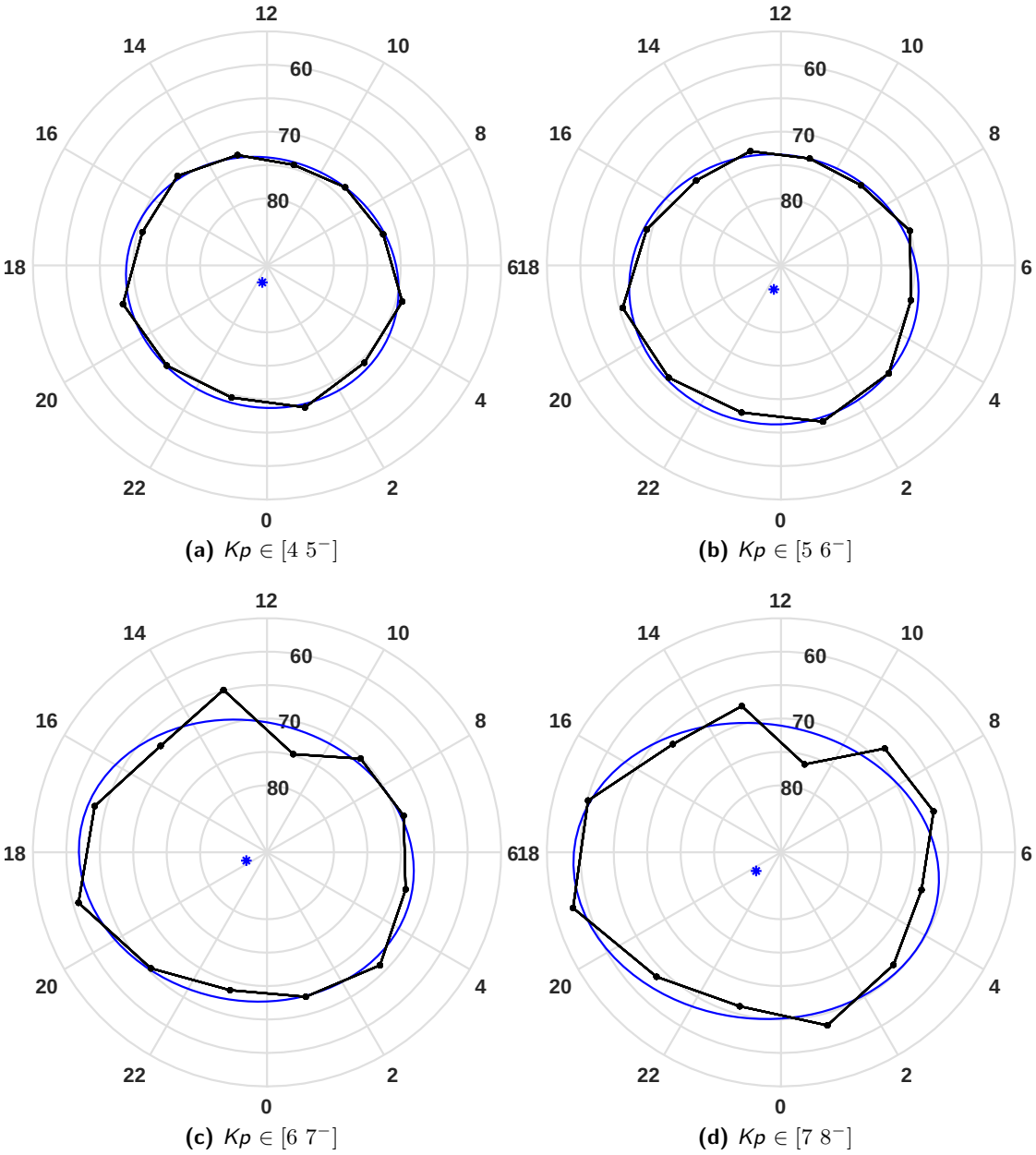

(a) $Kp \in [4\ 5^{-}]$ **(b)** $Kp \in [5\ 6^{-}]$

(c) $Kp \in [6\ 7^{-}]$ **(d)** $Kp \in [7\ 8^{-}]$

Figure C.4: Figure C.3, continued with five additional Kp ranges.

Appendix D

Results from intensity model

The following pages present results for the IM method for the 1st of January 2015 and 4th of January 2015 in Figure D.1 and D.2. Figures D.3 to D.6 shows the results for the 1D SECS, 2D SECS, LCM and IM method for the 6th of November 2001 and 24th of January 2015.

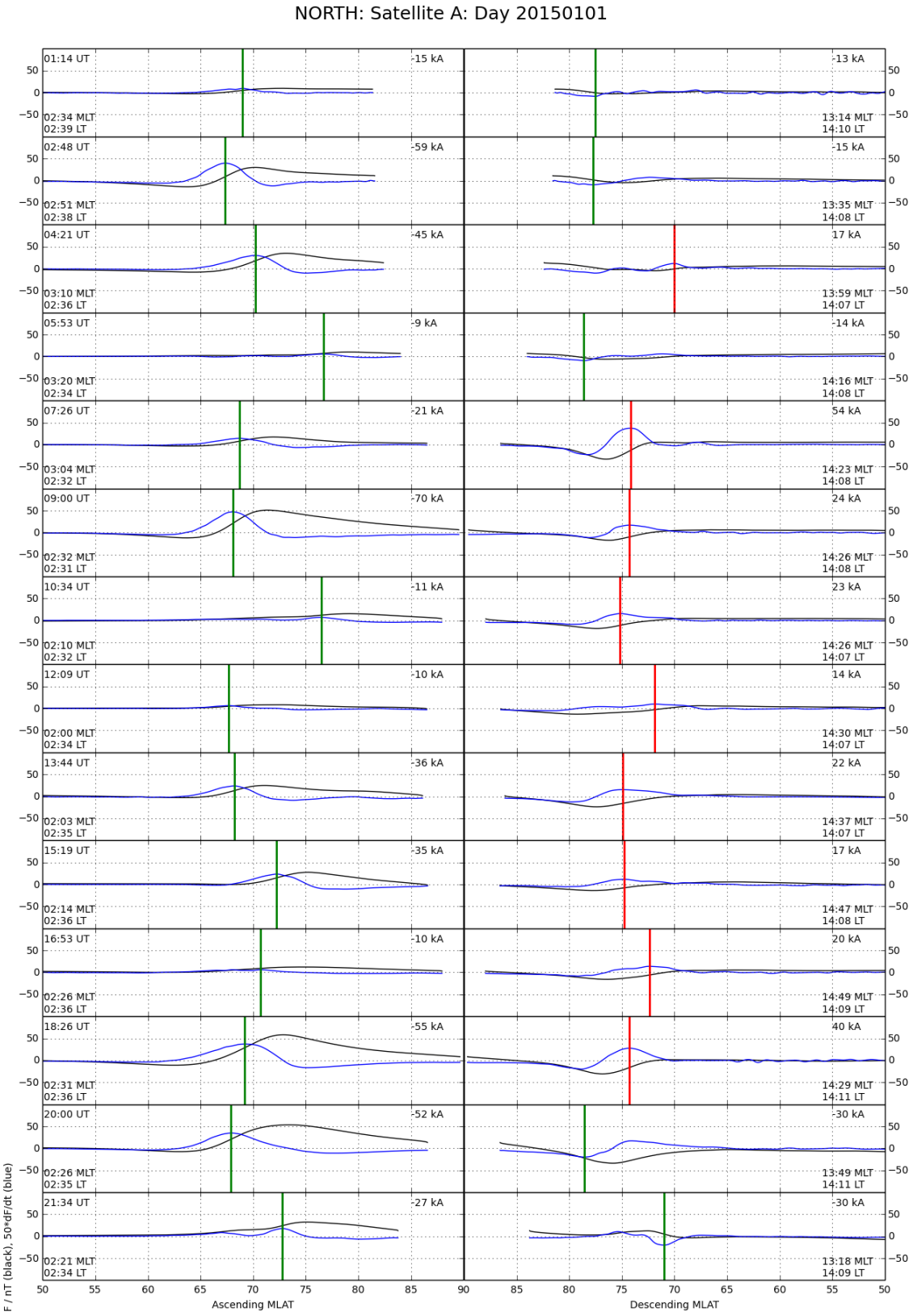

Figure D.1: IM estimates of the peak sheet current density for the 1st of January 2015, divided into ascending (left) and descending (right) orbits.

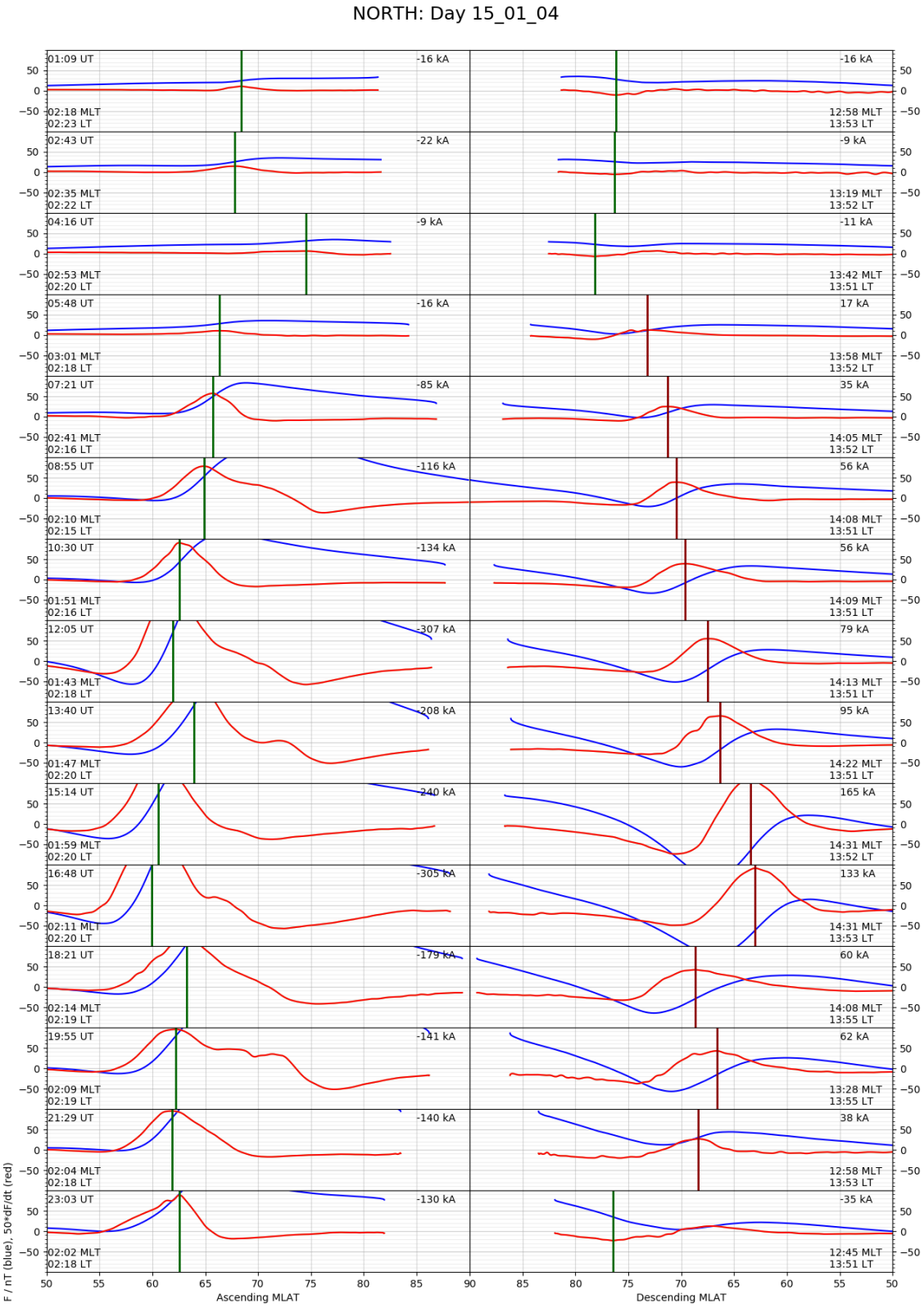

Figure D.2: IM estimates of the peak sheet current density for the 4th of January 2015, divided into ascending (left) and descending (right) orbits.

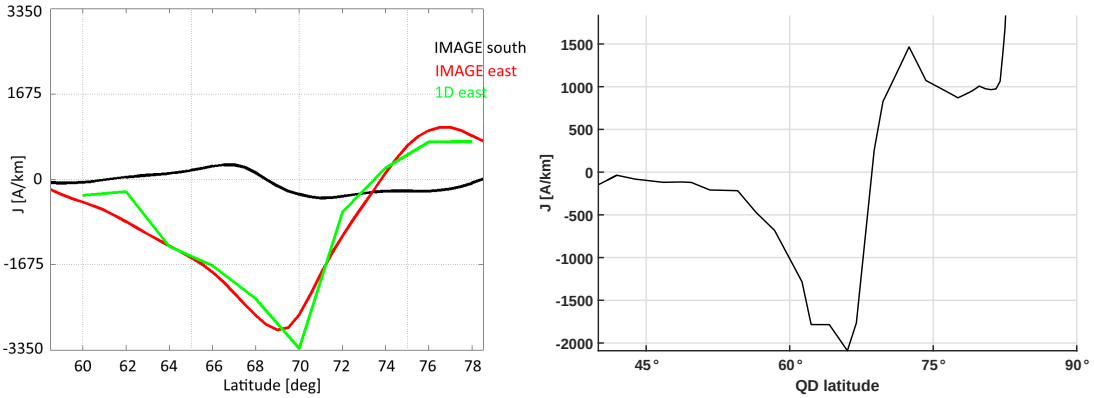

(a) Source: Juusola [2016] **(b)** This thesis

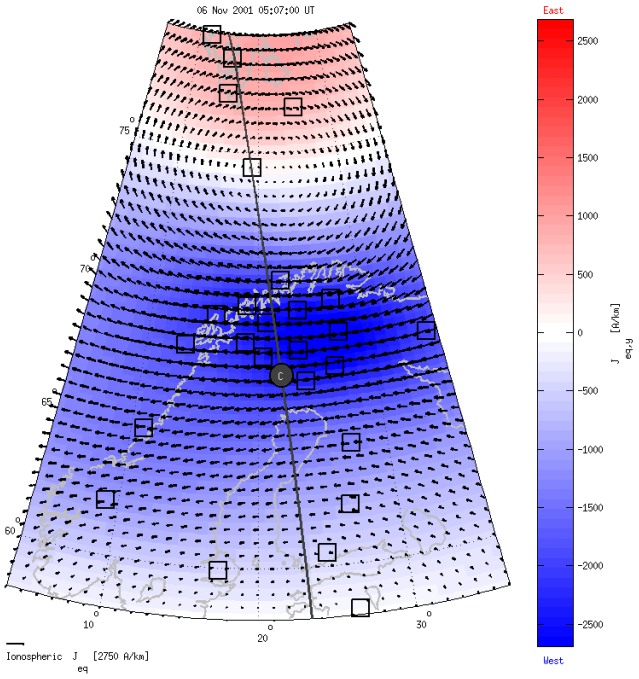

(c) Source: Juusola [2016]

Figure D.3: Auroral sheet current densities for an western electrojet crossing, estimated by (a) 1D SECS method, provided by Liisa Juusola [Juusola, 2016], (b) LCM and (c) 2D SECS method, also provided by Liisa Juusola [Juusola, 2016] for the 6th of November 2011 from 04:47 to 05:13 UT (CHAMP orbit 7383). The polar crossing was during moderately disturbed magnetic activity with a Kp value of 9^-. The green line in (a) marks the 1D SECS solution, the red, the estimated 2D SECS solution along the satellite track, and the black, the magnetic field residuals. (b) is found using a minimization of the second order difference of the L_1 norm including a Huber weighted misfit measure. The last figure (c) gives the full 2D SECS solution with the satellite track of Alpha and Charlie marked by the black lines, and the sheet current density given in colour. Red marks an eastern current, and blue, a western current, and black arrows the strength and direction of the sheet currents. A reference arrow is printed in the bottom left corner of the figure. Estimates given in (a) and (b) are based on *Swarm* A observations of the magnetic residual field.

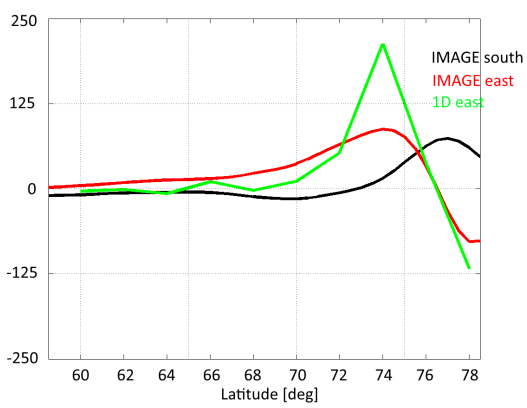

(a) Source: Juusola [2016]

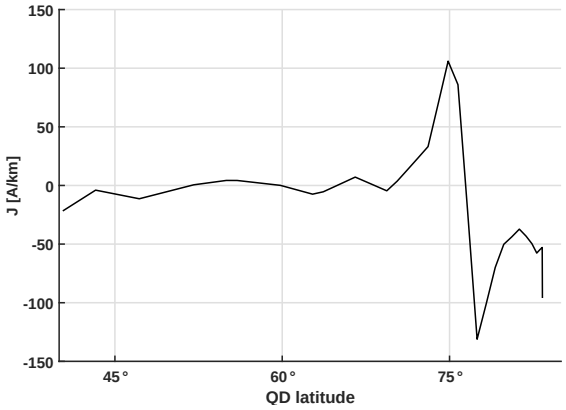

(b) This thesis

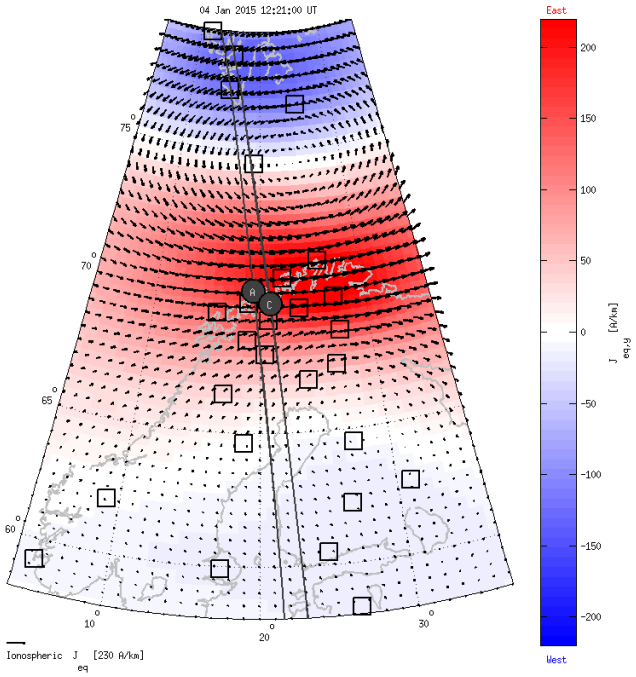

(c) Source: Juusola [2016]

Figure D.4: As Figure D.3 for an eastern electrojet crossing, on the 24th of January 2015 from 11:48 to 13:22 UT (Swarm Alpha orbit 6554). The polar crossing was during slightly disturbed magnetic activity with a Kp value of 2^-.

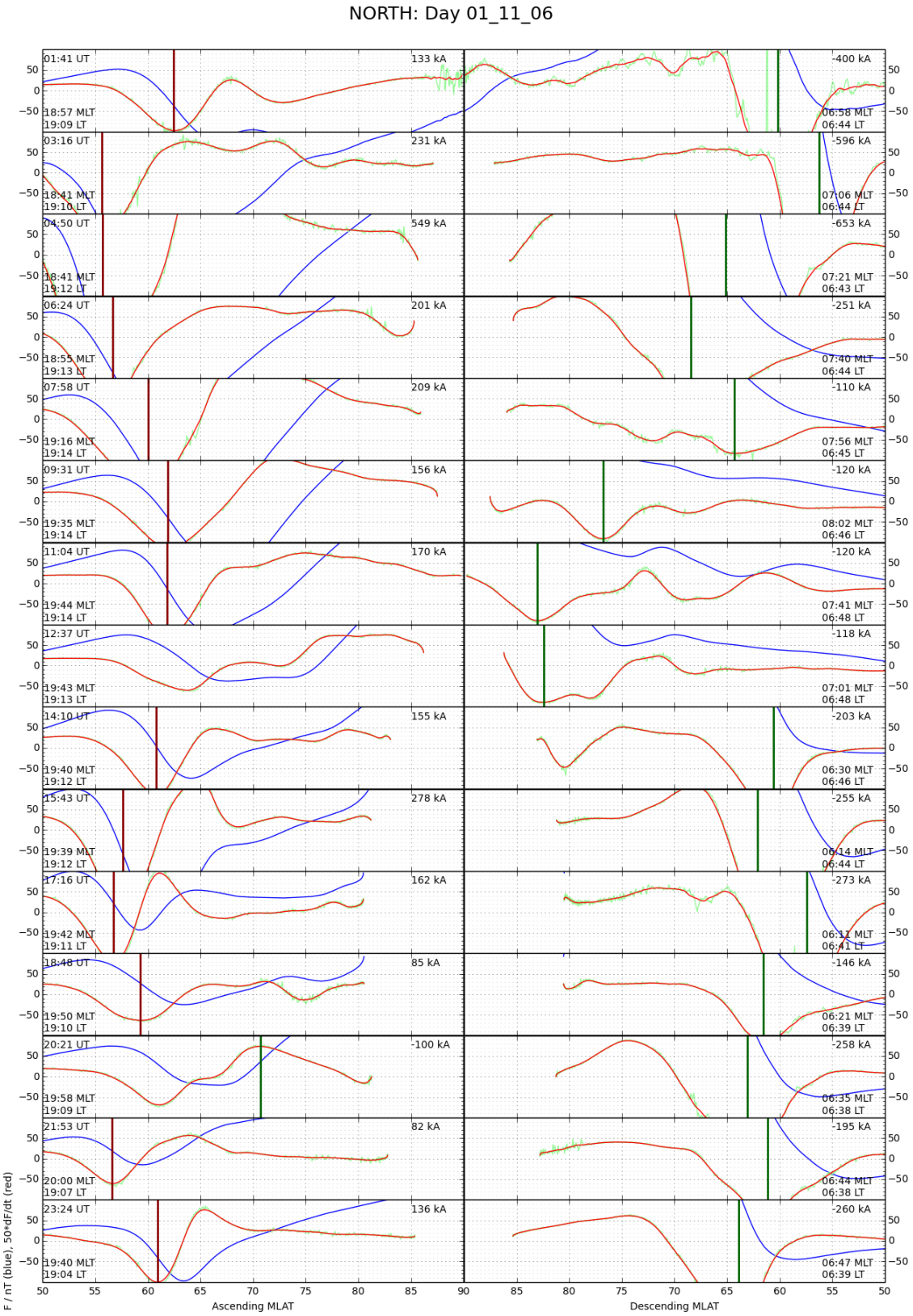

Figure D.5: IM estimates of the peak sheet current density for the 11th of November 2001, divided into ascending (left) and descending (right) orbits.

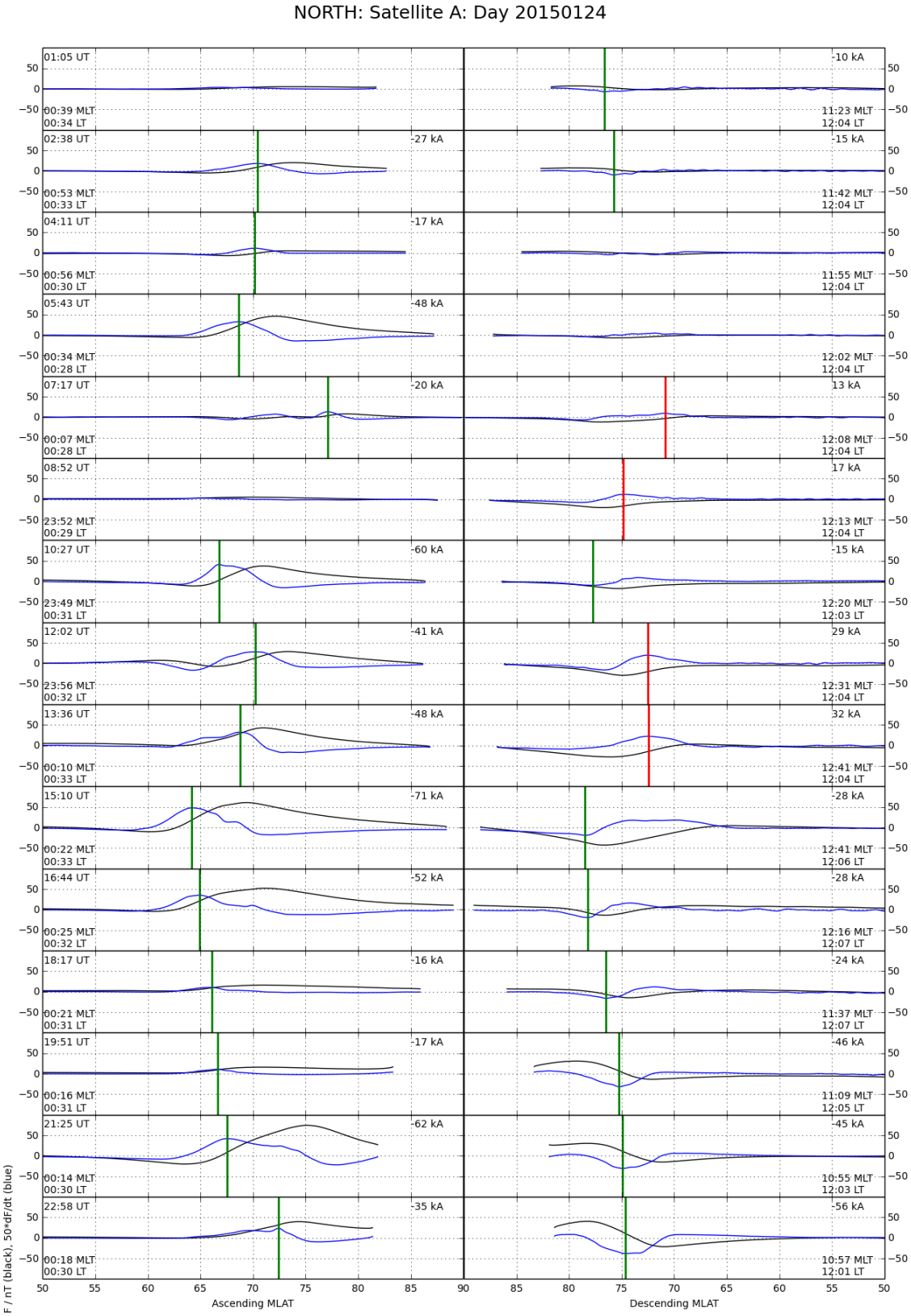

Figure D.6: IM estimates of the peak sheet current density for the 24th of January 2015, divided into ascending (left) and descending (right) orbits.